Electronic Theses and Dissertations   Graduate School

2014

Broadband Approaches And Beam-Scanning Techniques For Reflectarray Antennas

Yilin Mao
University of Mississippi

BROADBAND APPROACHES AND BEAM-SCANNING TECHNIQUES FOR

REFLECTARRAY ATNENNA

A Dissertation
presented in partial fulfillment of requirements
for the degree of Doctor of Philosophy
in Engineering Science
The University of Mississippi

by

YILIN MAO

August 2014

ABSTRACT

Reflectarray antennas combine the numerous advantages of reflector antennas and phased array antennas and create a hybrid high-gain antenna with a low-profile, low-mass, easy-fabrication, and diversified radiation performance. However, it still has some inherent drawbacks, such as limited bandwidth and scanning range, which are targeted in this dissertation.

- At first, the array theory approach for radiation analysis of reflectarray antennas is described and implemented. Numerical results are then presented and compared with reference results to confirm its reliability.

- As the most critical influential factor to the reflectarray bandwidth, the element bandwidth was studied at first, and the effects of element shape and substrate thickness were investigated.

- Then, a comprehensive study was performed to investigate the bandwidth performance of reflectarrays on the system level. The effect of aperture size, element bandwidth and phase synthesis method was discussed in sequence. Particularly, a novel phase synthesis approach was proposed, which enables reflectarray to achieve a significant bandwidth improvement even with elements of narrow bandwidth. Prototypes are fabricated and tested to validate the idea.

- Since the reflectarray antenna is a hybrid product of reflector and phased array antennas, its main beam could be steered by either rotating its feed or reconfiguring its element phases. The former way was explored at first. An improved phase design was proposed for reflectarrays mimicing parabolic-cylindrical reflectors to expand its scanning range.

- The published achievements of reconfigurable reflectarrays design are reviewed and it is found that currently efficiency is a big problem. A 1-bit 10×10 reconfigurable reflectarray using PIN diode was designed, fabricated and measured to explore the energy loss, and experimental results showed that 14% efficiency could be reached.

In summary, some improved designs regarding bandwidth and scanning performance for reflectarrays are proposed in this dissertation. Various factors affecting reflectarray bandwidth are investigated, which shall provide some guidelines regarding bandwidth improvement. On the other hand, two designs are presented to explore the beam scanning characteristic of reflectarray antenna, by mechanical and electrical ways respectively. Several prototypes have been fabricated and measured, demonstrating the novel features and potential applications of reflectarray antennas.

DEDICATION

This work is dedicated to my dear friends, Lisen Zhu and Lili Du, and my dear sister, Wenjuan

Luo, without whose love and support I could not finish it.

ACKNOWLEDGMENTS

I would like to sincerely thank my advisors Dr. Atef Z. Elsherbeni and Dr. Fang Yang. I could not make it without their guidance, help, encouragements and support. They lead me into the amazing world of electromagnetics, and more importantly, they show me how a good researcher should be. I am so grateful that they are always open for my ideas, motivate me to execute it, follow up and give suggestions to my results and findings. They also gave me the chance to conclude and decide the next in light of their mentorship. I learned a lot from them, and feel so lucky that I met them in Olemiss and became one of their students. I am really so proud of it. I would also like to thank Dr. Ramanarayanan Viswanathan and Dr. Xin Dang for serving as my committee members. Thanks are also given to Dr. Kaifong Lee for his help, as well as to Dr. Ang Yu and Dr. Payam Nayeri for their technical support.

I want to thank my parents; without their love and support, I would not come to US to pursue this Ph.D. program, which opens a whole new world for me. The study life in Oxford will be a beautiful memory in all my life.

I would also like to thank my best friends Wenjuan Luo, Lisen Zhu, Lili Du, and Qian Qiao for their always accompany with me during the tough time in my graduate study, as well as Fang Guo, who assisted me a lot when I was in Tsinghua University. I would also like to thank my other colleges in Olemiss and Tsinghua.

TABLE OF CONTENTS

LIST OF FIGURES

LIST OF TABLES

CHAPTER I

INTRODUCTION

1.1 An Overview of Reflectarray Antenna Development

As a combination of traditional parabolic reflector and phased array antenna, microstrip reflectarray has become a popular choice for high-gain antenna for long distance communications. The reflectarray antenna received a lot of attention since the revolutionary breakthrough of printed circuit technology in the 1980's, which enables the easy-fabrication and makes it more attractive. It substitutes the bulky curved surface of reflector antenna with a planer radiation array while it takes use of space-fed way to eliminate the design of the complicated power dividing and feeding networks, which hence greatly reduce the insertion loss of transmission line existing in phased array antenna.

The principle of reflectarray has been explained in books and lots of papers such as [1]. Briefly, by appropriately tailoring the reflection phase of each element on the aperture surface, it could generate a required reflection pattern out of the incoming wave on the reflectarray. For example, in order to form a high-gain pencil beam, the reflectarray is manipulated to yield a planer reflected phase front perpendicular to the given pointing direction.

The reflectarrays have a severe drawback of narrow bandwidth performance which is mainly due to two factors [1]: the inherent narrow bandwidth behavior of microstrip elements

and the differential spatial phase delay resulting from different path lengths from the feed to each element. The latter is more restrictive on the element phase in term of frequency behavior that it requires the element to have an ideal phase-shift proportional to the frequency, which shall be − βL with β being the propagation constant in the air. However, as demonstrate in [2], the bandwidth limitation produced by the differential path lengths is only significant for electrically very large apertures with small f/D ratios, and it has been demonstrated in[3] that by using True Time Delay (TTD) technique, this problem could be solved. Actually, more study has been performed to address the former one, which is the dominant factor of narrow bandwidth performance for reflectarrays of a medium size. Normally after carefully tuning the element dimension the phase curves obtained at different frequencies are almost parallel with each other, which means an excellent element bandwidth behavior. In some published work, it is reported that simulated 1 dB bandwidth of more than 19% could be achieved with peak efficiency of 62% reached [4].

In addition, as another attractive feature, the research of the beam scanning capability of microstrip reflectarray has received a lot of attention recently. For reflector antennas, beam scanning is often realized by mechanically rotating the antenna or its feed, while for phased array, it is achieved by varying the excitation phase or amplitude of each element. As a combination of these two antennas, reflectarray is able to carry on the beam-scanning by either of these two ways, which provides more design choices. Table 1-1 summaries the independent control ability over each single element for these three types of antennas. Apparently although the spatial illumination helps to deduce the energy loss, it makes the reflectarray to lose the independent control of the excitation amplitude of each single element, which somehow limits the scanning range compared to phased array antenna.

Table 1-1 The comparison of independent control ability over each single element between reflector, phased array and reflectarray antenna.

Independent control of	Phase of single element	Amplitude of single element
Reflector	No	No
Phased array	Yes	Yes
Reflectarray	Yes	No

1.2 The State of the Art Research

One of the main drawbacks in reflectarray designs is its limited bandwidth performance, which is inherent with the microstrip printed structures. Single and multi-layer reflectarrays have been designed to achieve broad band performance with various complicated element shapes. Considerable improvements have been made and many experimental studies have been published. Different bandwidth improvement techniques such as multi-layer element structures, true time-delay lines, and subwavelength elements have been studied and bandwidths of more than 20% have been reported.

On the other hand, the design of reflectarrays with wide scanning angles is also a challenging field. The compensation phases of the elements in the reflectarrays are so designed to mimic the cylindrical reflector to scan the main beam to larger angles off broadside. Another advantage of reflectarrays is the ability of the antenna to directly control the element reflection phase. Some reconfigurable reflectarrays are designed using low-loss phase shifters in every element of the array. These beam scanning reflectarrays require a switch board to control the main beam direction; however, considerable challenges lie in improving the performance of these beam scanning antennas, especially the antenna efficiency.

1.3 Contribution of this Dissertation

In Chapter 2, some basic design and analysis methods for reflectarray antenna are presented. Several cases have been verified and it helps to confirm the accuracy of the developed code. Chapters 3 to 6 propose the main contributions of our work on reflectarray antenna, which mainly regards two aspects: reflectarray bandwidth and its beam scanning capability, as shown in Fig. 1-1.
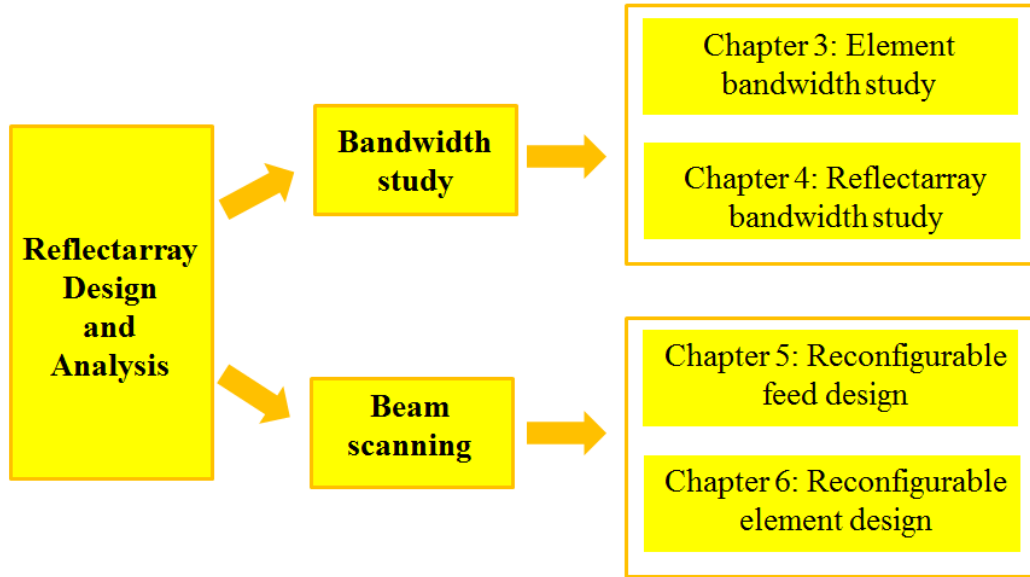
Fig. 1-1 A graphic view of the contributions of this dissertation.

A comprehensive study is performed on the reflectarray bandwidth on element and system level in sequence. Since the element bandwidth usually plays an important role in the reflectarray performance, it is studied in Chapter 3 at first, where the effect of element shape and substrate thickness is demonstrated. After that, the bandwidth characteristics of reflectarrays were investigated on the system level mainly in three aspects in Chapter 4: element bandwidth, aperture size and phase synthesis method. Particularly, a novel wideband phase synthesis

approach, which is able to considerably increase the bandwidth of the reflectarray antenna at the cost of a minor gain loss irrespective of the element frequency behavior, is proposed. A lot of comparison work was made and six reflectarrays prototypes have been fabricated and measured to validate the theoretical study.

Since the beam could be scanned with reflectarray by changing either the feed or the planer reflective surface, Chapter 5 and Chapter 6 presented two designs based on these two ways, respectively. In Chapter 5, the reflectarray phase design mimics a cylinder parabolic surface and the beam scanning is performed by mechanically rotating the feeding array. Specially, the compensation phases of the elements are so optimized that the scanning performance is significantly improved compared to the traditional design. While in Chapter 6, the scanning reflectarray is built on a 1-bit reconfigurable element system, and the design details are presented. It is found that the selection of the reference phase plays a big role in the scanning performance of the RRA, especially the ones with small aperture sizes.

CHAPTER II

GENERAL PROCEDURE FOR REFLECTARRAY DESIGN

In this chapter, the general procedure of reflectarray design is reviewed. First the verification of element simulation is discussed. Next different phasing techniques are described, followed by investigation of substrate thickness effect. Finally array theory, as well as three different methods of directivity computation is presented for the evaluation of antenna performance, including the radiation pattern, directivity and gain. Good agreement is observed compared with reference results. The verification work in this chapter serves as a solid and reliable ground for the reliability of the calculated results of the future designs in this dissertation.

2.1 Overview of Reflectarray Antenna Design Procedure

A typical reflectarray consisted of two parts: a feeding source and an array of scattering elements distributed on a planar aperture, and each element is individually designed to compensate a certain phase by manipulating their reflection phases. For example, as shown in Fig. 2-1 which demonstrates the most simple reflectarray design to mimic the reflector surface, the reflection phase of the mn^{th} element is designed to be equal to the electrical path length of $\overline{ab} + \overline{bc}$. Obviously, the required compensation phases for different elements are various. After

all the reflection phases are determined, array theory is utilized to predict the far-field performances.
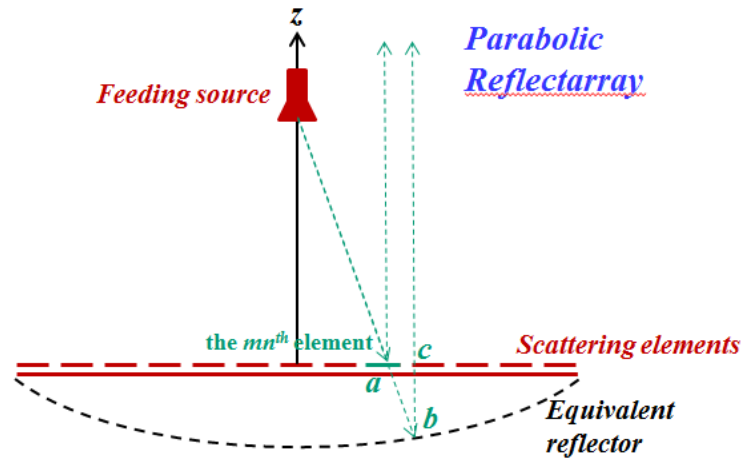
Fig. 2-1 A system of reflectarray to mimic a reflector antenna.

Most generally, the procedure for reflectarray design is given in Fig. 2-2.
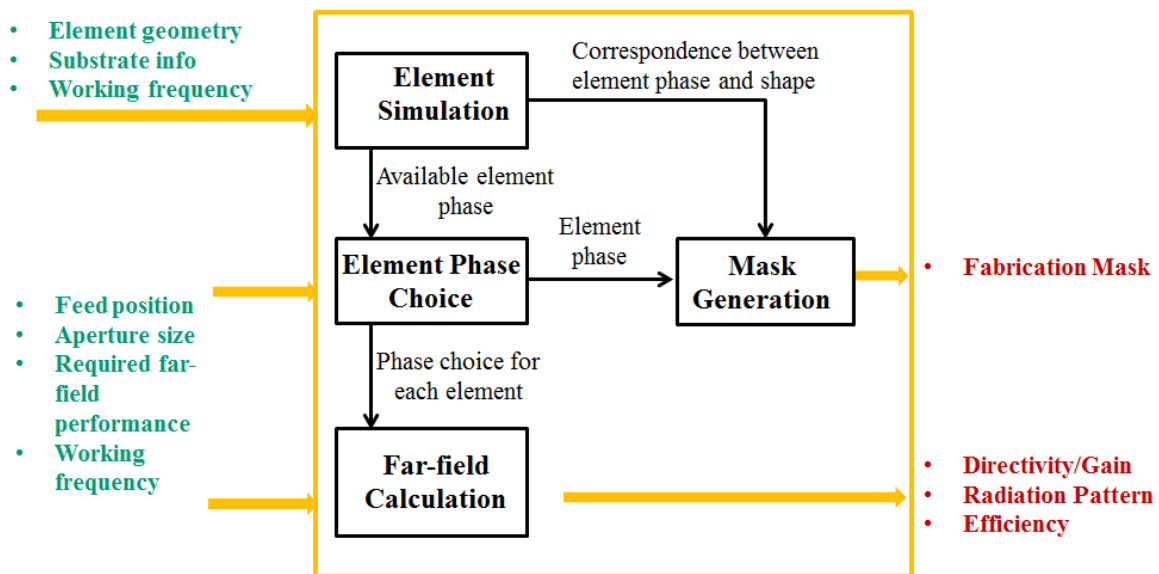
Fig. 2-2 General design procedure for a reflectarray antenna.

Once the reflectarray design specifications are obtained, two separate steps shall be carried out at first: (1) element simulation, and (2) element phase choice. The selection of element geometry and substrates are made according to the design target. For example, thick substrate and double-resonance geometry are usually desirable for wide-band reflectarray design. A correspondence between element geometry and shape, i.e. Phase vs. Dimension curve, is obtained after the element simulation, which helps to choose the correct size for each unit. And the determination of element phase also depends on the design requirement. For example, the reflectarray aperture phase distributions are quite different for single pencil beam and contour beam designs. In the next step, the radiation pattern is computed at the working frequency, as well as the directivity, gain and efficiency. In the final step, the PCB mask is generated to facilitate the fabrication, followed by measurement.

2.2 Comparison and Verification of Different Simulation Tools

Usually commercial electromagnetic simulation tools are used to perform the simulation for a single unit. Different from conventional microstrip patch antennas, in order to account for the coupling effect among the elements, as shown in Fig. 2-3, Periodical Boundary Condition (P.B.C.), combined with Floquet mode, is used to mimic an infinite array environment. Two approximations are made here: 1) the array is considered to be infinite; 2) all the elements are considered to be of the same size.
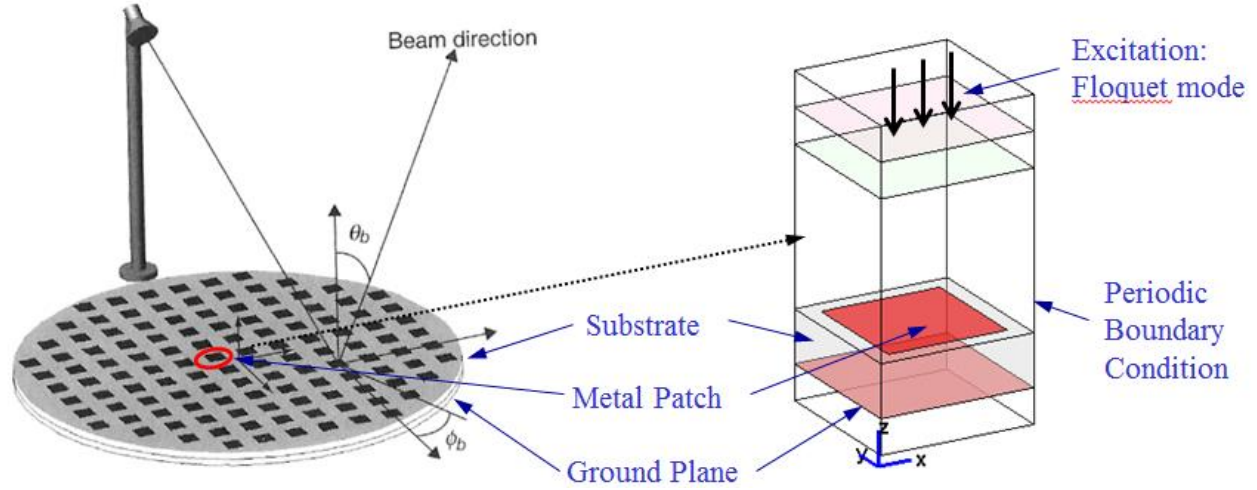
Fig. 2-3 Configuration of a single cell in simulation tools.

In this section, three different kinds of tools are used to simulate a square patch array as displayed in Fig. 2-4, where the sizes of all the element patches are the same (a-g). All the patches are arranged in periodic square lattice whose periodicity is a and etched on a grounded substrate with thickness of h. And the information of the three tools is as shown in Table 2-1.

(a)   (b)
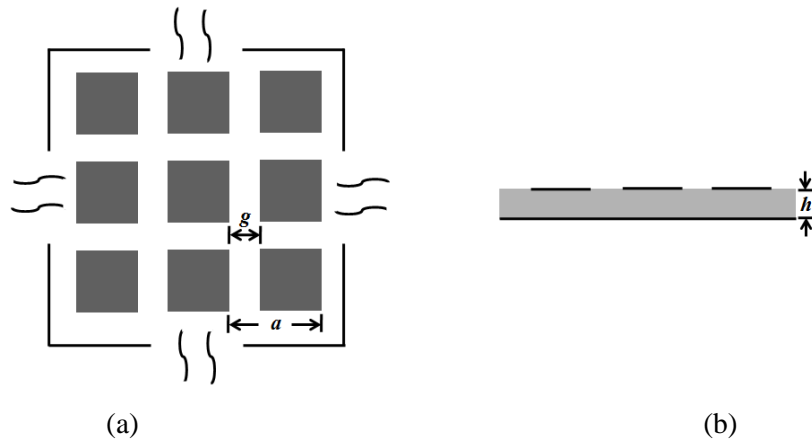
Fig. 2-4 (a) Top view and (b) side view of a square patch array.

Table 2-1 Information of different tools

Software	Technique	Version
HFSS	FEM	Version 13.0.1
Ansoft Designer	MoM	Version 6.1.2
CST Microwave Studio	Time-domain Finite Integration Technique	Version 2012.01

In order to further verify the accuracy of simulation results both for normal and oblique incidence, we are going to compare them with some analytical results obtained by that

$$\Gamma^{TM} = \frac{Z_s^{TM} - Z_0^{TM}}{Z_s^{TM} + Z_0^{TM}} = \frac{Z_s^{TM} - \eta_0 cos\theta_i}{Z_s^{TM} + \eta_0 cos\theta_i} \tag{2.1.a}$$

$$\Gamma^{TE} = \frac{Z_s^{TE} - Z_0^{TE}}{Z_s^{TE} + Z_0^{TE}} = \frac{Z_s^{TE} - \eta_0/cos\theta_i}{Z_s^{TE} + \eta_0/cos\theta_i} \tag{2.1.b}$$

where

$$Z_s^{TM} = \frac{j\omega\mu_0\mu_r \frac{tan(\beta h)}{\beta} cos^2\theta_2}{1 - k_0^2(\varepsilon_r + 1)a\frac{tan(\beta h)}{\pi\beta}\ln(1/sin\frac{\pi g}{2a})cos^2\theta_2} \tag{2.2.a}$$

$$Z_s^{TE} = \frac{j\omega\mu_0\mu_r \frac{tan(\beta h)}{\beta}}{1 - k_0^2(\varepsilon_r + 1)a\frac{tan(\beta h)}{\pi\beta}\ln\left(1/sin\frac{\pi g}{2a}\right)(1 - \frac{1}{\varepsilon_r + 1}sin^2\theta_i)} \tag{2.2.b}$$

where ω is the angular frequency, $\beta = \sqrt{k_0^2\varepsilon_r - k_t^2}$ is the propagation constant along the normal direction of the substrate with $k_t = k_0 sin\theta$ being the tangential component of the wavenumber, ε_r is the relative permittivity of the dielectric substrate, μ_r is the relative permeability of the dielectric substrate, θ_i is the incident angle, and $\theta_2 = \arcsin(sin\theta_i/\sqrt{\varepsilon_r})$. These two analytical models presented in equation (2.2) are published in [5] specifically for square patch arrays under

the conditions when $g \ll a$ and $k_0 a \sqrt{(\varepsilon_r + 1)/2} \ll 2\pi$, and have been verified to be in good agreement with experimental results in [6].

Three cases are going to be compared, where the entire element configurations are chosen exactly the same as those used in [6]:

$$a = 5.113 \ mm, g = 0.33 \ mm, h = 1.54 \ mm, and \ \varepsilon_r = 4.4(1 - j0.02)$$

And the difference only lies in the incident waves as listed in Table 2-2:

<p align="center">**Table 2-2** Information of incident waves for case 2.1</p>

Case ID	Incident Wave Polarization	Incident Angle (θ, φ)
Case 2.2.a	**TM**	**(0°, 180°)**
Case 2.2.b	**TM**	**(30°, 180°)**
Case 2.2.c	**TE**	**(30°, 180°)**

The comparison of analytical and simulated results for these three cases are demonstrated in Fig. 2-5, Fig. 2-6 and Fig. 2-7, respectively, where very good agreement between each other are observed.
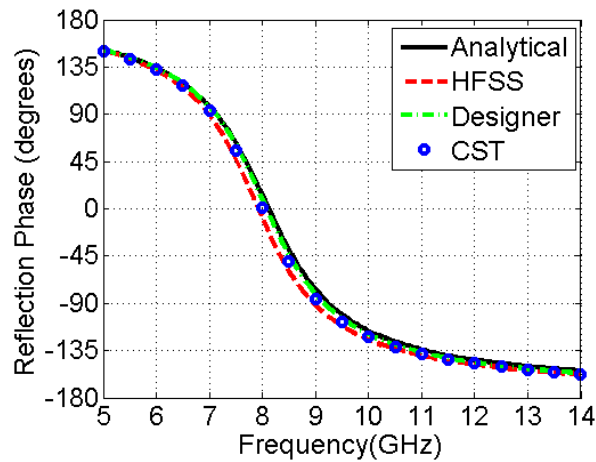
<p align="center">**Fig. 2-5** Comparison of phase curves for case 2.2.a.</p>
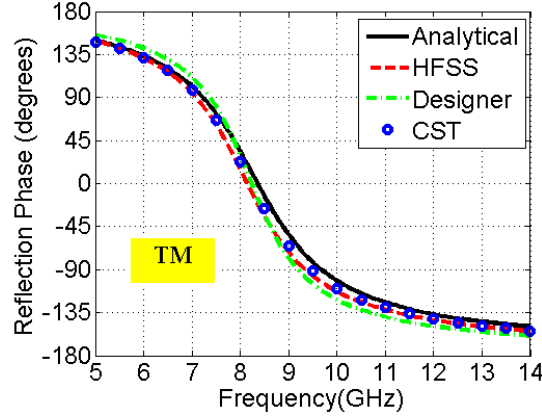
Fig. 2-6 Comparison of phase curves for case 2.2.b.
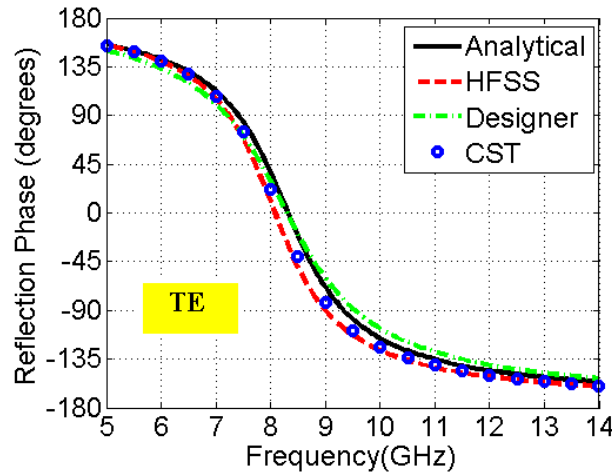
Fig. 2-7 Comparison of phase curves for case 2.2.c.

2.3 Different Element Phasing Techniques

The phase shift is obtained by varying one or more of the geometrical characteristics of the element. As shown in Fig. 2-8, for linearly polarized reflectarrays, the most commonly used approaches are basically based on two different principles: variable size technique, where the resonant frequency shifts as the size changes, thereby varying the reflection phase; variable stub length technique, where the signal travelling distance changes as the stub length becomes different, thereby varying the reflection phase. Both of them are demonstrated in the following.

12

<center>(a)   (b)</center>
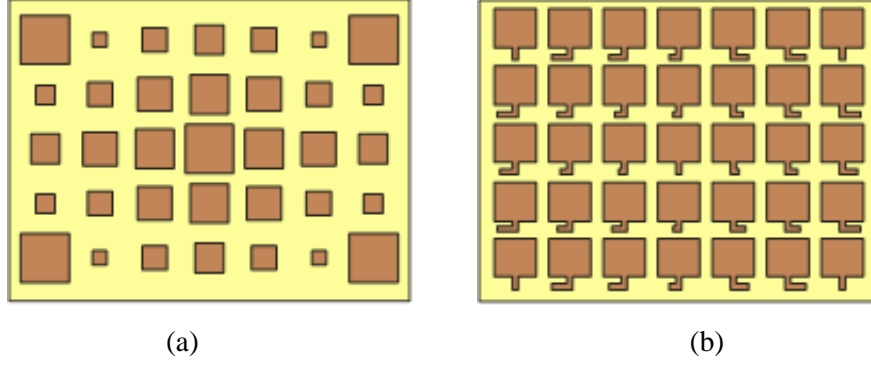
Fig. 2-8 Different phasing techniques for linear-polarization elements (a) variable element size (b) variable stub length.

In order to verify the simulation accuracy, the unit configurations for both techniques are chosen to be the same as in [7]. Both of the elements are based on a substrate with 1.52 mm thickness and 3.5 relative permittivity, and they are evaluated at 10 GHz under normal incidence. Moreover, the side length of the square arrangement lattice is 20 mm.

2.3.1 Phasing Technique of Variable Element Size

As mentioned before, the original case was published in [7], where the dimension is reprint in Fig. 2-9 for the convenience. The rectangular patch is 10 mm long and the reflection phase is changed as the width *A* differs. The published phase curve was also included in Fig. 2-9 for 10 GHz.
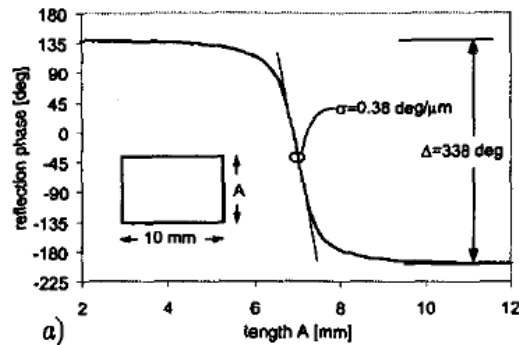
Fig. 2-9 Dimension and published curve for variable size technique demonstration [7].

<center>13</center>

The same case was repeated again with both HFSS and Designer, and the simulation results are illustrated in Fig. 2-10, which shows good agreement with each other.
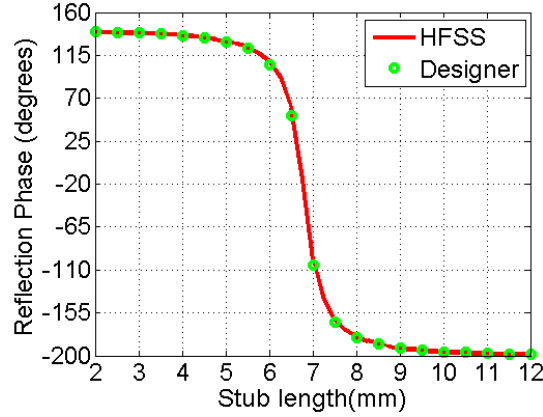
Fig. 2-10 Repeated results for variable size technique demonstration.

2.3.2   Phasing Technique of Variable Stub Length

The geometry chosen for this technique is also based on the published case in [7], where the dimension is reprinted in Fig. 2-11. The rectangular patch is 10 mm long and 6.9 mm wide, and a stub with 0.11 mm width is attached to the patch in the center of the long side. The published phase curve at 10 GHz was also included in Fig. 2-11 for reference.

This case was repeated again with both HFSS and Designer, and the geometry is re-sketched in Fig. 2-12 for a better view. All the dimensions are clearly specified in the paper except for the position of the patch. However, since it is a periodical structure, theoretically this value should not have any effect on the reflection phase; hence 10 mm was chosen. The results are illustrated in Fig. 2-13. Very good agreement was observed between HFSS and Designer results, although it can be seen that there is some discrepancy compared with the reference results.
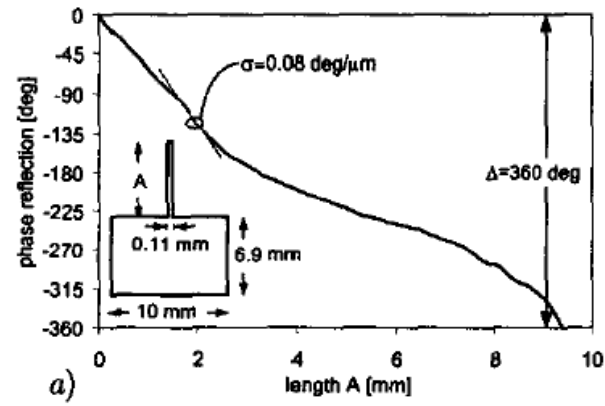
Fig. 2-11 Dimension and published curve for variable stub length technique demonstration [7].
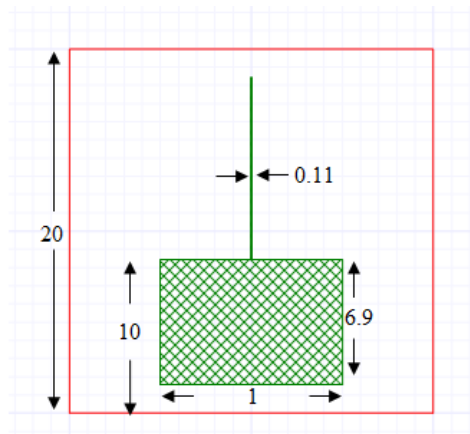
Fig. 2-12 Geometry of the patch element attached with open-end stub.
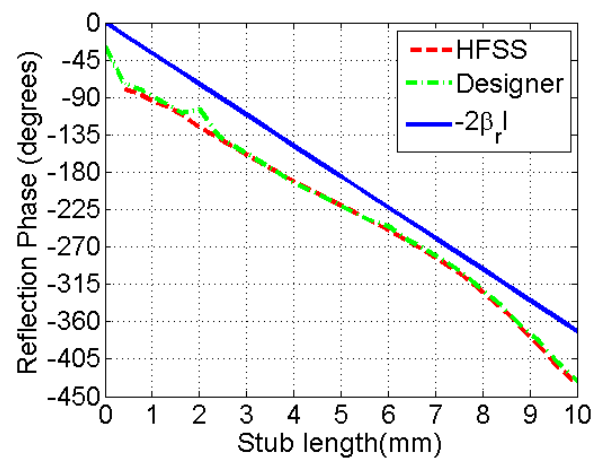
Fig. 2-13 Repeated curve for variable stub length technique demonstration.

15

To further study the principle of realization of the phase tuning, some analytical investigation is made. At first, the substrate and stub information were input in the LineCalc software to calculate the effective ε_r of the system. As shown in Fig. 2-14, $\varepsilon_r = 2.392$, therefore the effective wave number is 18.56 degree/mm, which is computed as below

$$\lambda = \frac{c/\sqrt{\varepsilon_r}}{f} = 0.194m$$

$$k = \frac{360\ degree}{\lambda \times 10^3} = 18.56\ degree/mm$$

The curve $-2\beta_r l$ was also displayed in Fig. 2-13. It is observed that in terms of slope, it is similar to the two simulation curves, which verifies that reflection phase is attributed to the phase delay along the stub.
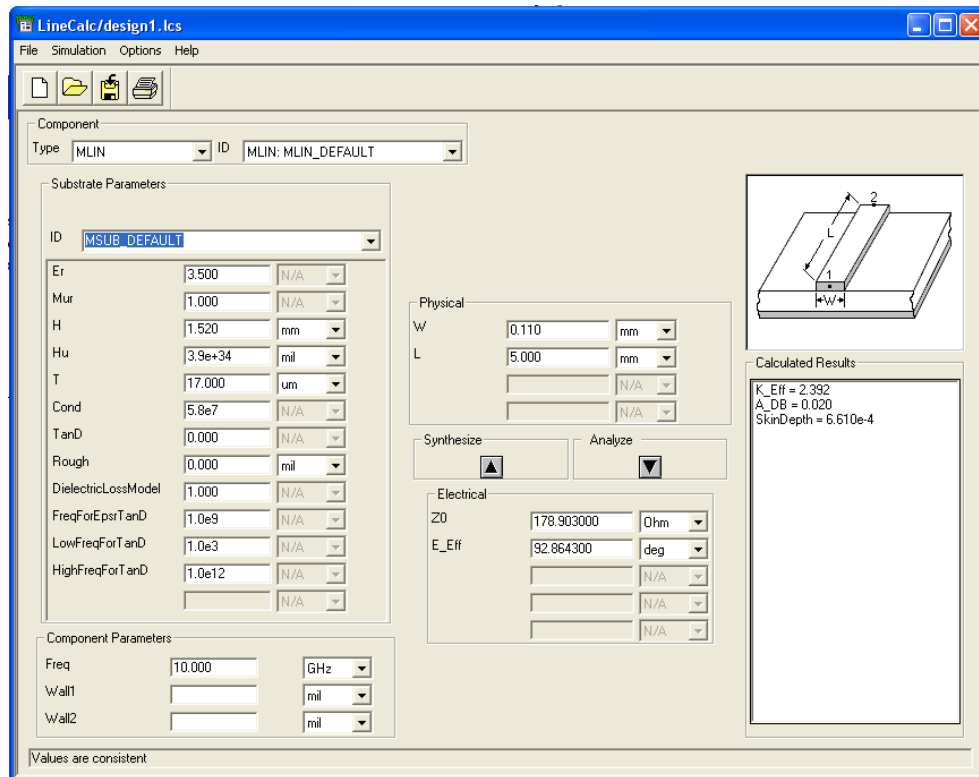
Fig. 2-14 Configuration in LinCalc software.

For an electrically large reflectarray, since the different spatial phase delay effect becomes significant, the ideal phase-shift should be proportional to the frequency, and one of the solutions is to use true-time delay (TTD) [3], which uses the stub length to adjust the reflection phase. Based on the previous study, it is shown that for an element with a certain stub length, its phase shift is proportional to $f\sqrt{\varepsilon_r}$. However, since ε_r just slightly changes as frequency differs, this kind of element is a good candidate for electrically large reflectarray.

2.3.3 Effect of Thickness

The thickness of the substrate has a big impact on the achievable phase range. Generally, as the thickness increases, the phase range becomes smaller. The patch element was chosen as an example. Assuming the operation frequency is 32 GHz, three different thicknesses are chosen for substrate, 0.79 mm (0.08λ), 1.58mm (0.16λ), and 3.18mm (0.34λ), and the corresponding curves are shown in Fig. 2-15. It is observed that the phase ranges are 271.4^o, 170.9^o, and 14.0^o for 0.79 mm, 1.58 mm, and 3.18 mm, respectively, which verifies the conclusion.
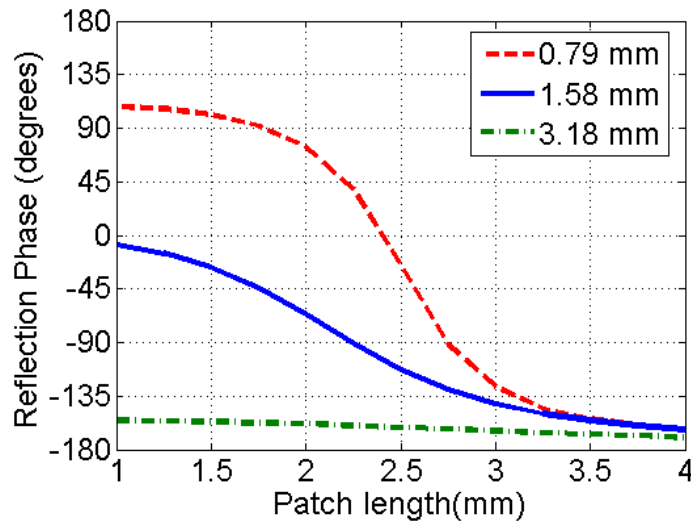
Fig. 2-15 Phase curve obtained with different substrate thickness.

As illustrated in Fig. 2-16, when θ_i is not zero anymore, it affects the element reflection phase. For the TE case, E field only has y component, the reflection phase barely change irrespective of the θ_i. However, for the TM case, E field has two components, x component and z component. As θ_i increases, the x component becomes weaker while the z component becomes stronger; therefore, the reflection phase is somehow changed correspondingly. How much it changes depends on the element shape and substrate. Here, assuming the element is a square patch and the ε_r is fixed, the substrate thickness effect is studied.
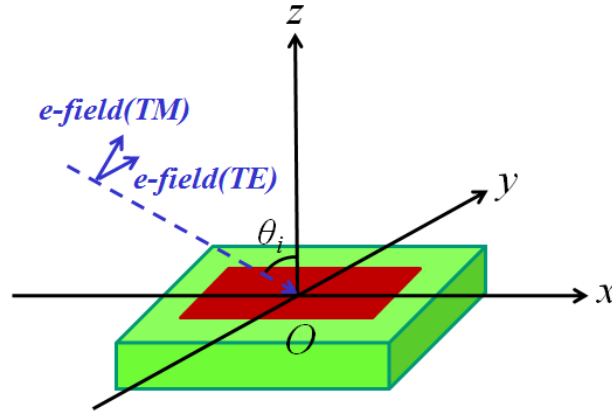
Fig. 2-16 Demonstration of incident TE/TM wave.

In order to examine how the oblique incidence influences the reflection phase as the substrate thickness varies, the square patch elements at 32 GHz under different incidence (θ_i, φ_i) = (0°, 180°), (30°, 180°) and (60°, 180°) were evaluated using the equation (2.1). Other parameters are as below:

$$a = 4.6843mm, g = 0.9 \, mm, and \, \varepsilon_r = 2.2$$

The results are shown in Fig. 2-17. The thickness changes from 0.8 to 3.15 mm for all the three different incidence situations. It is observed that as the incident angle increases, the phase difference correspondingly increases, especially for the TM case. However, since the normal

incidence could present good approximation for oblique conditions for a proper f/D configuration, we usually only investigate normal case for most of the designs to simplify the procedure.
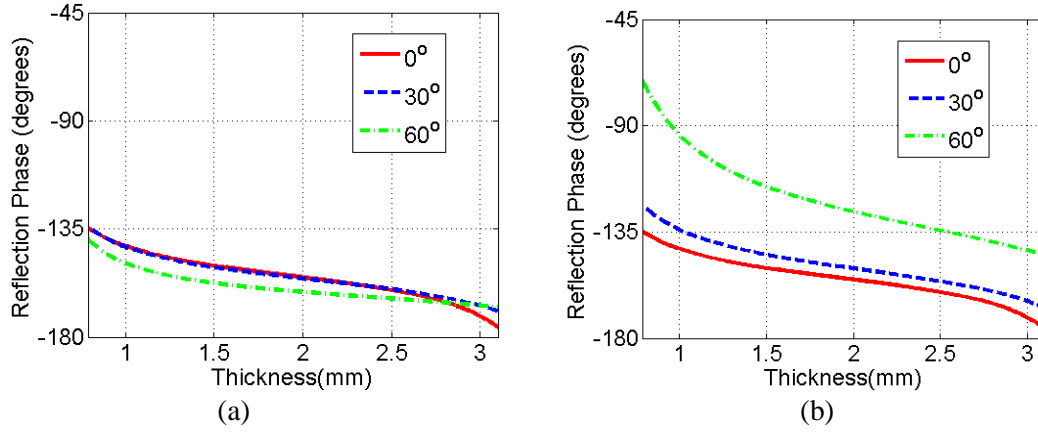
Fig. 2-17 Thickness effect under the conditions of (a) TE and (b) TM.

2.4   Radiation Pattern Calculation

2.4.1   Theory to Calculate Radiation Pattern
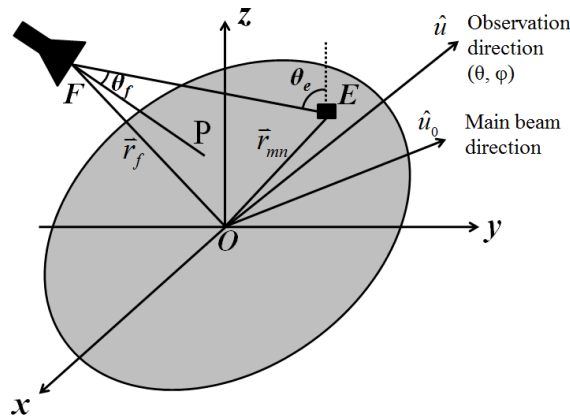
Fig. 2-18 The coordinate system for reflectarray antenna.

As depicted in Fig. 2-18, there are totally three coordinate systems in the reflectarray system: the aperture coordinate system, the local element coordinate system, and the feed coordinate system, as listed in Table 2-3.

Table 2-3 Three different coordinate systems used in reflectarray design

	System center	$\theta=90^\circ$ plane	$\theta=0^\circ$ direction
Aperture coordinate	**O** **(the center point of the aperture)**	**reflectarray aperture**	$\overrightarrow{OZ}$
Local element coordinate	**E** **(the center point of the mn^{th} element)**	**reflectarray aperture**	$\overrightarrow{OZ}$
Feed coordinate	**F** **(the center point of feed aperture)**	**feed aperture**	$\overrightarrow{FP}$

And the notations in Fig. 2-18 are summarized in the Table 2-4:

Table 2-4 Important geometric quantities for a circular reflectarray

Quantity	Formula
the θ quantity of mn^{th} element in the feed coordinate	θ_{fmn}
the θ quantity of feed in the local coordinate of mn^{th} element	θ_{emn}
Feed location	$F\,(-h{\cdot}tan\theta_i,\ 0,\ h)$
Feed beam point (FBP)	$P\,(x_0,\ y_0,\ 0)$
Element location	$E\,(x_{mn},\ y_{mn},\ 0)$
Position vector from center to element	$\vec{r}_{mn} = \overrightarrow{OE} = x_{mn}\hat{x} + y_{mn}\hat{y}$
Position vector from feed to FBP	$\vec{r}_0 = \overrightarrow{FP} = (x_0 + h\cdot tan\theta_i)\hat{x} + y_0\hat{y} + (-h)\hat{z}$
Distance between feed and FBP	$r_0 = |\vec{r}_0|$

Position vector from feed to element	$\vec{r}_{fmn} = \overrightarrow{FE} = (x_{mn} + h \cdot tan\theta_i)\hat{x} + y_{mn}\hat{y} + (-h)\hat{z}$
Distance between feed and element	$r_{fmn} = |\vec{r}_{fmn}|$
Unit vector from feed to element	$\hat{r}_{fmn} = \dfrac{\vec{r}_{fmn}}{r_{fmn}}$
Distance between element and FBP	$s_{mn} = |\overrightarrow{EP}|$
Feed pattern parameter	$cos\theta_{fmn} = \dfrac{r_0^2 + r_{fmn}{}^2 - s_{mn}{}^2}{2r_0 r_{fmn}}$
Element pattern parameter in receiving mode	$cos\theta_{emn} = \dfrac{h}{r_{fmn}}$

Array theory is used to calculate the radiation pattern, where the element amplitude and phase need to be known. It is simple and fast, but could not predict the cross-polarization performance. Regarding the amplitude, to simplify the calculation, both the feed horn and element pattern are approximated by a cosine q model, such that the excitation amplitude of each element on the aperture could be expressed as

$$A_{mn} = \frac{cos^{q_f}\theta_{fmn}(m,n) \cdot cos^{q_e}\theta_{emn}(m,n) \cdot |\Gamma_{mn}|}{r_{fmn}} \tag{2.3}$$

where q_f is the q factor of the feed pattern, q_e is the q factor of the element pattern which is 1 unless otherwise specified, and $|\Gamma_{mn}|$ is the magnitude of reflection coefficient for each element. Regarding the total phase for each element, there are three terms: e^{-jkr} to account for the incident phase, $e^{j\varphi_{mn}}$ to account for element reflection phase and $e^{j\vec{r}_{mn}\cdot\hat{u}}$ to account for the observation direction. It is worthwhile to point out that as previously mentioned since the infinite-array approximation is used in the unit simulation, φ_{mn} does include the coupling effects. With all the approximations, the calculation of radiation pattern for each observation point could be simplified to a scalar form [8]

$$E(\theta, \varphi) = cos^{q_e}\theta \sum_{m=1}^{M} \sum_{n=1}^{N} A_{mn}e^{-jkr_{fmn}}e^{j\varphi_{mn}}e^{jk\vec{r}_{mn}\cdot\hat{u}} \tag{2.4}$$

where $cos^{q_e}\theta$ represents the radiation pattern of element in the transmission mode, assuming that all the elements have the same element pattern.

The ideal reflection phase φ_{rmn} for mn^{th} element is calculated as:

$$\varphi_{rmn} = k \cdot (r_{fmn} - \hat{u}_0 \cdot \vec{r}_{mn}) + \Delta\varphi \tag{2.5}$$

where $\hat{u}_0$ is the main beam direction and $\Delta\varphi$ is a constant phase. However, practically for each element it is impossible to choose a dimension whose corresponding phase is exactly the same as the ideal one. It is due to two factors: quantization error and phase range limit. The quantization error is basically determined by the fabrication technique, and we normally choose 0.05mm as the quantization step. As for the phase range limit, it is relevant to the element design.

In practice, normally the selection principle is to minimize the phase error $|\varphi_{rmn} - \varphi_{mn}|$ as much as possible. One thing worthwhile to point out is that when the required phase is out of the achievable phase range, which means that we have to choose either the maximum or the minimum available element phase for φ_{mn}, saying $\max(\varphi_{simulate})$ and $\min(\varphi_{simulate})$, we need to compare $|\varphi_{mn} - \max(\varphi_{simulate})|$ and $|\varphi_{mn} - 360 - \min(\varphi_{simulate}|$. If the former value is smaller, we choose the $\max(\varphi_{simulate})$, otherwise we choose $\min(\varphi_{simulate})$.

2.4.2   Definition and Principle Plane 1(P.P.1) and Principle Plane 2(P.P.2)

Usually, the far field patterns are only plotted in two perpendicular planes, defined as the *principal planes* (P.P.1, P.P.2). Fig. 2-19 gives an intuitive understanding of P.P.1 and P.P.2 planes, where $U_0(\theta_0, \varphi_0)$ is the main beam direction. As it shows, P.P.1 is the plane which includes z axis and U_0. As for P.P.2, it is a plane though OU_0 and the angle formed by P.P.2 and xy plane is θ_0.
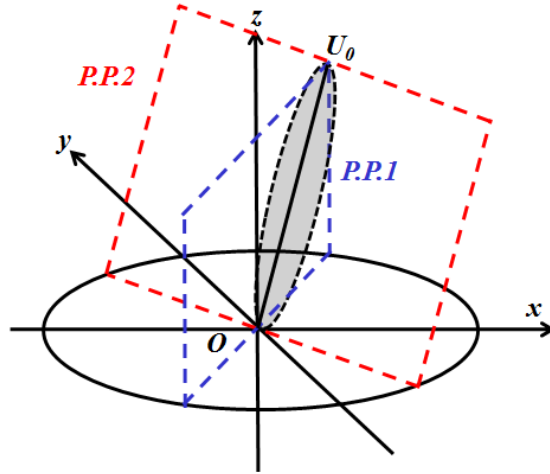
Fig. 2-19 The definitions of P.P.1 and P.P.2.

Hence, when calculated the radiation pattern in P.P.1 plane could be easily defined as a set of (θ, φ) with $\varphi = \varphi_0$. Regarding P.P.2, it is obvious that the range of φ is from $(\varphi_0 - 90^\circ)$ to $(\varphi_0 + 90^\circ)$, while for each corresponding θ, it requires some additional computation.
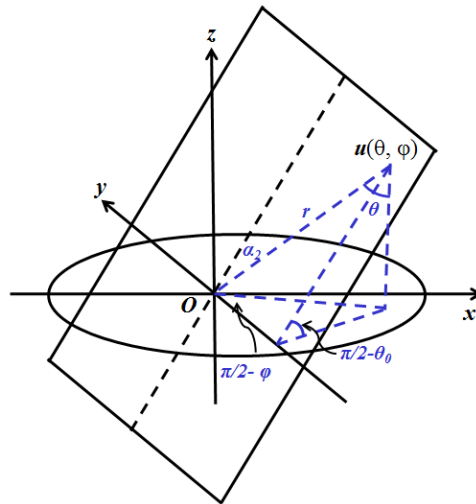
Fig. 2-20 Geometrical demonstration of the calculation of P.P.2 plane.

As shown in Fig. 2-20, u(θ, φ) represents an arbitrary point in the P.P.2 plane. What have already been known are the two angles θ_0 and φ, then based on the geometrical calculation, it could be obtained that

$$\theta = \arctan(tan\theta_0/\cos(\varphi - \varphi_0)) \tag{2.6}$$

$$\alpha_2 = \begin{cases} \arccos\left(\cos\left(\theta\right)/\cos\left(\theta_0\right)\right), \varphi \geq 0 \\ -\arccos\left(\cos\left(\theta\right)/\cos\left(\theta_0\right)\right), \varphi < 0 \end{cases} \tag{2.7}$$

2.4.3 Determination of Valid Elements for a Circular Aperture

When the aperture shape is circular, since all the elements are arranged in periodic square lattice in a reflectarray, some of them needs to be ruled out. Our judging criterion is that: if it is satisfied for a certain element that:

$$0 < \frac{R - (|\vec{r}_{mn}| + p/2)}{R} < 1 \tag{2.8}$$

where R is the radius and p is the periodicity, we consider this element a valid one for a circular reflectarray,.

2.4.4 Verification

2.4.4.1 Calculation of Radiation Performance with Ideal Element Phase

Three cases with different incident angles and main beam directions are employed to verify the calculation of radiation pattern in both P.P.1 and P.P.2 planes. The detailed information of system parameters for each case is listed in Table 2-5. One thing needs to be pointed out is that the element phase in each case is selected exactly the same as the ideal one defined in (2.5).

Table 2-5 System parameters for the three cases

	Frequency	D	Periodicity	q_f	Z_feed	θ_i, φ_i	(θ_0, φ_0)
Case:2.4.4.1.a	32 GHz	17λ	λ/2	6.5	10.5 λ	(30°, 180°)	(0°, 0°)
Case:2.4.4.1.b	32 GHz	17λ	λ/2	6.5	10.5 λ	(30°, 180°)	(30°, 0°)
Case:2.4.4.1.c	32 GHz	17λ	λ/2	6.5	10.5 λ	(0°, 0°)	(30°, 45°)

The calculation results are shown in Fig. 2-21, Fig. 2-22 and Fig. 2-23. They are compared with the reference results, and very good agreement was demonstrated for all the three cases.

(a)   (b)
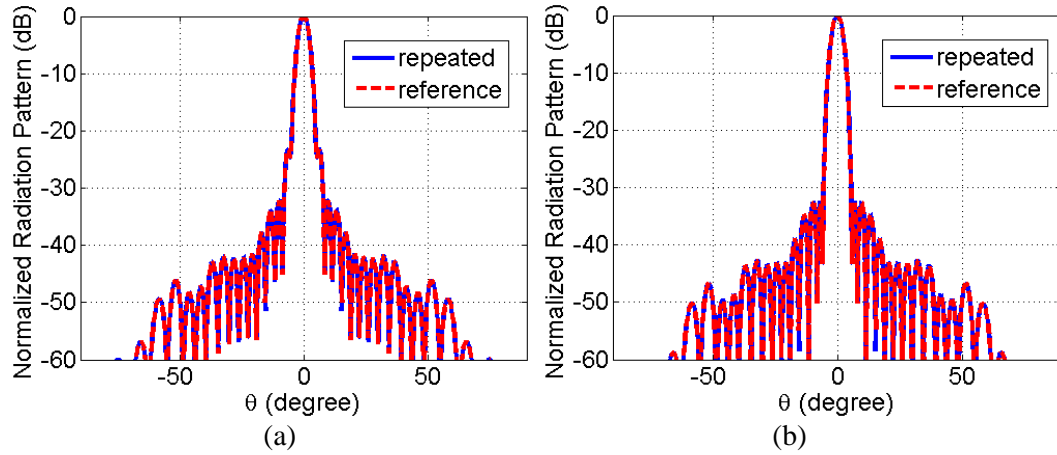
Fig. 2-21 Repeated and referred radiation pattern for case 2.4.4.1.a (a) P.P.1 plane and (b) P.P.2 plane.

(a)   (b)
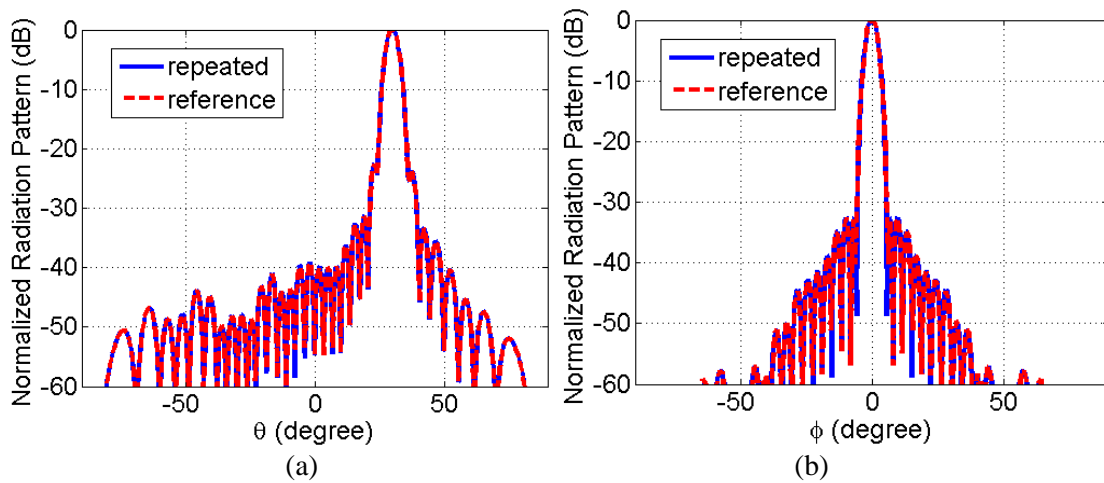
Fig. 2-22 Repeated and referred radiation pattern for case 2.4.4.1.b in (a) P.P.1 plane and (b) P.P.2 plane.
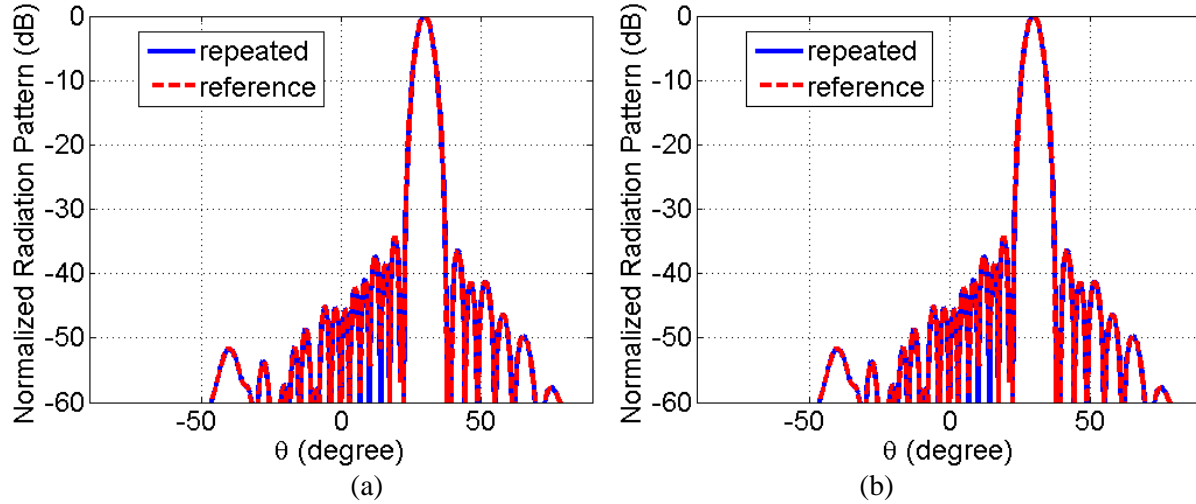
Fig. 2-23 Repeated and referred radiation pattern for case 2.4.4.1.c in (a) P.P.1 plane and (b) P.P.2 plane.

2.4.4.2 Calculation of Radiation Performance with Simulated Element Phase

Two more cases with different incident angles and main beam directions are employed to verify the calculation of radiation patterns. Different from the previous three cases, the element phases used in these two are selected from the practical simulation results following the rule described at the end of section 2.4.1. And the detailed information of configuration for each case is listed in Table 2-6.

Table 2-6 System parameters for the two cases with simulated elements phase

	Frequency	D	Periodicity	q_f	Z_feed	θ_i, φ_i	(θ_0, φ_0)
Case: 2.4.4.2.a	**32 GHz**	**17λ**	**λ/2**	**6.5**	$(0, 0, 117.1\text{mm})$	$(0^o, 0^o)$	$(0^o, 0^o)$
Case: 2.4.4.2.b	**32 GHz**	**17λ**	**λ/2**	**6.5**	$(-45.9\text{mm}, 0, 98.4\text{mm})$	$(25^o, 0^o)$	$(30^o, 0^o)$

The calculation results are shown in Fig. 2-24 and Fig. 2-25. They are compared with the reference results; it is observed that there is some small discrepancy between the repeated and referred results. However, overall the calculation results are acceptable.
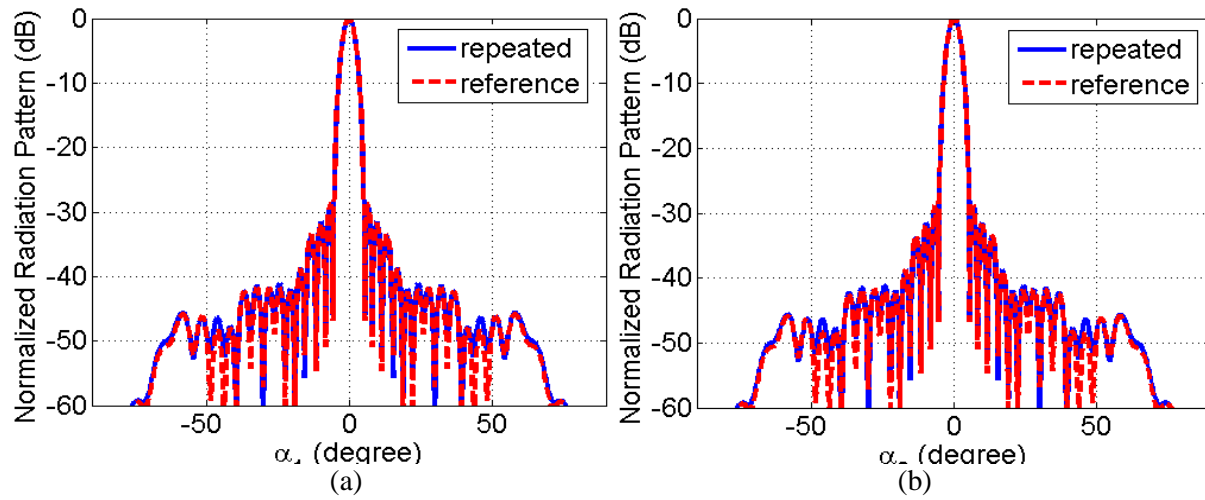
Fig. 2-24 Repeated and referred radiation pattern for case 2.7.a in (a) P.P.1 plane and (b) P.P.2 plane.
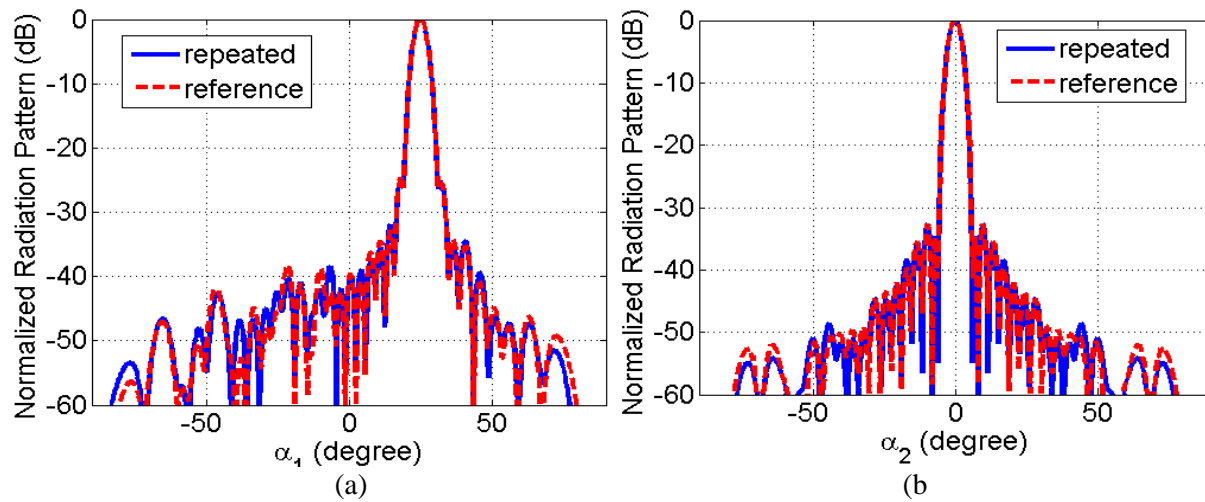
Fig. 2-25 Repeated and referred radiation pattern for case 2.7.b in (a) P.P.1 plane and (b) P.P.2 plane.

2.5   Directivity and Gain Calculation

2.5.1 Theory of Directivity Calculation

2.5.1.1 Method 1: Standard Definition of Directivity

The 1st method is based on the definition of directivity, and the directivity is calculated as following:

$$D_0 = \frac{4\pi|E(\theta_m, \varphi_m)|^2}{\int_0^{2\pi}\int_0^{\pi/2}|E(\theta,\varphi)|^2 \sin\theta d\theta d\varphi} \tag{2.9}$$

2.5.1.2 Method 2: Bessel Function Method

The double-summation in equation (2.4) could be manipulated as a single-summation

$$E(\theta,\varphi) = cos^{q_e}\theta \sum_{n'=1}^{N'} A_{n'}e^{-jkr_{fn'}}e^{j\varphi_{n'}}e^{jk\vec{r}_{n'}\cdot\hat{u}} \tag{2.10}$$

Therefore, the denominator in equation (2.9) could be written as

$$DEN \equiv \int_0^{2\pi}\int_0^{\pi/2}\left|cos^{q_e}\theta \sum_{n'=1}^{N'} A_{n'}e^{-jkr_{fn'}}e^{j\varphi_{n'}}e^{jk\vec{r}_{n'}\cdot\hat{u}}\right|^2 \sin\theta d\theta d\varphi$$

$$= \int_0^{2\pi}\int_0^{\pi/2} cos^{2q_e}\theta \sum_{n'=1}^{N'}\sum_{m'=1}^{M'} A_{n'}A_{m'}^*e^{-jk(r_{fn'}-r_{fm'})}e^{j(\varphi_{n'}-\varphi_{m'})}e^{jk(\vec{r}_{n'}\cdot\hat{u}-\vec{r}_{m'}\cdot\hat{u})} \sin\theta d\theta d\varphi \tag{2.11}$$

Which is reduced to

$$DEN = \sum_{n'=1}^{N'}\sum_{m'=1}^{M'} w_{n'}w_{m'}^* \int_0^{\pi/2} cos^{2q_e}\theta \sin\theta d\theta \int_0^{2\pi} e^{jk(\vec{r}_{n'}\cdot\hat{u}-\vec{r}_{m'}\cdot\hat{u})} d\varphi \tag{2.12}$$

Where

$$w_{n'} = A_{n'}e^{-jkr_{fn'}}e^{j\varphi_{n'}}$$

$$w_{m'}^* = A_{n'}e^{jkr_{fm'}}e^{-j\varphi_{m'}}$$

Since

$$\vec{r}_{n'} \cdot \hat{u} = x_{n'} sin\theta cos\varphi + y_{n'} sin\theta sin\varphi$$

$$\vec{r}_{m'} \cdot \hat{u} = x_{m'} sin\theta cos\varphi + y_{m'} sin\theta sin\varphi$$

The 2nd integration term in equation (2.12) could be written as

$$\int_0^{2\pi} e^{jk(\vec{r}_{n'}\cdot\hat{u}-\vec{r}_{m'}\cdot\hat{u})} d\varphi = \int_0^{2\pi} e^{jk(x_{n'}sin\theta cos\varphi + y_{n'}sin\theta sin\varphi - x_{m'}sin\theta cos\varphi - y_{m'}sin\theta sin\varphi)} d\varphi$$

$$= \int_0^{2\pi} e^{jksin\theta[\Delta x_{nm'}cos\varphi + \Delta y_{nm'}sin\varphi]} d\varphi \qquad (2.13)$$

Where

$$\Delta x_{n'm'} = x_{n'} - x_{m'}$$

$$\Delta y_{n'm'} = y_{n'} - y_{m'}$$

Now defining

$$\rho_{n'm'} = \sqrt{(\Delta x_{n'm'})^2 + (\Delta y_{n'm'})^2}$$

$$\varphi_{n'm'} = \arctan\frac{\Delta y_{n'm'}}{\Delta x_{n'm'}}$$

Then

$$\Delta x_{n'm'} = \rho_{n'm'}cos\varphi_{n'm'}$$

$$\Delta y_{n'm'} = \rho_{n'm'}sin\varphi_{n'm'}$$

And the equation (2.13) becomes

$$\int_0^{2\pi} e^{jk(\vec{r}_{n'}\cdot\hat{u}-\vec{r}_{m'}\cdot\hat{u})} d\varphi = 2\pi\int_0^{2\pi} \frac{1}{2\pi} e^{jksin\theta[\rho_{n'm'}cos\varphi_{n'm'}cos\varphi + \rho_{n'm'}sin\varphi_{n'm'}sin\varphi]} d\varphi$$

$$= 2\pi\int_0^{2\pi} \frac{1}{2\pi} e^{jk\rho_{n'm'}sin\theta cos(\varphi_{n'm'}-\varphi)} d\varphi \qquad (2.14)$$

Based on the integrals of Bessel function

$$J_0(x) = \frac{1}{2\pi}\int_0^{2\pi} e^{jxcos\varphi} d\varphi$$

Equation (2.14) reduces to

$$\int_0^{2\pi} e^{jk(\vec{r}_{n'}\cdot\hat{u}-\vec{r}_{m'}\cdot\hat{u})}d\varphi = 2\pi J_0(k\rho_{n'm'}\sin\theta) \tag{2.15}$$

Therefore the denominator could be simplified as

$$DEN = 2\pi \sum_{n'=1}^{N'} \sum_{m'=1}^{N'} w_{n'}w_{m'}^* \int_0^{\frac{\pi}{2}} \cos^{2q_e}\theta\sin\theta J_0(k\rho_{n'm'}\sin\theta)d\theta \tag{2.16}$$

Since $q_e = 1$, the integration term in equation (2.16) could be solved as

$$\int_0^{\frac{\pi}{2}} \cos^{2q_e}\theta\sin\theta J_0(k\rho_{n'm'}\sin\theta)d\theta =$$

$$= \begin{cases} \dfrac{\sin(k\rho_{n'm'}) - k\rho_{n'm'}\cos(k\rho_{n'm'})}{(k\rho_{n'm'})^3} & \rho_{n'm'} \neq 0 \\ \dfrac{1}{3} & \rho_{n'm'} = 0 \end{cases} \tag{2.17}$$

Thus the denominator becomes a double-summation formula without any integration

$$DEN = \begin{cases} 2\pi \displaystyle\sum_{n'=1}^{N'} \sum_{m'=1}^{N'} w_{n'}w_{m'}^* \dfrac{\sin(k\rho_{n'm'}) - k\rho_{n'm'}\cos(k\rho_{n'm'})}{(k\rho_{n'm'})^3} & \rho_{n'm'} \neq 0 \\ \dfrac{2\pi}{3} \displaystyle\sum_{n'=1}^{N'} \sum_{m'=1}^{N'} w_{n'}w_{m'}^* & \rho_{n'm'} = 0 \end{cases} \tag{2.18}$$

Which is independent of (θ, φ). Finally, the formula to calculate directivity after using Bessel function could be expressed as

$$D_0 = \frac{4\pi|E(\theta_m, \varphi_m)|^2}{2\pi \sum_{n'=1}^{N'} \sum_{m'=1}^{N'} w_{n'}w_{m'}^* I_0} \tag{2.19}$$

Where

$$I_0 = \begin{cases} \dfrac{\sin(k\rho_{n'm'}) - k\rho_{n'm'}\cos(k\rho_{n'm'})}{(k\rho_{n'm'})^3} & \rho_{n'm'} \neq 0 \\ \dfrac{1}{3} & \rho_{n'm'} = 0 \end{cases}$$

2.5.1.3 Method 3: Illumination Efficiency

The directivity of a reflectarray can also be calculated as

$$D_0 = D_{ideal} \times \eta_{ill} \tag{2.20}$$

Where

$$D_{ideal} = \frac{4\pi A}{\lambda^2} \times cos\theta_0$$

Regarding the illumination efficiency, it is a product of taper and phase efficiency [9], and it could be calculated as shown below:

$$\eta_{ill} = \frac{\left|\sum_{m=1}^{N}\sum_{n=1}^{N} A_{mn} e^{-jk|\vec{r}_{mn}-\vec{r}_f|} e^{j\varphi_{mn}} e^{jk\vec{r}_{mn}\cdot\hat{u}_0} ds\right|^2}{A \sum_{m=1}^{N}\sum_{n=1}^{N} A_{mn}^2 ds} \tag{2.21}$$

Therefore, the directivity is obtained as

$$D_0 = \frac{4\pi A}{\lambda^2} \times cos\theta_0 \times \frac{\left|\sum_{m=1}^{N}\sum_{n=1}^{N} A_{mn} e^{-jk|\vec{r}_{mn}-\vec{r}_f|} e^{j\varphi_{mn}} e^{jk\vec{r}_{mn}\cdot\hat{u}} ds\right|^2}{A \sum_{m=1}^{N}\sum_{n=1}^{N} A_{mn}^2 ds} \tag{2.22}$$

Apparently, the computational time of the directivity is reduced from a $O(4N^2)$ to $O(N^2)$ to $O(N)$.

2.5.2 Theory of Gain Calculation

2.5.2.1 Gain Computation

The gain of reflectarray is calculated as shown in (2.32), which takes into account the spillover efficiency and element efficiency

$$G_0 = D_0 \times \eta_s \times \eta_{el} \tag{2.23}$$

Regarding the computation of spillover efficiency and element efficiency, they will be explained in more details in the next.

2.5.2.2 Spillover Efficiency Computation

The term 'spillover' is defined in [10], and it is defined in [11] for conventional reflectors. For reflectarrays, η_s is defined as the percentage of the radiated power from the feed which is intercepted by the reflecting aperture [12].
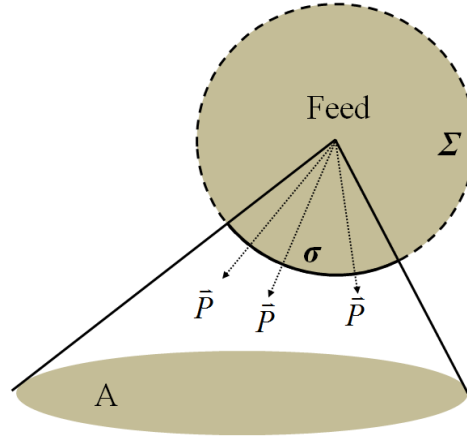
Fig. 2-26 Reflectarray geometry for η_s analysis.

As illustrated in Fig. 2-26, the evaluation of η_s is thus through the following equation:

$$\eta_s = \frac{\iint_\sigma \vec{P}(\vec{r}) \cdot d\vec{s}}{\iint_\Sigma \vec{P}(\vec{r}) \cdot d\vec{s}} \tag{2.24}$$

where the denominator is the total power radiated by the feed, expressed as an integration of the fluxes of the Poynting vector $\vec{P}(\vec{r})$ over the entire spherical surface centered at the feed, which is denoted by Σ, while the numerator is the portion of the power intercepted by the aperture, expressed as an integral over a portion σ of the sphere, where σ and the array aperture share the same solid angle with respect to the feed. However, practically it is somehow difficult to determine the boundary of σ in general cases such as offset feed case or a square aperture.

Therefore, an alternative approach is by performing the integral over the array aperture instead of on the surface σ of the sphere,

$$\eta_s = \frac{\iint_A \vec{P}(\vec{r}) \cdot d\vec{s}}{\iint_\Sigma \vec{P}(\vec{r}) \cdot d\vec{s}} \tag{2.25}$$

Where the Poynting vector $\vec{P}(\vec{r})$ can be written in terms of the feed coordinates as:

$$\vec{P}(\vec{r}) = \hat{r} \frac{(cos\theta_{fmn})^{2q_f}}{r_{fmn}^2} \left(0 \le \theta_{fmn} \le \frac{\pi}{2}\right)$$

And the infinitesimal area $d\vec{s}$ on the surface of a sphere of radius r, is given by

$$d\vec{s} = \hat{r} r_{fmn}^2 sin\theta d\theta d\varphi$$

Hence the denominator can be written as

$$I_d = \int_{\varphi=0}^{2\pi} \int_{\theta=0}^{\pi/2} (cos\theta_{fmn})^{2q_f} sin\theta d\theta d\varphi = \frac{2\pi}{2q_f + 1} \tag{2.26}$$

However, in order to integrate the Poynting vector along the aperture surface, it should be re-written in Cartesian coordinates and is obtained that

$$\vec{P}(\vec{r}) = \frac{1}{r_{fmn}^3} (cos\theta_{fmn})^{2q_f} [x_{mn}\hat{x} + (y_{mn} + h \cdot tan\theta_i)\hat{y} + (-h)\hat{z}]$$

Which leads to that

$$\vec{P}(\vec{r}) \cdot d\vec{s} = \frac{h}{r_{fmn}^3} (cos\theta_{fmn})^{2q_f} dxdy \tag{2.27}$$

Finally, the spillover efficiency is obtained as:

$$\eta_s = \frac{2q_f + 1}{2\pi} \iint_A \frac{h}{r_{fmn}^3} (cos\theta_{fmn})^{2q_f} dxdy \tag{2.28}$$

Where A is determined by the aperture boundary equation. Two verification cases of η_s are presented, where the two system configuration are depicted in Fig. 2-27 and the configuration parameters are shown in Table 2-7.
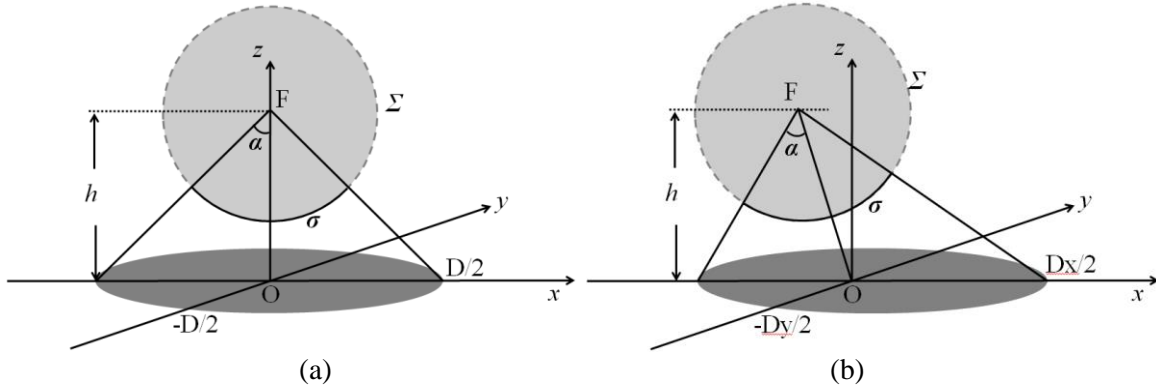
Fig. 2-27 Reflectarray configuration for (a) case 2.8.a and (b) 2.8.b.

Table 2-7 Configuration parameters for the two cases in case 2.8

Case	θ_0	h (mm)	q_f	x_0	y_0
2.6.2.1.a	0°	340	6	0	0
2.6.2.1.b	25°	340	6	0	0

In the first case, the feed horn is located in the z axis, where α denotes half of the solid angle and D is the diameter of the circular aperture. In this case, the η_s could be analytically calculated based on equation (2.24)

$$
\eta_s = \frac{\iint_\sigma \vec{P}(\vec{r}) \cdot d\vec{s}}{\iint_\Sigma \vec{P}(\vec{r}) \cdot d\vec{s}} = \frac{\int_0^{2\pi} \int_0^\alpha \cos^{2q_f}\theta \sin\theta d\theta d\varphi}{\int_0^{2\pi} \int_0^{\frac{\pi}{2}} \cos^{2q_f}\theta \sin\theta d\theta d\varphi} = \frac{\frac{2\pi}{2q_f+1}(1-\cos^{2q_f+1}\alpha)}{\frac{2\pi}{2q_f+1}}
$$

$$
= 1 - \cos^{2q_f+1}\alpha \tag{2.29}
$$

34

Different solid angles α are chosen to verify the formula given in (2.28), as shown in Fig. 2-28(a), and a very good agreement was observed.

For the 2nd case, assuming the array aperture subtends the same solid angle about the feed as the 1st case, η_s for case 2 shall be the same as that in case 1. However, since the array plane is not perpendicularly intercepting the feed beam anymore, the integration shown in (2.27) is performed in an elliptical area, whose boundary equation reads:

$$y^2 + (xcos\theta_0)^2 = (xsin\theta_0 + h/cos\theta_0)^2 tan^2\alpha \qquad (2.30)$$

The integration over this elliptical area could be implemented with the Matlab command *quad2d*, where the integration limits read respectively:

$$x_{min} = -h \times [\tan(\alpha - \theta_0) + \tan\theta_0] \qquad (2.31.a)$$

$$x_{max} = h \times [\tan(\alpha + \theta_0) - \tan\theta_0] \qquad (2.31.b)$$

$$y_{min} = -\sqrt{(xsin\theta_0 + h/cos\theta_0)^2 tan^2\alpha - (xcos\theta_0)^2} \qquad (2.31.c)$$

$$y_{max} = \sqrt{(xsin\theta_0 + h/cos\theta_0)^2 tan^2\alpha - (xcos\theta_0)^2} \qquad (2.31.d)$$

And the results are shown in Fig. 2-28(b).
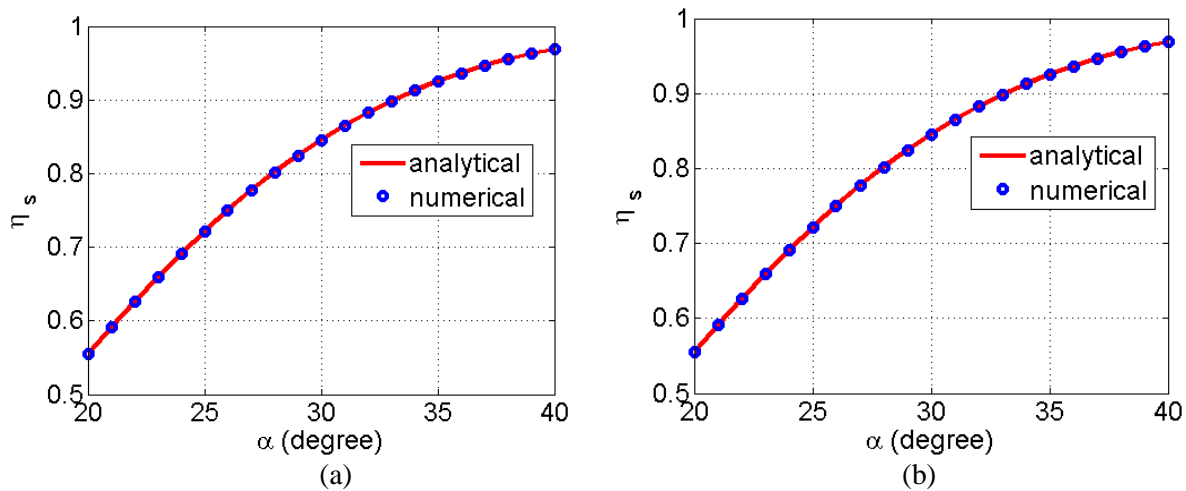
Fig. 2-28 Verification of η_s calculation for (a) case 2.8.a and (b) case 2.8.b.

2.5.2.3 Element loss efficiency

It is noted that although the term $|\Gamma_{mn}|$ is included in equation (2.3), when A_{mn} is substituted in equation (2.9), somehow it is cancelled out in the nominator and denominator, especially for the case where $|\Gamma_{mn}|$ is the same for all the elements. Hence, in order to take into account the element loss effect, the energy dissipated in the substrate material and metallic, η_{el} is introduced as below:

$$\eta_{el} = \frac{\sum_{n=1}^{N} \sum_{m=1}^{N} (A_{mn}|\Gamma_{mn}|)^2}{\sum_{n=1}^{N} \sum_{m=1}^{N} (A_{mn})^2} \tag{2.32}$$

2.5.2.4 Other Efficiency

There are some other efficiency factors, such as those associated with the feed loss, polarization loss and mismatch loss, which somehow depends on specific cases; and they will not be included in the calculation of gain.

2.5.3 Verification

2.5.3.1 Verification of Directivity Calculation

Two cases 2.4.3.1.a and 2.4.3.1.b are used to do the verification of directivity calculation and the reference examples are from [8]. All the other configuration parameters are chosen exactly the same as case 2.4.4.2.a and 2.4.4.2.b, respectively, except for the q_f factor. As the computation is performed from 28 GHz to 36 GHz, the q_f factor changes correspondingly. The q_f value is 5, 6.5 and 8.3 for 30 GHz, 32 GHz and 34 GHz, respectively, while the values at other frequencies are interpolated with a 2nd order polynomial based on these three points. The verification results are shown in Fig. 2-29, where the red dash lines are the reference results

while the blue solid lines are the repeated ones. It is obvious that the results agree with each other very well.
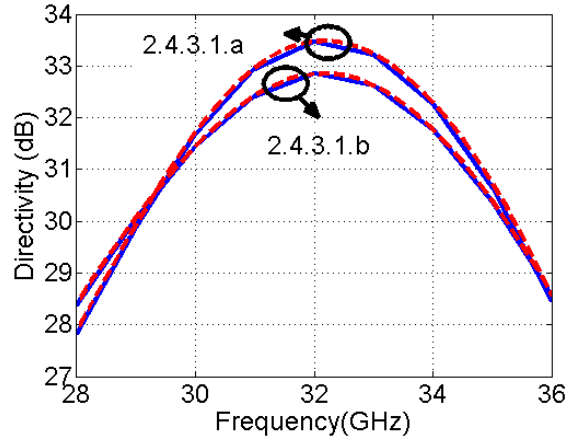
Fig. 2-29 Repeated and referred directivity for case 2.7.a and case 2.7.b. Blue solid curve for repeated results, and red dash curve for the reference result.

2.5.3.2 Comparison of Different Methods

Two more cases are used to compare the results from different methods, and their configuration parameters are exactly the same as case 2.4.4.2.a and 2.4.4.2.b, respectively. For each case, the comparison is made for both directivity and gain, and the results are summarized in Table 2-8, 2-9, 2-10, and 2-11. It shows good agreement among different methods, and the maximum difference is less than 0.1 dB. In addition, the calculation time is compared in Table 2-12, which shows that method 3 is much faster than the other two.

Table 2-8 Comparison of directivity for a broadside reflectarray (unit: dB)

	Method 1	Method 2	Method 3
17λ x 17λ	33.4777	33.4700	33.4429
34λ x 34λ	39.6214	39.5898	39.5621
50λ x 50λ	43.0380	42.9686	42.9437

Table 2-9 Comparison of gain for a broadside reflectarray (unit: dB)

	Method 1	Method 2	Method 3
17λ x 17λ	33.1428	33.1351	33.1080
34λ x 34λ	39.2873	39.2558	39.2281
50λ x 50λ	42.7029	42.6335	42.6086

Table 2-10 Comparison of directivity for a 25° offset reflectarray (unit: dB)

	Method 1	Method 2	Method 3
17λ x 17λ	32.8476	32.8476	32.8255
34λ x 34λ	38.9469	38.9469	38.9192
50λ x 50λ	42.3248	42.3248	42.3006

Table 2-11 Comparison of gain for a 25° offset reflectarray (unit: dB)

	Method 1	Method 2	Method 3
17λ x 17λ	32.4729	32.4729	32.4508
34λ x 34λ	38.5755	38.5755	38.5477
50λ x 50λ	41.9528	41.9528	41.9285

Table 2-12 Comparison of time for a broadside reflectarray (unit: seconds)

	Method 1	Method 2	Method 3
17λ x 17λ	60.85	3.27	2.64
34λ x 34λ	150.82	10.19	3.86
50λ x 50λ	263.68	46.79	5.25

2.6 Mask file generation

After the geometry for each element is determined, the next step is to generate a .PCB file for fabrication. The file format of .PCB file for our application is shown in Fig. 2-30, which includes three parts. The 1st part is the file head, which consists of fixed four lines, 2nd part is the file body, whose content is dependent on the aperture, and the last part is the file end, which consists of fixed three lines. Regarding the file body, Fig. 2-30 gives an example of a single rectangular which starts with two lines, '0' and 'SOLID'. The next 16 lines are used to describe the position of four corners of the rectangular, in the order of upper left point, bottom left point, upper right point and bottom right point. And for each corner, there are four lines to specify its x and y coordinates: the 1st line is the indicator for the x coordinate, the 2nd line is the x value, the 3rd line is the indicator for the y coordinate, and the 4th line is the y value. Hence, there are totally 18 lines for an individual rectangular. It is worthwhile to mention that for a rectangular loop, is could be split into four rectangular. Fig. 2-31 demonstrates an example of fabrication mask displayed in HFSS software, based on an imported .PCB file.

0	
SECTION	
2	
ENTITIES	
0	} Section head for an individual rectangular
SOLID	
10	Indicator for the *x* value of the upper left point
-0.022443750	*x* value of the upper left point
20	Indicator for the *y* value of the upper left point
0.022443750	*y* value of the upper left point
11	Indicator for the *x* value of the bottom left point
-0.022443750	*x* value of the bottom left point
21	Indicator for the *y* value of the bottom left point
0.019743750	*y* value of the bottom left point
12	Indicator for the *x* value of the upper right point
-0.019743750	*x* value of the upper right point
22	Indicator for the *y* value of the upper right point
0.022443750	*y* value of the upper right point
13	Indicator for the *x* value of the bottom right point
-0.019743750	*x* value of the bottom right point
23	Indicator for the *y* value of the bottom right point
0.019743750	*y* value of the bottom right point
…(other elements)	
0	
ENDSEC	
0	
EOF	

File head
File body
File end

Fig. 2-30 File format of .PBC file.
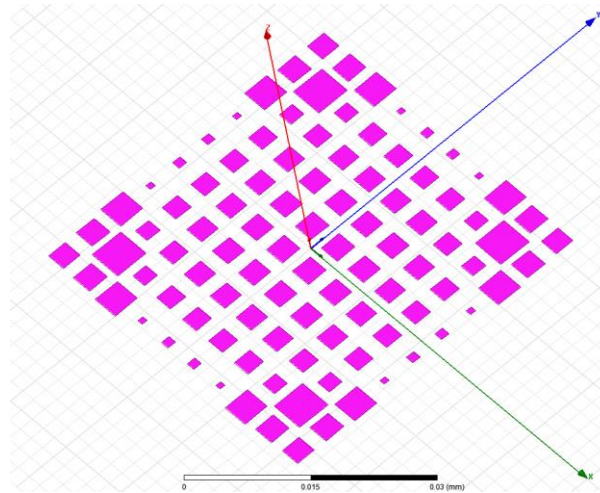
Fig. 2-31 Display of imported . PBC file in HFSS.

40

CHAPTER III

ELEMENT BANDWIDTH STUDY

One crucial factor that limits the reflectarray bandwidth is its element bandwidth. Generally the microstrip patch element has a bandwidth of about 3 to 5 percent [1]. To achieve a wider band, a lot of efforts have been made, techniques such as using multi-layers[13][14] and multi-resonance structures [15][16] have been employed. In this chapter, it is not our target to develop some novel shapes, but to explore elements in a more generous way, and hopefully it could provide some guidelines for the element choice in future designs. Therefore, elements of different shapes and substrate thicknesses are compared mainly in terms of phase range and element bandwidth.

3.1 Introduction to the Characteristics of Reflectarray Elements

In [7], the author defined four parameters as "figures of merit" to evaluate the element performance: (1) the range of the reflection phase; (2) the bandwidth; (3) the sensitivity to mechanical tolerances, and (4) the cross-polarization level. The reflection phase range mainly affects the directivity; the element bandwidth has a great impact on the reflectarray bandwidth; the sensitivity to mechanical tolerance determines the quantization error, therefore affects the directivity; and the cross-polarization level is another factor to influence the directivity. In this chapter, we mainly focused on the first three merits.

Especially, the element bandwidth is defined as below. For example, as shown in Fig. 3-1(a), the phase curves were obtained at different frequencies, centering at 13.5 GHz. By calculating the phase differences between other frequencies and center frequency, the results of phase errors were obtained as shown in Fig. 3-1 (b), and those two frequencies at which the maximum absolute value of phase difference is 45° are referred as upper and lower limit frequencies, indicated by f_u and f_l, respectively. And the element bandwidth is defined by maximum phase error is defined as

$$BW\_max = \frac{f_{u\_max} - f_{l\_max}}{(f_{u\_max} + f_{l\_max})/2}$$

(a)   (b)
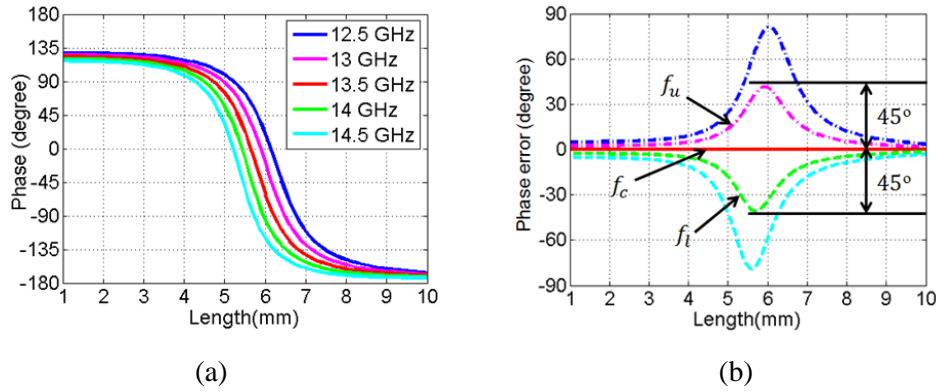
Fig. 3-1 (a) Phase curves obtained at different frequencies (b) the definition for the upper and lower extreme frequencies in the definition of element bandwidth.

3.2 The Comparison of Different Elements

Starting from the basic element shapes, square patch, square loop and cross-dipoles, as shown in the Fig. 3-2, are studied at first. For each element shape, the dimension mainly contributing to the phase variation is depicted as "*a*", and it is referred as phasing parameter; while for the square loop and cross-dipole shapes, the width of the loop and dipole also slightly

affect the element performance, and they are referred as tuning parameter. In most of the cases they are only used to optimize the element bandwidth here.

(a)   (b)   (c)
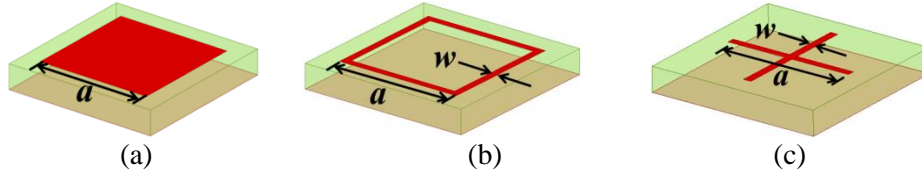
Fig. 3-2 Geometry demonstration for (a) patch and (b) loop and (c) cross-dipole.

For the variable-size phasing method, the phase varying is due to the element resonating. All the three elements above are of single-resonant, which means that their phase range is below 360°. For these three elements, all of them have the same periodicity and substrate given as:

cell element size = 11.2 mm, ε_r = 2.55

Fig. 3-3 shows the phase curves of these three different elements at 13.5 GHz when the substrate thickness is 1.58 mm, and it is observed that the resonant dimensions are respectively around 5.65 mm, 4.6 mm and 7.1 mm for patch, loop and cross-dipole antennas. Moreover, the current distribution simulation is also performed at these dimensions as depicted in Fig. 3-4, which shows that these three elements shapes resonated at the fundamental modes of patch, loop and dipole antenna.
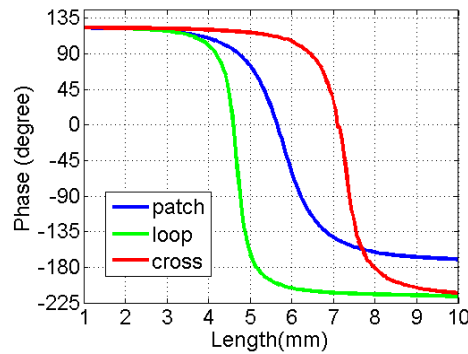
Fig. 3-3 Phase curves obtained at 13.5 GHz for patch/loop/cross-dipole elements.
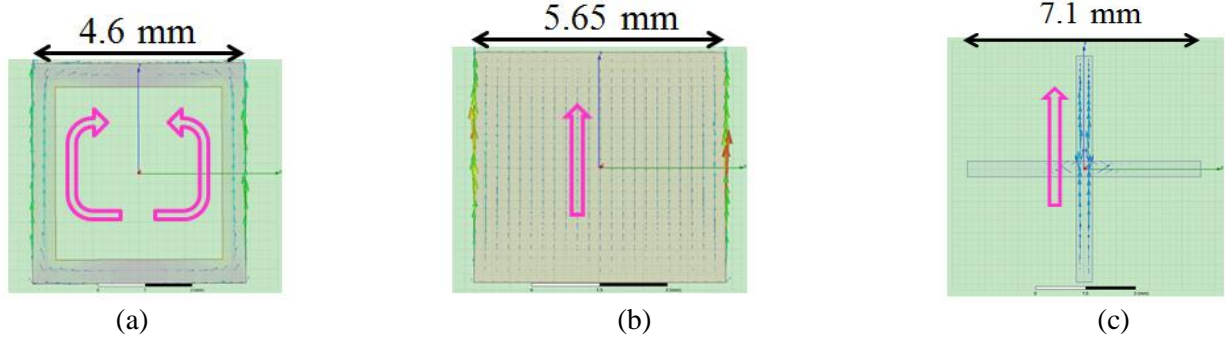
Fig. 3-4 Current flow at the resonance geometry for (a) loop and (b) patch and (c) cross-dipole.

3.2.1 Comparison among Elements of Different Shapes

At first, effect of element shapes on element performance is studied, where both the loop width and dipole width are 0.5 mm. The element simulation results are shown in Fig. 3-5, and it can be seen that patch element has the smoothest curve but with the smallest phase range while loop and cross elements have the similar element bandwidth, which verifies again that a slow slop transition in phase characteristics is usually accompanied with an overall smaller phase range. Moreover, according to the definition of element bandwidth defined in the previous section, the phase errors at each frequency, comparing to the center frequency, are calculated and depicted in Fig. 3-6.
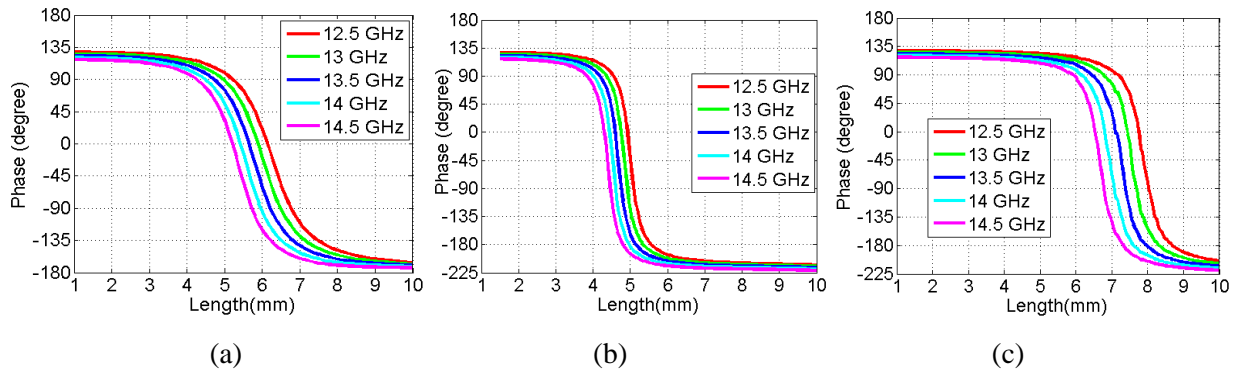
Fig. 3-5 The phase curves of (a) patch (b) loop and (c) cross-dipole.

The phase range at 13.5 GHz and element bandwidth is summarized in Table 3-1, and it shows that in terms of element bandwidth: patch >loop>cross, while in terms of phase range: patch<loop<cross.

(a)   (b)   (c)
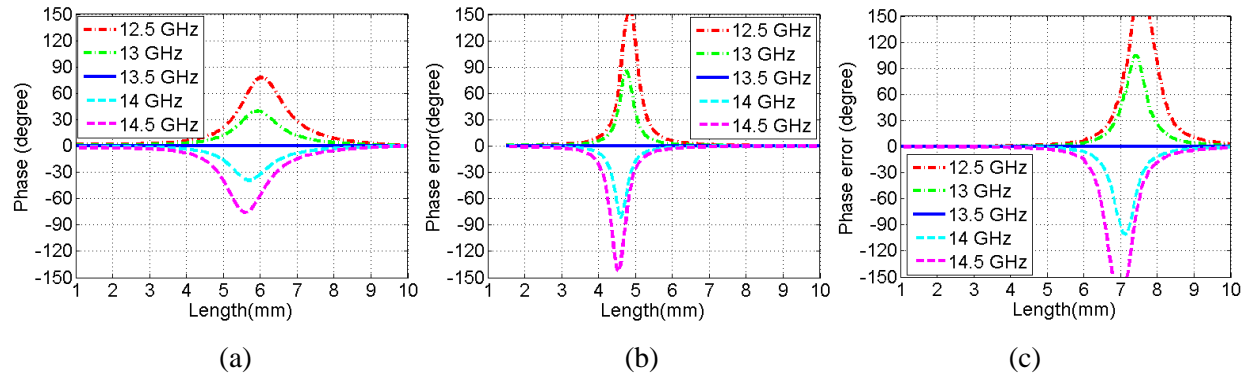
Fig. 3-6 The phase errors compared to the one obtained at center frequency for (a) patch (b) loop and (c) cross-dipole.

Table 3-1 The summary of the phase range at 13.5 GHz and element bandwidth

	patch	Loop	Cross-dipole
Phase range @ 13.5 GHz	293.0^o	339.7^o	335.6^o
Element bandwidth	7.6%	5.3%	4.8%

3.2.2 Comparison among Elements of Different Substrate Thickness

Secondly, the effect of substrate thickness on element performance is studied. When the substrate thickness is increased, usually the slop inclination becomes less vertical at the cost of phase range, thereby essentially increasing the bandwidth and decreasing the quantization error in fabrication. Theoretically, it could be explained with Q factor theory in patch antenna. It is well known that when the substrate thickness increases, the Q factor decreases, thus the traditionally defined bandwidth are increased, hence increasing the linearity of the phase curves.

45

In order to show the thickness effect, the three elements are investigated with different substrate thickness. Three different of thickness, 0.79 mm, 1.58mm and 3.18 mm, are chosen for the purpose of investigation.

The phase curves obtained at 13.5 GHz for patch elements of different substrate thicknesses are shown in Fig. 3-7. Apparently as the substrate thickness increases, the phase curves become more linear and the phase range is greatly reduced.
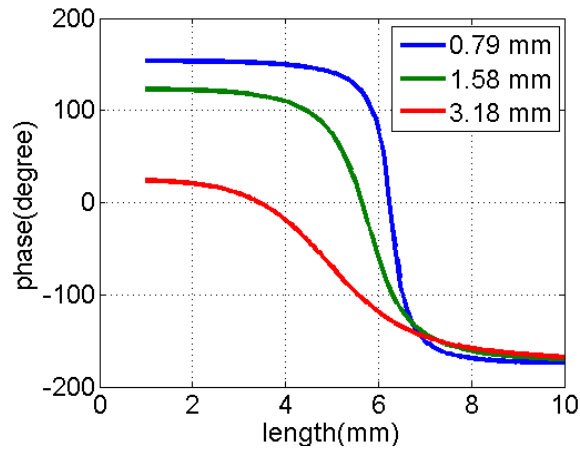
Fig. 3-7 Comparison of phase curve obtained at 13.5 GHz for patch elements of different substrate thickness.

In order to study the element bandwidth, phase curves at various frequencies are collected and demonstrated in Fig. 3-8. Moreover, the phase errors are calculated and shown in Fig. 3-9. It is seen that when the thickness is 0.79 mm, the phase error could reach around 90° when the frequency is only 0.5 GHz shifted. Contrarily, even the frequency shift is 1 GHz the phase error is only around 30° when the substrate thickness is 3.18 mm. The phase ranges at 13.5 GHz and the element bandwidth for patch elements of various substrate thicknesses are summarized in Table 3-2.

(a) t = 0.79 mm   (b) t = 1.58 mm   (c) t = 3.18 mm
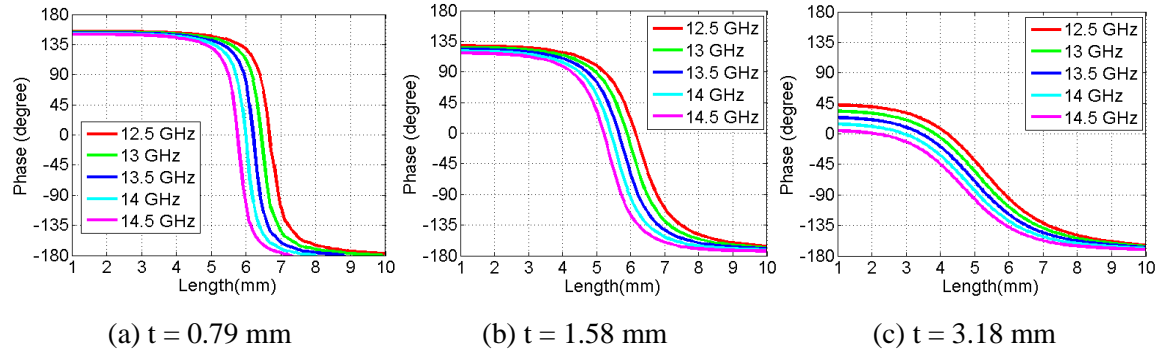
Fig. 3-8 Comparison of phase curve for patch elements of different substrate thickness.

(a) t = 0.79 mm   (b) t = 1.58 mm   (c) t = 3.18 mm
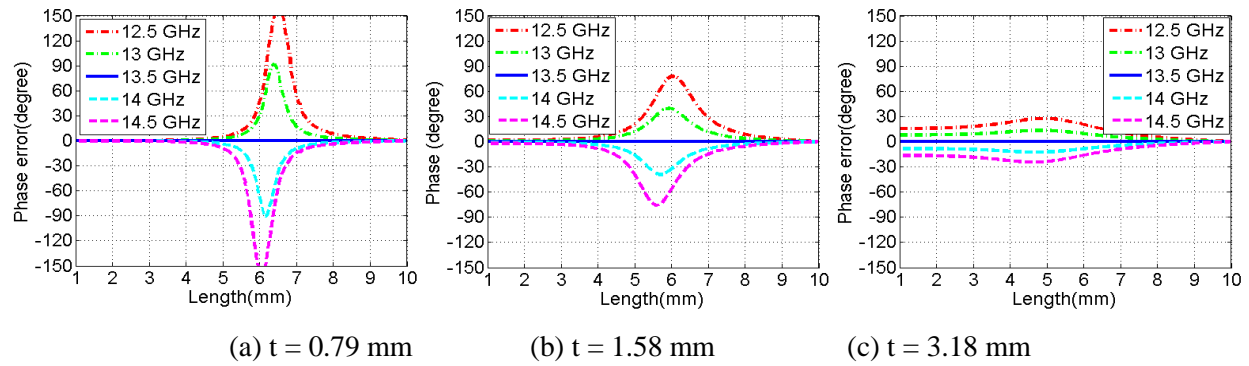
Fig. 3-9 Comparison of phase errors for patch elements of different substrate thickness.

Table 3-2 Summary of phase ranges at 13.5 GHz and element bandwidth for patch elements of different substrate thickness

	t = 0.79 mm	**t = 1.58 mm**	**t = 3.18 mm**
Phase range(@13.5 GHz)	327.6^o	293.0^o	191.9^o
Element bandwidth	5.1%	7.6%	14.7%

Similar analysis is performed to the loop elements with loop width being 0.5 mm and similar phenomenon is observed, which are demonstrated in Fig. 3-10, 3-11 and 3-12, as well as Table 3-3.
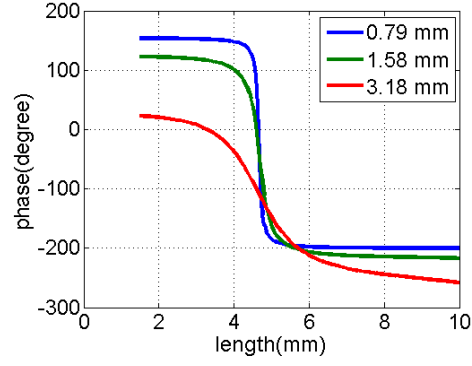
Fig. 3-10 Comparison of phase curve obtained at 13.5 GHz for loop elements of different substrate thickness.

(a) t = 0.79 mm   (b) t = 1.58 mm   (c) t = 3.18 mm
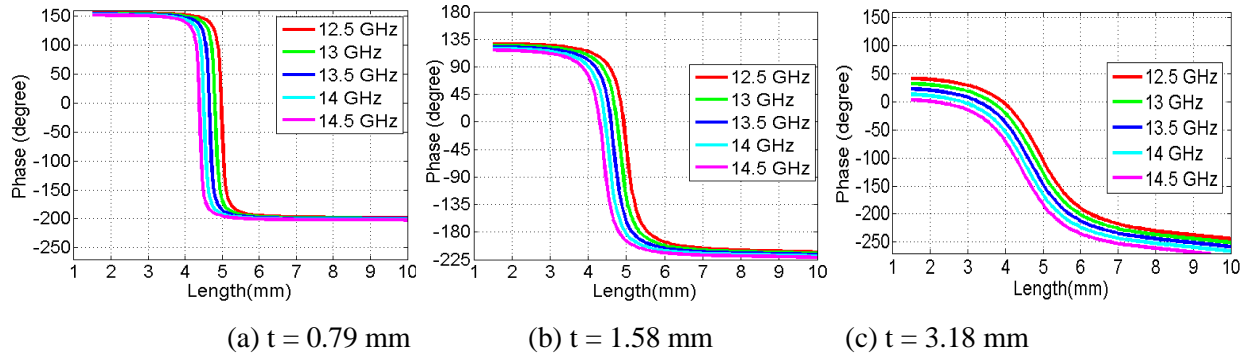
Fig. 3-11 Comparison of phase curve for loop elements of different substrate thicknesses.

(a) t = 0.79 mm   (b) t = 1.58 mm   (c) t = 3.18 mm
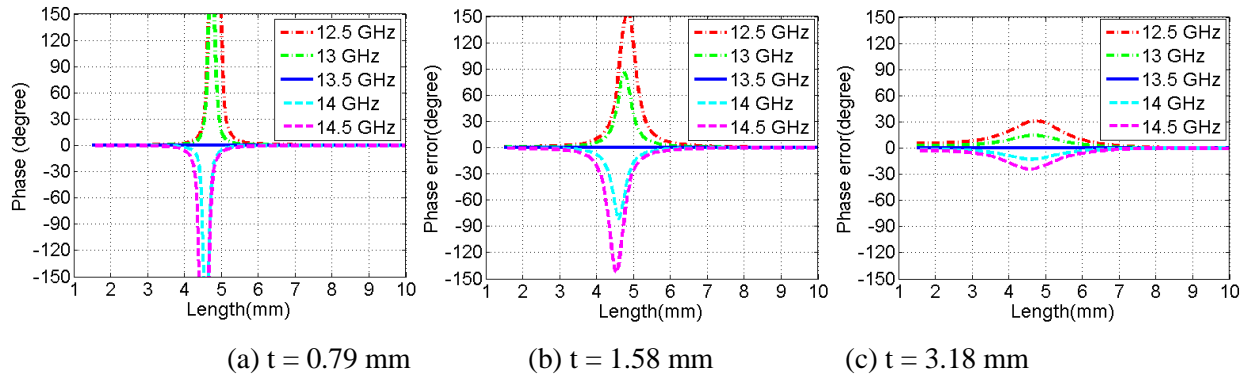
Fig. 3-12 Comparison of phase errors for loop elements of different substrate thicknesses.

Table 3-3 Summary of phase ranges at 13.5 GHz and element bandwidth for loop elements of different substrate thickness

	t = 0.79 mm	t = 1.58 mm	t = 3.18 mm
Phase range(@13.5 GHz)	**353.7°**	**339.7°**	**281.1°**
Element bandwidth	**3.9%**	**5.3%**	**11.9%**

Similar analysis is made to the cross-dipole elements with dipole width being 0.5 mm and similar phenomenon is observed, which are demonstrated in Fig. 3-13, 3-14 and 3-15, as well as Table 3-4.
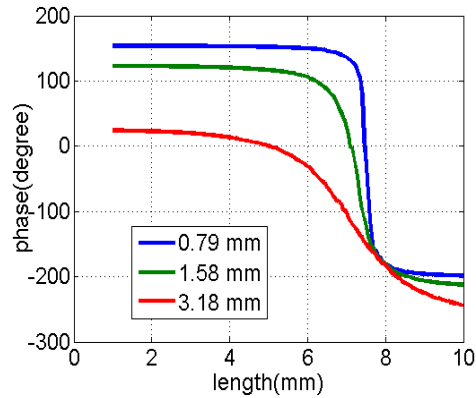
Fig. 3-13 Comparison of phase curve obtained at 13.5 GHz for cross-dipole elements of different substrate thickness.

(a) t = 0.79 mm   (b) t = 1.58 mm   (c) t = 3.18 mm
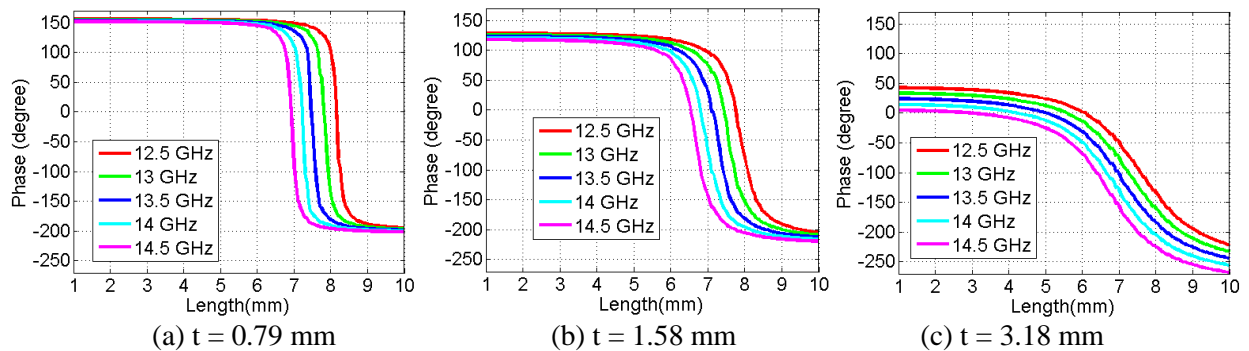
Fig. 3-14 Comparison of phase curve for cross-dipole elements of different substrate thicknesses.

(a) t = 0.79 mm   (b) t = 1.58 mm   (c) t = 3.18 mm
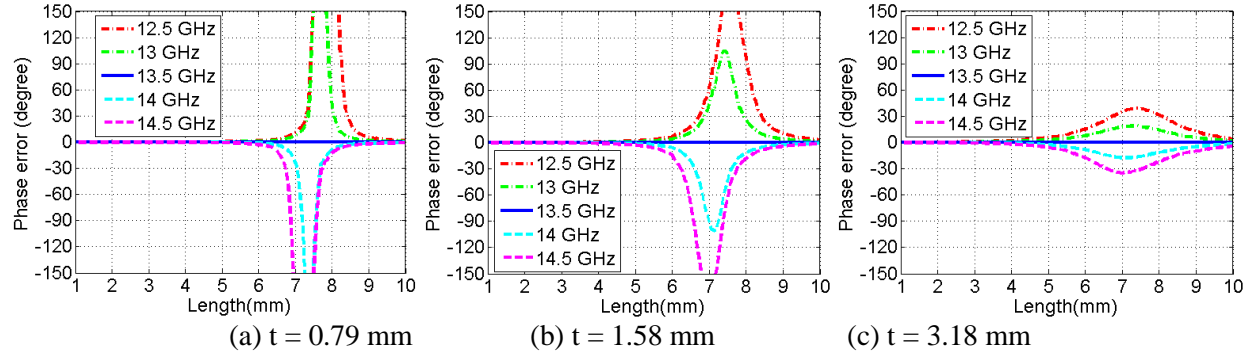
Fig. 3-15 Comparison of phase errors for cross-dipole elements of different substrate thickness.

Table 3-4 Summary of phase ranges at 13.5 GHz and element bandwidth for cross-dipole elements of different substrate thickness

	t = 0.79 mm	t = 1.58 mm	t = 3.18 mm
Phase range(@13.5 GHz)	352.2°	335.6°	268.2°
Element bandwidth	3.7%	4.8%	10.4%

3.2.3 Comparison among Loop Elements of Different Loop Width

Then the parametric study of loop width is studied. Three different loop width, 0.5 mm, 1 mm and 1.5 mm, are chosen to show how it influences the element bandwidth. The similar analysis is made as before and the results are shown in Fig. 3-16 and 3-17, as well as Table 3-5.

It is seen that the change of the loop width slightly affects the element bandwidth and phase range. However, when the loop width increases, the bandwidth is increased a little.

(a) *w* = 0.5 mm   (b) *w* = 1 mm   (c) *w* = 1.5 mm
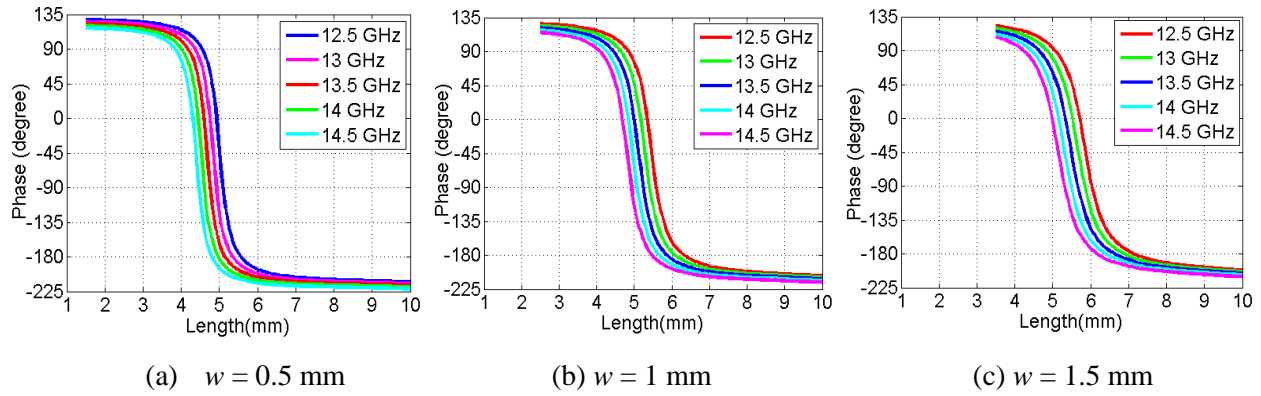
Fig. 3-16 Comparison of phase curve for loop elements of different loop width.

(a) *w* = 0.5 mm   (b) *w* = 1 mm   (c) *w* = 1.5 mm
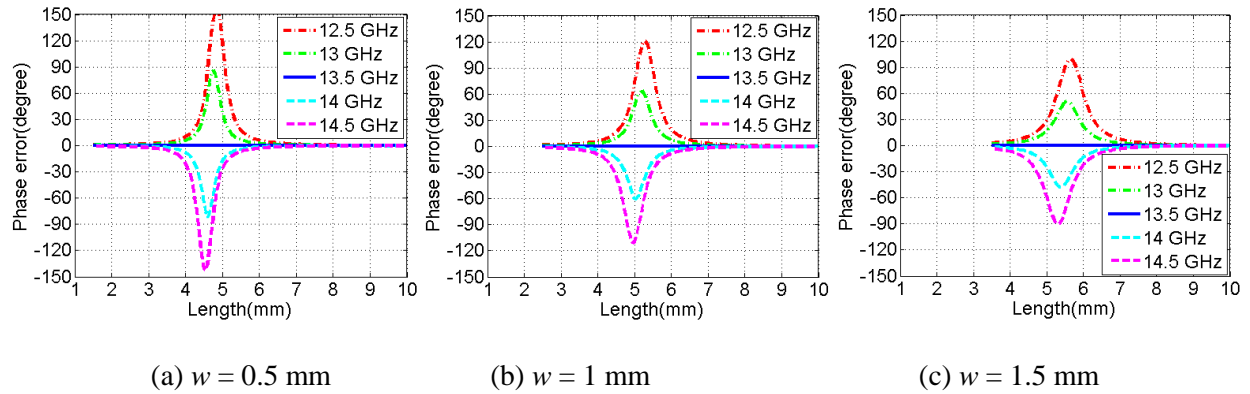
Fig. 3-17 Comparison of phase errors obtained for loop elements of different loop width.

Table 3-5 Summary of phase ranges at 13.5 GHz and element bandwidth for loop elements of different loop width

w	0.5 mm	1 mm	1.5 mm
Phase range@13.5 GHz	339.7^o	332.5^o	327.0^o
Element bandwidth	5.3%	6.0%	6.7%

3.2.4 Comparison among Cross-dipole Elements of Different Dipole Width

Then the parametric study of dipole width is studied. Three different dipole width, 0.5 mm, 1 mm and 1.5 mm, are chosen to show how it influences the element bandwidth. The similar analysis is made as before and the results are shown in Fig. 3-18 and 3-19, as well as

Table 3-6. It is seen that the dipole width slightly affects the element bandwidth and phase range. However, when the dipole width increases, the bandwidth also increased a little.

(a) $w = 0.5$ mm　　　　(b) $w = 1$ mm　　　　(c) $w = 1.5$ mm
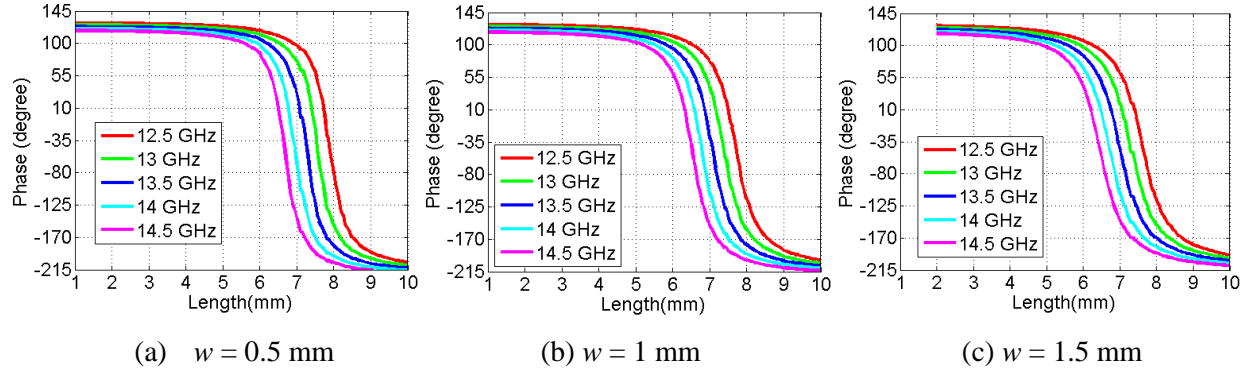
Fig. 3-18 Comparison of phase curve for cross-dipole elements of different dipole width.

(a) $w = 0.5$ mm　　　　(b) $w = 1$ mm　　　　(c) $w = 1.5$ mm
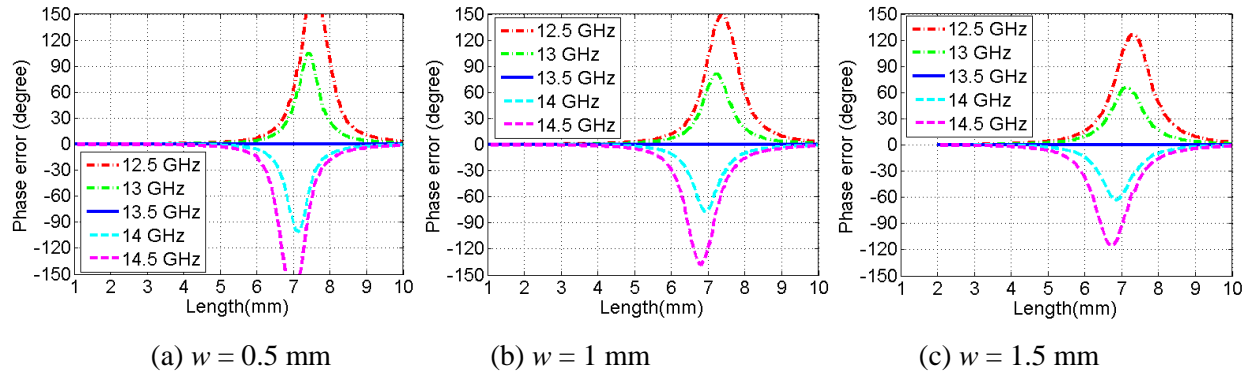
Fig. 3-19 Comparison of phase errors obtained for cross-dipole elements of different dipole width.

Table 3-6 Summary of phase ranges at 13.5 GHz and element bandwidth for cross-dipole elements of different dipole width

w	0.5 mm	1 mm	1.5 mm
Phase range@13.5 GHz	335.6^{o}	330.1^{o}	324.3^{o}
Element bandwidth	4.8%	5.3%	5.8%

3.3 Summary of Element Bandwidth Study

In summary,

➢ Regarding element shape:

In terms of element bandwidth: patch ＞ loop＞ cross-dipole;

In terms of phase range: patch ＜ loop ＜ cross-dipole;

➢ Regarding substrate thickness:

In terms of element bandwidth: for all the element shapes, 0.79 mm ＜1.58 mm ＜3.18 mm

In terms of element bandwidth: for all the phase range, 0.79 mm ＞1.58 mm ＞3.18 mm

➢ Regarding loop/cross-dipole width:

In terms of element bandwidth: for both the elements, 0.5 mm ＜ 1 mm ＜ 1.5 mm

In terms of element bandwidth: for both the elements: 0.5 mm ＞ 1 mm ＞ 1.5 mm

The detailed results are summarized in Table 3-7 and 3-8, which shows that all the considered factors can affect the element performance thereby the reflectarray: the phase range mainly relates to the peak directivity; the element bandwidth mainly relates to the reflectarray bandwidth, however, since a narrower element bandwidth is usually accompanied with a more strict requirement on fabrication tolerance, practically the designed directivity or gain could be greatly degraded under a moderate fabrication accuracy if elements of very narrow-bandwidth are used.

Table 3-7 Summary of phase ranges at 13.5 GHz and element bandwidth for patch /loop / cross-dipole element itched on various substrate thicknesses

t	Patch		Loop		Cross-dipole	
	Phase range	BW	Phase range	BW	Phase range	BW
0.79 mm	327.6^{o}	5.1%	353.7^{o}	3.9%	352.2^{o}	3.7%
1.58 mm	293.0^{o}	7.6%	339.7^{o}	5.3%	335.6^{o}	4.8%
3.18 mm	191.9^{o}	14.7%	281.1^{o}	11.9%	268.2^{o}	10.4%

Table 3-8 Summary of phase ranges at 13.5 GHz and element bandwidth for loop / cross-dipole element of different loop/dipole width

w	Loop		Cross-dipole	
	Phase-range	BW	Phase-range	BW
0.5 mm	339.7^{o}	5.3%	335.6^{o}	4.8%
1.0 mm	332.5^{o}	6.0%	330.1^{o}	5.3%
1.5 mm	327.0^{o}	6.7%	324.3^{o}	5.8%

CHAPTER IV

INVESTIGATION INTO REFLECTARRAY BANDWIDTH

It is well known that the reflectarrays have a severe drawback of narrow bandwidth which is mainly due to factors [1]: the inherent arrow bandwidth behavior of microstrip elements, and the differential spatial phase delay resulting from different path lengths from the feed to each element.

A lot of efforts have been made to address the former limitation, and all of them focus on the element performance improvement[4][13][16][17][18][19][20]. After carefully tuning the element dimensions, the phase curves obtained at different frequencies can be almost parallel with each other. However, it is worthwhile pointing out that most wideband elements have certain undesirable characteristics: a thick substrate is used, which is heavier, causes more and oblique incident illumination; more complex geometrical configurations are used, which requires complicated and lengthy design process; the wideband elements are usually large and difficult to fit in dual-band reflectarrays with two sets of elements, each of which corresponds to one design frequency. Regarding the constraint factor due to the differential spatial phase delay as demonstrated in [2], it is only significant for electrically very large apertures with small *F/D* ratios. And the typical solutions to this limitations are a true time delay design [3] and three-layer stacked reflectarray [14].

55

Optimization techniques are often implemented to perform phase synthesis for wideband reflectarrays. Instead of designing the reflectarray at the center frequency, one can minimize the summed phase error (the difference between the desired and realized phases) at multiple frequencies simultaneously [4][14][19]. Or, the desired far-field patterns on a prescribed frequency band were directly used in the synthesis technique to improve the frequency behavior [21][22]. However, such approach usually requires tuning several geometrical parameters of the elements to reach this goal, i.e., it could not circumvent the aforementioned problems associated with wideband elements.

In this chapter, the reflectarray bandwidth is investigated in a comprehensive way. The main contributing factors to the reflectarray bandwidth, aperture size, element bandwidth and phase synthesis method, will be elucidated one by one. Numerical studies are presented to show their impacts. Reflectarray antennas designed with different size, elements, substrate thickness and methods are demonstrated. More importantly, a novel wideband phase synthesis approach, which is able to considerably increase the bandwidth of the reflectarray antenna at the cost of a minor gain loss and somehow irrespective of the element frequency behavior. Finally, in order to verify the obtained theoretical conclusion, some experimental results are exhibited.

4.1 Three Main Contributing Factors to the Reflectarray Bandwidth

Generally there are three contributors, element bandwidth, aperture size, and phase synthesis method, exerting influences upon the reflectarray bandwidth.

4.1.1 Aperture Size Effect on the Reflectarray Bandwidth

In [3], it showed the bandwidth will be greatly degraded for large reflectarrays unless TTD technique is used. Here four cases of different aperture sizes, $13\lambda_0$, $25\lambda_0$, $50\lambda_0$ and

100 λ_0 , respectively, are calculated to demonstrate how the aperture size influences the reflectarray bandwidth. Other configurations are as below:

f_0 = 13.5 GHz, f/D = 0.735, q^f = variable, element shape = loop, substrate thickness = 1.58 mm, normal illumination
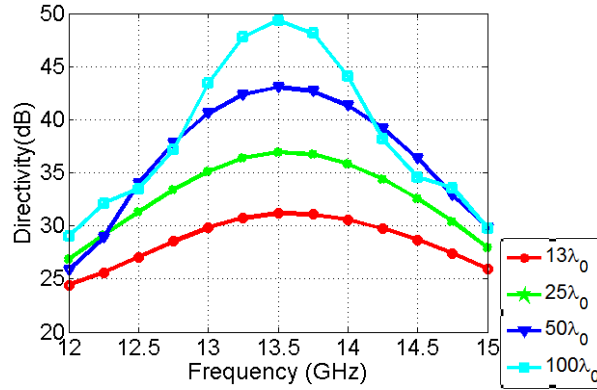
Fig. 4-1 Demonstration of aperture effect on the reflectarray bandwidth.

Table 4-1 Summary of directivity and bandwidth for reflectarray of different aperture sizes

Diameter	$13\lambda_0$	$25\lambda_0$	$50\lambda_0$
Directivity @13.5GHz (dB)	30.65	36.41	42.51
Bandwidth	7.8%	5.7%	4.5%

The comparison results are summarized in Table 4-1, as well as depicted in Fig. 4-1. Clearly when the diameter gets larger, the directivity increases at the expense of bandwidth.

4.1.2 Element Bandwidth Effect on the Reflectarray Bandwidth

Regarding the element bandwidth, as discussed in Chapter 3, both the element shape and substrate thickness have big impacts on the element bandwidth, which essentially plays a crucial role for the reflectarray bandwidth. It is a rule of thumb that the wider the element bandwidth,

the wider the reflectarray bandwidth. In this section, the influence of substrate thickness is shown firstly and then the element shape.

It has been displayed before that increment of the substrate thickness leads to an improvement on the element bandwidth, and it is shown here that it further broadens the reflectarray bandwidth. The three pre-mentioned element shapes are used to confirm the conclusion, and all the reflectarray designs have the same configuration that:

$f_0 = 13.5$ GHz, Diameter = 516 mm, $f/D = 0.735$, q^f = variable, normal incidence

(a)   (b)
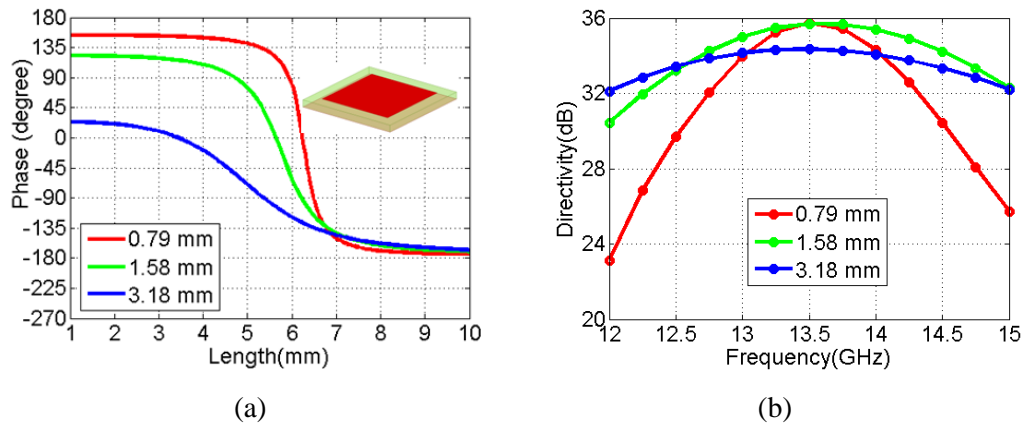
Fig. 4-2 (a) Phase curves for patch elements of various substrate thicknesses and (b) directivity bandwidth performance for reflectarray built on substrates of various thicknesses with diameter being 516 mm.

Table 4-2 Summary of directivity and bandwidth for reflectarray of different aperture sizes

Substrate thickness	0.79 mm	1.58 mm	3.18 mm
Directivity @13.5GHz (dB)	35.7	35.7	34.2
Bandwidth	5.5%	10.6%	15.0%

For a patch element, when the substrate thickness is 0.79 mm, 1.58 mm and 3.18 mm, respectively, the phase curves are displayed here in Fig. 4-2 (a), and the corresponding reflectarray directivity performance is summarized in Table 4-2 and illustrated in Fig. 4-2 (b). It

is confirmed that when the substrate gets thicker, the reflectarray bandwidth increases. One thing that needs to be pointed out is that when the substrate thickness changes from 1.58 mm to 3.18 mm, there is around 1.5 dB drop for directivity, which is caused by the phase range shrinkage. It is noted that when the thickness is 3.18 mm, the phase range is only 192°, almost half of a full cycle.

(a)   (b)
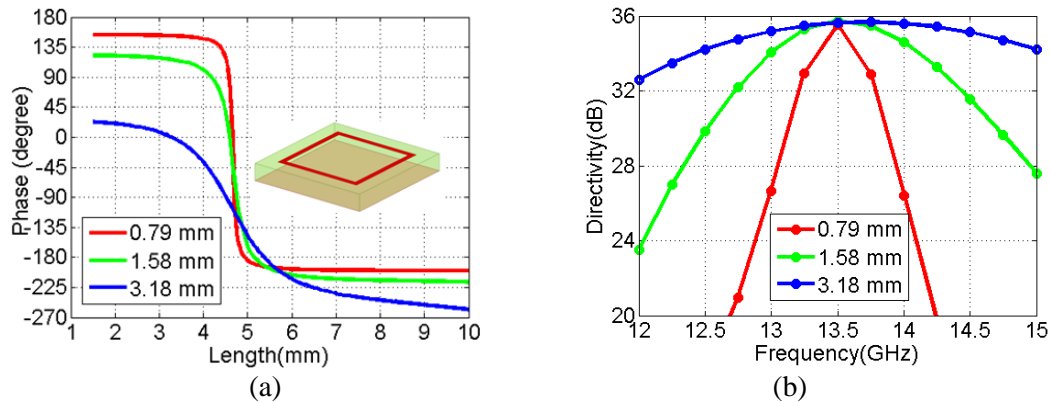
Fig. 4-3 (a) Phase curves for loop elements of various substrate thicknesses and (b) directivity bandwidth performance for reflectarray of various substrate thicknesses with diameter being 516 mm.

Table 4-3 Summary of directivity and bandwidth for reflectarray of different aperture sizes

Substrate thickness	0.79 mm	1.58 mm	3.18 mm
Directivity @13.5GHz (dB)	35.5	35.7	35.6
Bandwidth	0.2%	6.2%	14.8%

Similarly, for a square loop element, when the substrate thickness is 0.79 mm, 1.58 mm and 3.18 mm, respectively, the phase curves are shown in Fig. 4-33 (a), and the corresponding reflectarray performance is summarized in Table 4-3 and illustrated by Fig. 4-3 (b). The conclusion about the substrate thickness and reflectarray bandwidth is verified again.

(a)   (b)
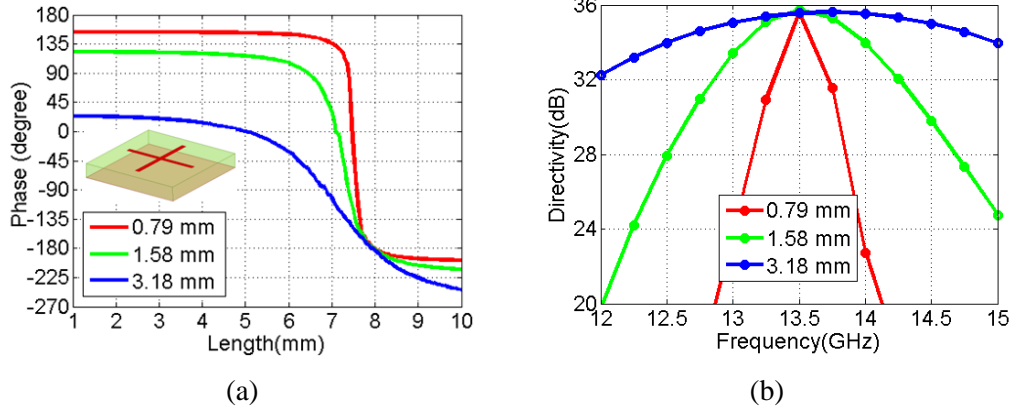
Fig. 4-4 (a) Phase curves for cross-dipole elements of various substrate thickness and (b) directivity bandwidth performance for reflectarray of various substrate thickness with diameter being 516 mm.

Table 4-4 Summary of directivity and bandwidth for reflectarray of different aperture sizes

Substrate thickness	0.79 mm	1.58 mm	3.18 mm
Directivity @13.5GHz (dB)	35.6	35.7	35.6
Bandwidth	0.2%	4.5%	14.0%

Finally, a similar comparison is made for the cross-dipole element, and similar phenomena are also observed as shown in Table 4-4 and Fig. 4-4.

One thing that needs to be pointed out is that when the substrate thickness is 1.58 mm, the directivity is usually the highest. The reason is that there are two factors controlling the element phase errors at the design frequency, which then influences the peak directivity. When the substrate thickness differs, phase range and quantization error both varies, which changes the phase errors in two opposite ways. When the substrate thickness is 1.58 mm, it allows a smaller quantization error compared to thinner substrate, while a larger phase range compared to the thicker one, hence it has the smallest total phase error and consequently the largest peak directivity.
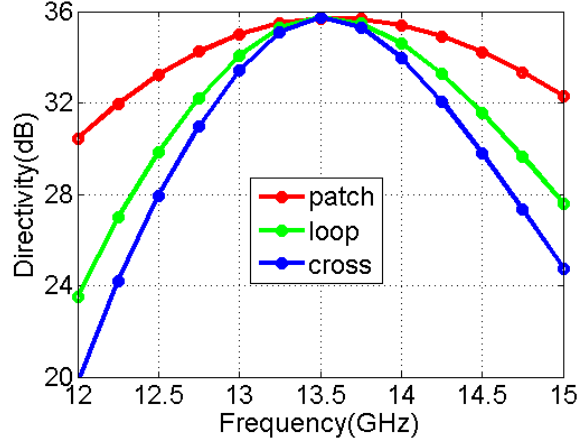
Fig. 4-5 Demonstration of directivity bandwidth performance for reflectarray consisting of different elements.

In order to show how the element shape affects the directivity, the previously used three element shapes were used for comparison again. The reflectarray configuration is as below:

$$f_0 = 13.5 \text{ GHz, Diameter} = 25\lambda, f/D = 0.735, q^f = 6.5, t = 1.58 \text{ mm}$$

Based on the study made in chapter 3, when the substrate thickness is 1.58 mm, the element bandwidth is respectively 7.6%, 5.3% and 4.8% for patch, square loop and cross-dipole elements. As depicted in Fig. 4-5, correspondingly the reflectarray consisted of cross-dipole elements has the smallest bandwidth 4.5%, while the one made of patch elements yields the biggest bandwidth, around 10.6%. Actually, there are many other published advanced element shapes which are of very broad bandwidth, usually whose main idea is to increase the substrate thickness while introducing another resonance to the element to compensate the phase range shrinkage.

4.2 Phase Synthesis Method Effect on the Reflectarray Bandwidth

The last effecting factor is the phase distribution, which also has a big influence on the reflectarray bandwidth. For the sake of convenience, four phase related concepts needs to be clearly defined at first:

- Required phase $\varphi^r_{mn}(f_0)$: is defined as the required phase delay for a certain mn^{th} element at a certain frequency f_0 limited to 360° range with reference phase being 0°

- Achieved phase $\varphi^a_{mn}(f_0)$: is defined as the finally realized phase delay for a certain mn^{th} element, at a certain frequency f_0 which is chosen from all the simulated phases following a certain routine

- Simulated phase $\varphi^s(f_0)$: is defined as the simulated phase delay at a certain frequency f_0, the achievable practical phase

- Phase error $pe_{mn}(f_0)$: is defined as the difference between the required and achieved ones for a certain mn^{th} element at a certain frequency f_0

The key to reflectarray designs is to find the most proper phase for each element to meet the design requirement. In the case of a single pencil-beam reflectarray, the required reflection phase of the mn^{th} element can be computed as:

$$\varphi^r_{mn}(f) := k \cdot \left(\left| \vec{r}_{mn} - \vec{r}_f \right| - \hat{u}_0 \cdot \vec{r}_{mn} \right) \tag{4.1}$$

Where k is the wavenumber in free space at frequency f, $\vec{r}_{mn}$ is the position vector of the mn^{th} element, $\vec{r}_f$ is the position vector of the feed and $\hat{u}_0$ is the unit vector of the main beam direction. Hence the phase error for the mn^{th} element is defined as:

$$PE_{mn}(f) = \left| \varphi^a_{mn}(f) - \varphi^r_{mn}(f) \right| \tag{4.2}$$

Which is apparently frequency dependent. The phase synthesis process is essentially to minimize the phase errors through analytical or numerical methods.

Here, we categorized the phase synthesis methods into three: method 1, single-frequency design; method 2, dual-frequency without optimization of reference phase; method 3, dual-frequency with optimization of reference phase.
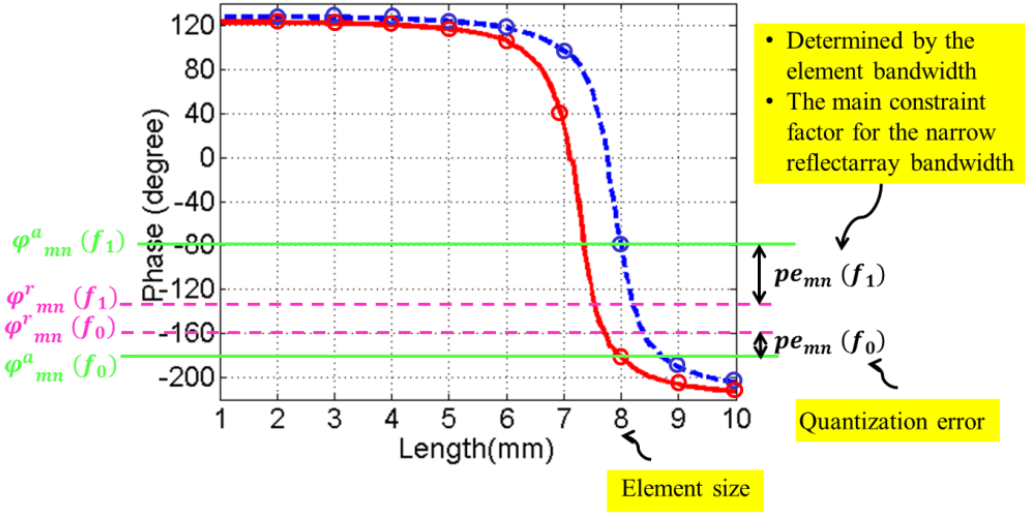
Fig. 4-6 Demonstration of methodology of method 1.

4.2.1 The Single-frequency Design Method

Method 1 refers to the most traditional one, where the optimal performance in terms of gain is targeted at a single design frequency. The design procedure is essential to minimize the phase error of each element only at the design frequency f_0 such that the cost function, CF_1, becomes:

$$CF_1 = PE_{mn}(f_0) \tag{4.3}$$

Where the phase error of each element is defined in (4.2).

As depicted in Fig. 4-6, there are two phase curves, red solid and blue dash, which correspond to frequency f_0 and f_1, respectively, and f_0 is the design frequency. Assuming the phasing geometry only changes from 2 mm to 10 mm at a step of 1 mm, there are only 9

achievable practical element phase. Following the methodology of method 1, for each element, the element geometry whose corresponding reflection phase has the smallest phase error with the required one at f_0 is chosen. For example, for the mn^{th} element, the required phase is $\varphi^r{}_{mn}(f_0)$, and clearly there is no simulated phase exactly at the intersection between the red curve and the purple dash line which indicates $\varphi^r{}_{mn}(f_0)$. Therefore, after computing the absolute difference between $\varphi^r{}_{mn}(f_0)$ and all the 9 simulated phases, 8 mm is chosen as the size of the mn^{th} element, and the introduced quantization error $pe_{mn}(f_0)$ could be represented by the distance between the purple and green lines at f_0 in the graph. After the procedure is performed for all the elements one by one, the design was done, and the gain could be calculated using array theory. However, when the frequency deviates from the design one, say f_1, for the certain phasing geometry of 8 mm, the practical element phase becomes $\varphi^a{}_{mn}(f_1)$, and the phase error becomes the difference between $\varphi^a{}_{mn}(f_1)$ and the newly required element phase $\varphi^r{}_{mn}(f_1)$, which is marked as $pe_{mn}(f_1)$ in the figure. For a reflectarray, when the aperture size and feed position are determined, $\left|\varphi^r{}_{mn}(f_0) - \varphi^r{}_{mn}(f_1)\right|$ is determined, hence, when the phase curve gets more sharper, $\left|\varphi^a{}_{mn}(f_0) - \varphi^a{}_{mn}(f_1)\right|$ consequentially increases, which leads to larger phase error at frequency f_1 and narrower reflectarray bandwidth.

In a word, when method 1 is used, for a certain element configuration, i.e. somehow determined phase range and quantization error, the maximum achievable peak gain is guaranteed at the center frequency and the reflectarray bandwidth is totally dependent on the element bandwidth. Unfortunately, due to the inherent narrow bandwidth characteristic of patch antenna, the reflectarray bandwidth is usually small.

4.2.2 The Dual-frequency Design Method without Optimization of Reference Phase

Compared with method 1, by the way of method 2 the reflectarray bandwidth could be broaden, usually at the cost of gain loss. It takes into account the gain performance at two properly separated frequencies f_1 and f_2, and the cost function becomes:

$$CF_2 = PE_{mn}(f_1) + PE_{mn}(f_2) \tag{4.4}$$

Therefore, two design frequencies within the objective frequency range are picked, and surely for a certain mn^{th} element, the required element phases, say $(\varphi^r_{mn}(f_1), \varphi^r_{mn}(f_2))$, are different from each other. Essentially, with method 2 it is assumed that ideally if the maximum achievable peak directivity could be reached at both frequencies simultaneously, then the combination of the two narrow bands could lead to a wide one, whose principle is quite similar to that of the U-slot method for patch antenna where a second resonance is introduced and the finally combined bandwidth becomes very large.

However, this approach usually requires simultaneously tuning multiple geometrical parameters of a complex element configuration in order to achieve good radiation performances at both design frequencies. Should simple reflectarrays such as crossed-dipoles or square-loops be adopted, such phase error minimization becomes impossible and the reflectarray designed by this approach would suffer considerable gain loss.

As illustrated in Fig. 4-7, the same set of nine simulated phases is again taken an example. For a certain mn^{th} element, the required element phase is $\varphi^r_{mn}(f_1)$ and $\varphi^r_{mn}(f_2)$ for the frequency f_1 and f_2, respectively. Then, a parametric study is performed for each phasing length, where the cost function CF_2 is calculated each time. Finally, the phasing geometry which corresponds to the smallest phase error is chosen for the mn^{th} element.
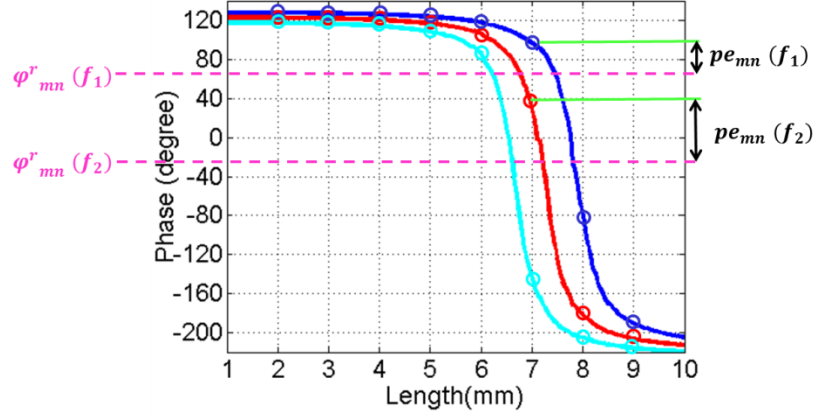
Fig. 4-7 Demonstration of methodology of method 2.

An example is made to understand the mechanism of the method 2. The reflectarray configuration is as below:

f_1 = 12.75 GHz, f_2 = 14.25 GHz, Diameter = 400 mm, Feed position = (-175 mm, 0, 375mm), q^f = variable, element shape = square loop, t = 1.58 mm, 25° oblique illumination

The calculated gain is plotted by red curve in Fig. 4-8. It is observed that there are two closely separated bands, whose peak values might not be exactly the two selected frequencies but are certainly due to them. And it is also seen that there is a dip in the middle. How low the dip goes basically depends on two things: 1) the element bandwidth and 2) the distance between the two design frequencies. By manipulating these two factors we could get either a wide-band or closely separated dual-band reflectarray. The black dash-dot curve is the theoretical maximum gain that can be obtained at each frequency and it is calculated single frequency per single frequency. By comparing the red curve and the black dot curve, it is noticed that after method 2 is applied, two closely separate bands are obtained at the cost of big gain loss due to the suboptimal phase characteristics at either specific frequency.
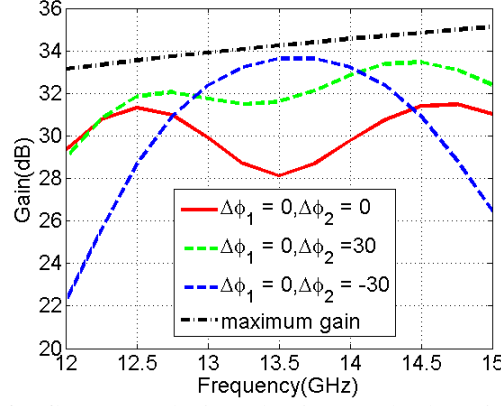
Fig. 4-8 The comparison of reflectarray designed using method 2 with different reference phases.

4.2.3 The Dual-frequency Design Method with Optimization of Reference Phase

It is well known that in reflectarray designs only the reflection phase relative to each other matters. A constant reference phase may be added to all the elements and it barely changes the overall performance of the reflectarray. This might as well be the reason that the reference phase has been overlooked since the inception of reflectarrays.

The above conclusion usually holds for the single-frequency approach. However, when two additional reference phases $\Delta\varphi_1$ and $\Delta\varphi_2$ are added to (4.1) for the dual-frequency approach, the required reflection phases become:

$$\varphi^{r\prime}{}_{mn}(f_1, \Delta\varphi_1) = k_1 \cdot \left(\left| \vec{r}_{mn} - \vec{r}_f \right| - \hat{u}_0 \cdot \vec{r}_{mn} \right) + \Delta\varphi_1 \qquad (4.5.a)$$

$$\varphi^{r\prime}{}_{mn}(f_2, \Delta\varphi_2) = k_2 \cdot \left(\left| \vec{r}_{mn} - \vec{r}_f \right| - \hat{u}_0 \cdot \vec{r}_{mn} \right) + \Delta\varphi_2 \qquad (4.5.b)$$

Then, two more cases are added. For the first case, represented by green dash curve, the $\Delta\varphi_1$ and $\Delta\varphi_1$ are set as 0 and 30 degrees, respectively; while for the second case, represented by blue dash curve, the $\Delta\varphi_1$ and $\Delta\varphi_1$ are set as 0 and -30 degrees, respectively. It is found that the introduction of different phases is capable of significantly changing the gain characteristics of the reflectarray, as shown in Fig. 4-8. Apparently the case of $(\Delta\varphi_1 = 0°, \Delta\varphi_2 = 30°)$ shows a

better performance than the other two cases in the figure. It gives us a hint about another bandwidth improvement method, the method 3, and it will be discussed later.
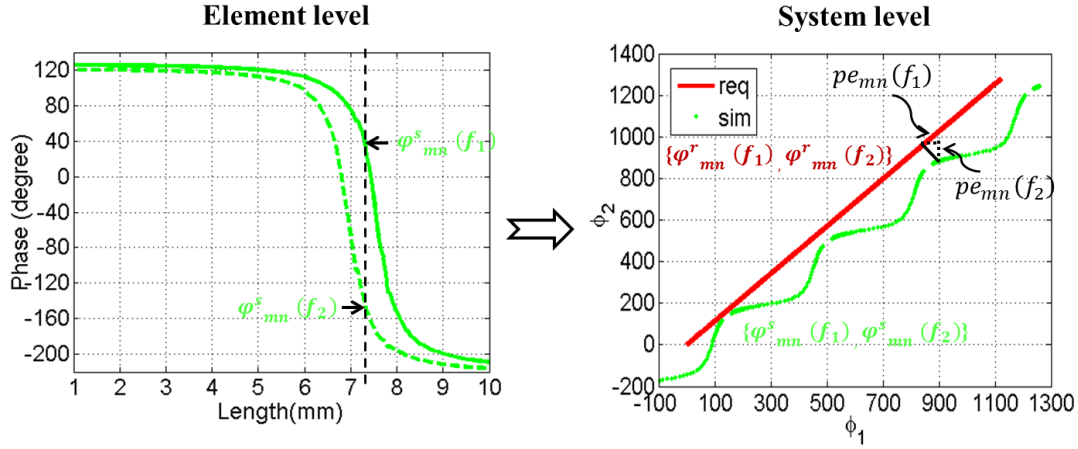
Fig. 4-9 left: Display of achievable practical phases in the traditional way; right: display of both required and achievable practical phases in the φ_1-φ_2 plane.

This dual-frequency design could also be illustrated by another kind of graph: φ1-φ2 plane, whose x axis corresponds to the required or achievable practical phase at f1, while y axis for required or achievable practical phase at f2, which enables it to display all the required phase pair $(\varphi^r_{mn}(f_1), \varphi^r_{mn}(f_2))$ and the achievable practical phase pair $(\varphi^s(f_1), \varphi^s(f_2))$ in a very straight-forward way. Fig. 4-9 (a) uses the conventional way to display the two phase curves respectively for f1 and f2. When a line paralleling to y axis is drawn, the two intersection points make one of the simulated phase pair $(\varphi^s(f_1), \varphi^s(f_2))$. By repeating the same procedure, all the possible pairs are obtained. If each pair is considered as a coordinate for a point in the φ_1-φ_2 plane, the set of all the points, represented with green dots, can be got and shown in Fig. 4-9 (b). One thing that needs to be mentioned is that by creating a large pool of simulated phases, i.e. the simulated phase pairs are repeated and shifted $\pm n \times 360^\circ$ several times, theoretically the

maximum phase error for a single element is limited within 180°. And the gaps existing in the green curve are due to the limited phase range. Similarly, all the required phase pairs are displayed in the same φ_1-φ_2 figure, represented with red dots. Therefore, for a certain element, the phase errors with any simulated phase pair $(\varphi^s(f_1), \varphi^s(f_2))$ are represented by the distances between these two points along x axis and y axis, respectively. Apparently the higher the coincidence degree between the green and red points, the smaller the phase error, and thereby the wider the bandwidth.

In order to increase the coincidence degree, usually there are two ways. It is noticed that there is a linear relationship between $\varphi^r_{mn}(f_1)$ and $\varphi^r_{mn}(f_2)$, which is readily obtained from (4.5). Hence, it is quite straightforward that it is better that the green curve is smoother or even straight. On the other hand, it also helps that multiple green curves could be generated, which essentially increase the achievable phase pairs (simulated phase pairs). Actually, how smooth the green curve can be relies on the element bandwidth. In order to show it, a comparison study is made. In Fig. 4-10, the red curves indicating the required phases are the same in both (a) and (b); however, the green and blue curves in the left and right figures represents the simulated phase pairs for square loop elements when the substrate thickness is 0.79 mm and 1.58 mm, respectively, and based on the previous knowledge, the latter one has a larger bandwidth. It is noticeable that an element with wider bandwidth corresponds to a smoother curve in φ_1-φ_2 plane, which then results into smaller phase error. For example, for a certain element marked with a black star, the practical element phase is indicated with pink arrow in both figures, and obviously the phase error, represented by the distance between the two points, is smaller in the right figure, which again confirms our previous conclusion that the wider element bandwidth, the smaller the phase error.
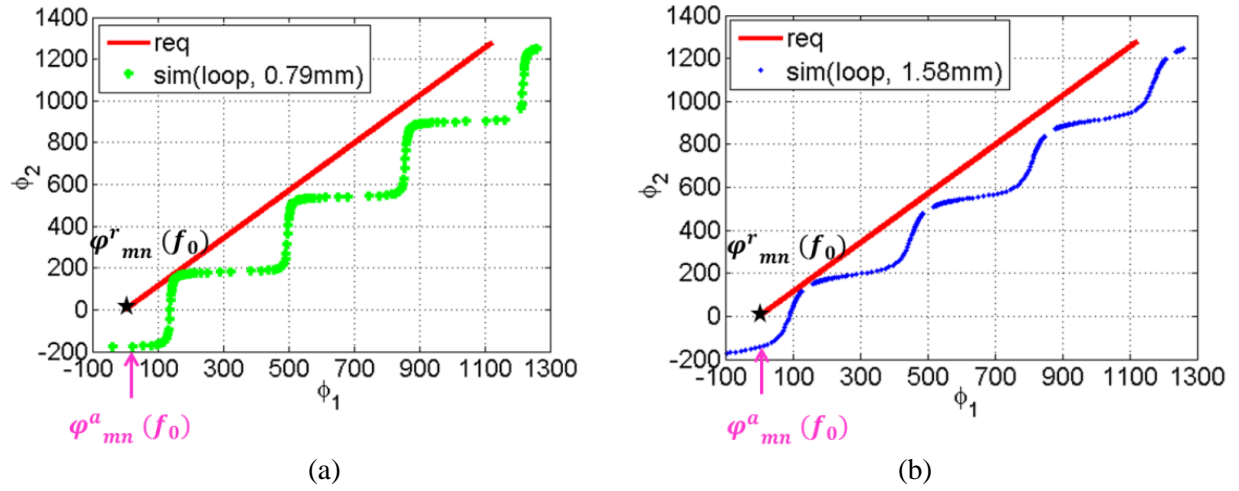
Fig. 4-10 Display of required phase pairs and achievable practical phase pairs in φ_1-φ_2 plane for reflectarray consisting of loop elements but built on (a) 0.79 mm substrate thickness and (b) 1.58 mm substrate thickness

In addition to improve the linearity of the simulated curve, another way is also used to help to satisfy the phase requirement at both frequencies. Basically the idea is to add more simulated phase curves in the φ_1-φ_2 plane, which essentially provides more choices for a certain required phase pair to match. In order to realize it, a second or even third phasing parameter is added, i.e. the element degrees of freedom are more than one. Take the square loop as an example. Supposing the loop width is not only a tuning parameter but also a phasing parameter, configured as 0.2 mm, 0.5 mm and 0.8 mm respectively, there are totally three phase curves in the φ_1-φ_2 plane, and if all the points are taken into account for the each cell, surely the reflectarray bandwidth performance is improved. Actually a lot of efforts have been made in this way.

Nevertheless, elements mounted on thicker substrate are more sensitive to the incident angle as shown in chapter 2, which means that the normal incident approximation in simulation might not be appropriate any more, especially for the elements close to the edge; and the multi-

phasing-geometry method requires a lot of effort for element simulation and geometry selection. Hence, another way is explored to broaden the reflectarray bandwidth, which leads to method 3.

The essential idea of method 3 is to take advantage of the reference phase, $\Delta\varphi$ in equation (4.5). In such case, the phase errors are modified accordingly:

$$PE_{mn}(f_1, \Delta\varphi_1) = \left| \varphi_{mn,a}(f_1) - \varphi_{mn,r}{}'(f_1, \Delta\varphi_1) \right| \qquad (4.6.a)$$

$$PE_{mn}(f_2, \Delta\varphi_2) = \left| \varphi_{mn,a}(f_2) - \varphi_{mn,r}{}'(f_2, \Delta\varphi_2) \right| \qquad (4.6.b)$$

Since the reference phase is constant at a certain frequency for all the elements, this procedure could not be done for each element one by one as before. Instead, a cost function targeting the total phase error of the whole reflectarray is constructed which can be mathematically expressed as:

$$CF_3(f_1, \Delta\varphi_1, f_2, \Delta\varphi_2) = \sum_{m=1}^{M} \sum_{n=1}^{N} [w_1 \times PE_{mn}(f_1, \Delta\varphi_1) + w_2 \times PE_{mn}(f_2, \Delta\varphi_2)] \qquad (4.7)$$

Where w_1 and w_2 are two weighting factors depending on the illumination intensity at the two design frequencies.

(a)   (b)
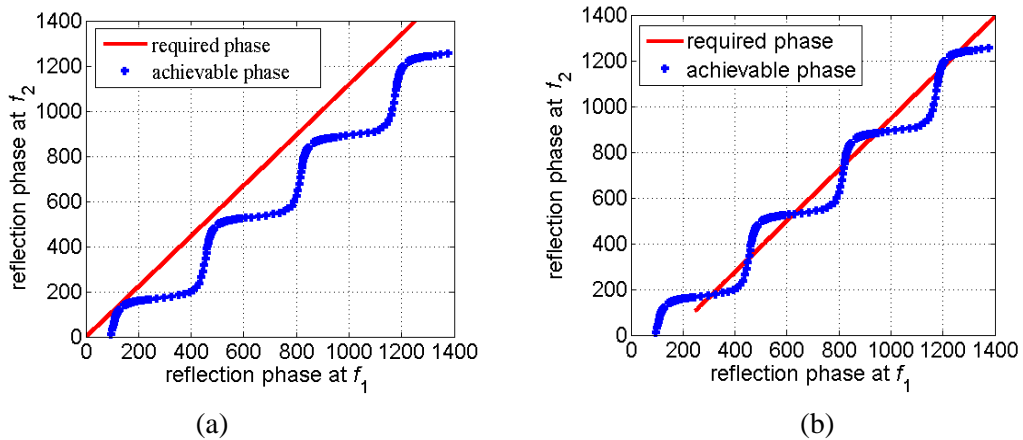
Fig. 4-11 Graphical illustration of the optimization procedure for method 3.
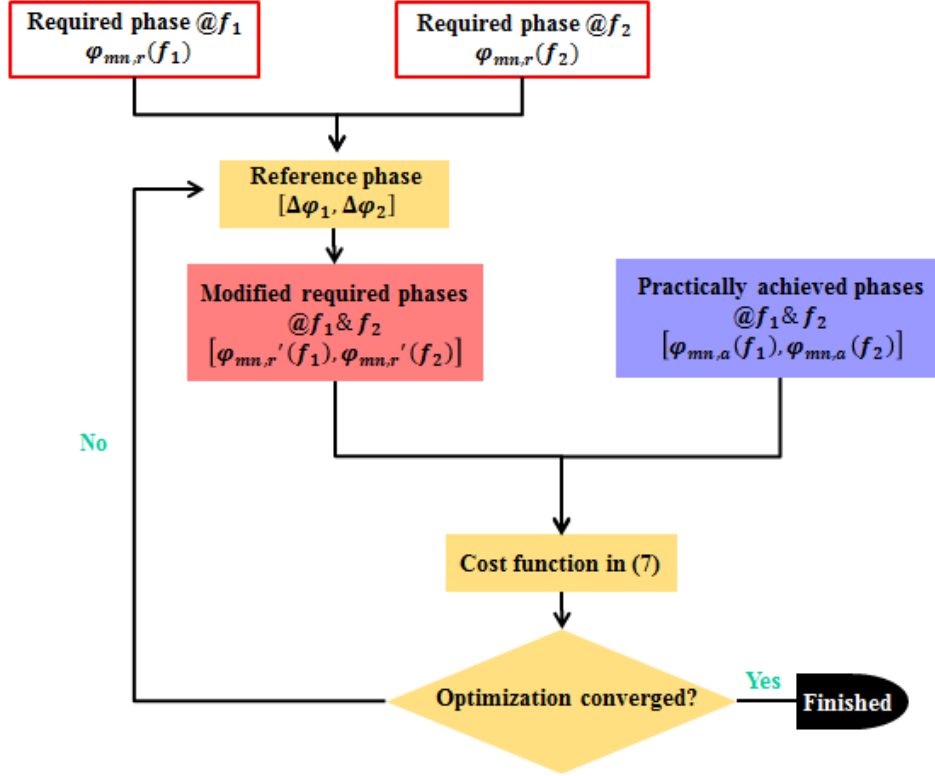
Fig. 4-12 Implementation of the proposed phase synthesis process.

Graphically speaking by φ_1-φ_2 plane, assuming green curve is fixed, the improvement of coincidence degree is done by shifting the red line up and down, or right and left, until these two curves match with each other the best, as displayed in Fig. 4-11. In actual implementation, in order to speed up the process, an iterative procedure based on PSO engine [23] is employed to minimize the cost function in (4.7). A flowchart of the optimization procedure is given in Fig. 4-12, which summarizes the above discussions.

In order to better understand the method 3 mechanism, three reflectarrays consisting of square –ring elements have been designed using the three phase synthesis approaches. The other reflectarray configurations are as below:

$f_1 = 12.75$ GHz, $f_2 = 14.25$ GHz, Diameter = 400 mm, Feed position = (-175 mm, 0, 375mm), $q^f =$ variable, $t = 1.58$ mm, 25° oblique illumination

The calculated gain performances of different approaches are illustrated in Fig. 4-13, which shows that the design process may remarkably affect the gain performance of the reflectarray. Firstly, the 1.5 dB gain bandwidth of the single frequency approach has been greatly enhanced to reach 16.7% by using the proposed approach. Secondly, compared with the dual-frequency approach, the proposed approach significantly improves the measured gains of the reflectarray within the entire frequency band of interest. In particular, at 13.5 GHz, the gain is improved by 3.5 dB. Thirdly, within the frequency band, the proposed approach shows a more stable gain response than the dual-frequency approach. The latter has a 2.3 dB gain variation while it is only 1.1 dB for the former. It is also noticed that the gain at the higher frequency is a little bit larger, and if we want to get a more flat gain performance, we could add two more weighting factors E_1 and E_2 to each frequency, and the cost function becomes

$$CF_4(f_1, \Delta\varphi_1, f_2, \Delta\varphi_2) = E_1 \times \sum_{m=1}^{M} \sum_{n=1}^{N} w_1 \times PE_{mn}(f_1, \Delta\varphi_1) + E_2 \times \sum_{m=1}^{M} \sum_{n=1}^{N} w_2 \times PE_{mn}(f_2, \Delta\varphi_2) \ (8)$$
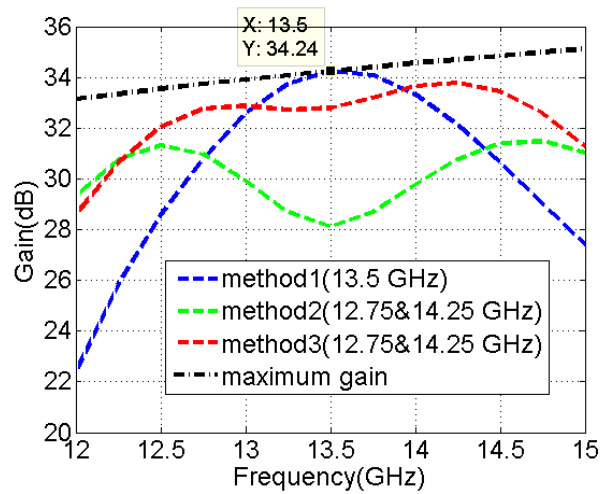
Fig. 4-13 The comparison of gain performance for reflectarrays of different design methods.

4.3 Fabrication and Experimental Results

4.3.1 Fabricated Prototypes

In order to verify the previous conclusions of the effect of element shape, substrate thickness and design method, six pieces of reflectarray are fabricated and measured. All of the designed reflectarray measures 40 x 40 cm^2, consisting of 35 x 35 elements printed on a grounded substrate (Taconic TLX -8, ε_r = 2.55, tan(δ)= 0.0019). The element grid spacing is 11.2mm, roughly 0.5 λ at 13.5 GHz. The planar surfaces lies in the (x, y) plane and is illuminated by a linear-polarized horn located at (-175 mm, 0, 375 mm), and radiates the maximum field in the direction $\theta = 15^o, \varphi = 0^o$. The information of element shape, substrate thickness, design method and design frequency is summarized in Table 4-5.

Table 4-5 Summary of the fabricated reflectarray in terms of element shape, substrate thickness, design method and design frequency

	Element shape	Substrate thickness	Design method	Design frequency
1	Patch	1.58 mm	Method 1	13.5 GHz
2	Cross	1.58 mm	Method 1	13.5 GHz
3	Loop	0.79 mm	Method 1	13.5 GHz
4	Loop	1.58 mm	Method 1	13.5 GHz
5	Loop	1.58 mm	Method 2	12.75 & 14.25 GHz
6	Loop	1.58 mm	Method 3	12.75 & 14.25 GHz

The fabrication process which is supposed to guarantee an etching tolerance of about ±0.05 mm was employed; however, practically the etching tolerance was not consistent for all of the reflectarray due to the manufacturer's problem. The pictures of all the fabricated reflectarrays are shown in Fig. 4-14.
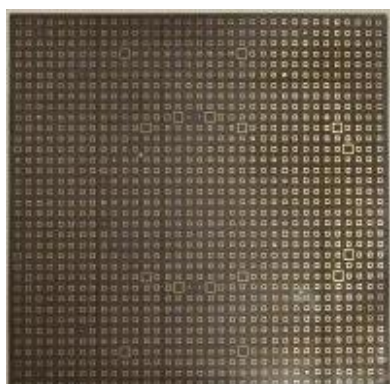
Fig. 4-14 Photographs of manufactured reflectarray for (a) RA No. 1 (b) RA No. 2 (c) RA No. 3 (d) RA No. 4 (e) RA No. 5 (f) RA No. 6

4.3.2 Measurement Setup

All the six RAs were measured with the far-field method as shown in Fig. 4-15 in two planes: E-plane and H-plane. As shown in Fig. 4-16, the H-plane is the *x-z* plane, and the E-plane is a plane with a tile angle (25°) related to *y-z* plane.
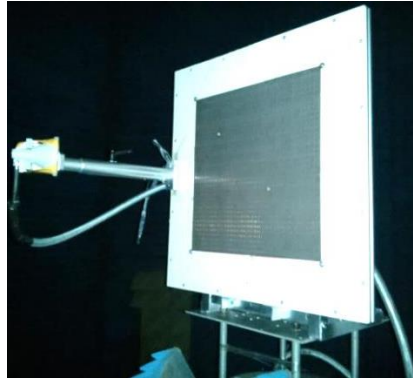
Fig. 4-15 Photographs of the system configuration during the measurement process.
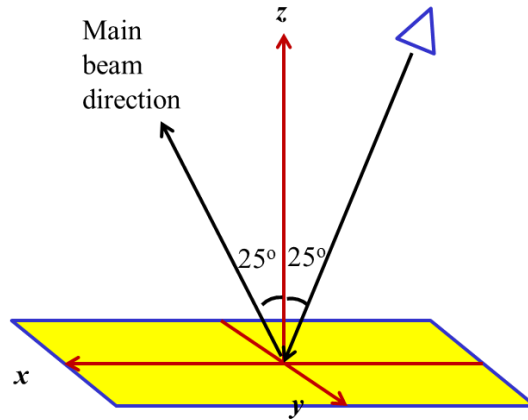
Fig. 4-16 Demonstration of the reflectarray coordinate system.

4.3.3 Measurement Results

The comparison of the calculated and measured radiation patterns in E-plane and H-plane are presented as follows. For the prototypes designed with the single-frequency method, only the

radiation patterns at the center frequency are demonstrated, otherwise, the patterns at the two design frequencies and center frequency are all displayed. However, for the purpose of comparison, the patterns at the two design frequencies and center frequency for the 4th one are also plotted.

4.3.3.1 The Measured Radiation Patterns in E-plane

The comparison of the measured and simulated radiation patterns in E-plane at center frequency for the first three prototypes is displayed in Fig. 4-17. Basically, good agreement is observed, especially in terms of the main beam width. However, it is observed that discrepancy for RA No. 2 and No. 3 in terms of side lobe levels is much higher than the one of RA No. 1. Considering that RA No. 2 and RA No. 3 consist of cross elements printed on 1.58 mm grounded substrate and square-loop elements printed on 0.79 mm grounded substrate, respectively, where the phase change mainly happens within a geometry variation of 1~1.5 mm, it is believed that the big difference is for the most part due to the fact that the etching process is not accurate enough.

(a)   (b)   (c)
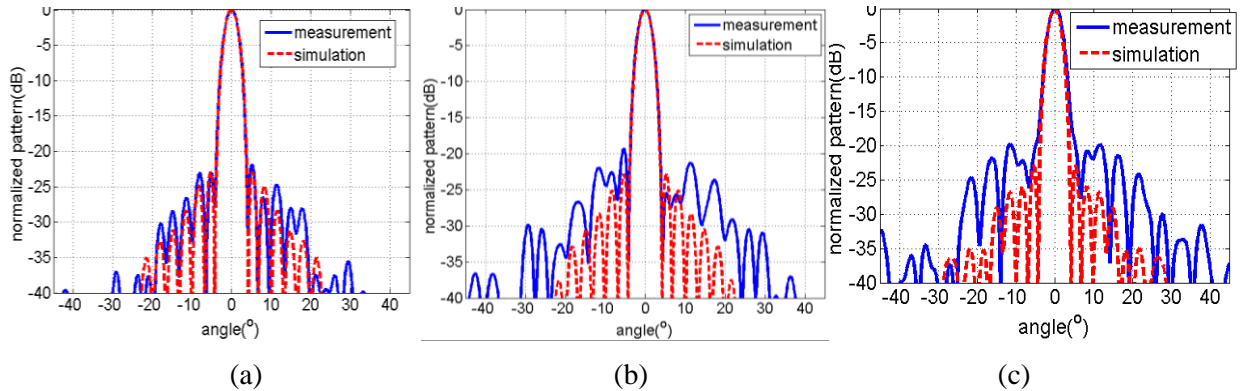
Fig. 4-17 Measured and calculated radiation patterns in E-plane at the center frequency for (a) RA (patch/1.58 mm/Method 1)(b) RA (Cross/1.58 mm/Method 1) (c) RA (Loop/0.79 mm/Method 1) .

The measurement results for the last three prototypes designed with different methods are more interesting, as shown in Fig. 4-18, Fig. 4-19, Fig. 4-20.

(a)　　　　　　　　　　(b)　　　　　　　　　　(c)
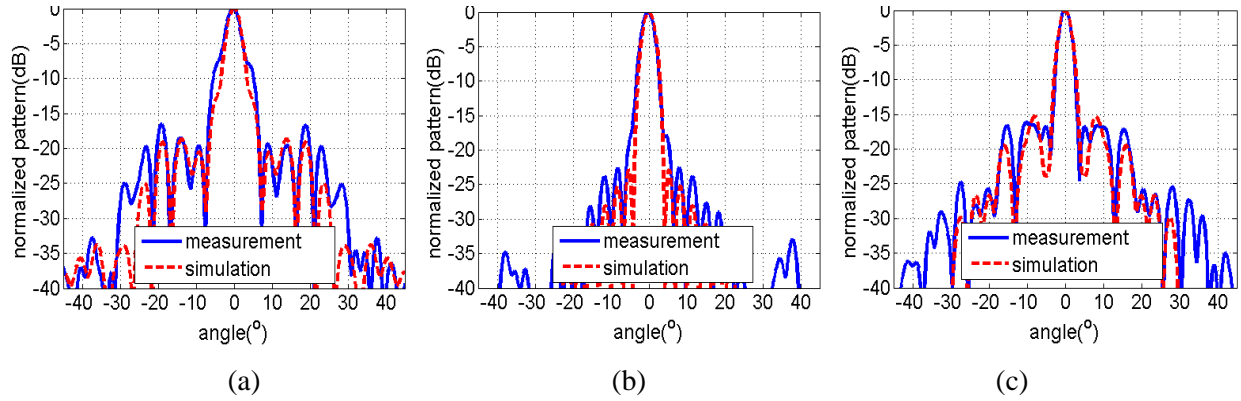
Fig. 4-18 Measured and calculated radiation patterns in E-plane for RA (Loop/1.58 mm/Method 1) (a) @12.75 GHz (b) @13.5 GHz (c) @14.25 GHz .

(a)　　　　　　　　　　(b)　　　　　　　　　　(c)
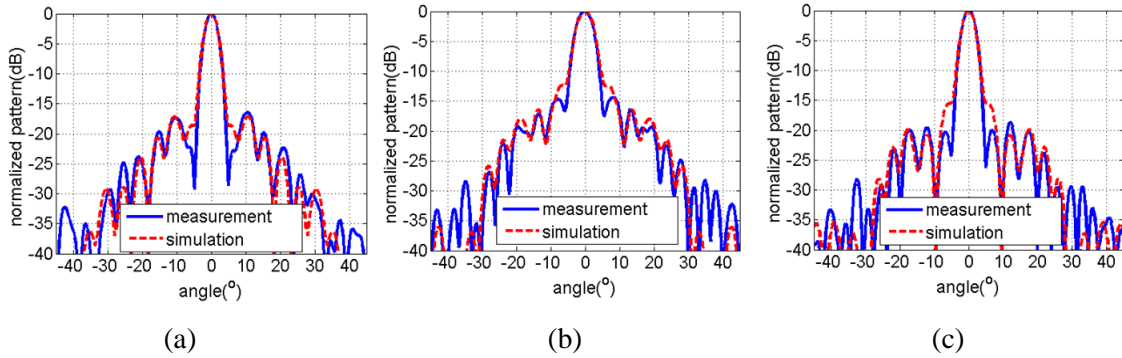
Fig. 4-19 Measured and calculated radiation patterns in E-plane for RA (Loop/1.58 mm/Method 2) (a) @12.75 GHz (b) @13.5 GHz (c) @14.25 GHz .
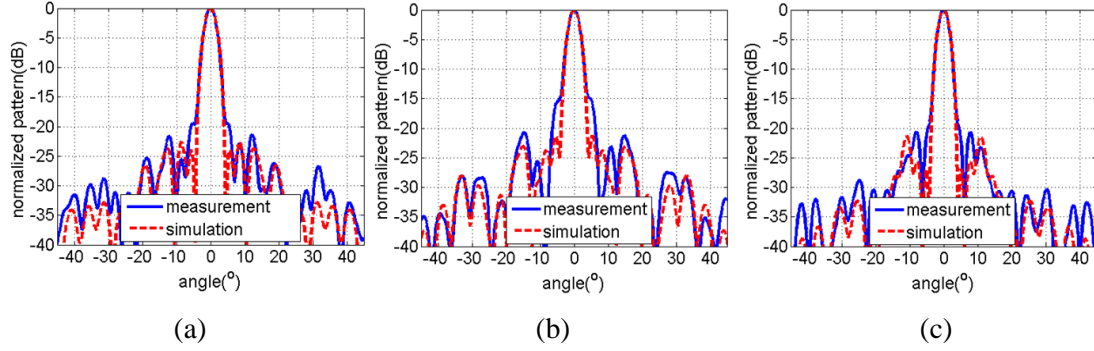
Fig. 4-20 Measured and calculated radiation patterns in E-plane for RA (Loop/1.58 mm/Method 3) (a) @12.75 GHz (b) @13.5 GHz (c) @14.25 GHz .

For the one designed with method 1, apparently the side lobe level becomes much higher at 12.75 and 14.25 GHz; while for the one designed with method 2, the one at center frequency has a poorer performance in terms of side lobe level. However, for the one designed with method 3, the side lobe level almost remains the same at the three frequencies. Furthermore, when the comparison is made between the radiation patterns obtained at 12. 75 and 14.25 GHz for the one designed with method 2 and method 3, respectively, it is found that the latter one has a lower side lobe level. The comparison of the measured co-polarization and cross-polarization radiation patterns in E-plane are displayed in Fig. 4-21 to Fig. 4-24, and it could be seen the cross-polarization basically below -25 dB.
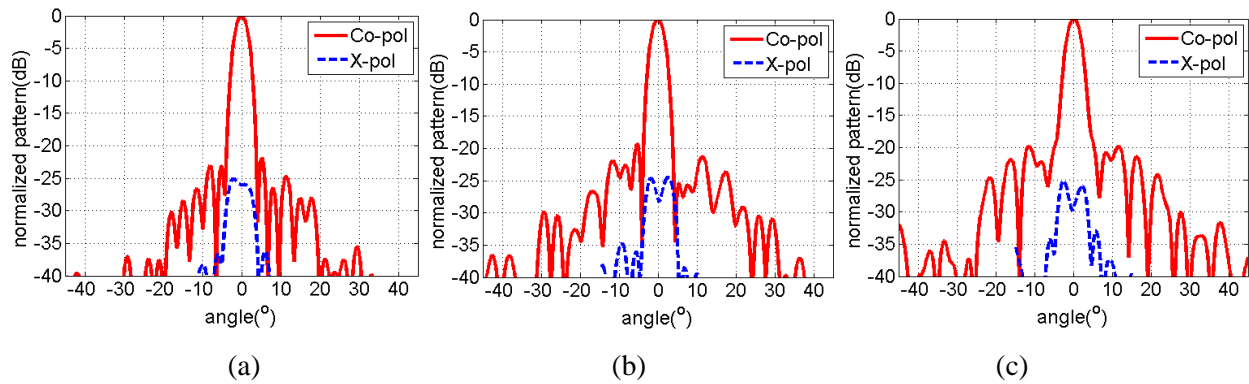
Fig. 4-21 Measured co-pol and cross-pol radiation patterns in E-plane at the center frequency for (a) RA (patch/1.58 mm/Method 1)(b) RA (Cross/1.58 mm/Method 1) (c) RA (Loop/0.79 mm/Method 1).
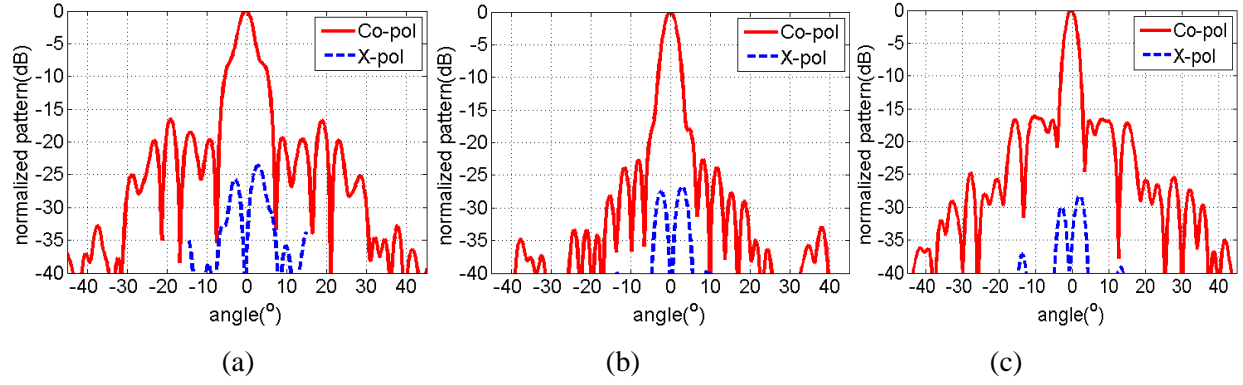
Fig. 4-22 Measured co-pol and cross-pol radiation patterns in E-plane for RA (Loop/1.58 mm/Method 1) (a) @12.75 GHz (b) @13.5 GHz (c) @14.25 GHz .
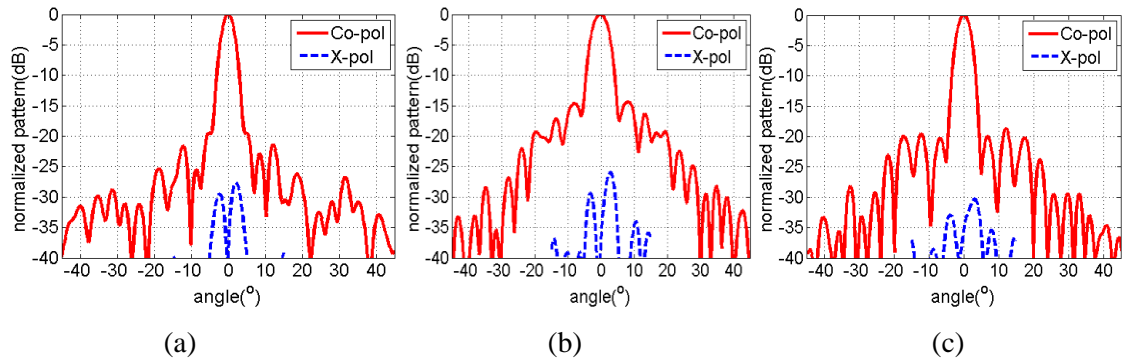
Fig. 4-23 Measured co-pol and cross-pol radiation patterns in E-plane for RA (Loop/1.58 mm/Method 2) (a) @12.75 GHz (b) @13.5 GHz (c) @14.25 GHz .
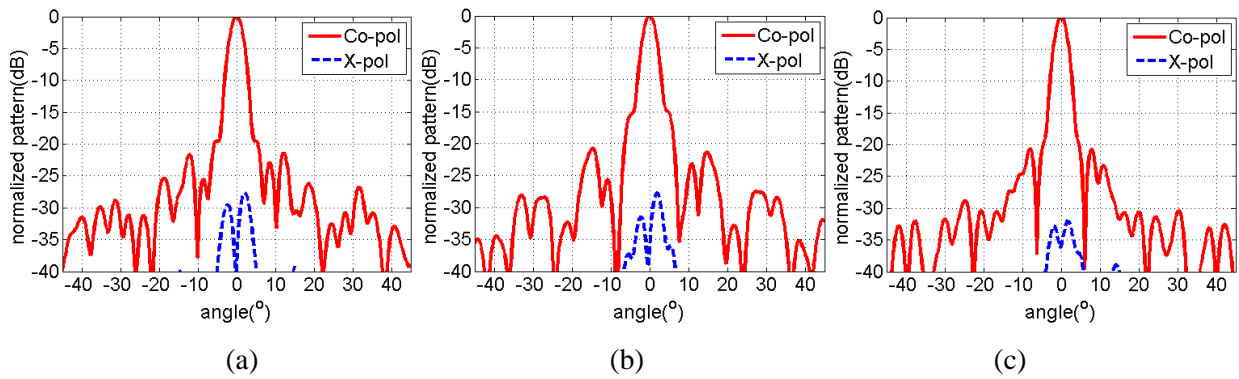
Fig. 4-24 Measured co-pol and cross-pol radiation patterns in E-plane for RA (Loop/1.58 mm/Method 3) (a) @12.75 GHz (b) @13.5 GHz (c) @14.25 GHz .

4.3.3.2 The Measured Radiation Patterns in H-plane

The measurement results in H-plane are demonstrated in Fig. 4-25 to Fig. 4-32, and similar observation was made as in E-plane.

(a)　　　　　　　　　　(b)　　　　　　　　　　(c)
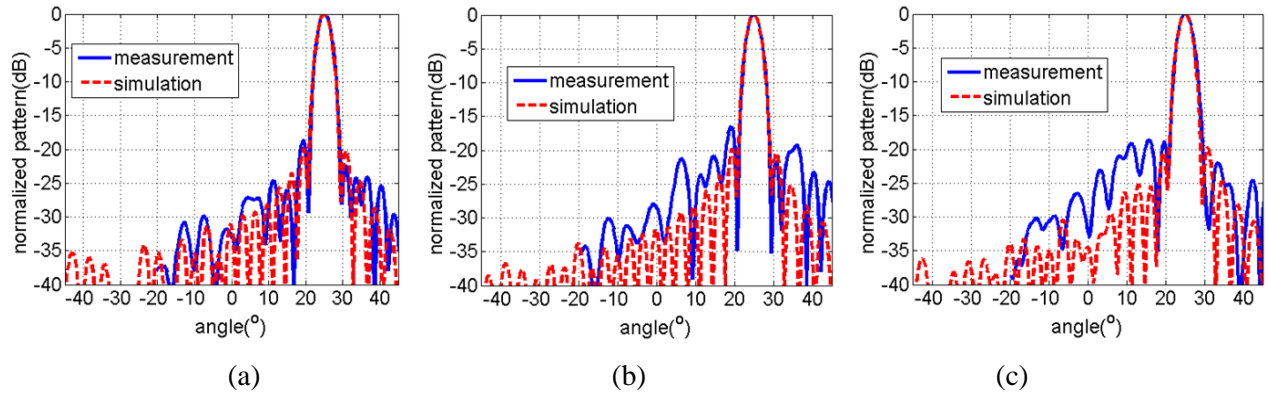
Fig. 4-25 Measured and calculated radiation patterns in H-plane at the center frequency for (a) RA (patch/1.58 mm/Method 1)(b) RA (Cross/1.58 mm/Method 1) (c) RA (Loop/0.79 mm/Method 1) .

(a)　　　　　　　　　　(b)　　　　　　　　　　(c)
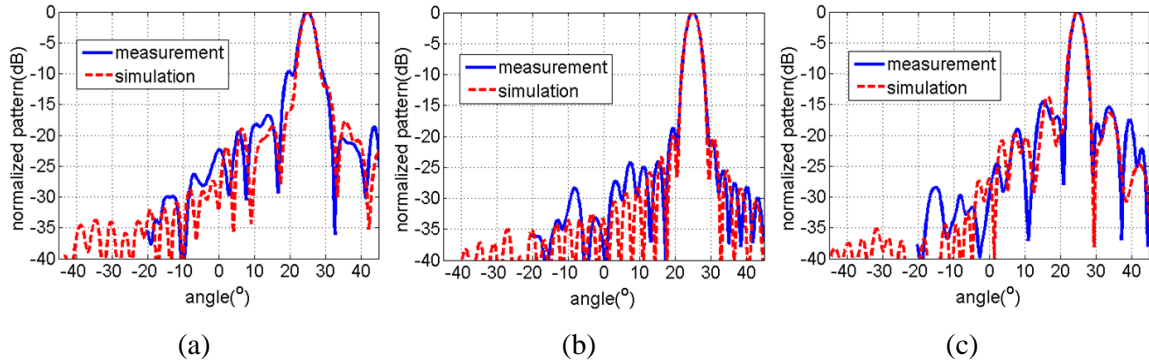
Fig. 4-26 Measured and calculated radiation patterns in H-plane for RA (Loop/1.58 mm/Method 1) (a) @12.75 GHz (b) @13.5 GHz (c) @14.25 GHz .
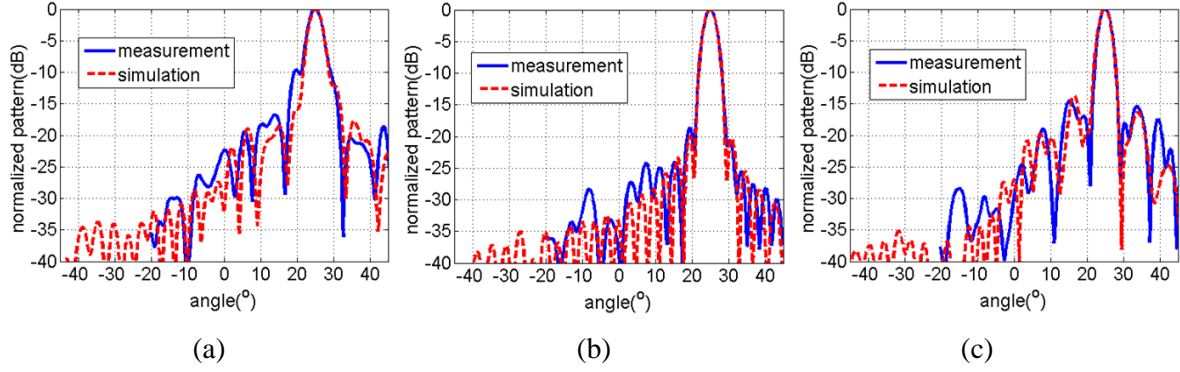
Fig. 4-27 Measured and calculated radiation patterns in H-plane for RA (Loop/1.58 mm/Method 2) (a) @12.75 GHz (b) @13.5 GHz (c) @14.25 GHz .
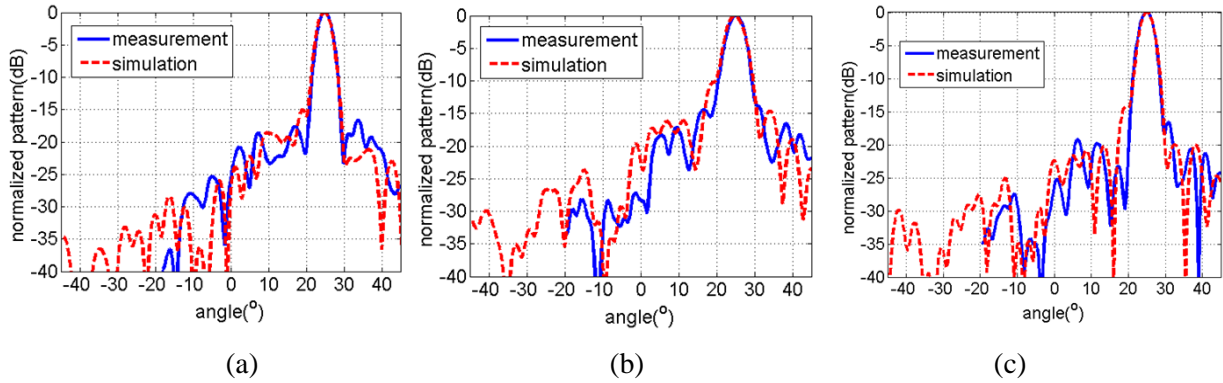
Fig. 4-28 Measured and calculated radiation patterns in H-plane for RA (Loop/1.58 mm/Method 3) (a) @12.75 GHz (b) @13.5 GHz (c) @14.25 GHz .
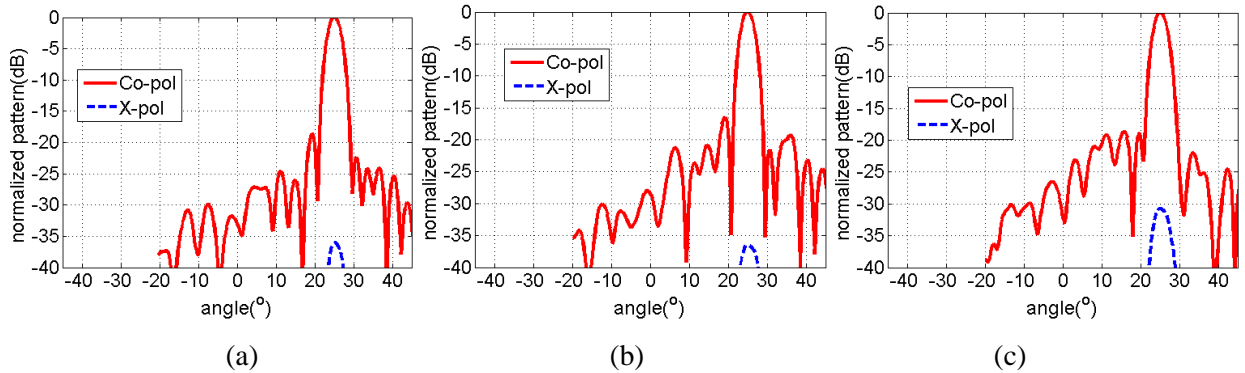
Fig. 4-29 Measured co-pol and cross-pol radiation patterns in H-plane at the center frequency for (a) RA (patch/1.58 mm/Method 1)(b) RA (Cross/1.58 mm/Method 1) (c) RA (Loop/0.79 mm/Method 1).
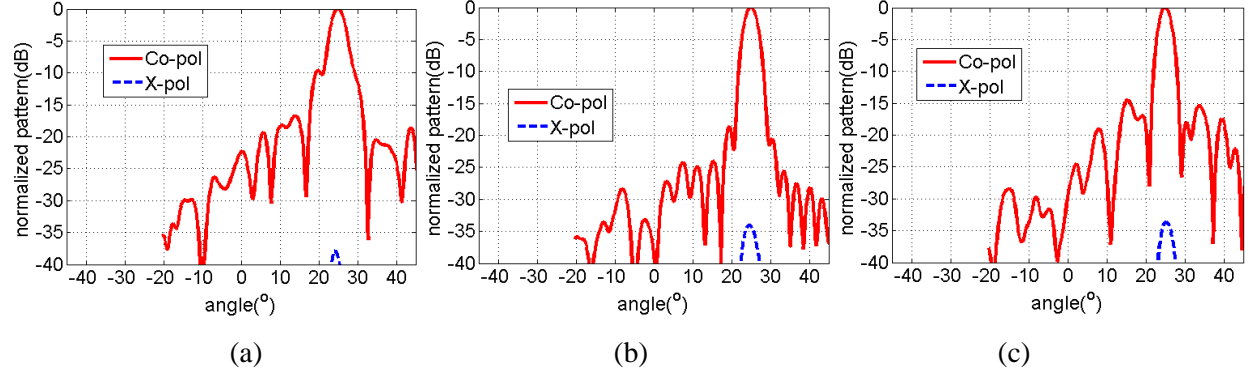
Fig. 4-30 Measured co-pol and cross-pol radiation patterns in H-plane for RA (Loop/1.58 mm/Method 1) (a) @12.75 GHz (b) @13.5 GHz (c) @14.25 GHz .
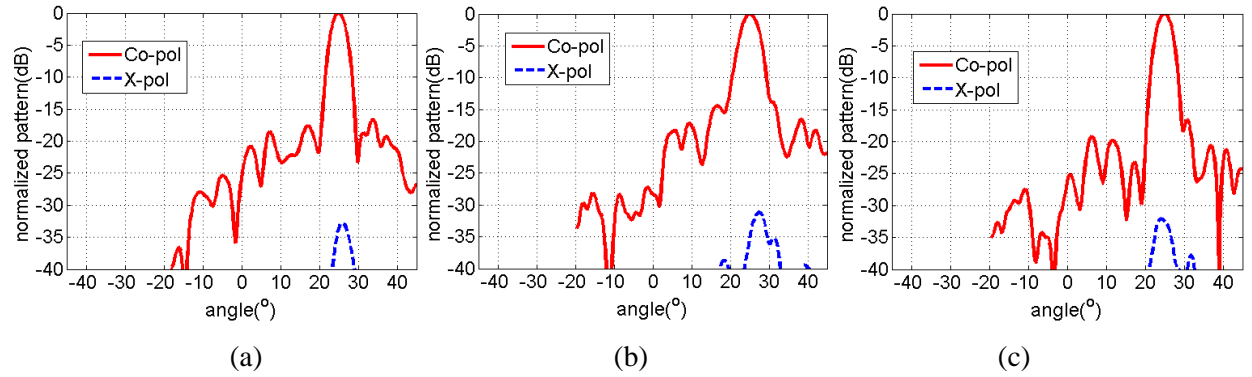
Fig. 4-31 Measured co-pol and cross-pol radiation patterns in H-plane for RA (Loop/1.58 mm/Method 2) (a) @12.75 GHz (b) @13.5 GHz (c) @14.25 GHz .
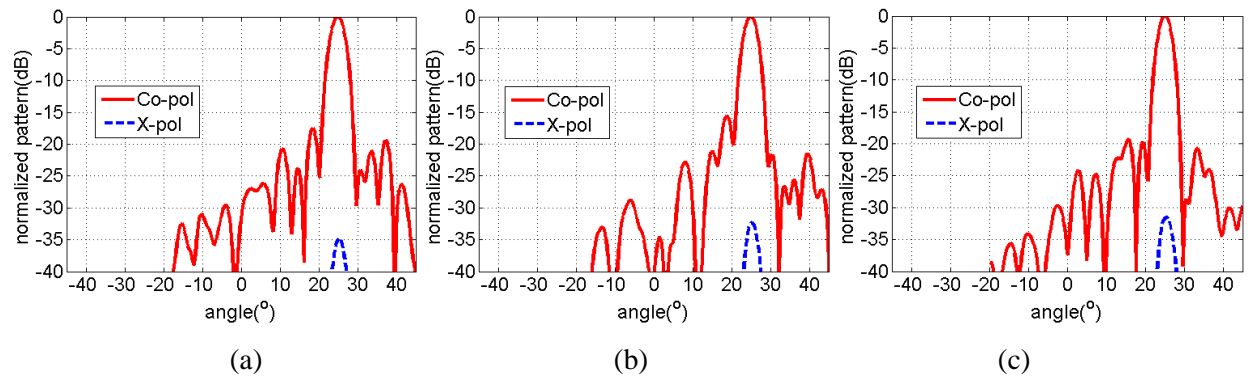
Fig. 4-32 Measured co-pol and cross-pol radiation patterns in H-plane for RA (Loop/1.58 mm/Method 3) (a) @12.75 GHz (b) @13.5 GHz (c) @14.25 GHz

4.3.3.3 The Measured Bandwidth Performance

The comparison of the calculated and measured gain and efficiency performance against frequency are demonstrated in Fig. 4-33 and Fig. 4-34, respectively. Although there is some discrepancy, a good resemblance is still observed between the calculated and measured curves. Regarding the difference between the measured and calculated results, it could be mainly contributed to the following three factors:

(i) Fabrication tolerance. When the element bandwidth is narrow, it becomes very prone to fabrication error. Take the square-loop element printed on 0.79 mm substrate as an example. As the side length varies from 4.55 to 4.8 mm, the phase shifts 265 degree, averagely around 45 degree per 0.05 mm. And there are totally 975 of 1225 elements whose side lengths are within this range. Other than this, a small variation in the loop width could also produce a big phase error. Therefore, the fabrication accuracy is the main reason for the big discrepancy between calculated and measured results. It is noted that for RA No. 1, consisted of the patch type element whose bandwidth is the largest, the gain drop at 13.5 GHz is 0.6 dB, compared to the computational result. It is also observed that biggest difference between calculated and measured results exist in No. 2 and No. 3 RAs, which is consistent with our previous observation regarding the radiation patterns;

(ii) RA system alignment. The planar surface and the feed horn are mounted on a supporting frame as shown in Fig.4-16. Ideally three things should be guaranteed during the alignment: the surface is mounted in the center of the white board without rotation referring to the two orthogonal sides; the horn is tilted at 25 degree; and the phase center of the horn is at the correct position. Compared to the first two, the last one is somehow difficult to be made sure.

Usually the aperture center is not the phase center of the horn, however, practically it is still used for the alignment, and this certainly introduces some phase error;

(iii) Measurement system alignment. Since the far-field measurement method is used and only two planes are measured, it is almost impossible to guarantee that the maximum radiation direction is detected in the measurement. During the process, we did manually adjust the frame position to search for a higher receiving signal, but it is still could not be assured. Note that, the difference between the gains measured in E-plane and H-plane is very small, which somehow shows that the measured results make sense.

(a)   (b)   (c)

(d)   (e)   (f)
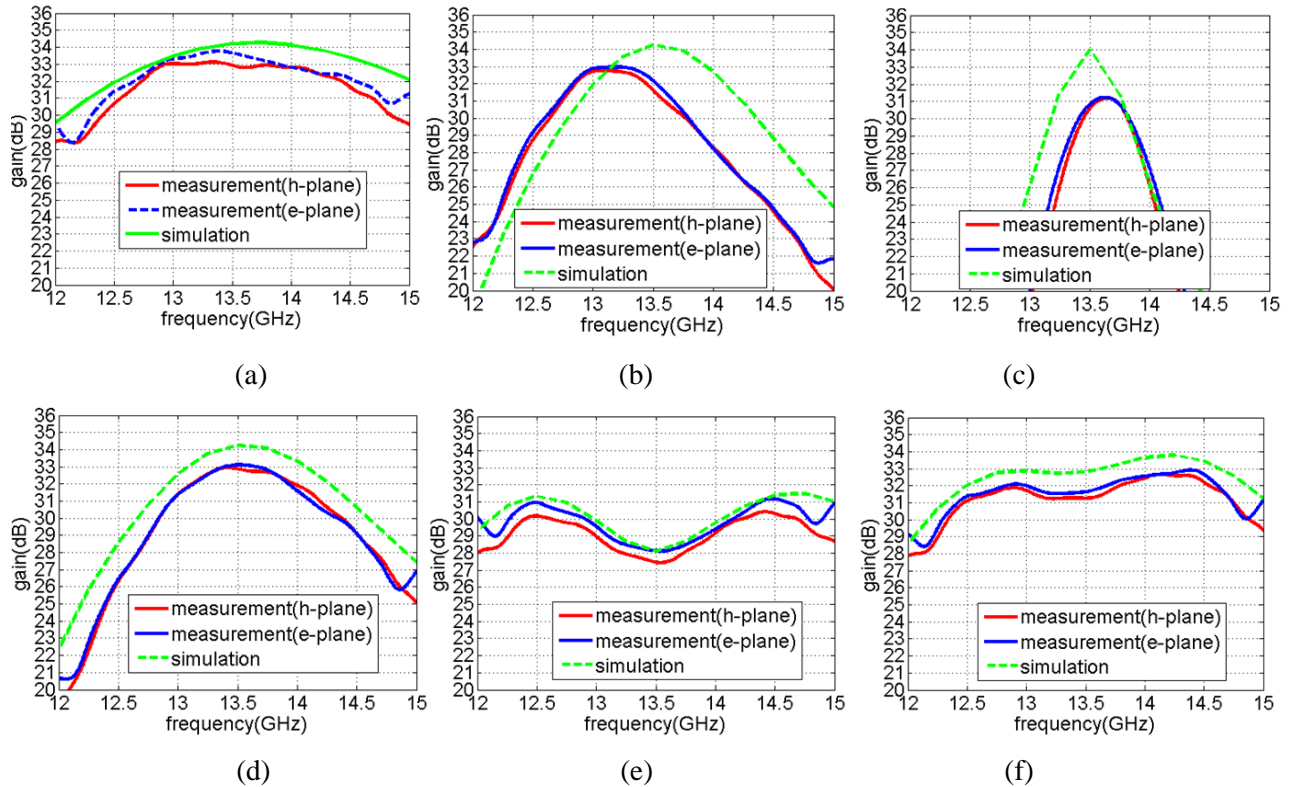
Fig. 4-33 Measured and calculated gain performance against frequency for (a) RA No. 1 (b) RA No. 2 (c) RA No. 3 (d) RA No. 4 (e) RA. No. 5 (f) RA. No.6.
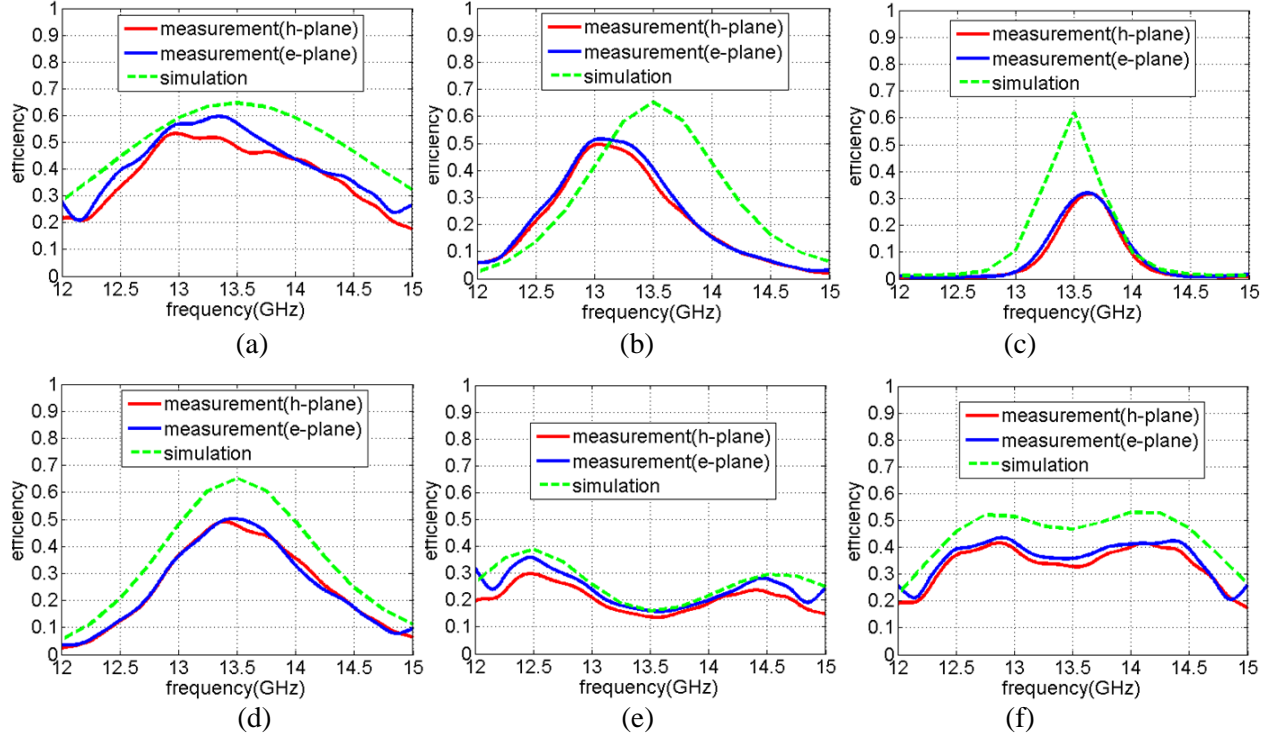
Fig. 4-34 Measured and calculated efficiency performance against frequency for (a) RA No. 1 (b) RA No. 2 (c) RA No. 3 (d) RA No. 4 (e) RA. No. 5 (f) RA. No.6.

4.4 Summary of the Influential Factors on the Bandwidth Performance of Reflectarrays

After re-organizing the measurement results, the effects of element shape, substrate thickness and design methods are validated as below.

4.4.1 Element Shape Effect

The comparison of element shape is made among RA No. 1, No. 2 and No. 4, and the results are displayed in Fig. 4-35 and Table 4-6. Clearly it demonstrates the RA consisting of patch elements yields the best performance in terms of bandwidth.

(a)   (b)
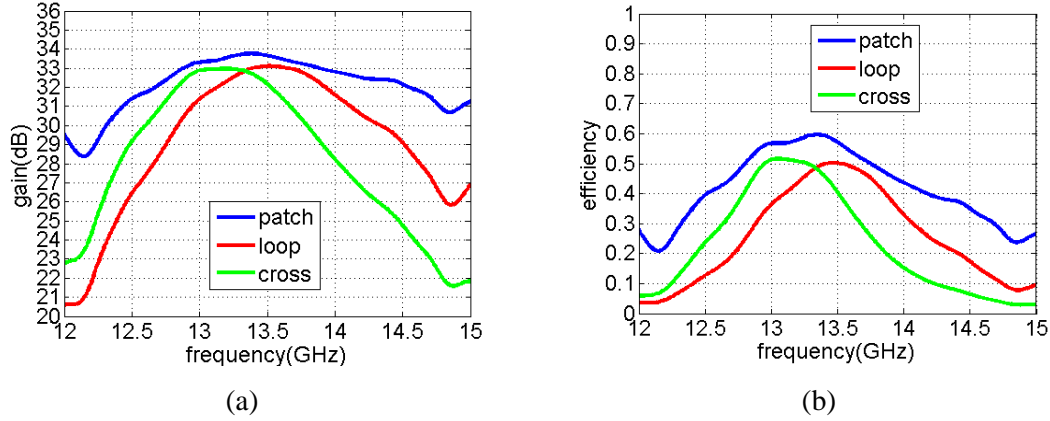
Fig. 4-35 The measured gain and efficiency performance of reflectarray consisting of different element shapes.

Table 4-6 Summary of the measured performance of reflectarray consisting of different element shapes

RA	Gain @13.5 GHz	Peak gain	Peak gain frequency	Peak efficiency frequency	1dB Bandwidth
No. 1 (patch)	33.67 dB	33.77 dB	13.4 GHz	13.35 GHz	8.9%
No. 2(cross)	32.13 dB	32.96 dB	13.2 GHz	13.05 GHz	5.4%
No. 4 (loop)	33.11 dB	33.11 dB	13.5 GHz	13.47 GHz	5.5%

4.4.2 Substrate Thickness Effect

The comparison of substrate thickness is made among RA No. 3 and No. 4, and the results are displayed in Fig. 4-36 and Table 4-7. Clearly it demonstrates the RA printed on thicker substrate yields better bandwidth performance. It is also noticed that there is a big difference between these two designs in terms of peak gain, again which is mainly to the fabrication error. It can be seen from Fig. 4-3 (a), the phase curve for the one with 0.79 mm thick substrate is very sharp. For example, a minor fabrication error of 0.05mm could lead to a phase error of roughly 100°.

	(a)	(b)
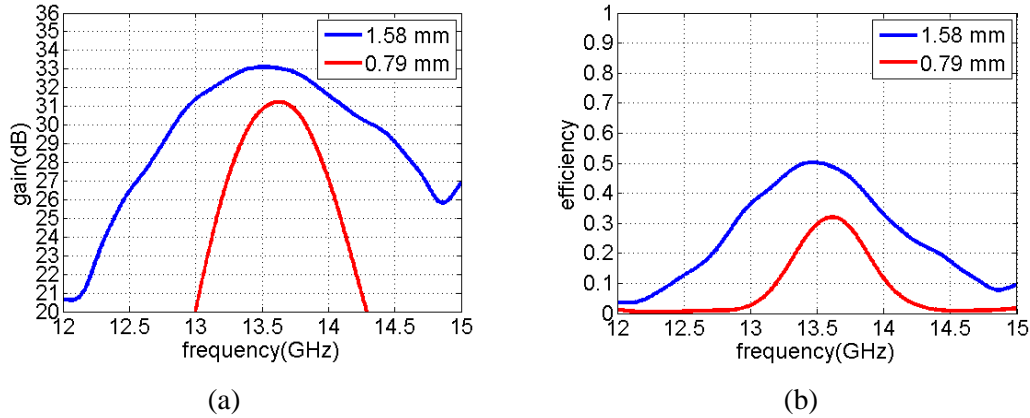
Fig. 4-36 The measured gain and efficiency performance of reflectarray built on different substrate thickness.

Table 4-7 Summary of the measured performance of reflectarray built on different substrate thickness

RA	Gain @13.5 GHz	Peak G	Peak gain frequency	Peak efficiency	Peak efficiency frequency	1dB BW
No. 3(0.79 mm)	30.86 dB	31.23 dB	13.63 GHz	32.0%	13.62 GHz	2.8%
No. 4(1.58 mm)	33.11 dB	33.11 dB	13.5 GHz	50.3%	13.47 GHz	5.5%

4.4.3 Phase Synthesis Method Effect

The comparison of design methods is made among RA No. 4, No. 5 and No. 6, and the results are displayed in Fig. 4-37 and Table 4-8. In Fig. 4-37 (a), the gain comparison figure, the black curve still indicates the theoretically maximum achievable gain which is obtained single frequency per single frequency. Note that, even for method 1, there is around 1.1 dB degradation for the measured gain at the center frequency, 13.5 GHz, which is mainly due to the fabrication error as discussed before. Hence, if a highly accurate etching process is employed, the method 3 could greatly increase the bandwidth within 1 dB gain. While method 2 produces similar gain performance at both design frequencies with a general big gain drop during the interested frequency range. It is observed, the measured efficiency at 13.5 GHz for No. 4 RA designed by

method 1 is around 50%, while the measured efficiency at 12.75 and 14.25 GHz for No. 5 RA designed by method 3 are both more than 40%.

Taking into account the gain drop cost during the broadening bandwidth process, the conventional bandwidth definition is meaningless, therefore, a new one is taken here. The 1.5 dB maximum gain band is defined between two frequencies whose corresponding gains are 1.5 dB lower than the one measured at 13.5 GHz by the single-frequency design method, as highlighted with yellow color area in Fig. 4-37(a).

(a)   (b)
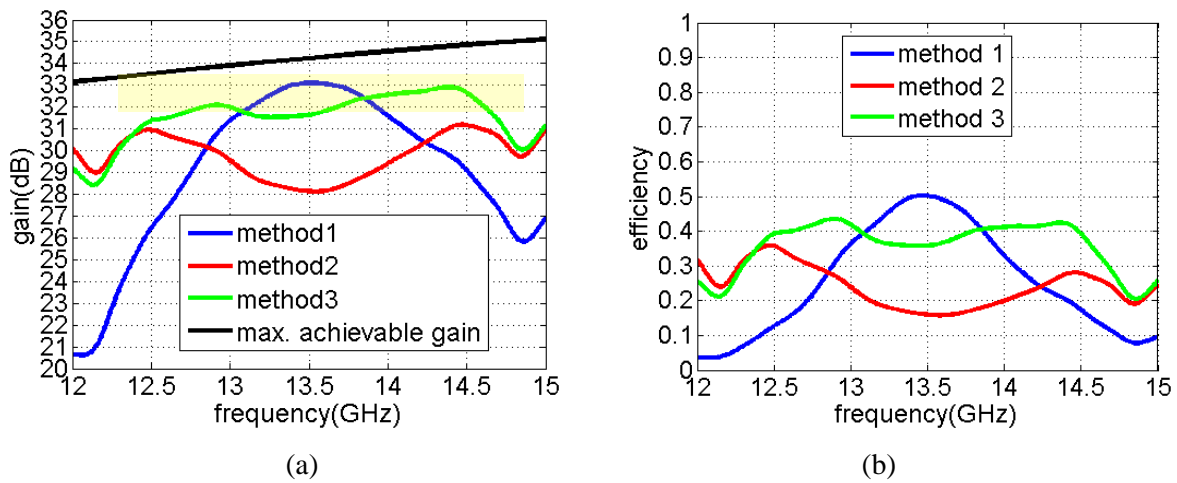
Fig. 4-37 The measured gain and efficiency performance of reflectarray designed with different methods.

Table 4-8 Summary of the measured performance of reflectarray designed with different methods

RA	Gain @12.75 GHz	Gain @13.5 GHz	Gain @14.25 GHz	η @12.75 GHz	η @13.5 GHz	η @14.25 GHz	1.5 dB maximum gain Bandwidth
No. 4 (method1)	28.97 dB	33.11 dB	30.29 dB	21.7%	50.2%	23.5%	7%
No. 5 (method2)	31.81 dB	31.65 dB	32.77 dB	30.0%	16.0%	24.33%	----
No. 6 (method3)	30.37 dB	28.14 dB	30.43 dB	41.7%	35.8%	41.6%	14.7%

CHAPTER V

A MODIFIED PARABOLIC-CYLINDRICAL REFLECTARRAY FOR IMPROVED BEAM
SCANNING CAPABILITYA

The parabolic cylinder antenna and its reflectarray counterpart are well known for the enhanced beam steering capability in the focal plane. However, the radiation performance degrades significantly for wide scan angels, for instance gain dropping and beam broadening, due to increased phase errors. In this chapter, the traditional design of parabolic-cylindrical reflectarray are introduced at first, then by exploiting the phase controlling capabilities in reflectarrays, an improved reflectarray based on conventional parabolic cylinder type designs but with optimized phases is proposed. A design of a *Ka*-band microstrip reflectarray antenna fed by a rotatable array is presented. The preliminary calculated results show that after optimization the scanning range can be significantly increased while maintaining similar radiation characteristics.

5.1 Overview of Beam Scanning Reflectarray Antenna Design

Beam-scanning antennas have found lots of applications in the fields of radar and satellite communication systems. Currently, in most of these applications, the choice is made between reflector antennas and phased array antennas based on the requirements of scan rate, scan volume, and cost. For reflector antennas, they are usually low-loss, but the scan range is somehow limited; while the attributes of the phased array are contrary. As reflectarray antennas,

the hybrid of these two high-gain antennas, have become more attractive these years, it is hoped

that a better trade-off could be achieved with reflectarrays.

For a reflectarray, assuming all the elements patterns are the same, array factor

determines the scanned beam direction, which is expressed as:

$$AF(\hat{u}) = \sum_{n=1}^{N} A_n e^{j\varphi_{inc}} e^{j\varphi_{ele}} e^{j\beta(\vec{r}_n \cdot \hat{u})} \tag{5.1}$$

Since the reflectarray is a space-fed system, A_n is seldomly used to reconfigure the radiation

pattern. Therefore, the beam scanning is generally based on three mechanisms:

- Displaced feed: effective factor $\rightarrow \varphi_{inc}$

- Reconfigurable elements: effective factor $\rightarrow \varphi_{ele}$

- Displaced feed + reconfigurable elements: effective factors $\rightarrow \varphi_{inc} + \varphi_{ele}$

It is noticed that the 1st is similar to what one usually uses to steer the beam of reflector

antennas, while the 2nd is similar to phased arrays design. Both of these two will be investigated

in chapter 5 and chapter 6, respectively.

Regarding the mechanism of displaced feed, as the name suggests, the dynamic patterns

are realized by changing the spatial delay via the placement of feed. Investigation results of the

scanning and defocusing characteristics of reflectarrays have been presented in [24], which

concluded that for a conventional parabolic reflectarray, the scanning range is very limited. It

mainly studied the effect of the subtended angles, which equals to $atan\frac{D/2}{f}$ as shown in Fig. 5-

1, denoted as θ_o. It compared the gain loss and beam deviation factor in both reflectarrays and

parabolic reflectors as a function of scan angle in beamwidths, which are reprinted in Fig. 5-2.

Clearly the gain loss and beam deviation are less severe for larger f/D ratios or smaller values of

subtended angles
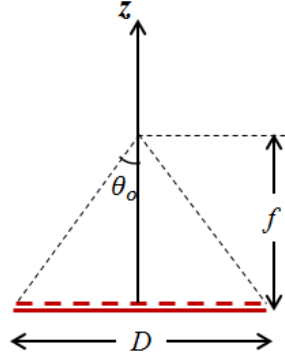
Fig. 5-1 The definition of subtended angle in RA system.
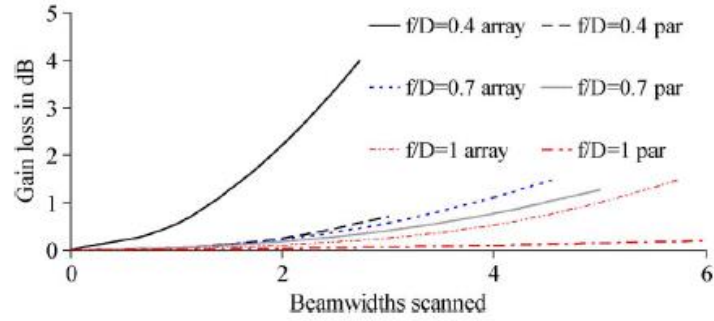
(a)
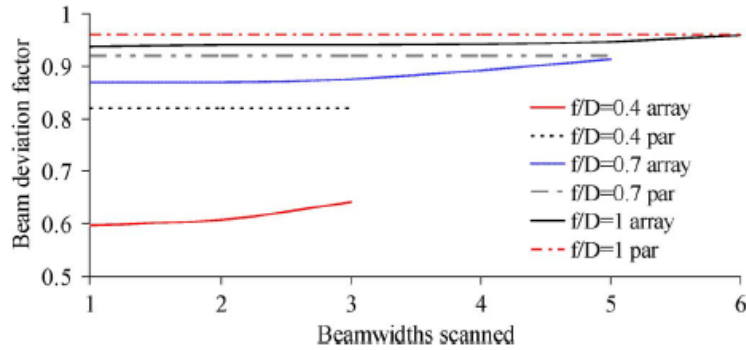
(b)

Fig. 5-2 (a) Gain loss as a function of beam scan (b) Beam deviation factor as a function of beam scan [24].

The author also compares the normal and offset cases, and it showed that scan performance is poorer for an offset system compared to the symmetric system. However, in reality, offset systems are usually utilized to avoid the blockage effect.

Various approaches to improve the scan coverage have been tried. One of the ideas is to blur the focal point. A bifocal design has been proposed in [25], where a single-reflector bifocal aperture phase distribution is proposed for the reflectarray antenna. The scanning performance of the parabolic-type and bifocal-type reflectarray optimized based on PSO engine were compared in the paper and reprinted here in Fig. 5-3 for convenience, also tabled in Table 5-1 Scanning performance of parabolic and optimized bifocal design Table 5-1. Although the latter suffers roughly 2.5 dB in the broadside direction and a broader beam, it achieves a scan loss less than 0.5 dB across the 60° scan range.

(a)   (b)
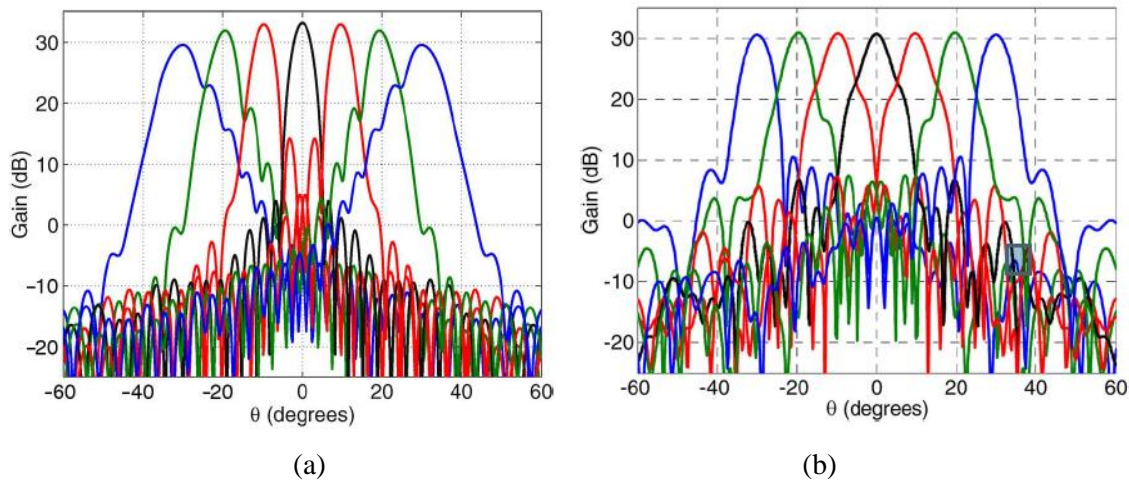
Fig. 5-3 Scanned gain patterns of reflectarray antennas: (a) parabolic-type; (b) optimized bifocal-type.

Table 5-1 Scanning performance of parabolic and optimized bifocal design

Gain (dB)	-30°	-20°	-10°	0°	10°	20°	30°
Parabolic	29.7	31.9	33.0	33.4	33.0	31.9	29.7
Bifocal (PSO)	31.4	31.6	31.0	30.6	31.0	31.6	31.4

Another idea is inspired by the parabolic cylinder antennas. The beam scanning capability of a parabolic cylinder antenna fed by an array along the focal line has been explored

in [26]. Fig. 5-4 shows its system configuration and Fig. 5-5 displayed the published measured results.
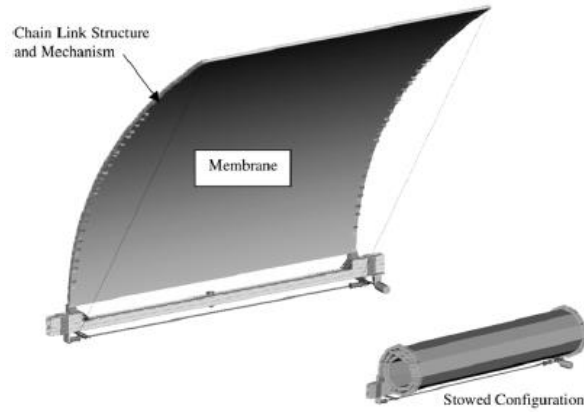
Fig. 5-4 The configuration of a parabolic-cylindrical reflector [26].
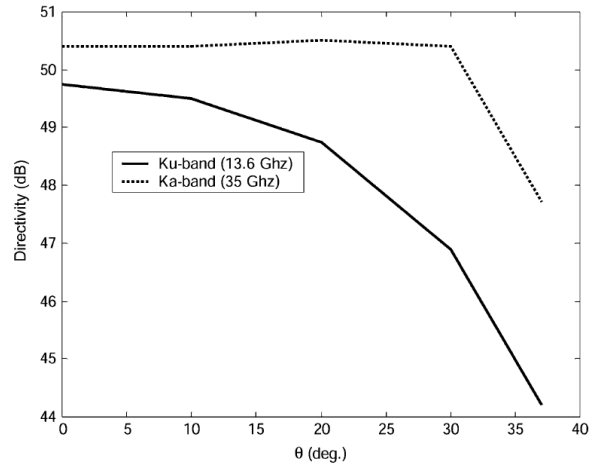
Fig. 5-5 The scanning performance of the parabolic-cylindrical reflector [26].

This antenna works at both *Ku* and *Ka* bands, and the experimental results demonstrated that a roughly 30° scan angle is achieved within 3-dB gain loss for the Ku band. And for *Ka* band, the directivity drops dramatically beyond 30°, which is due to spillover. In order to take advantage of the favorable features of reflectarrays, a dual-frequency offset array-fed

reflectarray, which mimicked a parabolic cylinder, was developed in [27], which illustrated that the estimated directivity dropped 1.8 dB at 14.1 GHz when the scan angle reached 20°.

5.2 Reflectarrays Emulating Parabolic-Cylinders Reflectors

5.2.1 Overview of the Parabolic Cylindrical Reflectarray Design

As illustrated in Fig. 5-6, the reflectarray is designed to emulate a parabolic cylindrical reflector, and feeding array is placed in the rotating plane which contains the feed array axis. When the feeding beam illuminates the reflectarray, the main beam of the reflectarray is generated in a specular way. And when the feeding array is rotated in the rotating plane, it is expected that the main beam is consequently steered in the scanning plane.

For the convenient of description, *E* and *H*-plane of the reflectarray system are defined as depicted in Fig. 5-6. The *E*-plane is defined the same as the scanning plane; the *H*-plane is defined as the one which passes through the beam maximums of both the feeding array and reflectarray.

Therefore, it can be seen that reflectarray only focuses the energy in the *E*-plane, while in the *H*-plane, it merely acts as a mirror and the beam focusing is performed by the feeding arrays. As the feeding beam rotates, different portion of the aperture is illuminated, and the main beam direction of the reflectarray changes roughly the same as specular reflection. And this is the reason why an array instead of a single horn is needed as the primary feed, and its focusing capability also relates to the directivity of the reflectarray, which will be discussed in more later.
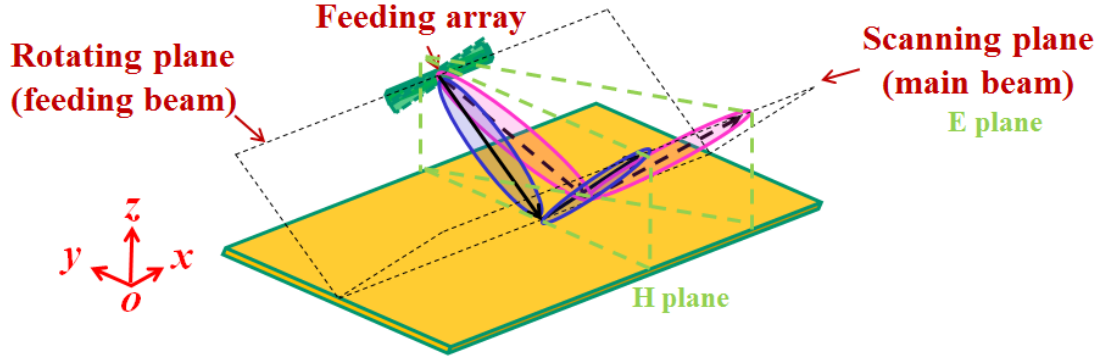
Fig. 5-6 Illustration of parabolic-cylindrical reflectarray system configuration.

As shown in Fig. 5-7, an example of a reflectarray measuring 600 mm × 400 mm offset-fed by a *Ka*-band (32.5 GHz) 16× 2 array is designed, and the H-plane main beam scan angle is 25°, which can always be achieved by controlling the phase variations of elements in the *y* direction of the reflectarray.

(a)   (b)
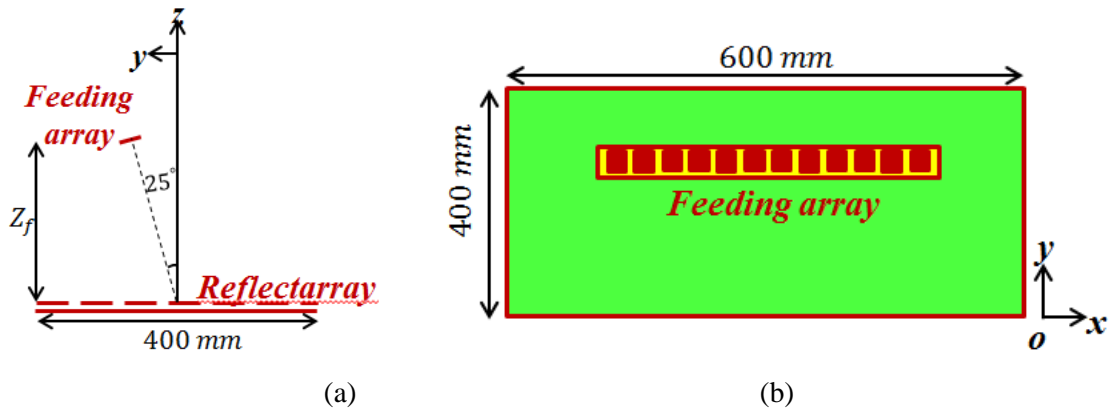
Fig. 5-7 Illustration of system configuration (a) side view and (b) top view.

- Design of element compensation phase

The design of element compensation phase follows the one used in [27]. As mentioned before, the elements within each column in *y*-direction, which may have various sizes or rotation angles according to the specific element design of one's choice, yield different reflection phases

96

to mimic a parabolic curve and boost gain of the system. In this design, the scan angle is 25°. The elements within each row in *x*-direction remain identical since they act like a mirror in the *E*-plane. In practical implementation, in order to emulate the cylindrical shape, compensation phases of the elements in the center column are calculated at first, then they are copied and pasted to all the other columns, which are depicted in Fig. 5-8.

Parabolic design

The element compensation phases in the center column is copied and pasted to each column

Parabolic Cylindrical design
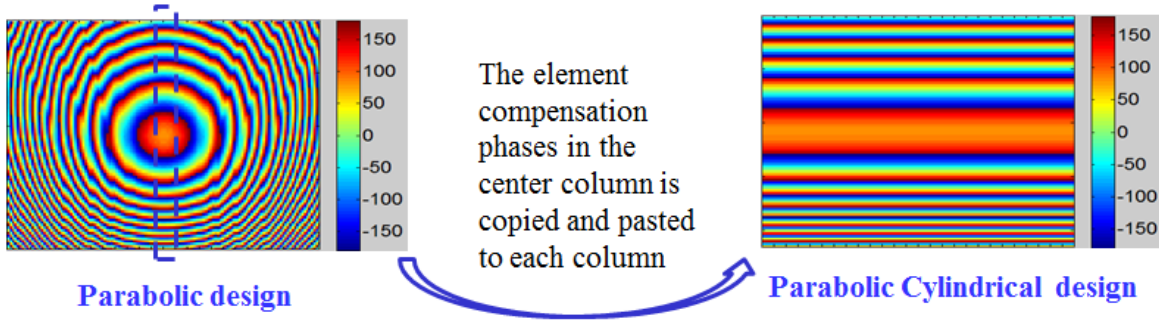
Fig. 5-8 Generation of element compensation phase for traditional parabolic cylindrical reflectarray.

- Design of the feeding array

Since the reflectarray reflected the feeding beam in the *E*-plane in the mirror way, the pattern characteristics in the *E*-plane basically resembles the *E*-plane pattern characteristics of the feed array. Hence, to achieve a good SLL, -30 dB Dolph-Tchebyscheff distributions are adopted as the excitation current amplitude distribution of the feeding elements. The calculation of the distribution coefficients are obtained using the formula given in [28].

5.2.2 Modified Calculation of the Incident Fields of Reflectarrays

Different from the traditional reflectarray with a standalone horn, the calculation of incident fields from a feeding array is more complicated. When the reflectarray is illuminated by a traditional horn, the incident field of each element is simply calculated as:

$$E_{mn}{}^{inc} = e^{-j \cdot k \cdot r_{mn}} \times \frac{1}{r_{mn}} \times \cos^{q_f} \theta_{fmn} \times \cos^{qe_{mn}} \theta_{emn} \qquad (5.2)$$

Which is based on the assumption that the reflectarray is in the far-field region of the feed horn. However, for the reflectarray illuminated by a feeding array, such assumption does not hold anymore. Nevertheless, the far-field condition could be applied to a single feeding element. Hence, ignoring the coupling effect, the total incident field on each reflectarray element is obtained by summing them up, expressed as:

$$E_{mn}{}^{inc} = \sum_{i=1}^{N} A_i \times e^{j\beta_i} \times e^{-j \cdot k \cdot r_{mn\_i}} \times \frac{1}{r_{mn\_i}} \times \cos^{q_f} \theta_{fmn\_i} \times \cos^{qe_{mn\_i}} \theta_{emn\_i} \qquad (5.3)$$

Where A_i is the excitation amplitude of the ith feed and β_i is the excitation phase of the ith feed. It is also noted that r_{mn}, θ_{fmn}, qe_{mn}, and θ_{emn} become r_{mn_i}, θ_{fmn_i}, qe_{mn_i}, and θ_{emn_i}, respectively, and this is because all of the parameters are feeding element dependent.

5.2.3 Effects of the Size and Height of the Feeding Array

In order to study the effect of configuration of feeding array on the incident amplitudes, investigation into combinations of different sizes and heights (Z_f) of feeding array are conducted, and the calculation results are demonstrated in Fig. 5-9, as well as tabled in Table 5-2. It is recorded that the Dolph-Tchebyscheff coefficients for the 16 and 32 elements are [0.2880, 0.3157, 0.4542, 0.6005, 0.7415, 0.8632, 0.9526, 1, 1, 0.9526, 0.8632, 0.7415, 0.6005, 0.4542, 0.3157, 0.2880] and [0.4386, 0.2418, 0.3020, 0.3668, 0.4352, 0.5058, 0.5772, 0.6478, 0.7160, 0.7801, 0.8386, 0.8899, 0.9327, 0.9659, 0.9885, 1], respectively.

Denoting the size of feeding array as $m \times n$, where m represents in the number of elements along the *x* axis and *n* represents the number of elements along the *y* axis, it is observed that:

- m mainly controls the directivity of the reflectarray. For both cases of feeding array elements measuring 1×16 and 2×16, the directivity is around 35 dB; while when m is increased to 32, the directivity increased by roughly 3 dB;

- Z_f and n mainly control the edge taper. Similar to the traditional reflectarray illuminated by stand-alone horn, it is clearly that as the feeding array position increases, the edge taper becomes larger, thereby decreasing the spillover efficiency. In addition, n also impacts the edge taper. For example, for case 1, 4, and 7, in all of which Z_f is 181.26 mm, when n is 1, the edge taper is -7.2 dB; however, when n increases to 2, the edge taper drops to around -13 dB. It is worthwhile pointing out that although m in case 4 and 7 equals 16 and 32, respectively, the difference in the edge taper is only 0.9 dB, which shows that the value of m rarely effects the spillover efficiency.
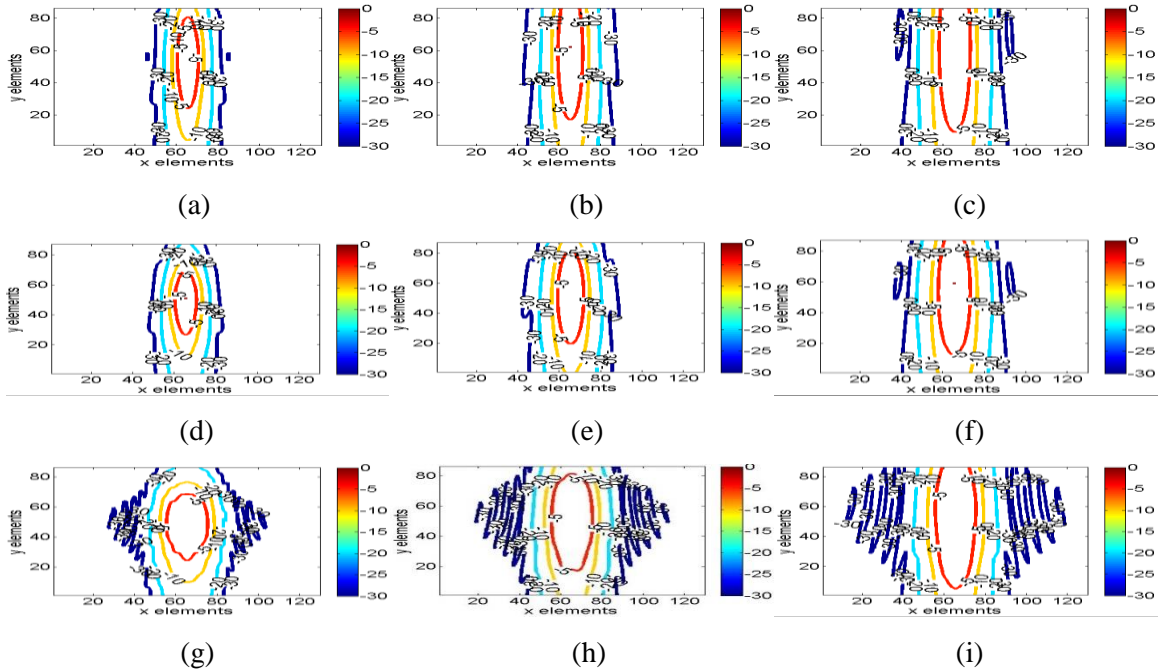
Fig. 5-9 Incident amplitude distribution of different feeding array configurations (a) case1; (b) case 2; (c) case 3; (d) case 4; (e) case 5; (f) case 6; (g) case 7; (h) case 8; (i) case 9.

Table 5-2 Calculated results for feeding arrays of different size and height

Case	Feed size	z_f	Edge taper	D (dB)	HPBW(H-plane)	HPBW(E-plane)
1		181.26 mm	-7.2 dB	34.9	$1.5°$	$7.9°$
2	1×16	271.89 mm	-2.2 dB	35.1	$1.5°$	$7.9°$
3		362.52 mm	-0.9 dB	35.2	$1.5°$	$7.9°$
4		181.26 mm	-13.8 dB	34.4	$1.5°$	$7.9°$
5	2×16	271.89 mm	-6.9 dB	35.0	$1.5°$	$7.9°$
6		362.52 mm	-3.0 dB	35.1	$1.5°$	$7.9°$
7		181.26 mm	-12.9 dB	37.5	$1.5°$	$4°$
8	2×32	271.89 mm	-6.9 dB	38.1	$1.5°$	$4°$
9		362.52 mm	-3.2 dB	38.2	$1.5°$	$4°$

In the following designs of this chapter, the size of the feeding array is selected to be 2×16, and Z_f is chosen to be 235.64 mm to achieve -10 dB edge taper.

5.2.4 Scanning Performance of Traditional Parabolic-Cylindrical Reflectarray

To further study the scanning performance of a parabolic-cylindrical reflectarray, the far-field performance of the designed traditional parabolic cylindrical reflectarray of four cases are calculated using the array theory, when the feeding array is rotated by 0°, 10°, 20°, and 30°. As demonstrated in Fig. 5-10, it is observed that the feeding beam could only illuminate part of the reflectarray aperture in all of the cases, and when it rotates, the bright area correspondingly moves to the edge. Nevertheless, the spillover is still acceptable for the case of 30°.

| (a) | (b) | (c) | (d) |
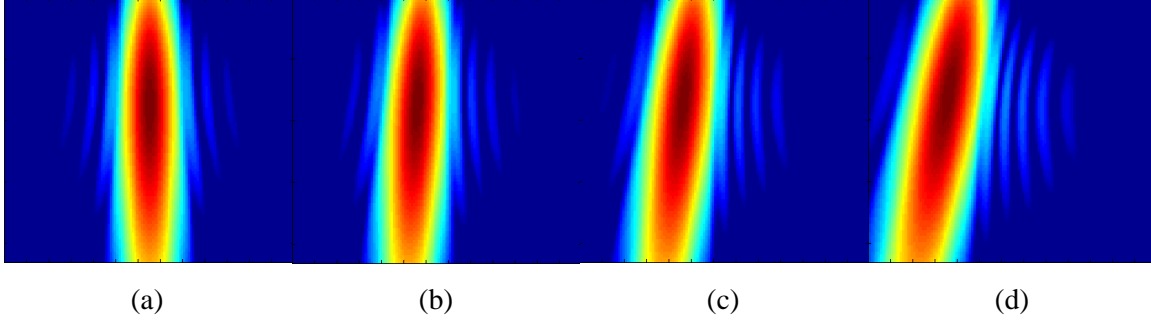
Fig. 5-10 Amplitude distribution of incident fields when feeding array is rotated by (a) 0°, (b) 10°, and (c) 20°, and (d) 30°.
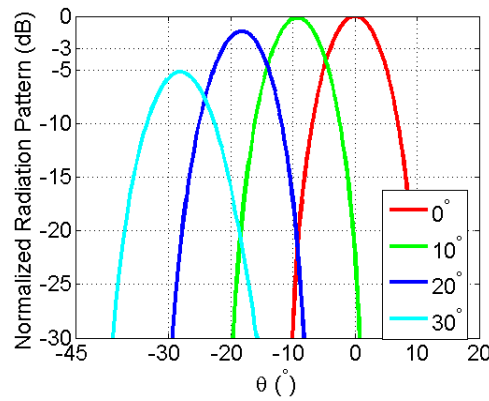
Fig. 5-11 The radiation patterns in the u-v plane when the array feed is rotated (a) 0°, (b) 15°, and (c) 30°.

The radiation patterns in *E*-planes of the four cases are plotted in Fig. 5-11, while the beam point directions and directivities are summarized in Table 5-3. It can be seen that as the feeding array rotates, the angle of main beam direction becomes larger, and the maximum angle deviation is 2° for the case of 30°. It is also noticed that the main beam width does not change much, but the directivity drops dramatically especially for the last case. Hence, the radiation patterns in the *u-v* plane are calculated to account for this scanning loss, and the results are shown in Fig. 5-12. It is observed that as the feed rotates, the main beam in the *H*-plane becomes much wider, and it is believed that this is the dominate factor for the directivity loss.

Table 5-3 BPD and achieved directivities for traditional parabolic-Cylindrical Reflectarray

Target	Beam Point Direction	D (dB)
$0°$	$0°$	34.9
$10°$	$9.2°$	34.7
$20°$	$18.3°$	33.5
$30°$	$28°$	29.7

(a)   (b)   (c)   (d)
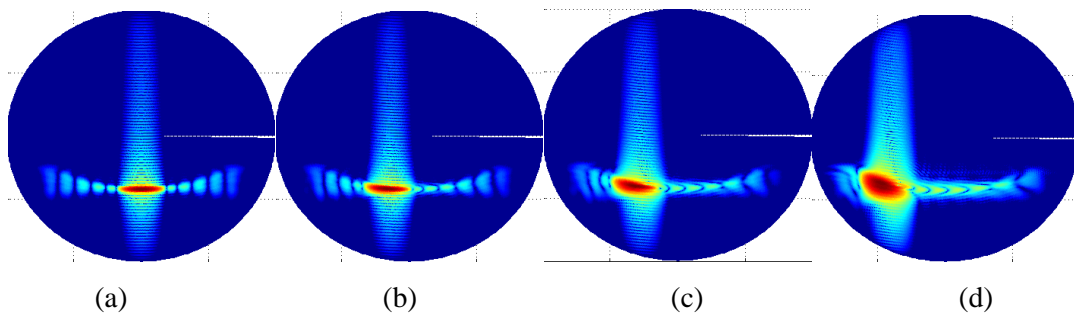
Fig. 5-12 The radiation pattern in the *u-v* plane when feeding array is rotated by (a) 0°, (b) 10°, and (c) 20°, and (d) 30°.

In order to study the cost of directivity loss for a wider scanning range achieved by this parabolic cylindrical reflectarray, a comparison between two groups is made. In one group, both of the two reflectarrays are traditional parabolic ones, and they are specifically designed to pointing to 0° and 30°, respectively. In the other group, the reflectarrays systems have the same aperture designs but with feeding array rotated by 0° and 30°, respectively. The calculated radiation patterns in the *u-v* planes are displayed in Fig. 5-13 and Fig. 5-14.

For the two cases of 0°, obviously the beamwidths in the *H*-planes are very similar to each other; however, it is noted that the parabolic reflectarray has a much smaller main beam in the *E*-plane, which is the main contributor to the 3 dB directivity loss. Nevertheless, when the

feeding array is rotated by 30°, the main beam of the parabolic cylindrical reflectarray in the *H*-plane becomes much wider, which is suspected to cause the dramatic directivity degradation.

(a)   (b)
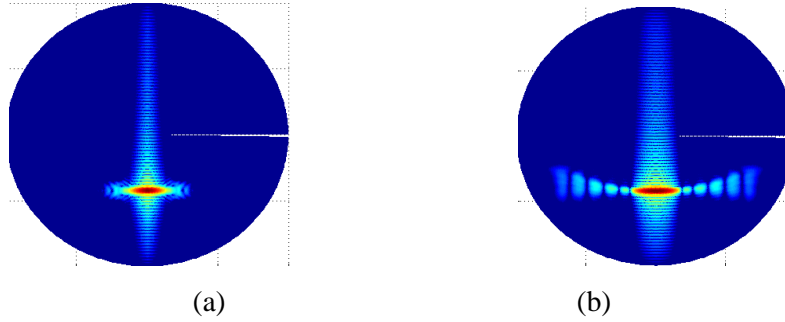
Fig. 5-13 The radiation patterns in the *u-v* plane (a) the parabolic reflectarray is designed to point to the normal direction while (b) the feeding array of the parabolic cylindrical reflectarray is rotated by 0°.

(a)   (b)
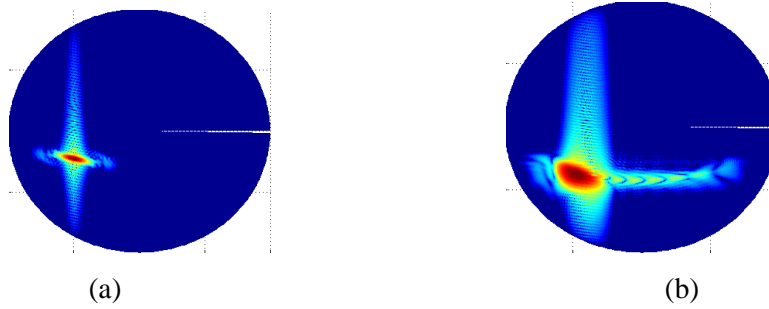
Fig. 5-14 The radiation patterns in the *u-v* plane (a) the parabolic reflectarray is designed to point to 30° while (b) the feeding array of the parabolic cylindrical reflectarray is rotated by 0°.

Table 5-4 Comparison of directivities between parabolic reflectarrays and traditional parabolic-cylindrical reflectarray

	0°	30°
Parabolic	37.7 dB	38.2 dB
Parabolic-cylindrical	34.9 dB	29.7 dB
Difference	2.8 dB	8.2 dB

5.2.5 Phase Error Analysis of Parabolic-Cylindrical Reflectarrays

In order to investigate the further reason behind this performance deterioration, a study of phase errors is performed. The compensated phases of parabolic and parabolic-cylindrical reflectarrays are calculated when the feeding array is rotated by 0° and 30°, respectively, as well as the phase difference. The results are illustrated in Fig. 5-15 and Fig. 5-16. The highlighted areas by the green dash lines are the illuminated areas on the aperture, where the inner and outer lines indicate the edge taper of -10 dB and -20 dB, respectively.

By comparing the phase errors in these two cases, it is shown that the main constraint factor for the scanning range is the spatial phase delays at different columns of elements. Mimicking a cylindrical surface, each column of elements is only supposed to focus the wave coming from the subarray directly located above them; however, as the array feed rotates, the spatial phase delay changes, resulting in increased phase errors and degraded radiation performance. Note that these phase errors inherently exist in the parabolic cylinder reflectors or reflectarray design.

(a)

(b)

(c)
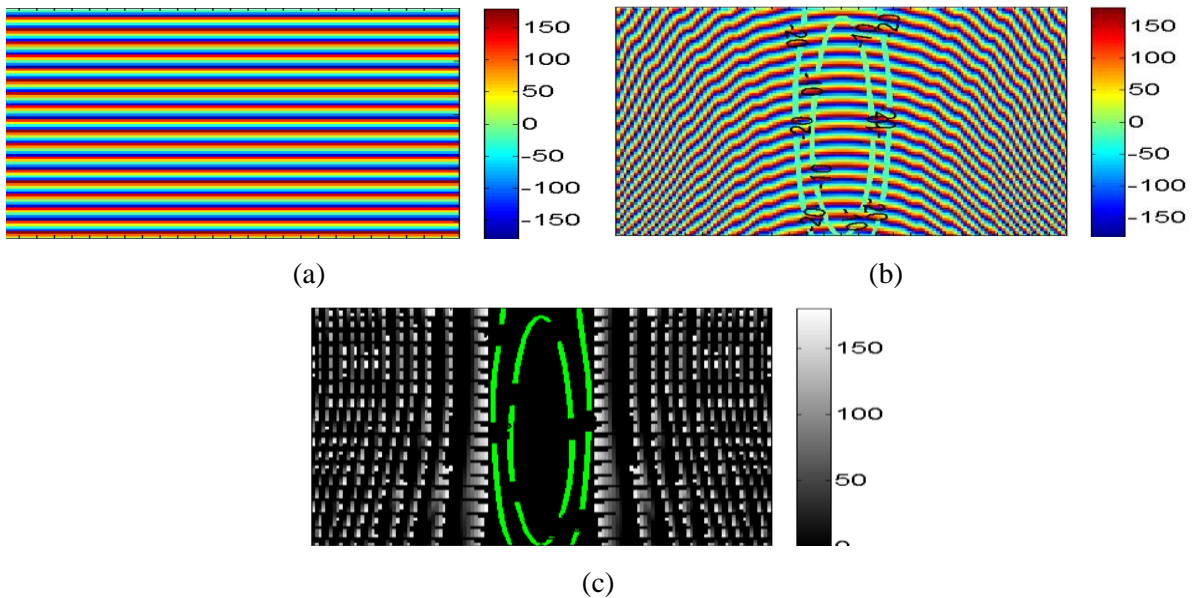
Fig. 5-15 (a) Compensated phase of parabolic reflectarray when the feed is rotated by 0°, (b) compensated phase of parabolic-cylindrical reflectarray when the feed is rotated by 0°, and (c) the difference of compensated phases between parabolic and parabolic-cylindrical reflectarrays when the feed is rotated by 0°.

(a)   (b)

(c)
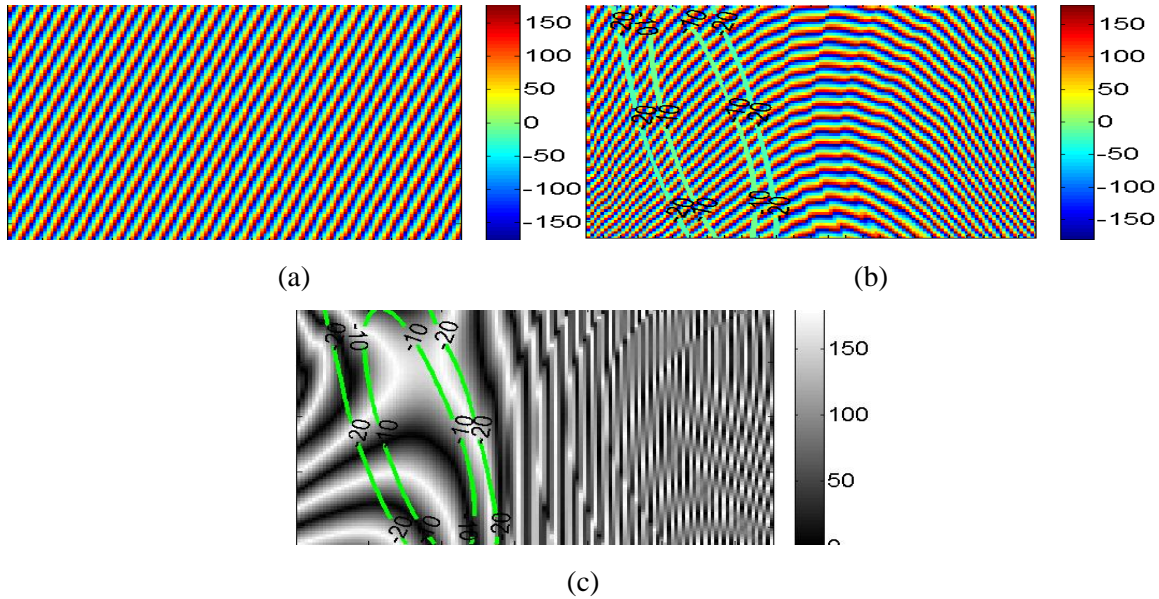
Fig. 5-16 (a) Compensated phase of parabolic reflectarray when the feed is rotated by 30°, (b) compensated phase of parabolic-cylindrical reflectarray when the feed is rotated by 30°, and (c) the difference of compensated phases between parabolic and parabolic-cylindrical reflectarrays when the feed is rotated by 30°.

5.3 Optimized Design of Parabolic-Cylindrical Reflectarrays

To overcome the aforementioned phase errors, the required phases over the reflectarray aperture are optimized to compensate for the intrinsic spatial phase delay, which is composed of two steps:

- At first, as shown in Fig. 5-17, generally speaking, the elements within each column are designed individually assuming that a point source is located at the array center and the reflected wave points in the specular direction. This procedure is repeated for each column, and the modified compensation phases are plotted in Fig. 5-18.

105

Accordingly, the calculated radiation patterns in *u-v* planes are demonstrated in Fig. 5-19. Apparently, the beams focused by the feeding array in the *E*-plane are somehow defocused by the reflectarray aperture for all of the cases, which leads to a considerable loss in directivity, which is tableted in Table 5-5.
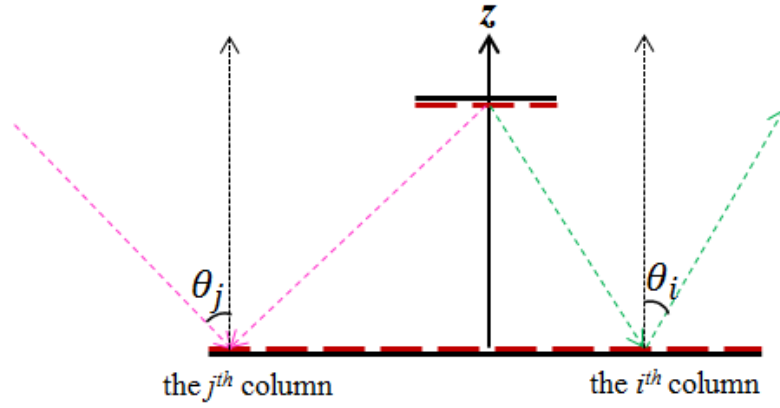
Fig. 5-17 Graphical illustration of the optimized design of parabolic-cylindrical reflectarray.
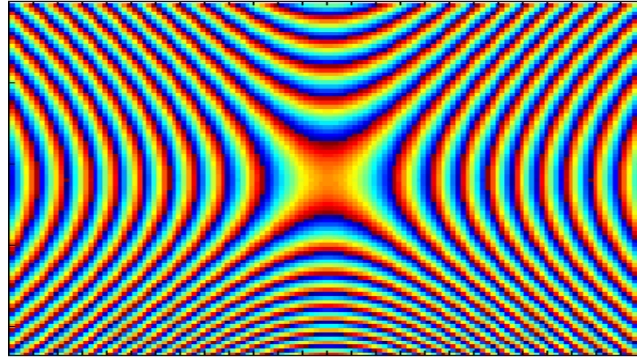
Fig. 5-18 The required compensation phase after modification.
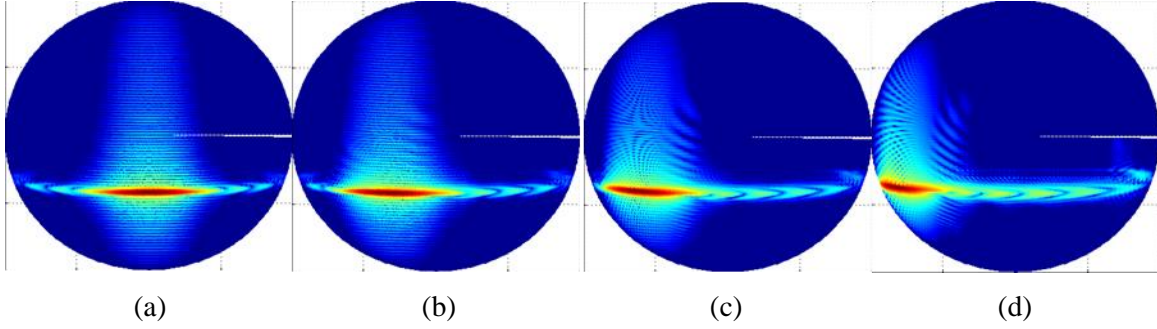
Fig. 5-19 The radiation patterns in the *u-v* plane when the array feed is rotated (a) 0°, (b) 10°, (c) 20°, and (d) 30°.

- Therefore, in order to maintain the mirror-like reflection in the *E*-plane, the elements in the center row are kept the same by changing the reference phase to each column. The required compensation phases after optimization are shown in Fig. 5-20. Apparently, the elements within each row in *x*-direction, except the center row, are different. Only the elements within the middle column remain the same as those in the conventional design. The difference increases as the elements are farther from the middle. The reflectarray now mimics a doubly curved surface, other than the parabolic cylinder in literature.

  The radiation patterns generated from the optimized aperture are demonstrated in Fig. 5-21. An almost constant beam width in the H-plane is observed even when the feed rotation angle reaches 30°, which suggests that a larger scan angle is achieved. The comparisons with the one obtained right after the 1st step and the traditional parabolic cylindrical design are made in Table 5-5 and Fig. 5-22, respectively, and the following conclusions are drawn:

- The 2nd step in the optimization is very crucial, otherwise the main beam in the *E*-plane generated by the feeding array could not be maintained;

- The scan capability of the parabolic cylindrical reflectarray can be greatly enhanced by this optimization methodology, and a 0.5 dB directivity variation is achieved within 30° scanning range;
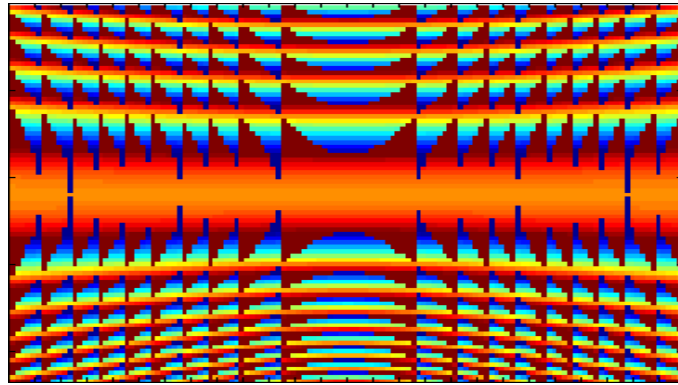
Fig. 5-20 The required compensation phases after optimization.
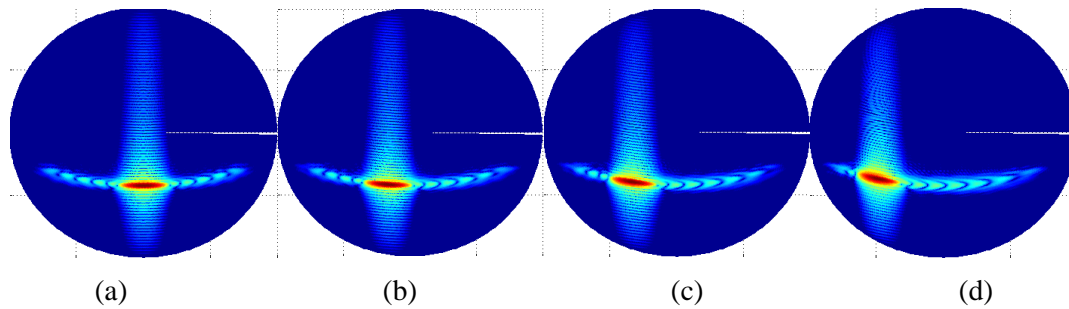
| (a) | (b) | (c) | (d) |

Fig. 5-21 The optmized radiation patterns in the u-v plane when the array feed is rotated (a) 0°, (b)15°, and (c) 30°.

Table 5-5 Directivities achieved after the 1st and 2nd step, respectively

	0°	10°	20°	30°
Directivities achieved after the 1st step	31.5 dB	31.4 dB	31.2 dB	30.8 dB
Directivities achieved after the 2nd step	34.8 dB	34.7 dB	34.6 dB	34.3 dB
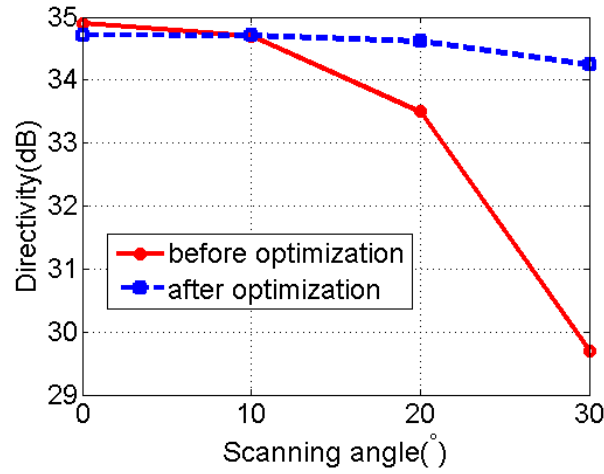
Fig. 5-22 Comparison of scanning loss before and after optimization.

Certainly such a wide scanning range is reached at the price of some gain lost. Similarly, the comparisons with traditional rababolic reflectarrays are made for the case of 0° and 30° in Fig. 5-23 and Fig. 5-24, respectively.

(a)   (b)
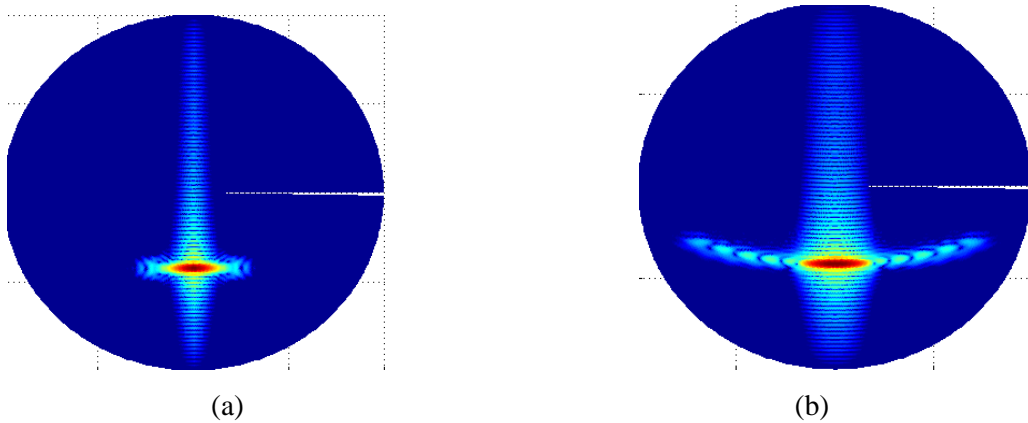
Fig. 5-23 The radiation patterns in the *u-v* plane when (a) the parabolic reflectarray is designed to point to the normal direction while and (b) the feeding array of the optimized parabolic cylindrical reflectarray is rotated by 0°.

It can be seen that the broadened beam in the E-plane is still the main contributor to the directivity loss; however, the main beam width in the *H*-plane only changes a little when it is

steered to 30°, which shows that this optimization method works well. As tableted in Table 5-6, the directivity is 3dB and 4dB for the case of 0° and 30°, respectively.

| (a) | (b) |
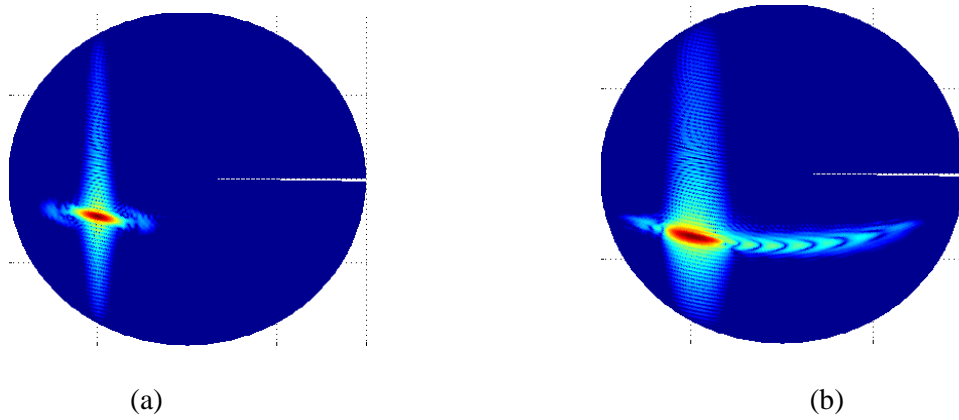
Fig. 5-24 The radiation patterns in the *u-v* plane when (a) the parabolic reflectarray is designed to point to 30° offset and (b) the feeding array of the optimized parabolic cylindrical reflectarray is rotated by 30°.

Table 5-6 Comparison of directivities between parabolic reflectarrays and modified parabolic-cylindrical reflectarray

	$0°$	$30°$
Parabolic	37.7 dB	38.2 dB
Parabolic-cylindrical	34.7 dB	34.2 dB
Difference	3 dB	4 dB

The compensated phases are calculated to again to show the phase error, and they are shown in Fig. 5-25 and Fig. 5-26 for the case of 0° and 30°, respectively. The corresponding phase errors of the traditional design are also reprinted for the convenience of comparison. It could be seen that for the former case, the phase errors in the illuminated area are almost same; however, for the latter case, the phase errors are greatly decreased.
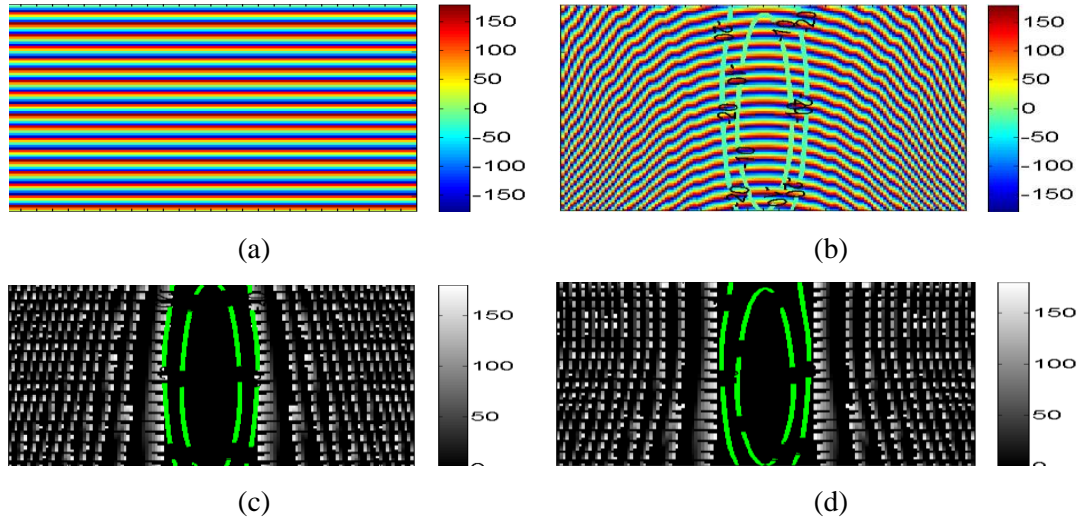
Fig. 5-25 (a) Reprint of compensated phase of parabolic reflectarray when the feed is rotated by 0°, (b) compensated phase of optimized parabolic-cylindrical reflectarray when the feed is rotated by 0°, (c) the difference of compensated phases between parabolic and optimized parabolic-cylindrical reflectarrays when the feed is rotated by 0°, and (d) reprint of the difference of compensated phases between parabolic and optimized parabolic-cylindrical reflectarrays when the feed is rotated by 0°.
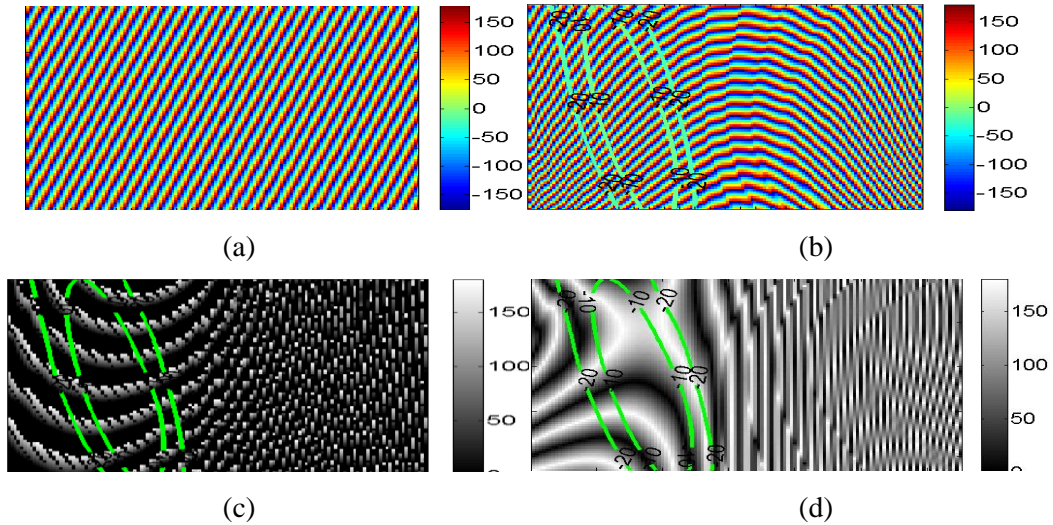
Fig. 5-26 (a) Reprint of compensated phase of parabolic reflectarray when the feed is rotated by 30°, (b) compensated phase of optimized parabolic-cylindrical reflectarray when the feed is rotated by 30°, (c) the difference of compensated phases between parabolic and optimized parabolic-cylindrical reflectarrays when the feed is rotated by 30°, and (d) reprint of the difference of compensated phases between parabolic and optimized parabolic-cylindrical reflectarrays when the feed is rotated by 30°.

5.4 A Practical Design of Optimized Parabolic-Cylindrical Reflectarrays

A practical design is developed with the main purpose of investigating the bandwidth performance. The simple patch shape element is chosen, which yields fairly wide and linear phase variation curves based on previous experiences. The substrate material used is Taconic Tlx-8 ($\varepsilon_r = 2.55, tan\delta = 0.0019$), and the sickness is selected to be 0.51 mm. The element simulation is done with HFSS using the periodical boundary condition, and its frequency behaviors within 31~34 GHz in terms of magnitude and phase are illustrated in Fig. 5-27(a) and Fig. 5-27(b), respectively. It is observed that the maximum element loss at 32.5 GHz is 0.19dB; and the maximum phase difference between the center and the two extreme frequencies (31 GHz and 34 GHz) are 56° and 67°, respectively.

(a)   (b)
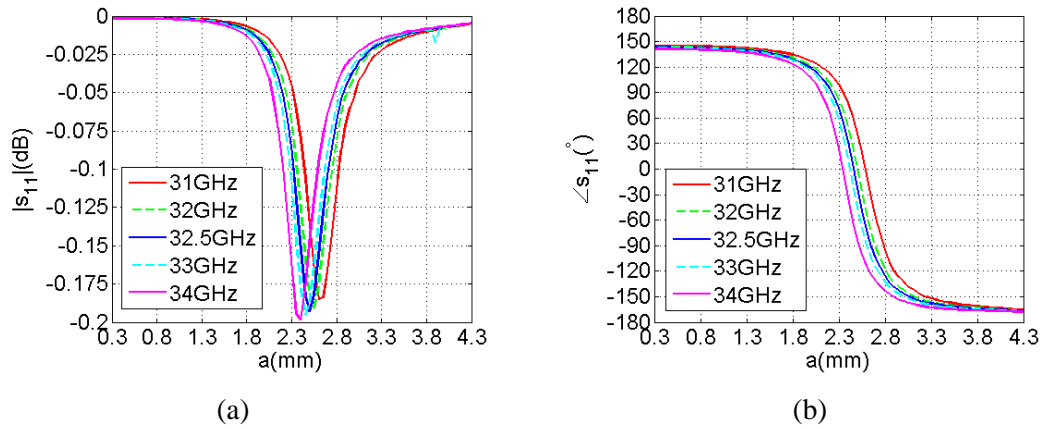
Fig. 5-27 (a) Amplitude and (b) phase response of elements at different frequency.

The scanning performances from 31 to 34 GHz are plotted in Fig. 5-28, and it is observed that:

- During this frequency range, for a certain scanning angle, the maximum directivity drop is less than 1 dB;

- During this scanning range, at a certain frequency, the maximum directivity drop is also less than 1 dB;

In addition, the 3D radiation patterns in *u-v* planes at three distinct frequencies are demonstrated in Fig. 5-29, Fig. 5-30, and Fig. 5-31, respectively, which shows that the gain loss is still mainly caused by the pattern distortion in the *H*-plane. Finally, Fig. 5-32 shows the mask layout for this optimized parabolic-cylindrical reflectarray.
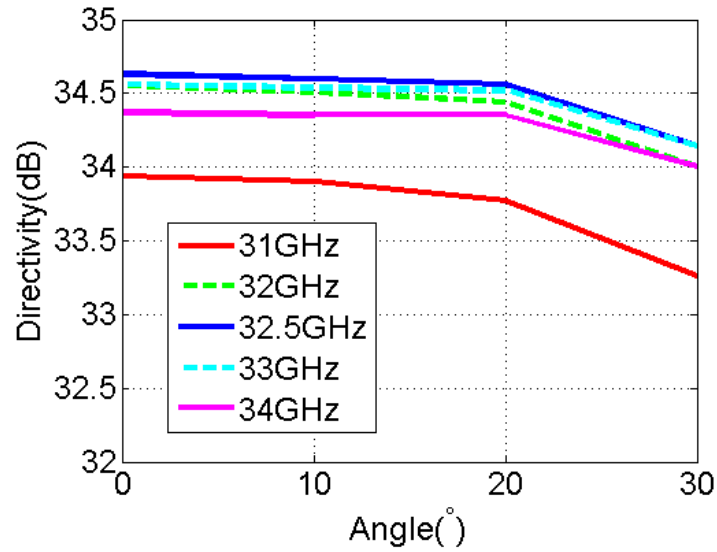
Fig. 5-28 The scanning performance at different frequencies.

(a)　　　　　　(b)　　　　　　(c)　　　　　　(d)

Fig. 5-29 The optmized radiation patterns in the u-v plane at 31 GHz, when the array feed is rotated (a) 0°, (b)10°, (c) 20°, and (d) 30°.
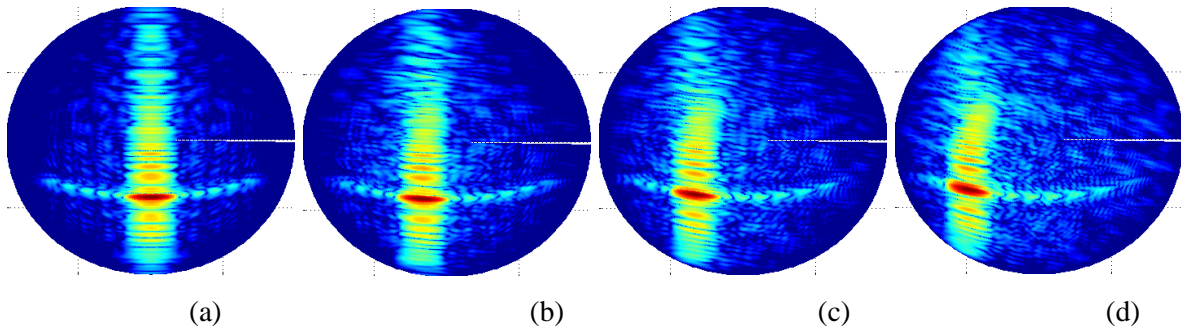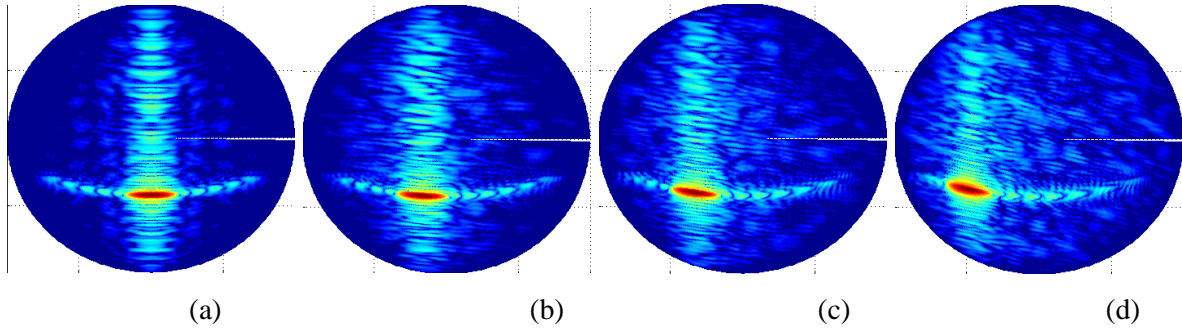
Fig. 5-30 The optimized radiation patterns in the u-v plane at 32.5 GHz, when the array feed is rotated (a) 0°, (b)10°, (c) 20°, and (d) 30°.

Fig. 5-31 The optmized radiation patterns in the u-v plane at 33 GHz, when the array feed is rotated (a) 0°, (b)10°, (c) 20°, and (d) 30°.
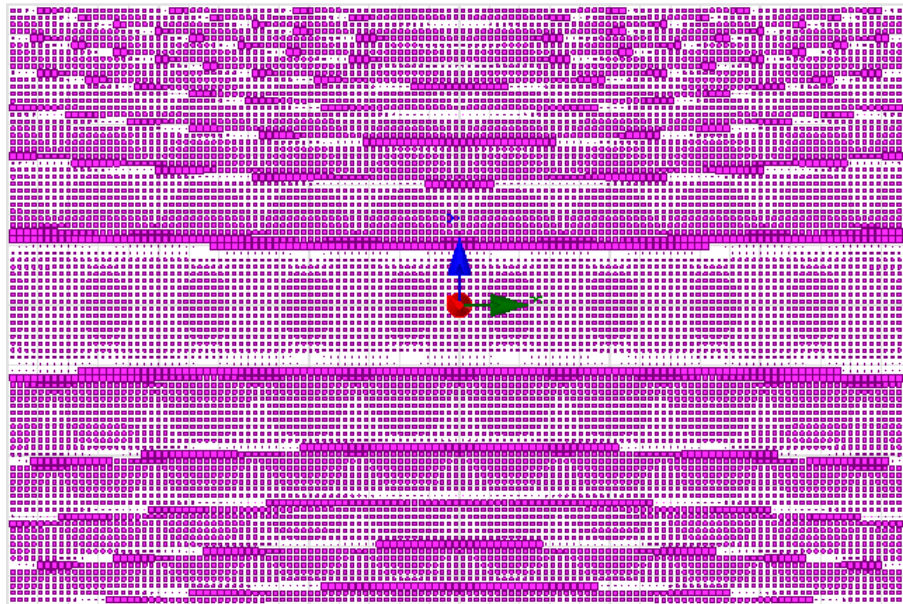
Fig. 5-32 Photo-etching mask of the optimized parabolic-cylindrical reflectarray.

CHAPTER VI

BEAM SCANNING REFLECTARRAY ANTENNA WITH 1-BIT RECONFIGURABLE ELEMENTS

In this chapter, the design of a 1-bit 10×10 elements reflectarray antennas (RRA) is demonstrated step by step, aiming to shed some light on the selection of analog vs. digital designs, lower-bit vs. higher-bit designs, cross-polarization problems in element designs, biasing-circuitry designs, and measurements, etc.. At first, a brief review of RRA design is made in terms of the phasing techniques, re-configurability mechanisms, and the antenna performance. After that, three different element structures are evaluated, and finally one of them is selected for the practical implementation of a 10×10 RRA. And what comes last is the fabrication and measurement of this 10×10 RRA, as well as the detailed analysis of the results.

6.1 Overview of Reconfigurable Reflectarray Antenna Design

6.1.1 Literature Review

As mentioned in Chapter 5, another way to implement a beam-scanning reflectarray is quite similar to phased array antennas, which is achieved by the means of dynamic phase control of each element. However, the spatial feed of RRA can improve the efficiency and reduce the cost remarkably compared with phased arrays, which require complex feeding network and expensive transmit/receive (T/R) modules.

Electronically RRA has received an increasing interest in the areas like space and terrestrial communications, and remote sensing, and they potentially exhibit exceptional performance in scanning/tracking velocity, coverage modification, and robustness against interference. Extensive and impressive advances in RRA have been made over the past 20 years, and some key experimental achievements regarding the efficiency performance has been tabled in Table 6-1. It is worthwhile mentioning that all of these RRAs are capable of continuous scanning and it is noticed that efficiency is a big problem for all of these designs. In [29], the 4-layer radiation element is consisted of a microstrip patch and a single-bit PIN diode. A large RRA comprised of 160×160 elements operating at 60 GHz was successfully implemented and the experimental results proved its reconfigrability. However, it is noticed that the reflection loss is 5.3 dB and 2.7 dB for the on and off state, respectively, which is relatively high. In the design presented in [30], the illumination loss of 4 dB could be reduced to 1 dB for a large reflectarray [31], and the element loss was estimated at 2.1dB. Furthermore, two additional factors were mentioned: one being the fabrication error, which possibly lead to misalignment between different layers and mis-impedance match; the other one being the effect of the oblique incidences.

In the RRA demonstrated in [32], aperture-coupled patches gathered by pairs to a common delay line were used, and the efficiency reaches more than 60%. However, it is noticed this design could not perform a continuous beam scanning, but only switched between $\pm 5°$.

Table 6-1 Some key experimental achievements for the published works

Design	Scale	Device	G	η_{perror}	η_{RL}	η_s	η_i	η_{x-pol}	η_{radome}	η_{tot}
[29]	160*160	1-bit	42.0 dB	41% -3.9 dB	40% -4.0 dB	88% -0.6 dB	84% -0.8 dB	--	79% -1.0 dB	9.5%

[33]	10×10	1-bit	11.42 dB	93.3% -0.3 dB	43.4% -3.64 dB	22.3% -6.51 dB	--	96.6% -0.15 dB	--	7.85%
[34]	3×15	varactor	9.3 dB	--	--	--	--	--	--	
[30]	5×6	varactor	13.3 dB	--	61.7% -2.1 dB	40.7% -3.9dB	39.0% -4.0dB	negligible	--	14%
[35]	7×10	1-bit	11.5 dB	83.2% -0.8 dB	66.1% -1.8 dB	93.3% -0.3 dB	42.7% -3.7 dB	--	--	5%

6.1.2 Investigation of the Phase Shifter Technology

The phase control of each element in a RRA is usually accomplished by using discrete devices or tunable electromagnetics materials. The pros. and cons. are summarized in Table 6-2 [36][37].

Table 6-2 The advantages and disadvantages of different phasing techniques

		Advantages	Disadvantages
Varactor diode		1)Reliable; 2)High speed; 3)Market available; 4)Negligible power consumption;	1)High loss; 2)Poor linearity; 3)Medium/High cost;
PIN diode		1)Reliable; 2)Simple biasing circuit design; 3)High speed; 4)Market available; 5)Low cost; 6)Low loss	1)High bias power consumption; 2)High power consumption;
MEMS design		1)Very Low loss; 2)Negligible power consumption 2)High linearity; 3)High isolation;	1)The switching speed, reliability, ultimate yield and cost of such devices remain issues; 2) Foundry required for fabrication;
Exotic	Ferrite	1) High power handling capability;	1)High cost;

117

material		2) Negligible DC power consumption; 3) Potential for low loss and cost;	2)Complicated current switching circuitry; 3)Only1-bit design for digit control design; 4)Availability requires special facilities;
	Liquid Crystal	1)Low cost; 2)Simple biasing circuit design; 3)Easy fabrication and integration; 4)Dielectric absorption loss of LC reduces with frequency; 5)High speed;	1)High loss; 2)Might not be applicable for some frequency ranges; 3)Only 1-bit design for digit control design; 4)Availability requires special facilities;
Others		The concept of varying the height of the patches to change the reflected phase has also been examined.	

Among these various solutions, the lumped elements, particularly semiconductors elements such as PIN and varactor diodes, are used in most designs so far, which is mainly due to their maturity and availability. More importantly, such technologies do not demand advanced fabrication facilities or expertise. Between reflectarrays integrated with PIN and varactor diodes, which are digital and analog designs, respectively, the tradeoff is usually between dissipative loss, quantization loss and cost.

Although MEMS exhibits some good features when utilized in a RRA, like low-loss and high-linearity, considering its fabrication inconsistency, we finally selected PIN diodes.

6.1.3 Measurement of PIN-Diode

There are several good companies, such as MACOM, Skyworks and Hittite, and abundant of PIN diodes available in the market. Since the main concerns are maximum working frequency, package, insertion loss, and dimension, finally MADP-00907-14022 from MACOM is selected, and some of its properties are tabled in Table 6-3.

The most important parameters in our application are the total capacitance and series resistance. As shown in Fig. 6-1, typically people used two kinds of equivalent circuit models for the pin diodes: 1) the PIN diode is simply considered to present low resistance in the ON state and low capacitance in the OFF state; 2) an inductor is added in series with either the resistor or capacitor. Since it has been proved in [32] that the former one worked well, we chose this model. Moreover, because their values do not change a lot as the frequency varies, we simply used the ones specified in the Table 6-3.

Table 6-3 Information of different tools

Parameter	Condition	Units	Typ.	Max.
Total Capacitance	-10V, 1MHz	pF	0.025	0.030
Series Resistance	+10mA, 1GHz	Ω	5.2	7.0
Forward Voltage	+10mA	V	1.33	1.45
Reverse Leakage Current	Reverse Voltage = -45V	nA	-------	50
Switching Speed	10GHz	nS	2	--------
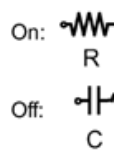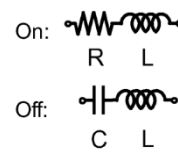
(a)   (b)

Fig. 6-1 Two different equivalent circuit models for a PIN diode, where (a) the PIN diode is simply considered to present low resistance in the ON state and low capacitance in the OFF state, and (b) the PIN diode is considered as a low resistance in series with an inductor in the ON state and capacitance in series with an inductor in the OFF state.

As shown in Fig. 6-2, a simple circuit was designed to measure the current vs. voltage curve of the PIN diode.

- A programmable DC power is used as the power supply;

- A multimeter is used to measure the current intensity;

- A biasing resistance is connected in series to control the current. For the purpose of verification, two resistors of different values, 100 Ω and 182 Ω, are used successively;
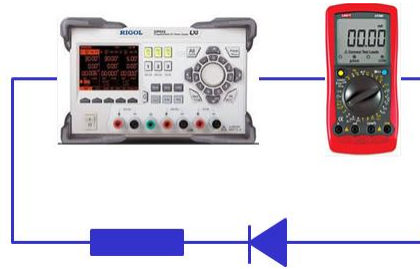
Fig. 6-2 The circuit to measure the current vs. voltage of the PIN diode.

The two current vs. voltage curves are displayed in Fig. 6-3 (a), corresponding to 100 Ω and 182 Ω, respectively, and a very good agreement between them is observed. Then, the required resistance vs. voltage was calculated and displayed in Fig. 6-3 (b), which suggests that if we expect the DC current to be within the range [10 mA, 13 mA], the resistance should be within the range [146 Ω, 187.6 Ω].

(a)   (b)
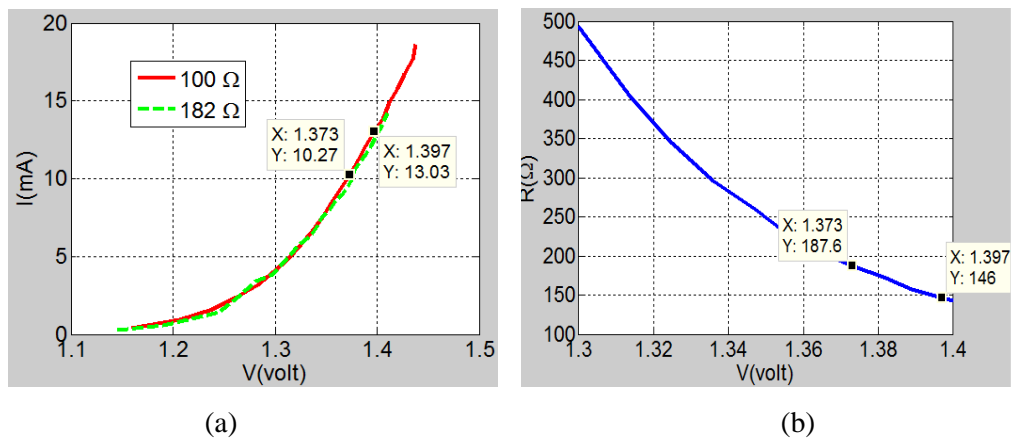
Fig. 6-3 (a) Current vs. Voltage curve of the PIN diode, and (b) Resistance vs. Voltage curve.

6.1.4 Effect of the Number of Bits for a Dynamic Digital RRA

The selection of the number of bits for a dynamic digital RRA is a tradeoff between several factors. Since the gain in the intended direction is usually the prime concern, the reduction in gain yielded by the digitally controlled designs needs to be taken into account in the design. However, in practical implementation, the benefit of lower quantization loss in higher-bit designs is often undermined by their complicated biasing circuit designs, which is a particularly acute issue in the RRA design. Since generally each cell of the array shall be controlled independently, the increase of bits potentially could result into thousands of control lines, which not only leads to a much more complicated biasing networking but also larger DC power consumption.

A summary of the advantages and disadvantages of lower-bit and higher-bit designs are tabled in Table 6-4.

Table 6-4 The advantages and disadvantages of lower-bit and higher-bit designs

	Lower-bit	Higher-bit
Advantages	1) Simple biasing design; 2) Easy implementation; 3) Low cost; 4) Low power dissipation;	1)Small gain loss; 2)Accurate beam pointing; 3)Low SLL;
Disadvantages	1) Large gain loss; 2) High SLL 3)Larger beam pointing error;	1)Complex biasing design; 2)Complicated implementation; 3)High cost; 4) High power dissipation;

In order to investigate the gain loss yielded by the reduction of bits quantitatively, the influence of the number of bits on the gain performance is evaluated using array theory. It has been evaluated in [38] with MEMS devices, and here a similar analysis is carried out assuming

the RRA has 10×10 elements. As described before, the key to design of a reflectarray antenna is the selection of compensation phase for each element. The required phase φ_{rmn} for the mn^{th} element is calculated as:

$$\varphi_{rmn} = k \times \left(r_{fmn} - \hat{u}_0 \times \vec{r}_{mn} \right) + \Delta\varphi , \tag{6.1}$$

Where k is the free space wavenumber, r_{fmn} is the spatial distance between feed and the mn^{th} element, $\hat{u}_0$ is the unit vector in the main beam direction, $\vec{r}_{mn}$ is the position vector of the mn^{th} element and $\Delta\varphi$ is a constant reference phase. For a N bit design, there are N phase options, and the implemented element phase is selected from the 2^N candidates based the least phase error principle.

The calculated results are displayed in Fig. 6-4. It can be seen that the gain loss is significant for the 1-bit configuration, and reaches 2 dB for broadside case. However, going from 2-bit to 3-bit, the gain loss drops to less than 0.5 dB. Finally, a 1-bit digital design is chosen for its simple biasing design.

(a)   (b)
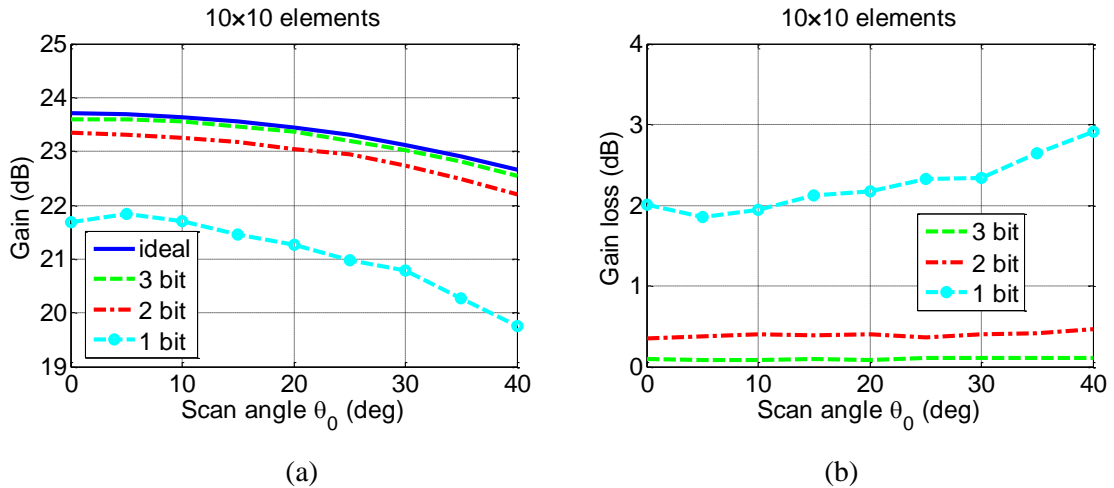
Fig. 6-4 (a) The scanning performance of a 10×10 RRA implemented with different numbers of bits and (b) the gain loss of a 10×10 RRA implemented with different numbers of bits.

6.2 Design of Reconfigurable Elements

Regarding the element design, there are two main concerns in the initial stage: the complexity of biasing circuitry design and the reconfigurability. Regarding the biasing network, there are generally three different configurations:

- On the top layer: it eliminates the necessity of through-vias insertion, but possibly introduces some spurious radiation due to the RF choke structure, as well as the DC control lines if the RF choke design is not good enough, which might interface with the radiation of the patch.

- On the ground layer: the undesirable radiation is suppressed, but the fabrication becomes more inconvenient and vias might have to be integrated which potentially introduce high cross-polarization.

- Below the ground layers: in this case, the DC line and patch antenna are usually printed on different substrates separated by a common ground plane, and hence, a large space is available to place the bias lines. More importantly, the undesirable interruption with the patch is suppressed. However, it might have the same via problem with the one on the ground layer.

Regarding the reconfigurability mechanisms, they could be generally categorized as shown in Fig. 6-5 based on their underlying theories. In terms of implementation, the active part could be either the patch or the slot if there is one:

- If patch is the active part: the reflection phase could be varied by either shift its resonant frequency or change the stub length connected to one of the edges. Regarding the former, there are various methods to achieve it: insertion of varactor diodes [39][40], shorting of one edge [29], and the change of the patch size [41][42].

- If slot is the active part: the reflection phase variation could be produced by either changing the slot length [43] or the length of the coupled MSL [44][30].

No matter what the principle is utilized to change the reflection phase, there are several issues that require careful attention in the design: reflection loss, ease of integration and fabrication and sensitivity to illumination angles.
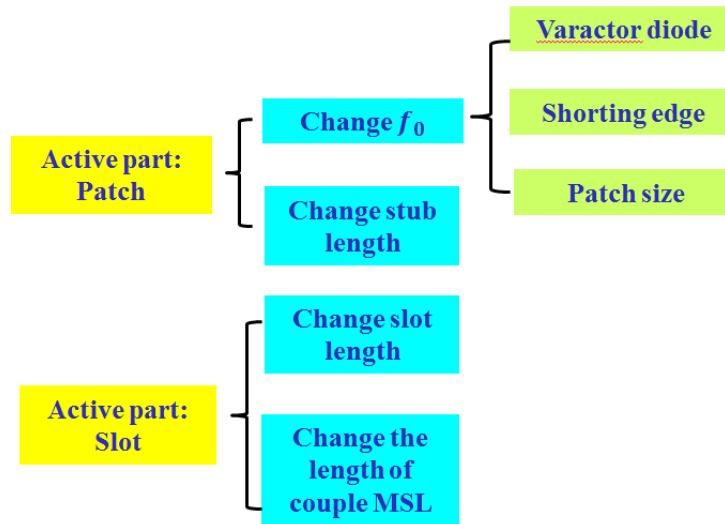
Fig. 6-5 Various reconfigurability mechanisms.

Three different element configurations are evaluated in the next. Since the mechanism of reconfigurability is investigated at first, the biasing circuitry parts are not going to be integrated at first.

Assuming we target to design an element capable of linearly dual polarization, TE and TM modes are both excited in the unit simulation.

6.2.1 The 1st Element Design

The reconfigurability principle of the 1st design roots in the loaded patch antenna, which essentially takes advantage of the resonant frequency shift. The basic model for the elements is

outlined in Fig. 6-6 and Fig. 6-7. A square microstrip patch is etched on the top, and the ground is situated into the middle of the two layers of substrates. Additionally, there are two vias inserted in the model: one starts from the patch and ends at the bottom layer, isolated from the ground, while the other one starts from the ground and ends at the bottom layer. It is noted that the former is positioned along the diagonal line of the square to make the geometry symmetric, aiming for simultaneous phase variations for the TE and TM modes, while the latter is situated in the middle of the patch. Finally, a short transmission line connects the two vias on the bottom layer.

The pin diode is implemented in the middle of the transmission line, and hopefully after the geometry is adjusted with full-wave analysis, the reflection phase changes by 180° when the pin diode switches. The geometry parameters are summarized in Table 6-5. One thing that needs to be mentioned is that unlike a traditional reflectarray element, since the ground layer is in the middle, two floquet ports are required in the simulation on the top and bottom, catching the reflected and transmitted signals, respectively.
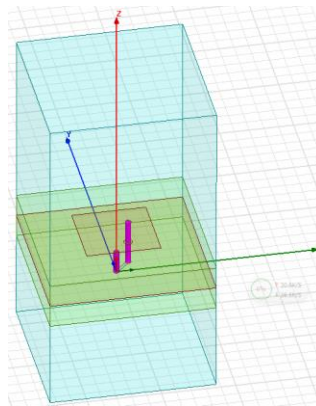
Fig. 6-6 The element structure for the 1st design without DC biasing structure.
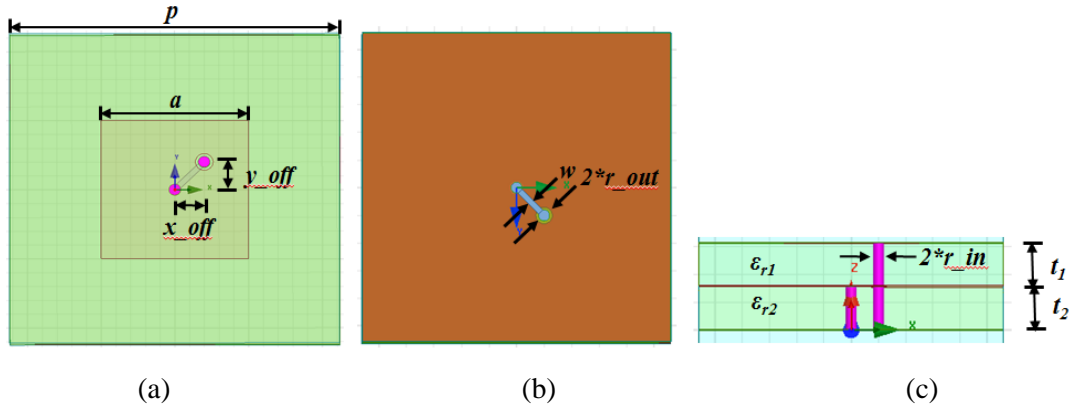
Fig. 6-7 Different views of the reconfigurable element: (a) top view of the top layer, (b) top view of the bottom layer, and (c) the side view.

Table 6-5 Initial values of the geometry parameters

p	*a*	*x_off*	*y_off*	*w*	*r_in*
11.2 mm	var	1 mm	1 mm	0.305 mm	0.2 mm
r_out	t_1	t_2	ε_{r1}	ε_{r2}	
0.3 mm	1.57 mm	1.57 mm	2.55	2.55	

For the purpose of verification, the commercial software HFSS and CST are both used. As shown in Fig. 6-8, the operation of adding a lumped element in HFSS and CST are very similar to each other, and there are only two things need to be defined: the value of the lumped device and its dimension.
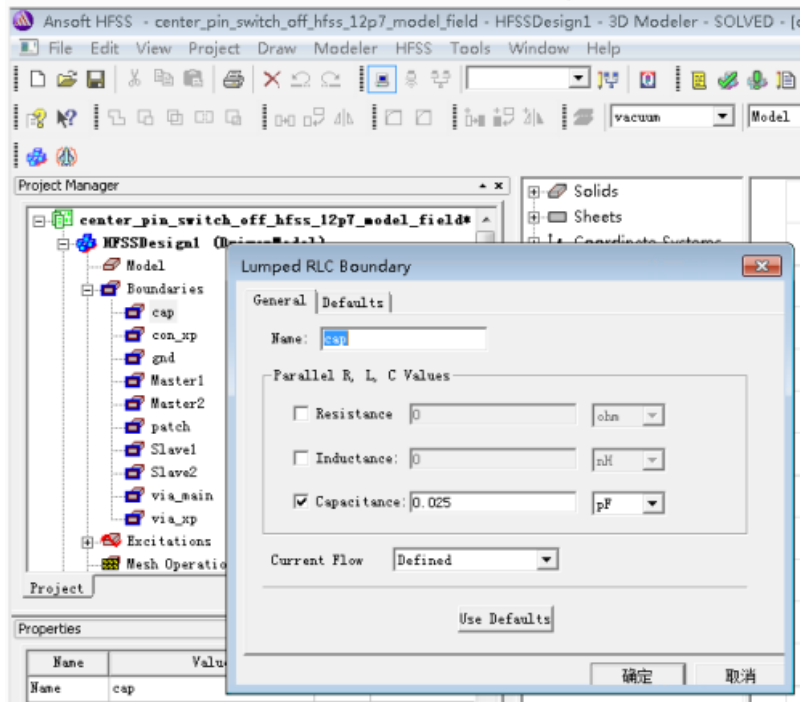
(a)
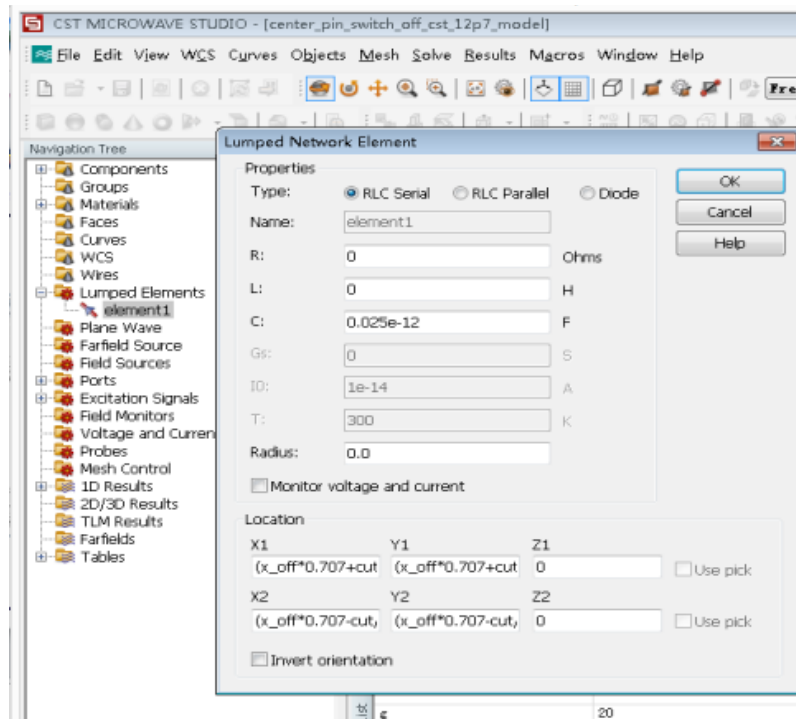
(b)

Fig. 6-8 The modeling of a lumped element in (a) HFSS and (b) CST.

The phases of reflection coefficients in TE mode as functions of the side length of the patch simulated with CST and HFSS are plotted in Fig. 6-9. As can be seen, they agree with each other very well, expect for the point where $a=3$mm, which is believed to be the converge problem. It is worthwhile pointing out that since the results have already been validated by two software, most of the following results will be only based on the HFSS simulations.
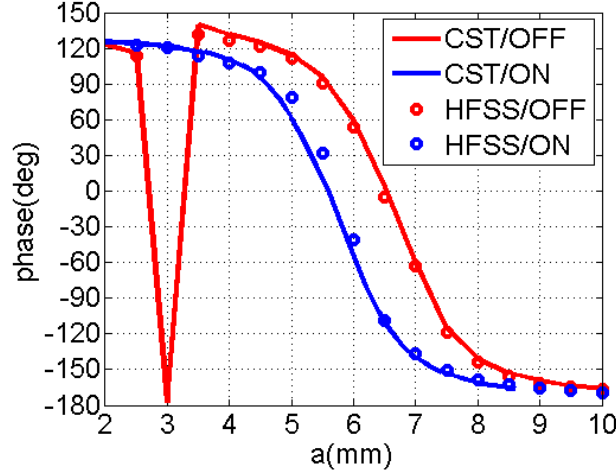
Fig. 6-9 The phase of the reflection coefficients for ON/OFF states simulated with CST and HFSS in TE mode.

In order to find a proper geometry which enables 180° phase difference as the pin diode switches, both the phase and magnitude of the reflection coefficients are investigated as illustrated in Fig. 6-10. Especially, the results when $a=5.5$mm and $a=6.5$mm are tabled in Table 6-6. It is observed that:

- There is a small resonance shift between the ON and OFF states, which verifies the reconfigurability mechanism of this structure.

- Based on the initial geometrical configuration, 180° phase difference could not be achieved by simply changing a.

- However, the more severe problem is the insertion loss. When $a=6.5$mm, the insertion loss is -11.8 dB in the OFF state.
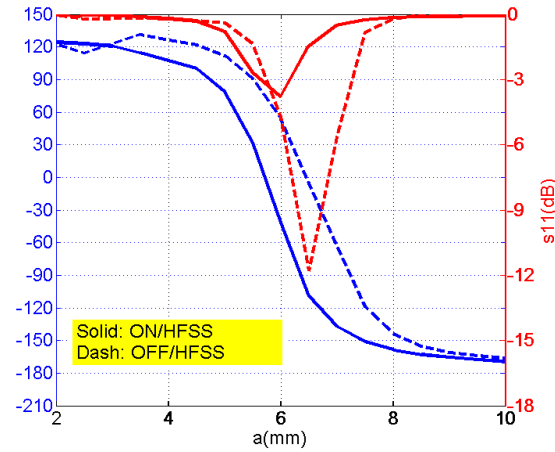
Fig. 6-10 The magnitude and phase of the reflection coefficients for ON/OFF states simulated with HFSS in TE mode.

Table 6-6 Information of different tools

a(mm)	S11(ON)	S11(OFF)	Δφ
5.5	-2.67 dB	-1.37 dB	60°
6.5	-1.48 dB	-11.8 dB	104°

From the point of equivalent circuit, apparently the input impedance seen from the patch into the through-via changes as its position varies. Hence, maintaining $x\_off = y\_off$, different values are tried for x_off, and the results are shown in Fig. 6-11, as well as tableted in Table 6-7. It is quite possible that the results do not get converged at some points due to the limited capacity of the computers. However, they still provide us with some valuable information:

- Generally the insertion loss is greater at the resonance when the state is OFF.

- It is possible that the 180° phase difference could be achieved if a prober *x-off* value is selected, but unfortunately it is very likely that it will be associated big insertion loss.

(a)

(b)

(c)
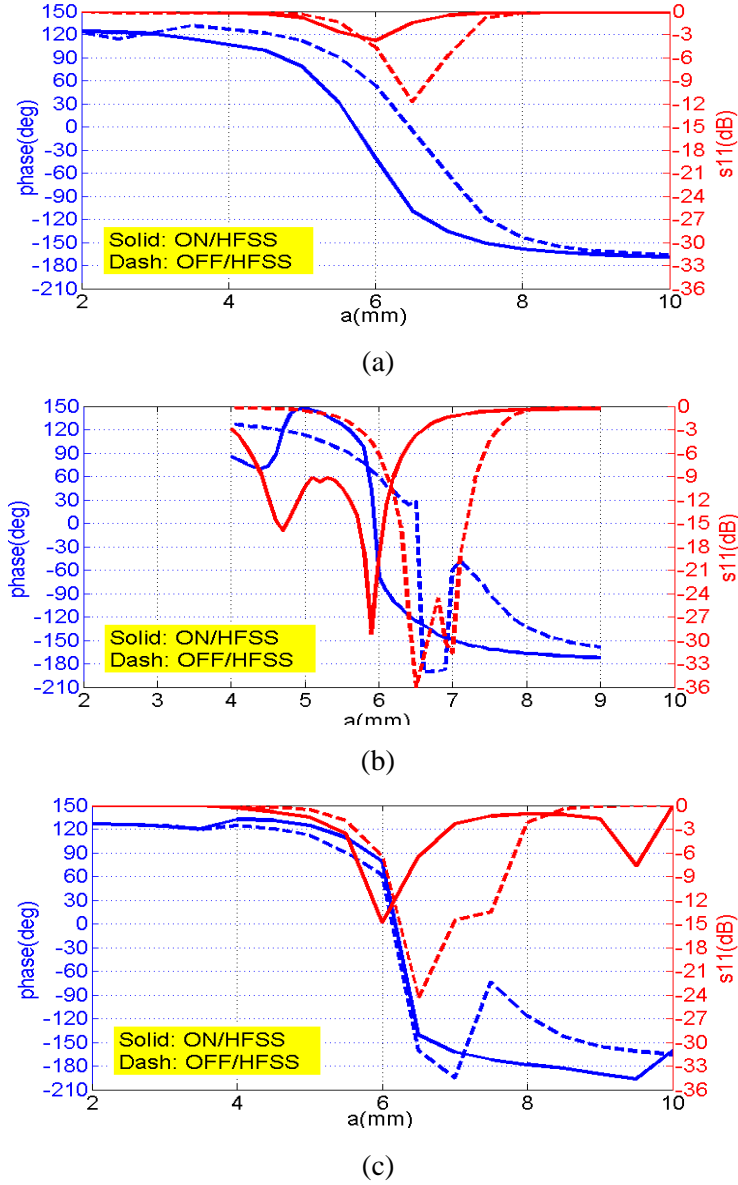
Fig. 6-11 Simulated reflection amplitude and reflection phase in TE modes verses patch length for different x_off values (a) x_off =1mm; (b) x_off =1.4mm; and (c) x_off =2mm.

Table 6-7 Achieved phase difference for different criteria of insertion loss

x_off(mm)	1	1.4	2
Max. phase difference (°) [$|s11| \geq \infty$]	104	153	99
Max. phase difference (°) [$|s11| \geq -3\text{dB}$]	60	60	62
Max. phase difference (°) [$|s11| \geq -1\text{dB}$]	33	33	40

In order to find out where the energy goes, the magnitudes of both reflection and transmission coefficients in TE mode are plotted for the OFF and ON states in Fig. 6-12. Moreover, the absorption, calculated as $1 - T^2 - R^2$, is also shown in the same figure. It is can be seen that the absorption is unexpectedly high, especially in the OFF state, which is somehow strange because the substrate used in the element is low-loss, and the metallic loss is by no means so high in our case. The corresponding E-fields distributions are then investigated and demonstrated in Fig. 6-13, which reveals that cross-polarization might be high for this configuration.

(a)   (b)
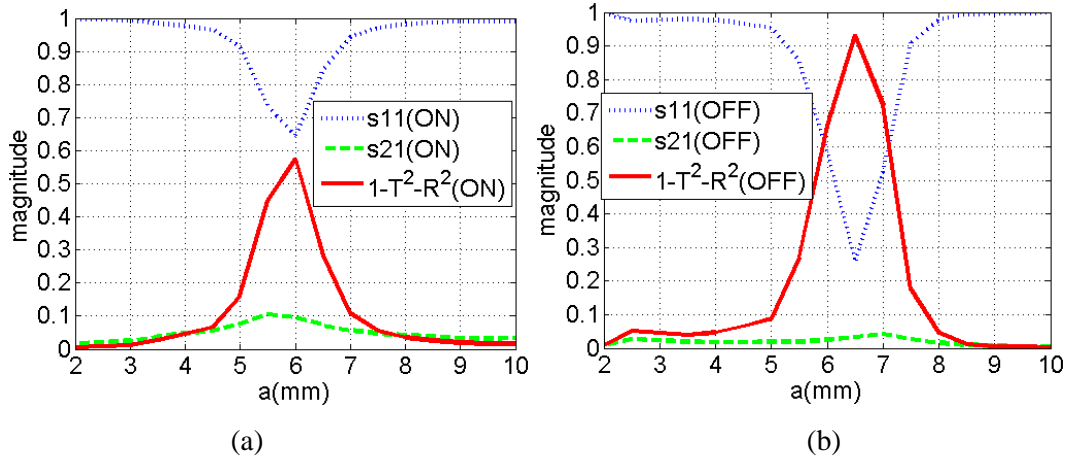
Fig. 6-12 The reflection, transmission and absorption coefficients in TE mode when x=6.5mm, for (a) ON state, and (b) OFF state.

(a)   (b)
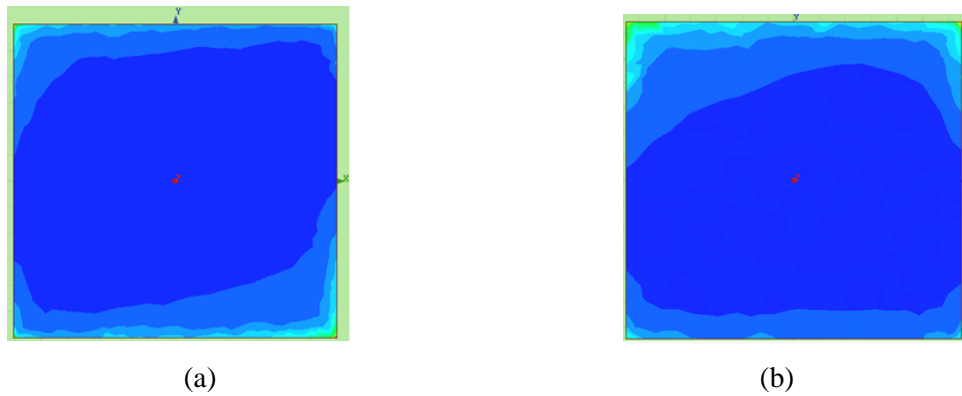
Fig. 6-13 E-field distribution when x=6.5mm, for (a) ON state, and (b) OFF state.

Therefore, cross-polarization is taken into account to calculate the absorption, and all the magnitudes of reflection and transmission coefficients for co-polarization and cross-polarization are plotted in Fig. 6-14. It is shown that:

- At the resonance, the cross-polarization reflection becomes the dominant one.

- It is also noticed that the absorbed energy in ON state is more than the one in OFF state, which may be due to the series resister.
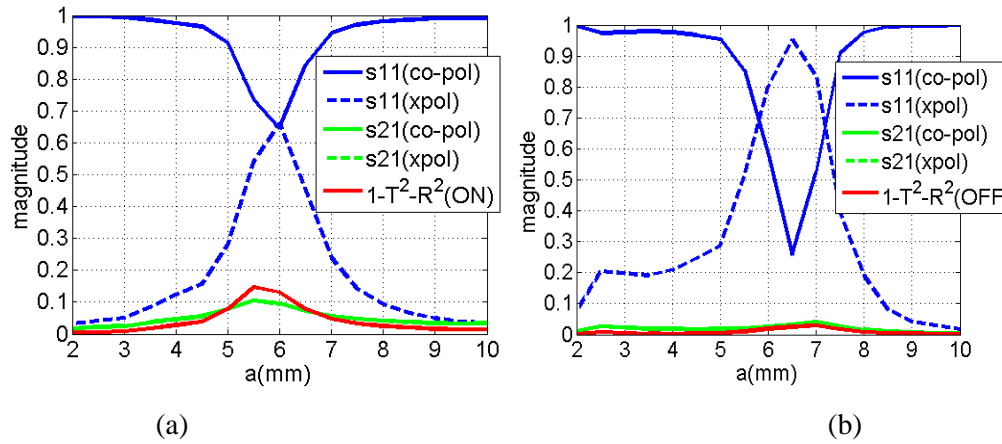
Fig. 6-14 The magnitudes of all the reflection/transmission coefficients and absorption when x=6.5mm, for (a) ON state, and (b) OFF state.

Based on the previous study, it is concluded that: although the integration and fabrication of such structure could be easily done with current fabrication technique, it is not recommended for the practical implementation because of its high loss, which is mainly due to the cross-polarization.

6.2.2 The 2nd Element Design

The reconfigurability principle of the 2nd design roots in the patch antenna loaded with open-end stubs, as demonstrated in Fig. 6-15, which shows the schematic of the reflectarray

element in a prospective way. Two open-end stubs are placed to two orthogonal edges of the patch antenna respectively, and two PIN diodes are situated between the transmission lines and the patches. It is expected that it acts more like a patch for the OFF state, hence a is the dominator factor to control the reflection phase; while for the ON state, l_1 and l_2 plays a paramount role in the phasing for TE and TM modes, respectively. Therefore, ideally the reflection phases could be independently controlled by a and l for the OFF and ON states, respectively, which might have some benefits for the phase optimization in the future. In such case, it will be desirable that the controllable phase range is 360° for each state, hence, the bent structure is also considered in case the transmission line needs to be extended to obtain larger phase shift. As illustrated in Fig. 6-16, two possible cases are considered, one with bent transmission lines, and the other one with straight ones. All the geometry parameters are summarized in Table 6-8.
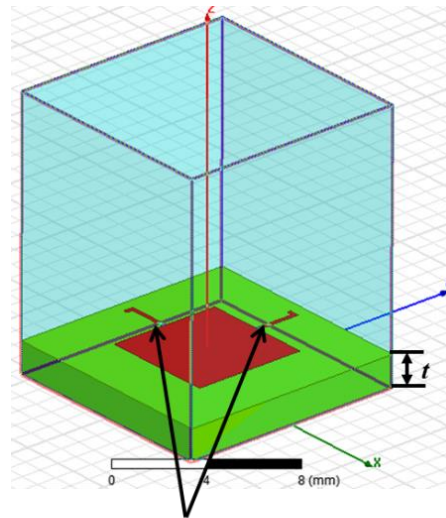
In practice, PIN diode is going to be inserted here

Fig. 6-15 Schematic of the reflectarray element.

(a)   (b)
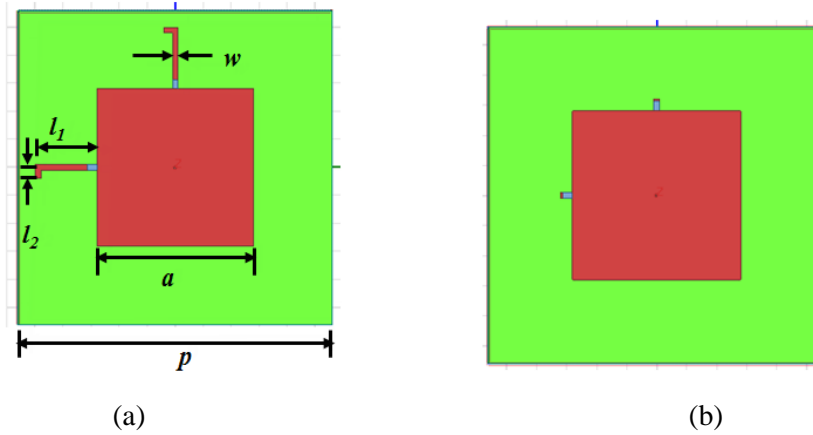
Fig. 6-16 Top view of unit configuration with (a) bent transmission lines and (b) straight transmission lines.

Table 6-8 Geometry parameters for the 2nd unit configuration

p	a	t	l_1	l_2	w	ε_{r1}
11.2 mm	Phasing	1.58 mm	Phasing	Phasing	Optimizing	2.55

Because the insertion loss caused by cross-polarization might be a big issue, the reflection coefficients for the ON state are considered at first. Different combinations of w, a, and l_1 are examined to study their effects. The magnitudes and phases of the reflection coefficients for the straight-line structure are displayed in Fig. 6-17 and Fig. 6-18, respectively. It is observed:

- The insertion loss is as small as less than 1dB for all of the cases;

- w has little effect on the reflection coefficient;

- l_1 is the dominant factor for the phase variation. However, a still has some impact on the phase range, and the maximum achieved one is 135° when a=5.6mm;
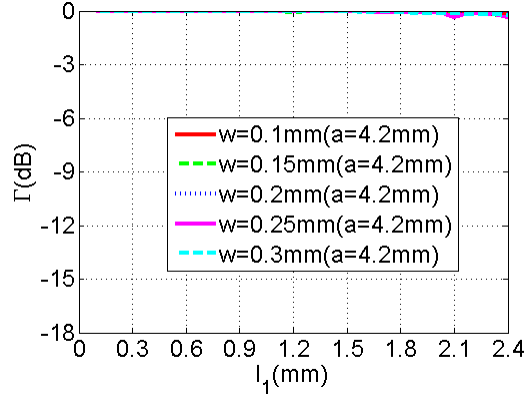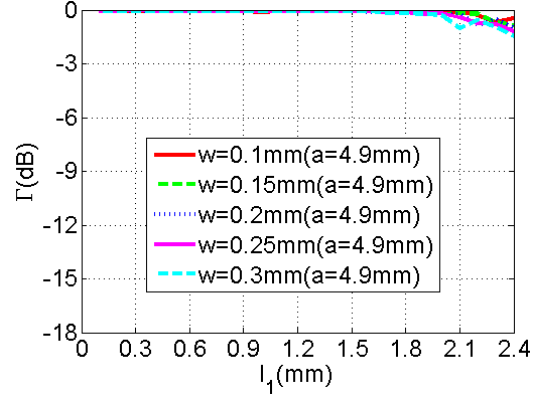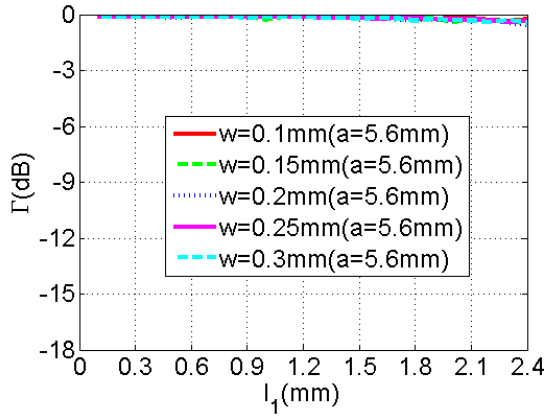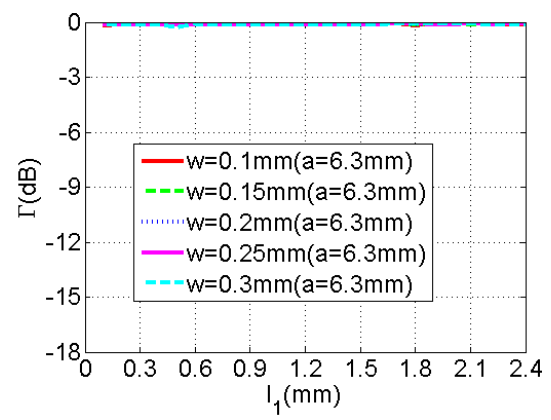
Fig. 6-17 Parametric study of *w* regarding the magnitudes of the reflection coefficients vs. l_1 for straight open-end stubs when (a) *a*=4.2mm (b) *a*=4.9mm (c) *a*=5.6mm, and (d) *a*=6.3mm.
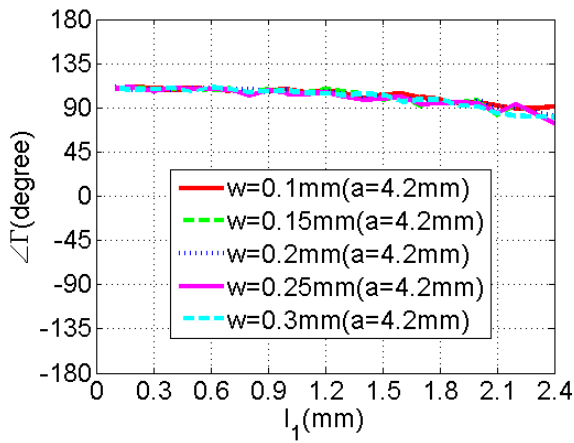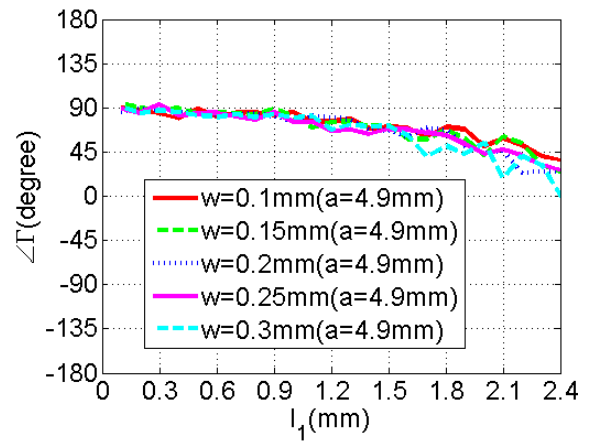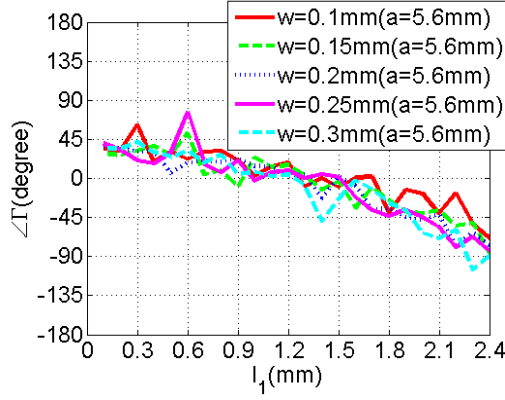
(c)
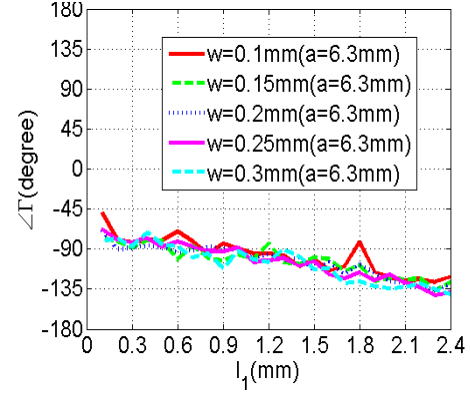
(d)

Fig. 6-18 Parametric study of *w* regarding the phases of the reflection coefficients vs. l_1 for straight open-end stubs when (a) *a*=4.2mm (b) *a*=4.9mm (c) *a*=5.6mm, and (d) *a*=6.3mm.

The magnitudes and phases of the reflection coefficients for the bent-line structure are displayed in Fig. 6-19 and Fig. 6-20, respectively. It is observed:

- For some certain values of a and l_1, the insertion loss is very high. For example, when *a*=4.2mm, the insertion loss is generally high for 0.5< l_1 <1mm;

- l_1 is still mainly responsible for the phase variation; however, *a* barely impacts the phase range anymore;

- *w* has little effect on the reflection coefficients;

(a)

(b)
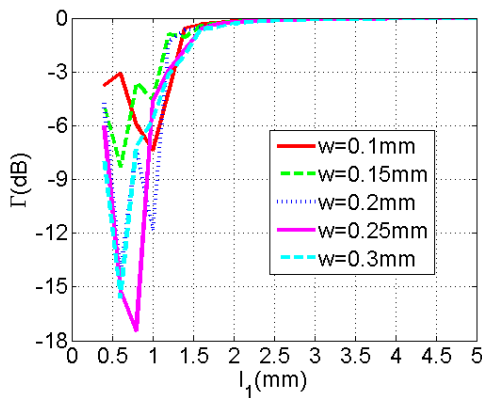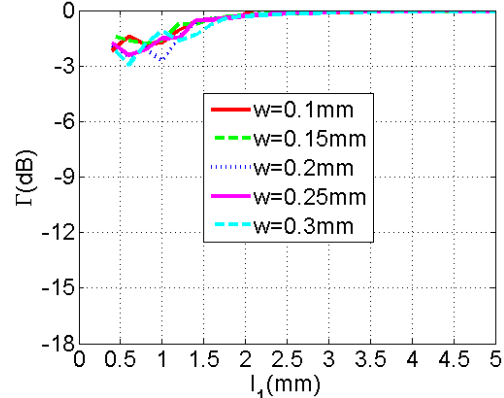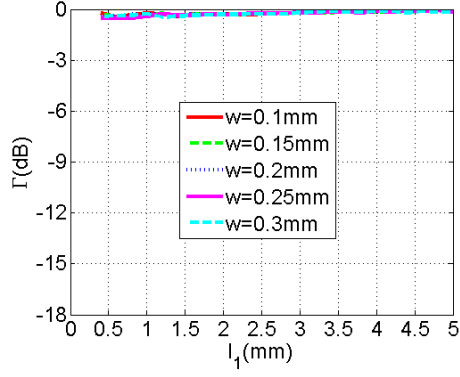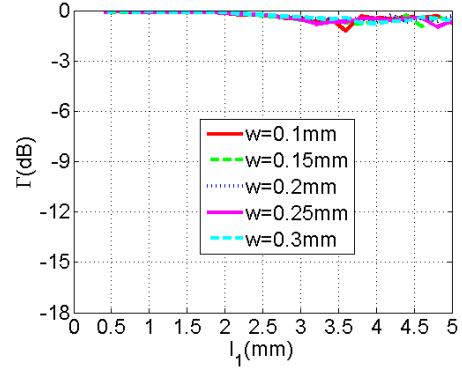
Fig. 6-19 Parametric study of *w* regarding the magnitudes of the reflection coefficients vs. l_1 for bent open-end stubs when (a) *a*=4.2mm (b) *a*=4.9mm (c) *a*=5.6mm, and (d) *a*=6.3mm.
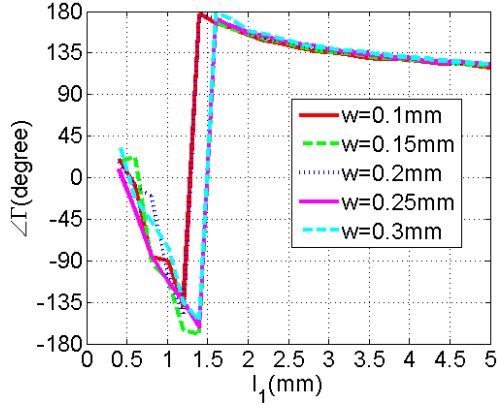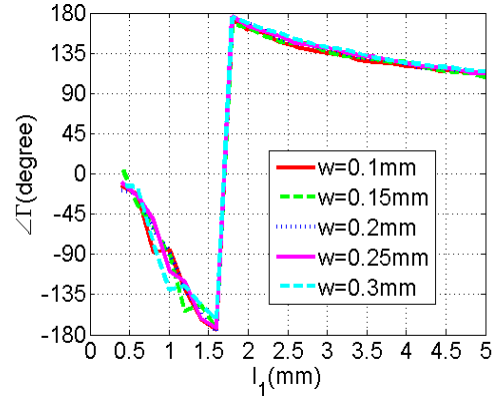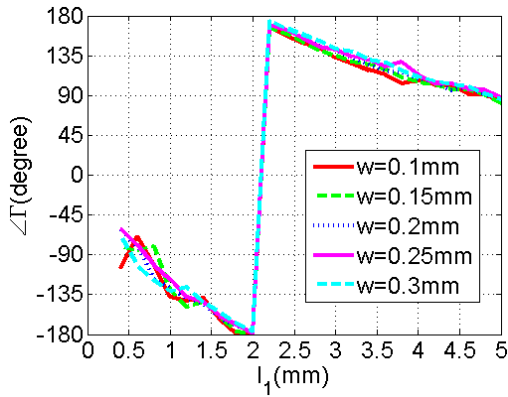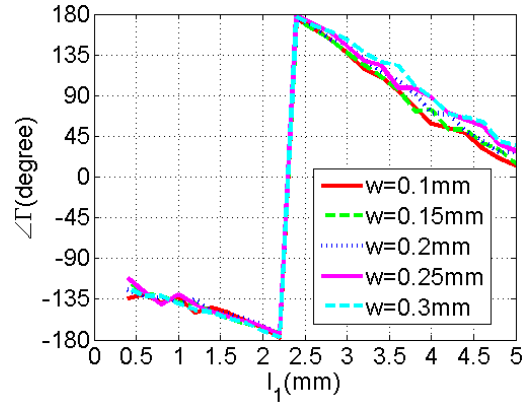
Fig. 6-20 Parametric study of *w* regarding the phases of the reflection coefficients vs. l_1 for bent open-end stubs when (a) *a*=4.2mm (b) *a*=4.9mm (c) *a*=5.6mm, and (d) *a*=6.3mm.

In order to explain the insertion loss, the co-polarization, cross-polarization, and absorption are investigated, and they are displayed in the same figure for a better view. It can be clearly seen from Fig. 6-21 (a), the cross-polarization is very high when $0.5 < l_1 < 1$mm, and the E-field distribution in Fig. 6-21 (b) suggests it is due to the bent structure.

(a)   (b)
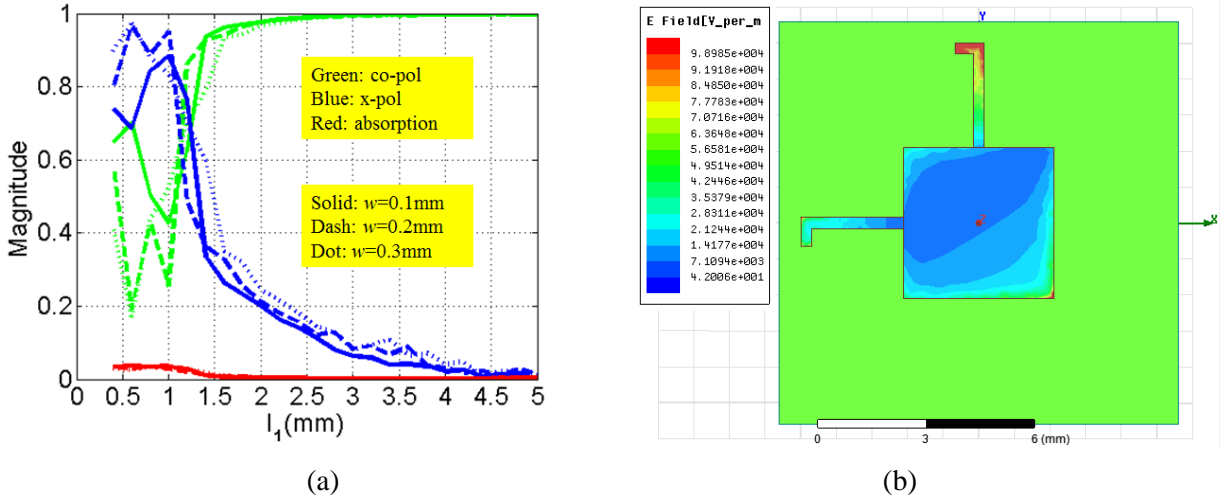
Fig. 6-21 (a) Magnitudes for co-polarization/cross-polarization/absorption when a=4.2mm for the bent case (b) The E-field distribution when a=4.2mm, l_1=0.8mm, and w=0.3mm.

Both the bent-line and straight-line structures are further investigated regarding whether they are good RRA element candidates in terms of their achievable phase difference and associated insertion loss. The magnitudes and phases of the reflection coefficients for the straight-line structure is displayed in Fig. 6-22 (a), which reveals that the optimization of l_1 permits one to achieve 180° phase difference with return loss roughly 0.5 dB. However, for the bent-line structure, as displayed in Fig. 6-22 (b), although 180° phase difference could also be reached, the insertion loss for the ON state is as large as 2 dB, which is too high.

(a)   (b)
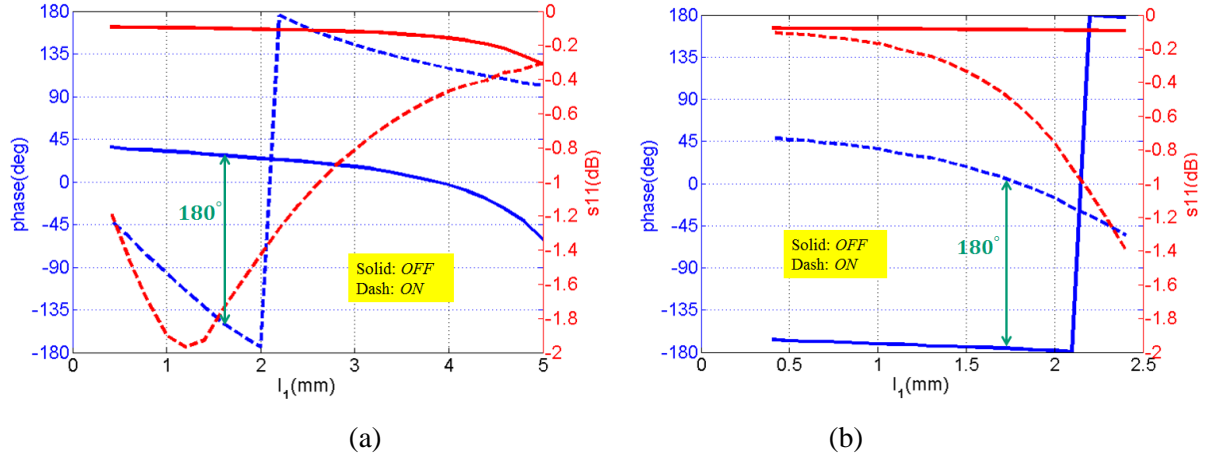
Fig. 6-22 The magnitudes and phases of the reflection coefficients for both ON and OFF states, a=5.6mm, for (a) straight structure and (b) bent structure.

Furthermore, in order to evaluate their capabilities of dual-polarization, the coherence between the TE and TM modes is evaluated. As displayed in Fig. 6-23 and Fig. 6-24, the magnitude and phase curves agree with each other very well for both straight and bent structuress, which suggests that such configuration is a good candidate for dual-linear polarizations.

(a)   (b)
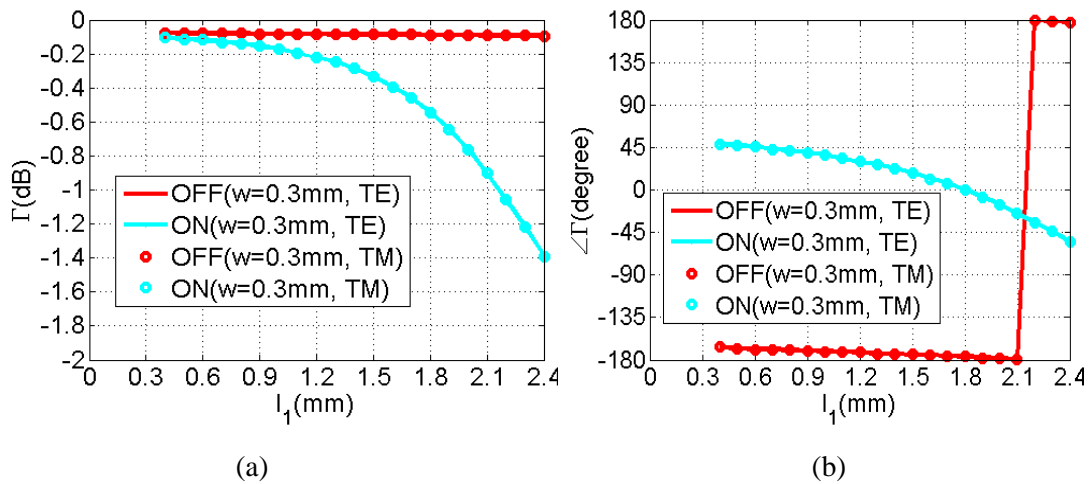
Fig. 6-23 The reflection coefficients for the straight case for both TE and TM modes in terms of (a) magnitudes and (b) phases.
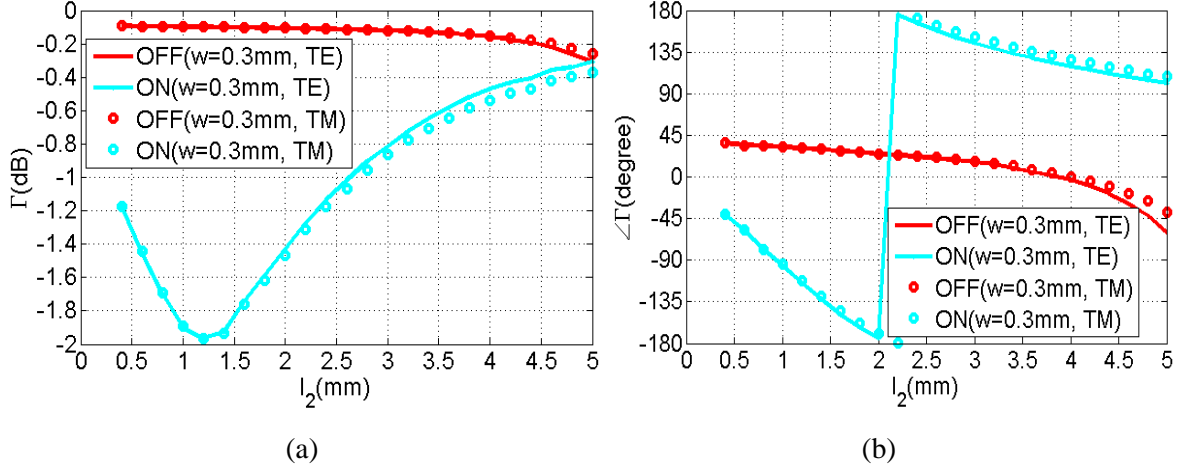
Fig. 6-24 The reflection coefficients for the bent case for both TE and TM modes in terms of (a) magnitudes and (b) phases.

Based on the previous study, it is concluded that: the integration and fabrication of such structure could be easily done with current PCB fabrication technique. More importantly, the insertion loss is low for this design, especially for the straight-line structure.

6.2.3 The 3rd Element Design

The reconfigurability principle of the 3rd design roots size reduction technique in the patch antenna. If a patch antenna is shorted on one edge, it acts as a quarter-wavelength structure, and the operation frequency consequently becomes half of its original one. When a partial shorting wall or a shorting pin is used instead, its fundamental resonant frequency could be further lowered.

Fig. 6-25 shows a prospective view of the 3rd element design. The top view and detailed view of the shorting part could be seen from Fig. 6-26. And all the geometry parameters are summarized in Table 6-9. It is noted that the blue-gray rectangular in Fig. 6-26 (b) represents the PIN diode based on the circuit pad layout suggestion from the manual. Besides, the choice of the dimensions of the via also follows the fabrication guidelines.
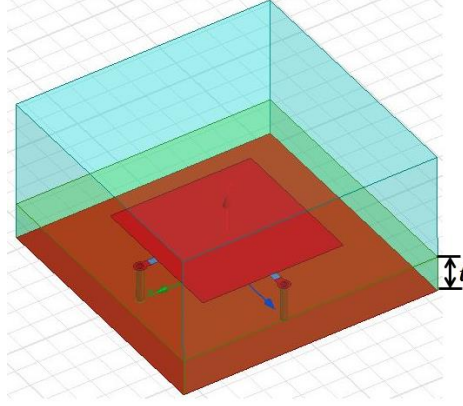
Fig. 6-25 The schematic of the unit configuration for the 3rd design.

| (a) | (b) |
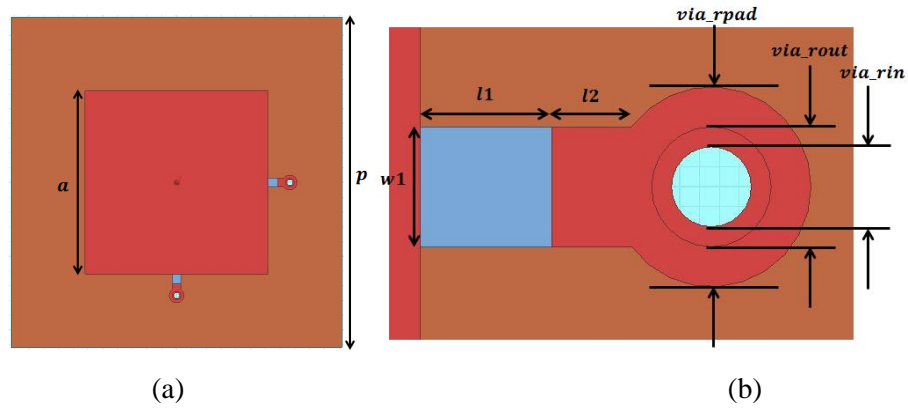
Fig. 6-26 (a) The top view of the unit and (b) the detailed view of the shorting part.

Table 6-9 Geometry parameters for the 3rd unit configuration

p	a	t	l_1	l_2	w_1	ε_{r1}
11.2 mm	phasing	1.58 mm	0.33 mm	0.2mm	0.33mm	2.55

The magnitude and phase of the reflection coefficients for ON/OFF states are displayed in Fig. 6-27, which shows that 180° phase difference is achievable with reasonable insertion loss less than 1 dB. Besides, in order to evaluate its suitability for a dual-linear polarization, the reflection coefficients for TE/TM modes are displayed in Fig. 6-28, which demonstrates a very good agreement between each other.
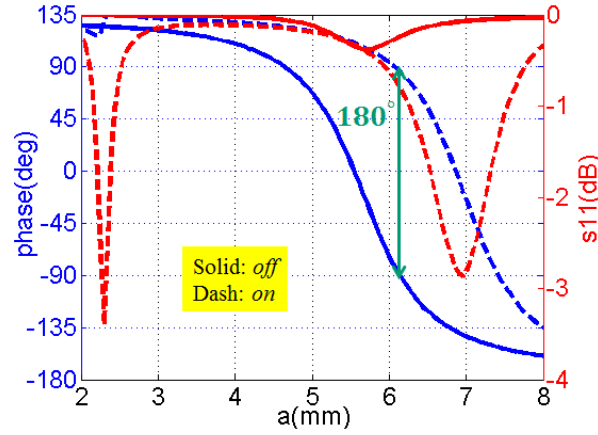
Fig. 6-27 The magnitude and phase of the reflection coefficients for ON/OFF states.

(a)   (b)
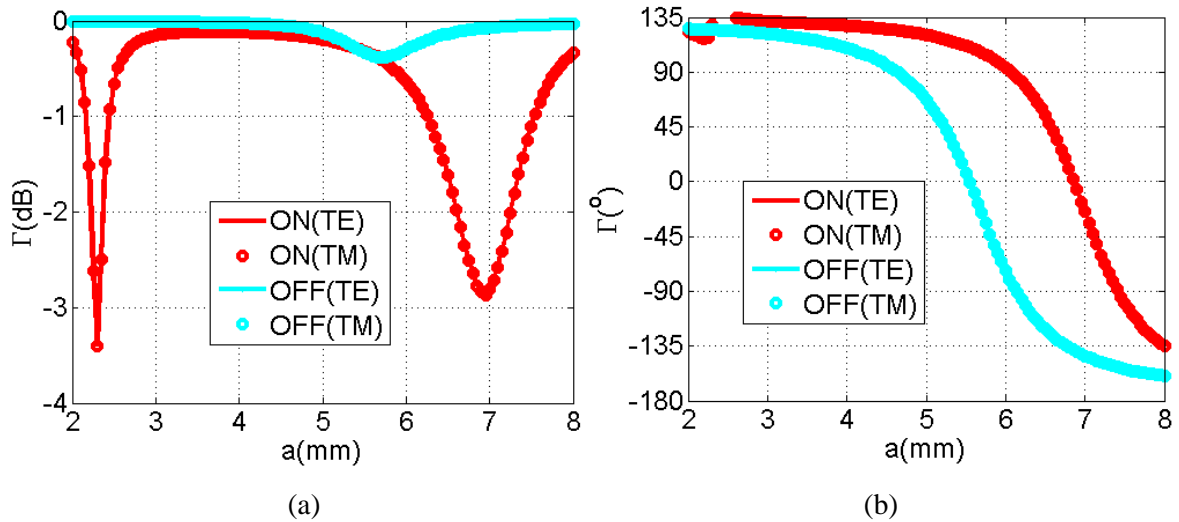
Fig. 6-28 The reflection coefficients for OFF/ON states in TE/TM modes, in terms of (a) magnitude, and (b) phase.

Based on the previous study, it is concluded that: the integration and fabrication of such structure could be easily done with current PCB fabrication technique. More importantly, the insertion loss is reasonable for this design.

Taking into account the possible biasing design, the 3rd one is possibly the simplest one among the three configurations.

142

6.3 Implementation of A 10 × 10 Reconfiguratble Reflectarray Antenna

6.3.1 Design of RF Choking Structures

For the purpose of demonstration, the 3rd design is chosen but simplified only for one linear polarization. However, in order to investigate the cross-polarization, TE and TM modes are included in the simulation, as displayed in Fig. 6-29.

(a)   (b)
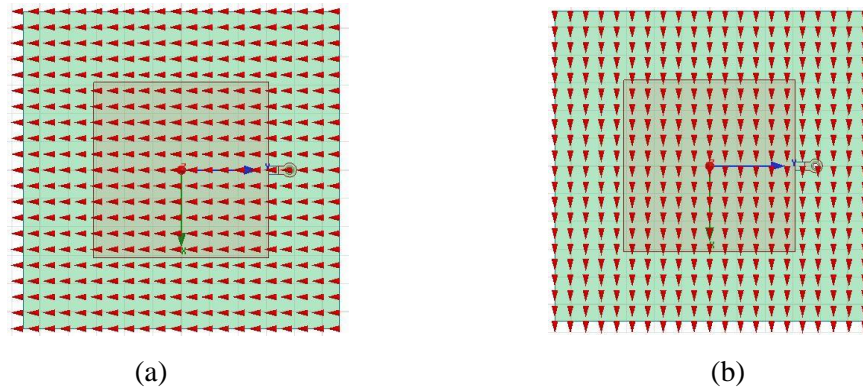
Fig. 6-29 Port field display in (a) TE mode, and (b) TM mode.

(a)   (b)
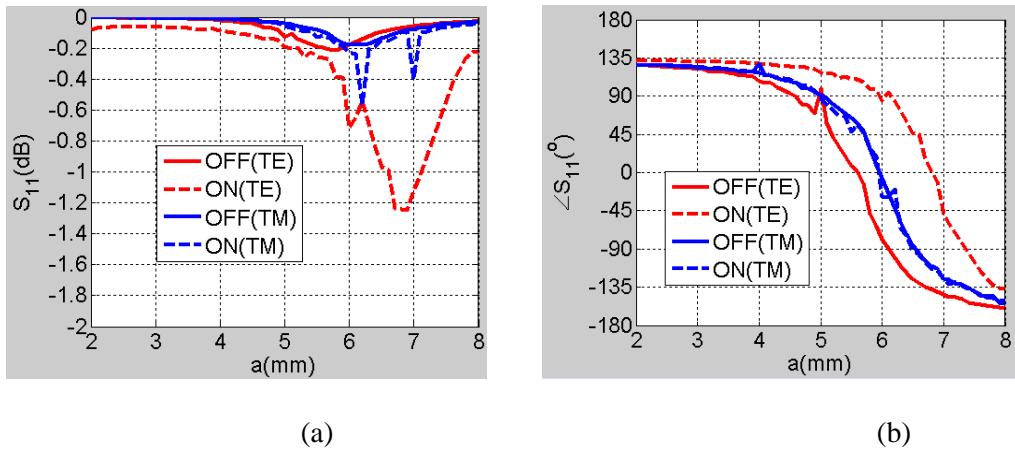
Fig. 6-30 The reflection coefficients for the bent case for both TE and TM modes in terms of (a) magnitudes and (b) phases.

The magnitudes and phases of the reflection coefficients are displayed in Fig. 6-30 (a) and Fig. 6-30 (b), respectively. It is observed:

- As expected, the switch on/off of the PIN diode barely changes the resonant frequency in TM mode;

- The phase difference between ON/OFF states achieves around 180° in TE mode when a=6mm;

- The insertion loss is less than 1 dB in TE mode when a=6mm;

    Three different configurations of DC biasing are integrated in the unit cell for comparison:

    For the 1st configuration, a through-via down to the bottom layer below the ground is added at the opposite edge of the shorted one to connect to the RF choke structure on the bottom layer, which is consisted of a quarter-wavelength transmission line and a quarter-wavelength radial stub. It is expected that when the DC control line is added it has little effect on the current distribution, thus barely changes the reflection magnitude and phase. The geometry of unit cell + RF choke is displayed in Fig. 6-31, while the one of unit cell + RF choke + DC line is demonstrated in Fig. 6-32.

(a)   (b)   (c)   (d)
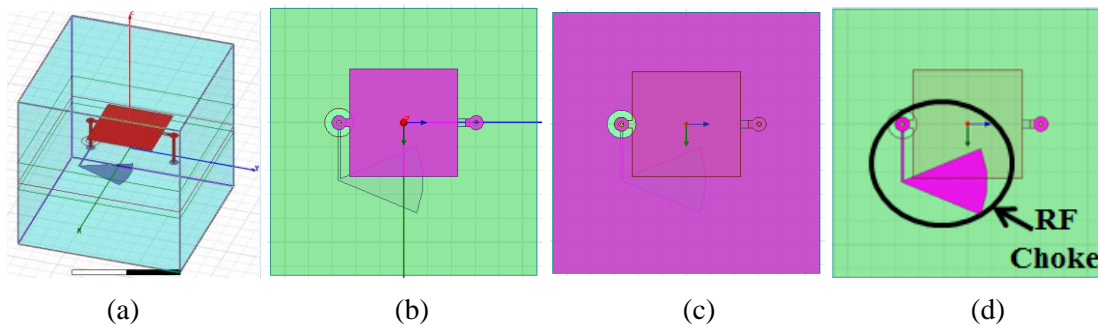
Fig. 6-31 Different views of unit with the 1st configuration + RF choke.

Fig. 6-32 Different views of unit with the 1st configuration + RF choke + DC line.

The phase and magnitude of the reflection phases for these two structures, with and without DC line, are displayed in Fig. 6-33. It is observed: return loss becomes significant when the RF choke structure is added and even bigger when the DC line is included; besides, there is big discrepancy between the reflection coefficients of these two structures.

Fig. 6-33 The reflection coefficients with and without DC line in TE mode in terms of (a) magnitudes and (b) phases.

For the 2nd configuration, some modifications are made based on the 1st configuration: the through- via is moved to the adjacent edge and the quarter-wavelength transmission line is moved to the top layer, aiming to decrease the effect of the through-via over the current

distribution on the patch. Similarly, the geometry of unit cell + RF choke is displayed in Fig. 6-34, while the one of unit cell + RF choke + DC line is demonstrated in Fig. 6-35.

| (a) | (b) | (c) |
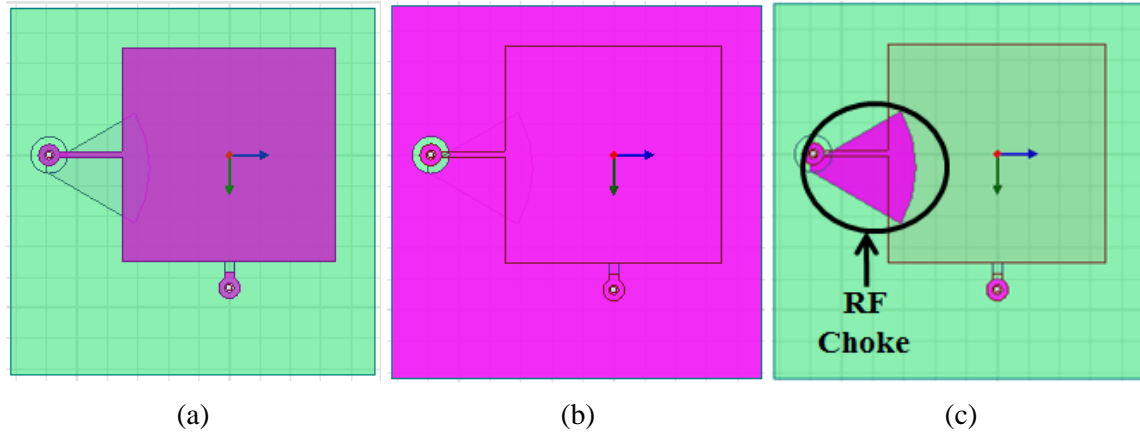
Fig. 6-34 Different views of unit with the 2nd configuration + RF choke.

| (a) | (b) | (c) |
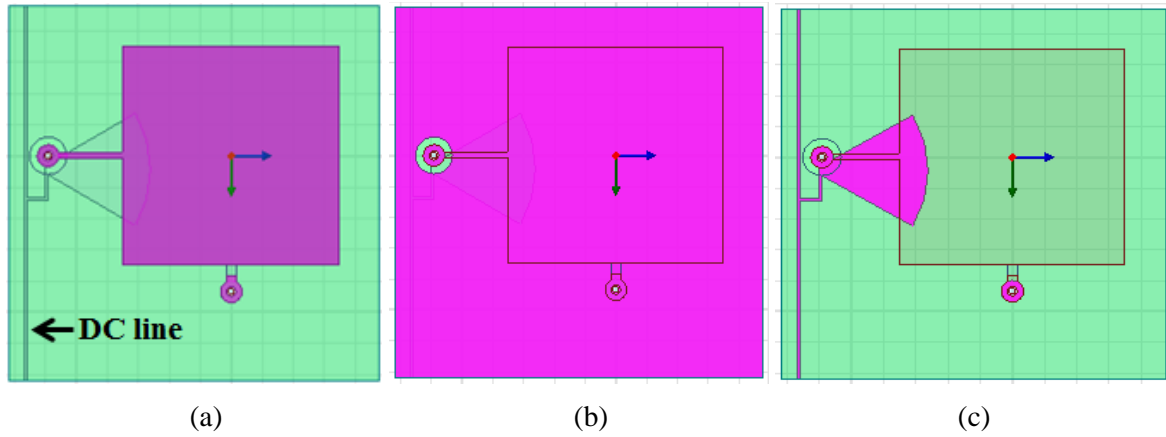
Fig. 6-35 Different views of unit with the 2nd configuration + RF choke + DC line.

The phase and magnitude of the reflection phases of these two structures, with and without DC line, are displayed in Fig. 6-36. It is observed: the return loss is greatly decreased after this RF choke structure is utilized; more importantly, the two curves between these two structures are in very good agreement with each other.
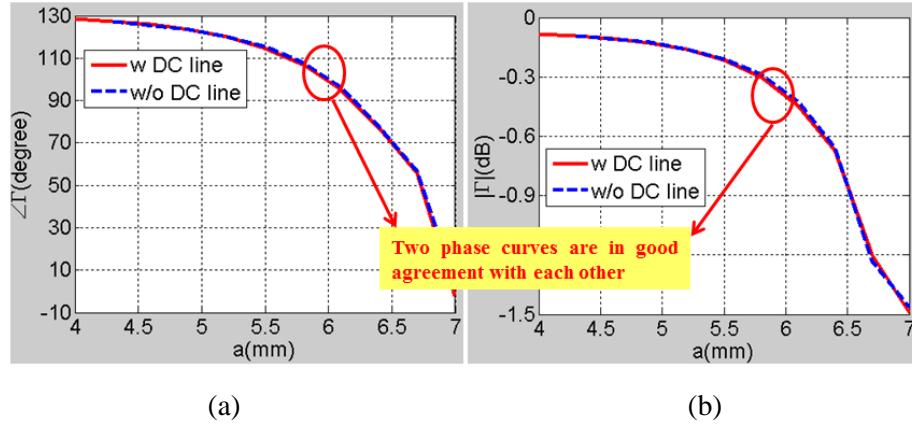
Fig. 6-36 The reflection coefficients with and without DC line in TE mode in terms of (a) magnitudes and (b) phases.

For the 3rd Configuration, some further modifications are made on the 2nd one: the length of the through-via is taken into account and a very short transmission line is added on the bottom layer; the length of the shorting edge and its parallel one are reduced to accommodate an optimized RF choke structure; furthermore, the DC line on the bottom layer is also changed for a better arrangement in an array environment later. Similarly, the geometry of unit cell + RF choke is displayed in Fig. 6-37, while the one of unit cell + RF choke + DC line is demonstrated in Fig. 6-38.

(a)　　　　　　　　　　(b)　　　　　　　　　　(c)
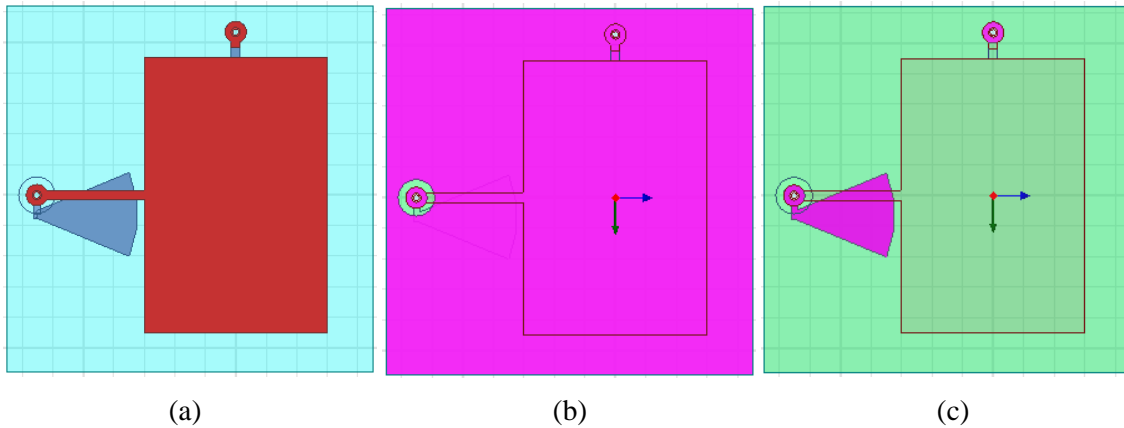
Fig. 6-37 Different views of unit with the 3rd configuration + RF choke.

(a)   (b)   (c)
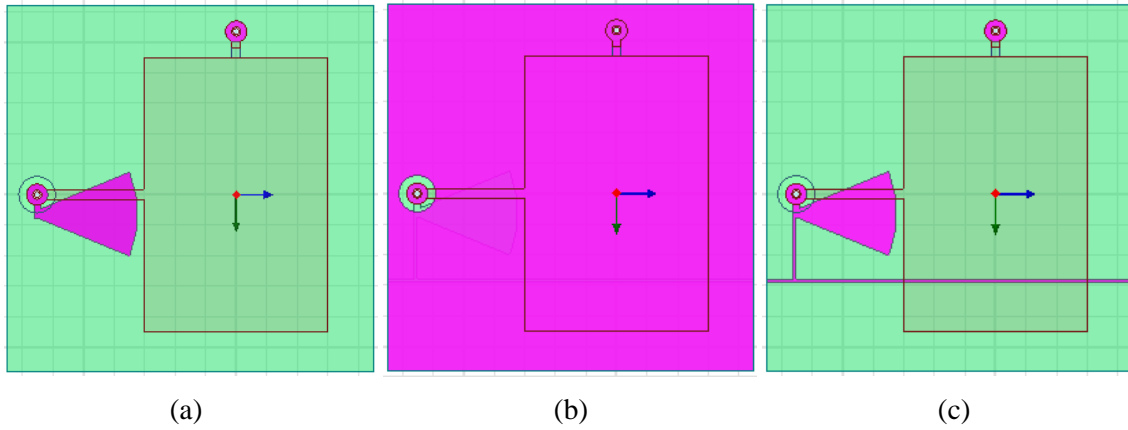
Fig. 6-38 Different views of unit with the 3rd configuration + RF choke + DC line.

The phase and magnitude of the reflection phases for these two structures, with and without DC line, are displayed in Fig. 6-39. It is observed: the return loss is increased for this RF choke design a little bit; however, the two curves for these two structures are in even better agreement with each other.

(a)   (b)
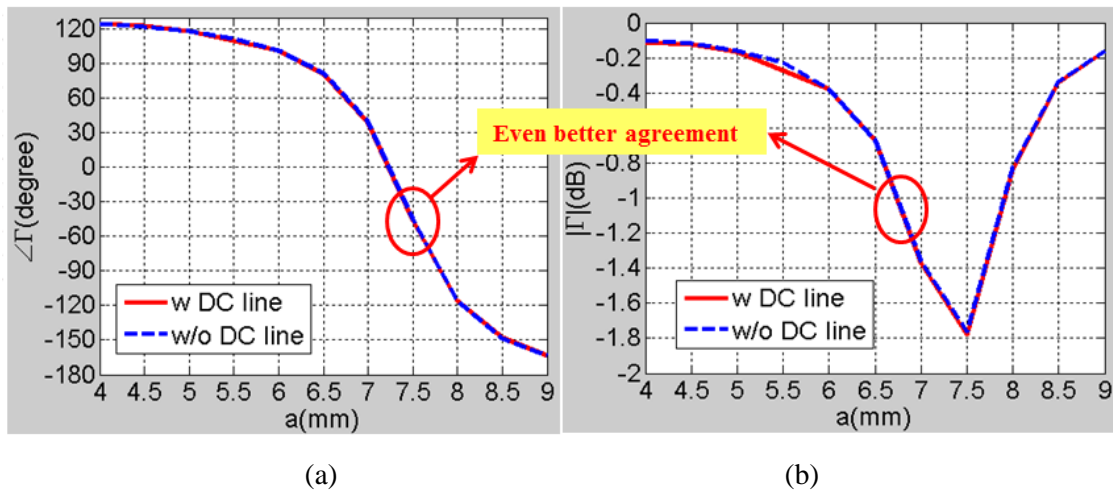
Fig. 6-39 The reflection coefficients with and without DC line in TE mode in terms of (a) magnitudes and (b) phases.

The 3rd configuration is carefully evaluated for the ON and OFF states, and the phases and magnitudes of the reflection coefficients are displayed in Fig. 6-40. Some of the phase differences between the ON and OFF states are tabled in Table 6-10. For example, when a=6.5 mm, the phase difference is roughly 193°, and the reflection loss is less than 0.7 dB.

(a)   (b)
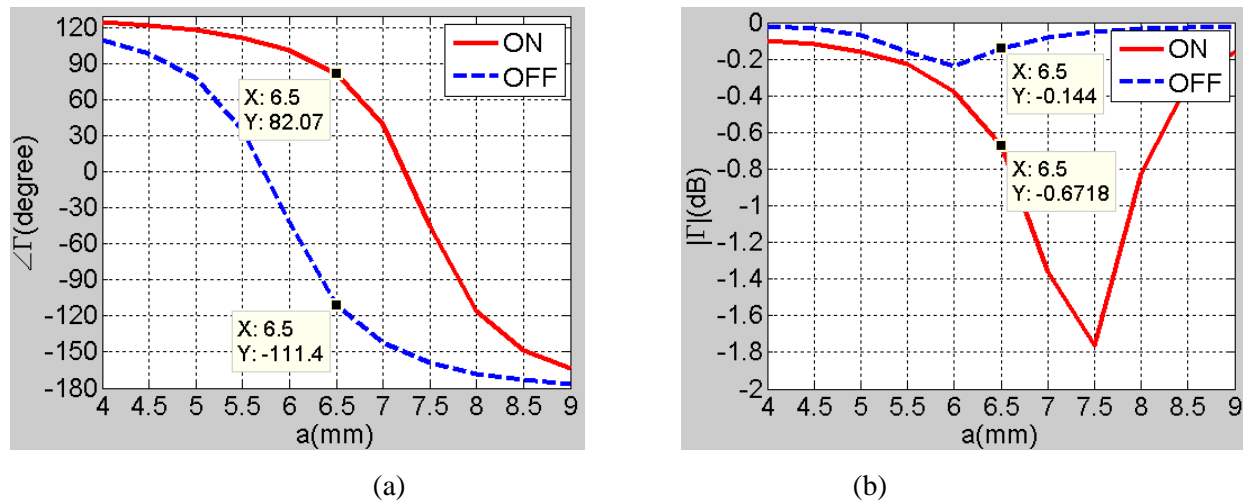
Fig. 6-40 The reflection coefficients for both ON/OFF states in terms of (a) magnitudes and (b) phases.

Table 6-10 Reflection phases achieved on ON/OFF states for different values of *a*

	6mm	6.5mm	7mm
ON	101°	82.0°	39.7°
OFF	-41.5°	-111.4°	-142.4°

6.3.2 Final Design for Practical Implementations

In order to further optimize the structure, a parametric study is made regarding *l*, and four different values of *l* are evaluated: 2.1 mm, 2.9 mm, 3.7 mm, and 4.1 mm. As displayed in Fig. 6-41, the phase curves of three different structures are compared: one with just shorted patch, one with shorted patch + RF choke, and one with shorted patch +RF choke + DC line.

(a)   (b)   (c)
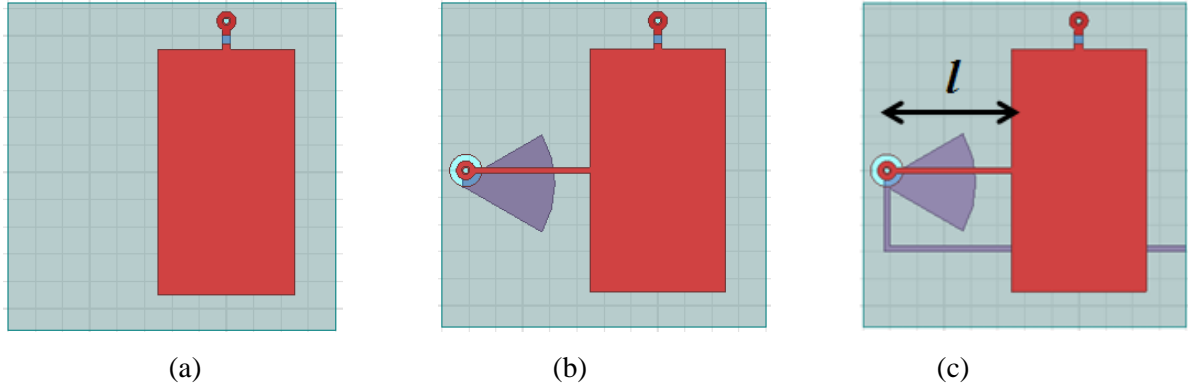
Fig. 6-41 The schematic of (a) shorted patch, (b) shorted patch + RF choke, and (c) shorted patch + RF choke + DC line.

The phase curves for different ls are shown in Fig. 6-42, and it is observed that l has little effect on the current distribution on the patch, and finally l is determined to be 2.9 mm. And the final configuration of the element is sketched in Fig. 6-43, and the equivalent circuit model of this element with RF choke is displayed in Fig. 6-44.
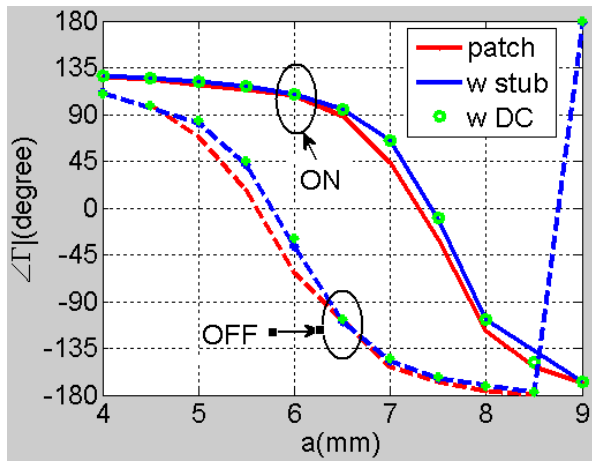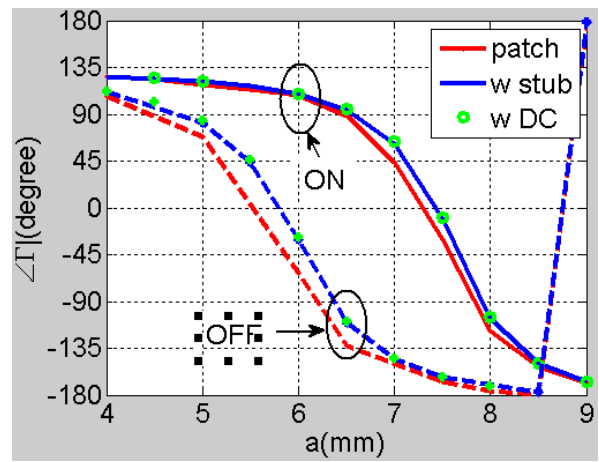
(a)   (b)
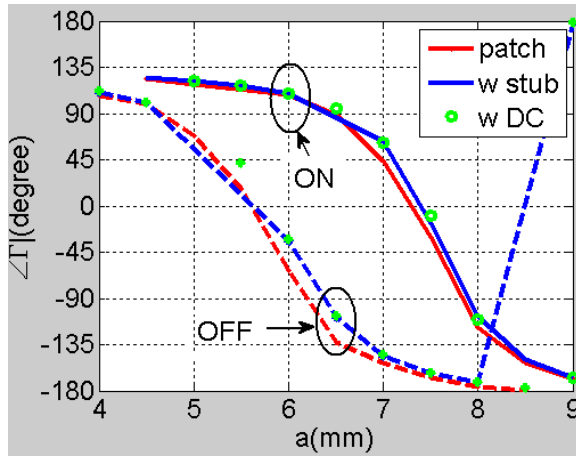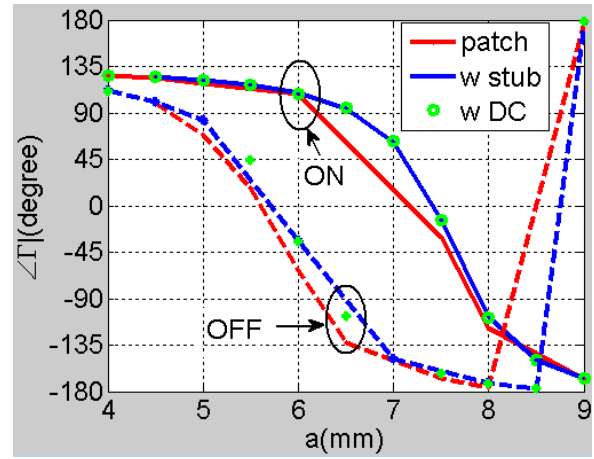
(c)   (d)

Fig. 6-42 The reflection coefficients for the bent case for both TE and TM modes in terms of (a) magnitudes and (b) phases.
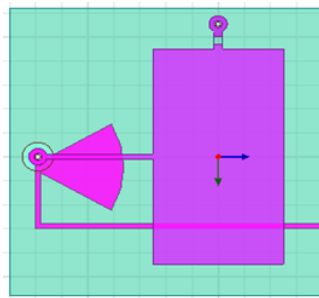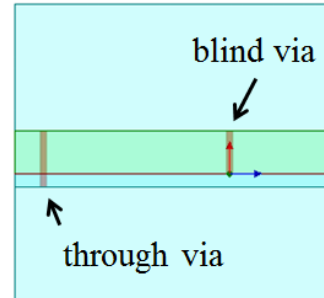
(a)   (b)

Fig. 6-43 (a) Top view and (b) side view of the optimized structured based on the 3rd biasing design.
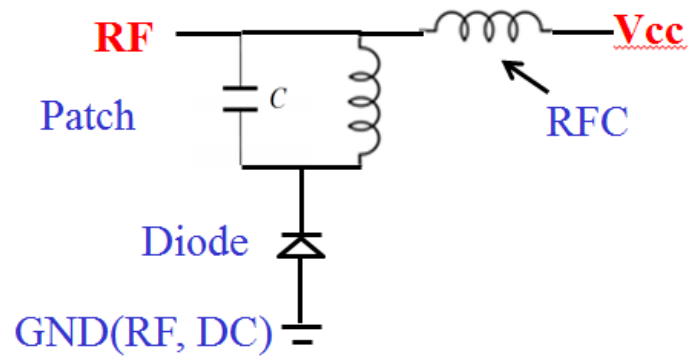
Fig. 6-44 Equivalent model for the optimized structure based on the 3rd biasing design.

The magnitude and phase of reflection coefficients for the optimized structure are displayed in Fig. 6-45. And it is observed that when *a*=6.25mm, the phase difference between the ON and OFF state is 180°, and the insertion loss is further decreased to be less than 0.5 dB.

(a)   (b)
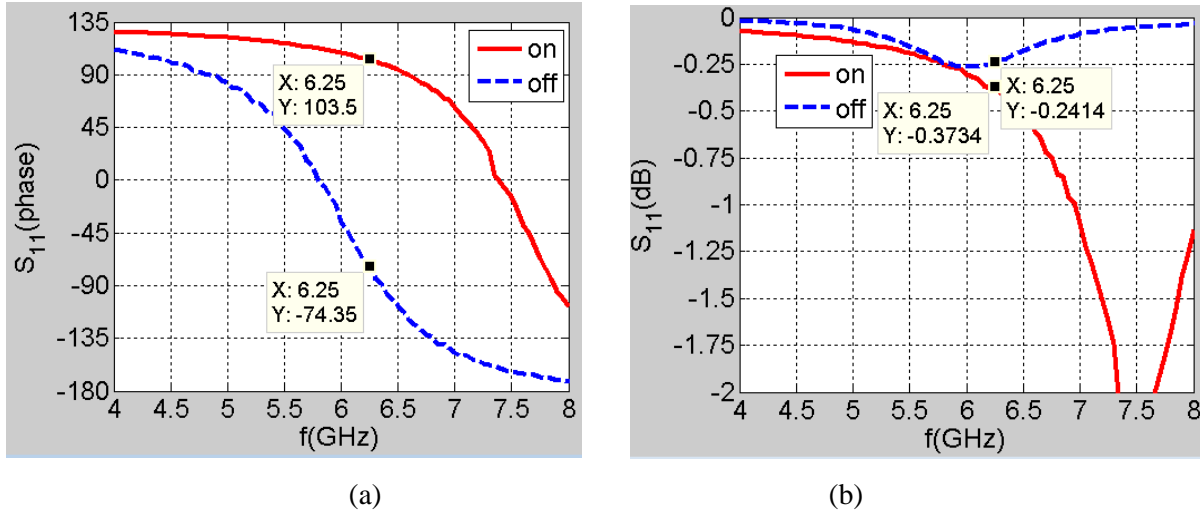
Fig. 6-45 The reflection coefficients for the optimized structure in TE mode in terms of (a) magnitudes and (b) phases.

Since a 10×10 RRA is going to be designed for the purpose of demonstration, the DC lines of all the elements are arranged in the way as shown in Fig. 6-46.
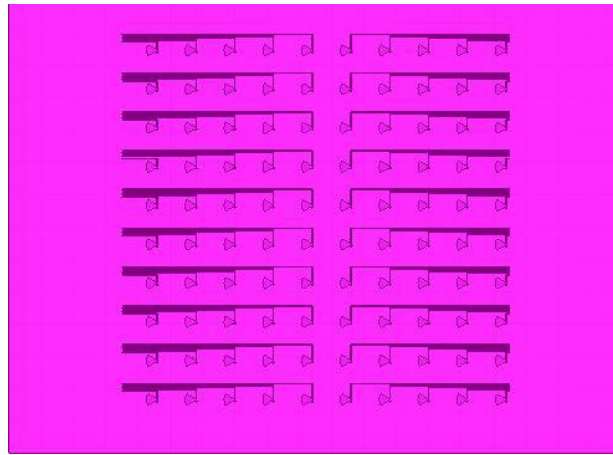
Fig. 6-46 Arrangement of DC lines on the bottom layer.

Therefore, as displayed in Fig. 6-47, totally five unit configurations with different *rfc_offset* will be included. It is desired that value of *rfc_offset* barely affects the reflection coefficients for both ON and OFF states, hence a parametric study regarding *rfc_offset* is performed and the results are shown in Fig. 6-48 and Fig. 6-49. It can be seen that all of the five curves in each figure are almost identical with each other, which validates the successful design of the RF choke design.

(a)   (b)   (c)   (d)   (e)
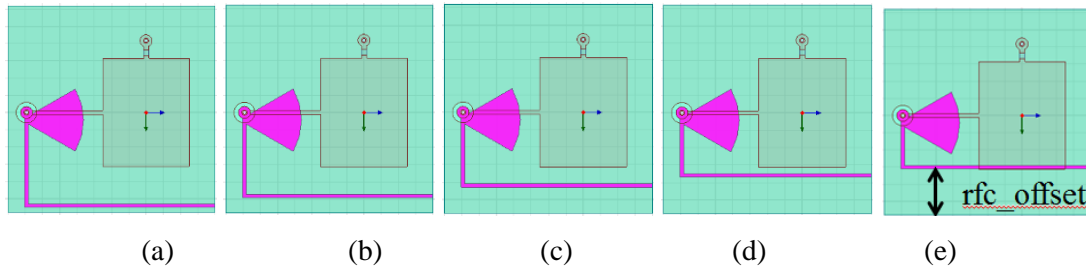
Fig. 6-47 The schematic of the optimized structure with (a) rfc_offset = 0.5 mm, (b) rfc_offset = 1.1 mm, (c) rfc_offset = 1.7 mm, (d) rfc_offset = 2.3 mm, and (e) rfc_offset = 2.9 mm.

(a)   (b)
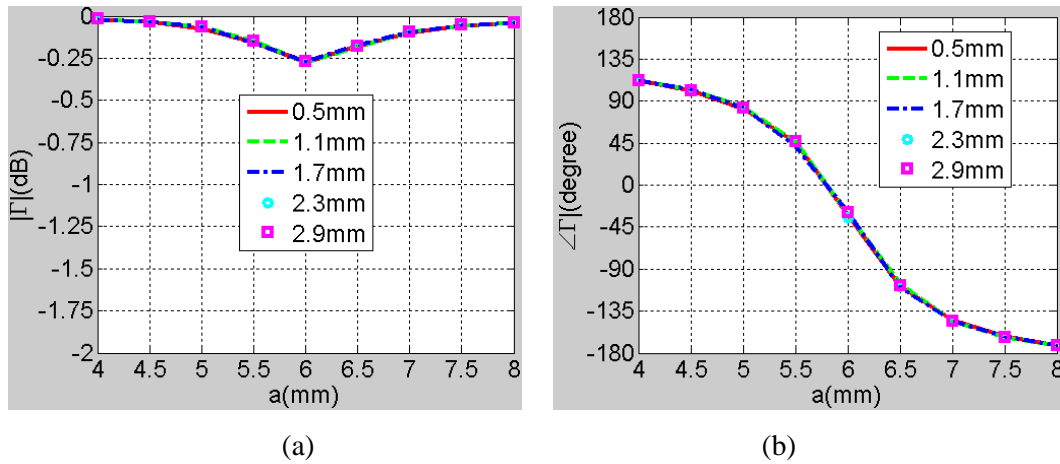
Fig. 6-48 The reflection coefficients for OFF state in terms of (a) magnitudes and (b) phases.

153

(a)   (b)
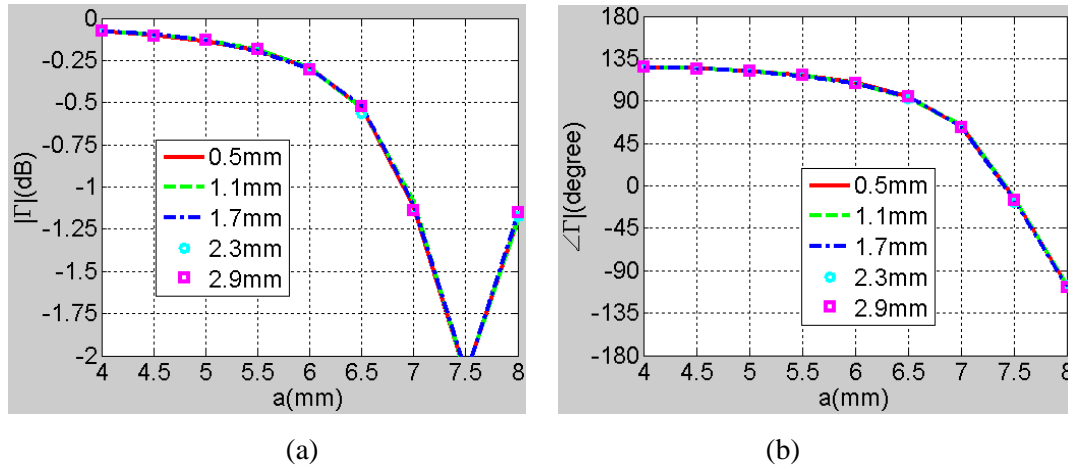
Fig. 6-49 The reflection coefficients for ON state in terms of (a) magnitudes and (b) phases.

One more modification is made after the fabrication technicians are consulted. As shown in Fig. 6-50, there are totally three kinds of vias in the PCB fabrication: through-via, blind-via, and buried- via, and the 1st one is much economic than the last two.

(a)   (b)   (c)
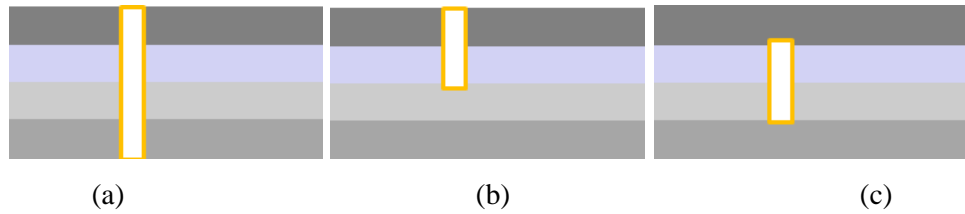
Fig. 6-50 Three kinds of vies: (a) through via, (b) blind via, and (c) buried via.

(a)   (b)
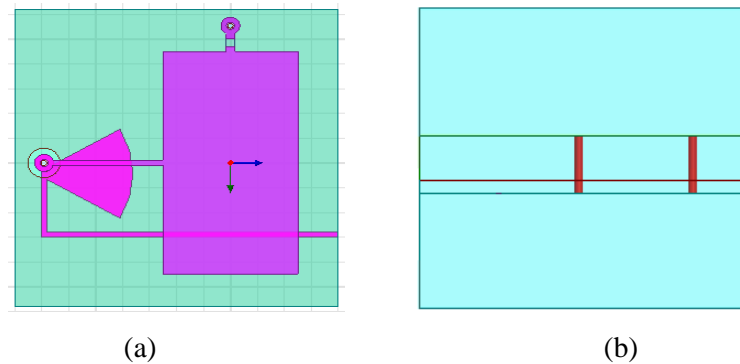
Fig. 6-51 (a) Top view and (b) side view of the finally optimized structured based on the 3rd biasing design.

Therefore, the blind-via is substituted with through via. Fig. 6-51 displays the modified structure, and the results of the structures with blind and through vias are compared in Fig. 6-52 and Fig. 6-53, which shows a very good agreement between these two.

(a) (b)
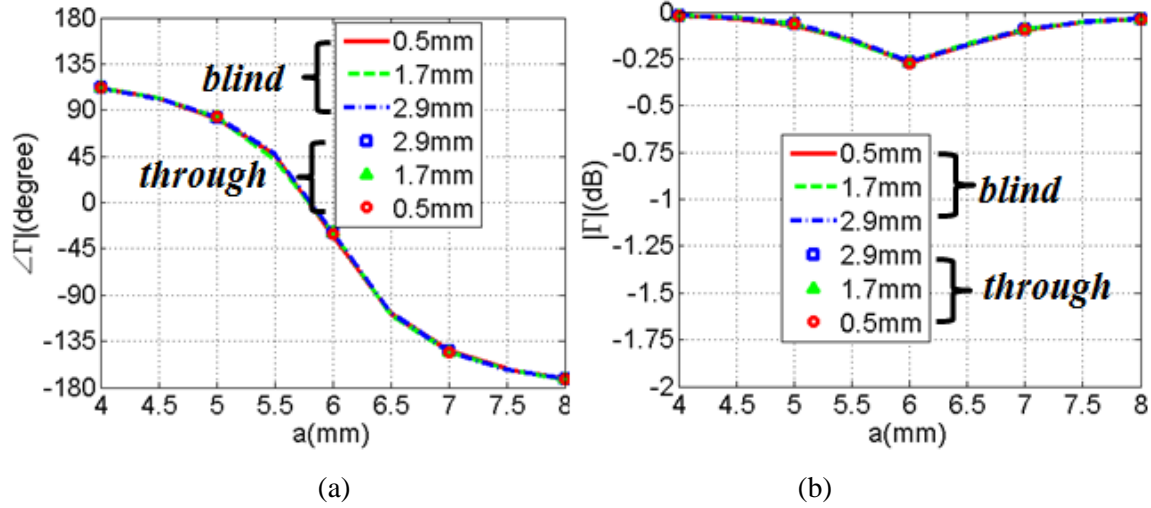
Fig. 6-52 The reflection coefficients for the OFF state between the two structures with blind and through vias in terms of (a) phases and (b) magnitudes.

(a) (b)
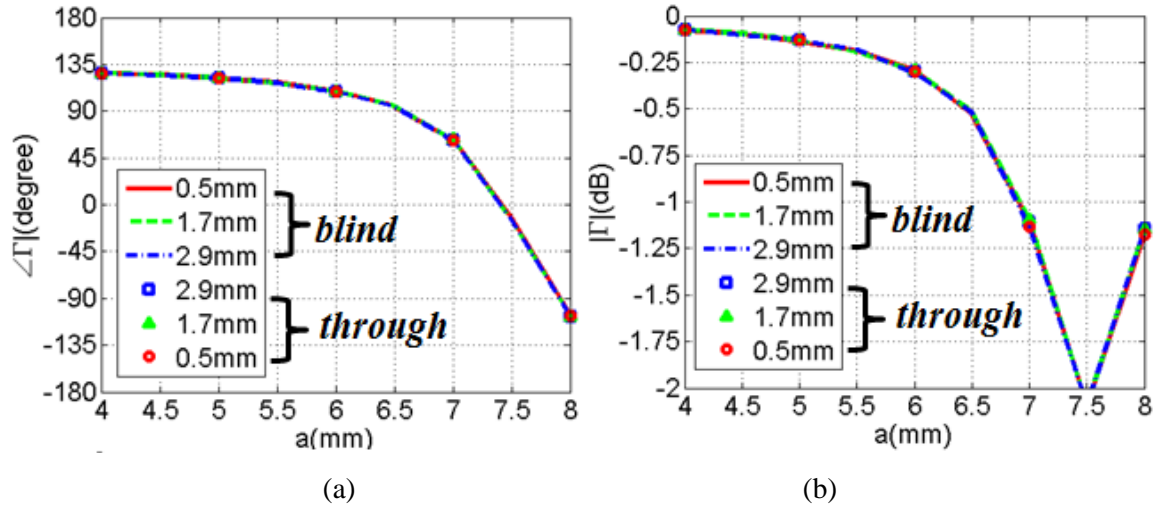
Fig. 6-53 The reflection coefficients for the ON state between the two structures with blind and through vies in terms of (a) phases and (b) magnitudes.

6.3.3 The Simulated Results of 10×10 RRA

For 1-bit design, there are only two phase options, α_1 and α_2. Therefore, elements needs to be divided into two groups, one with phase α_1 and the other with α_2. The dividing criteria depends on two boundary values φ_1 and φ_2 whose difference is normally 180°. Elements whose φ_{rmn} are within $[\varphi_1, \varphi_2]$ will be classified to the α_1 group, while others go to the α_2 group.

Assuming the feed position (x, y, z) is (0 mm, -51.3 mm, 110mm), the radiation patterns of the 1 bit 10×10 RRA are calculated using array theory. Six progressive scanning angles are studied, covering from 0° to 50° off broadside at a step of 10°. The gains obtained at different angles for the 1-bit reflectarray are compared with the ideal case in Fig. 6-54. It is observed that this 1-bit quantization causes an average reduction of 3.5 dB in gain, and particularly at 50° the QL is 5 dB.

Besides, the radiation patterns are also calculated for comparison, and they are displayed in Fig. 6-55. It is observed that the side lobe levels were raised a lot after the 1-bit device is added in each cell.
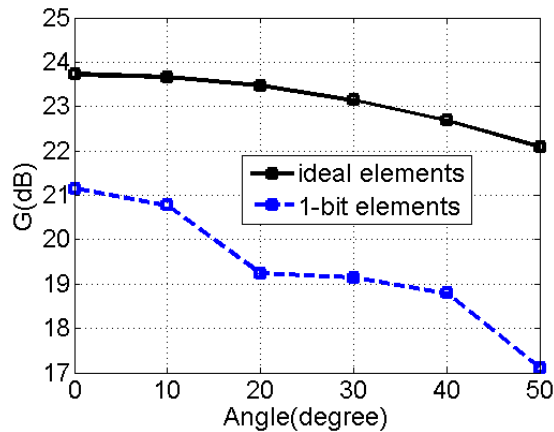
Fig. 6-54 Comparison of reflectarrays consisted of ideal and 1-bit elements in terms of gain.

(a)   (b)
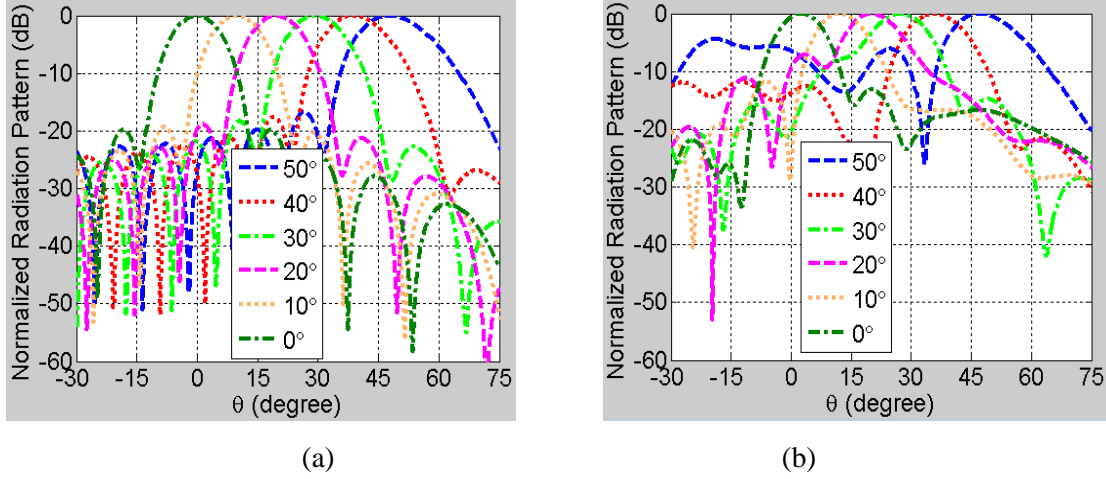
Fig. 6-55 Normalized radiation pattern of a RRA consisted of (a) ideal elements, and (b) 1-bit elements.

It is noticed from (6.1) that φ_{rmn} is somehow dependent on the reference phase $\Delta\varphi$, which could potentially optimize the RRA performance. In order to show its effect, two designs are proposed, with $\Delta\varphi$ being 0° and 40°, respectively. The comparison is made in terms of gain and radiation patterns, and the results are shown in Fig. 6-56 and Fig. 6-57. It is observed that the design with $\Delta\varphi$ being 40° have a much better performance in terms of both gain and radiation patterns.
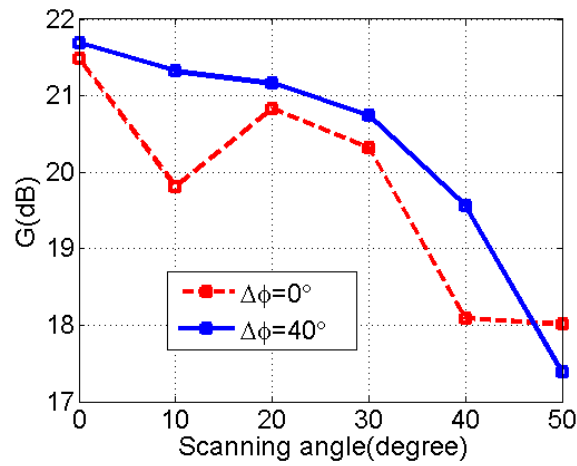
Fig. 6-56 Comparison of 1-bit reflectarray designs designed with $\Delta\varphi = 0^o$ and $\Delta\varphi = 40^o$.
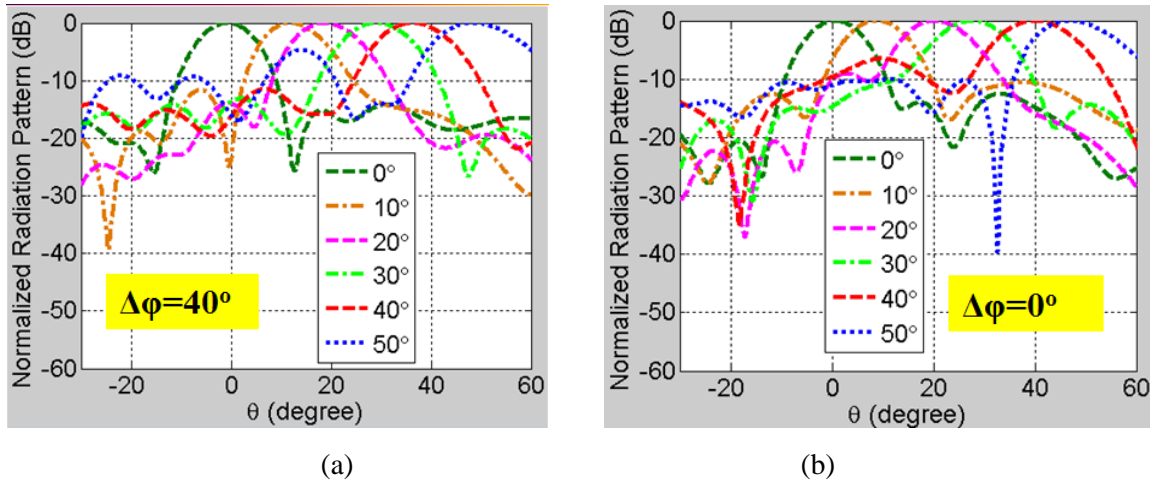
Fig. 6-57 Normalized radiation pattern of a RRA consisted of (a) ideal elements, and (b) 1-bit elements.

6.4 Fabrication of 10 x 10 Reconfigurable Reflectarray

6.4.1 Generation of the Fabrication Mask

The fabrication masks for this RRA include three layers, one for the patch layer, one for ground layer and the last one for bottom layer, all of which need to be assembled in Altium to facilitate the further fabrication. Since the masks are too complicated to be finished in Altium, these three layers are firstly generated in HFSS and exported in the DXF format, then imported and exported as DXF files again via the software AutoCAD, and finally imported in Altium. It is worthwhile mentioning that Altium (build 9.4.0.20159) could not recognize the DXF files directly exported from HFSS. Fig. 6-58 displays the imported DXF files in Altium, and it is noticed that there are no solid shapes but just contours, which needs to be filled later in as follows.

(a)	(b)
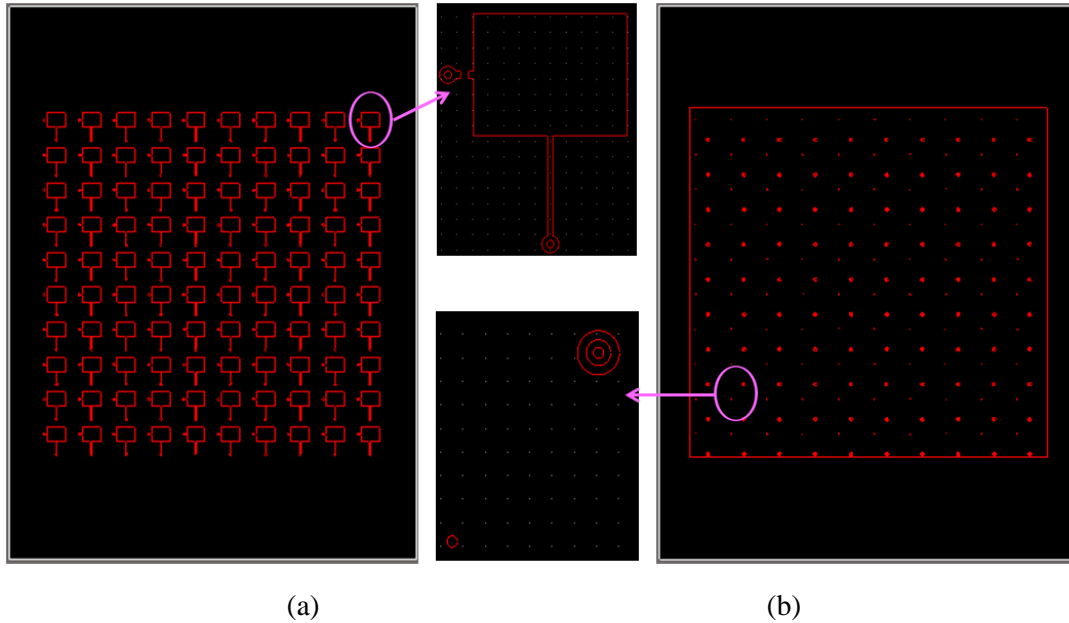
Fig. 6-58 Display of the imported DXF files for the (a) top layer and (b) middle layer.

In a word, all the contours included in the imported DXF file essentially serve the purpose of indicating the position, and more work needs to be done using Altium to specify the solid regions and different vias, which will be shown in the following:

Step 1: the layer stack needs to be defined at first.
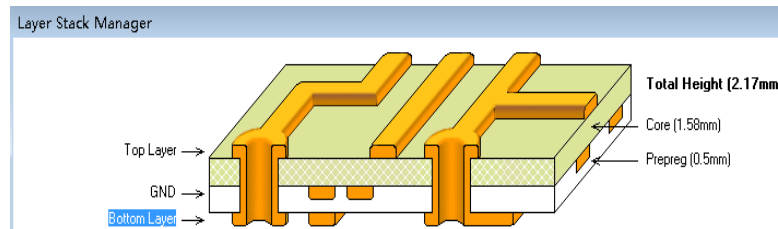
Fig. 6-59 Display of the layer stack in Altium.

Step 2: the DXF files for the top and bottom layers are imported at first, as shown in Fig. 6-60, and it is noticed that different layers are drawn in different colors.
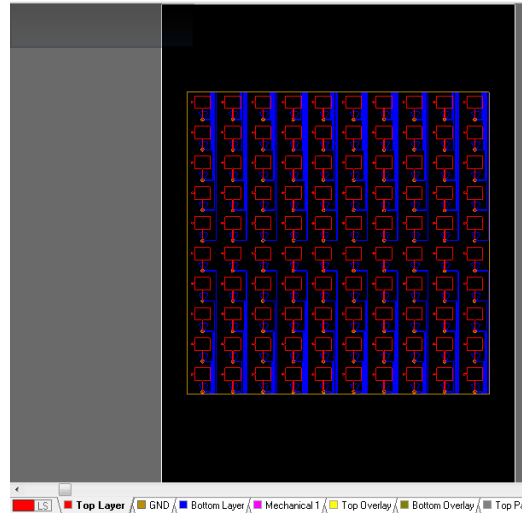
Fig. 6-60 Display of the imported top and bottom layers in Altium.

Step 3: as shown in Fig. 6-61, the DXF for the top layer is processed. The function *solid region* is used for the patch and transmission lines, while vias are directly added from the Altium library for the through vias. It is noticed that at this moment, nothing is done to the shorting vias yet which starts from top layer and ends at bottom layer.
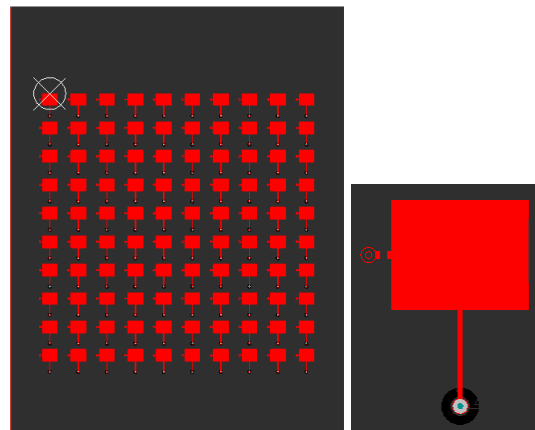
Fig. 6-61 Display of the processed top layer.

Step 4: as demonstrated in Fig. 6-62, the bottom layer is processed. The function *solid region* is used for the radial stub and the transmission lines, connectors are added directly from

160

the Altium library. In addition, the function *interactive routing connection* is utilized to connect the DC lines and the connectors.
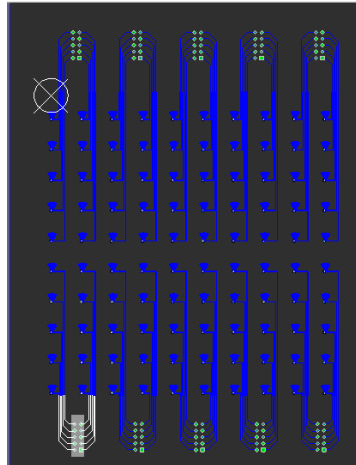
Fig. 6-62 Display of the processed bottom layer.

Step 5: as displayed in Fig. 6-63, the function *polygon pour* is used to spread the copper on the ground, and the function *clearance check rule* is used to build the clearance ring of the through vias on the ground. It is noticed that, the shorting pins still have not been specified in our structure.
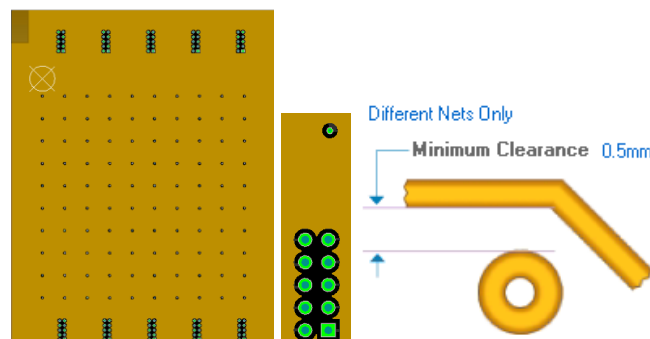
Fig. 6-63 Display of the ground layer processed with the clearance check rule.

Step 6: as displayed in Fig. 6-64, the shorting vias are added, and their start layer and end layer should be specified in the properties. As long as the function *polygon pour* is not applied to the ground layer again, there shall be no clearance gap between the shorting vias and the ground, and this is the trick. Fig. 6-65 displays the view of the multi-layer structure.
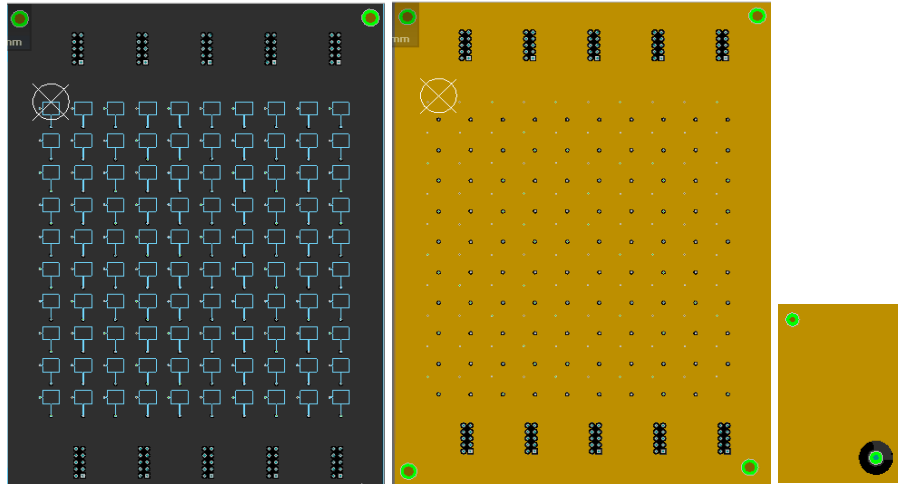
Fig. 6-64 Display of the ground layer including both the shorting pins and through vias.
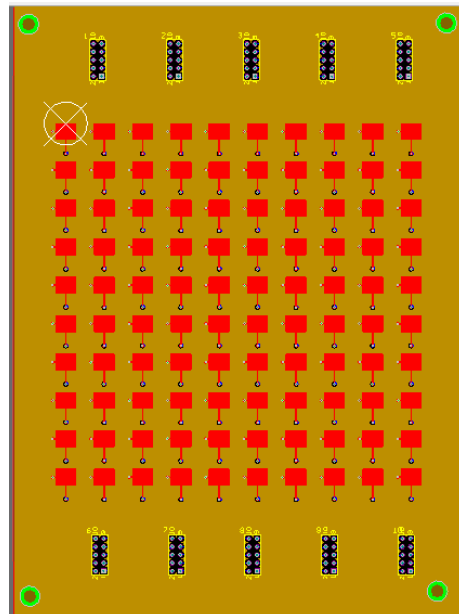
Fig. 6-65 The view of the multi-layer structure.

6.4.2 Generation of the Soldering Mask

The last thing we need to do is to generate the solder pad files. The operation steps are as below:

- Click File -> New -> Library -> PCB Library, and a new window will be opened for the new device;

- Click Tools -> IPC Footprint Wizard and choose CHIP as the component type, as shown in Fig. 6-66; (IPC stands for the Association Connecting Electronics Industries, which was founded in 1957 as the Institute for Printed Circuits)
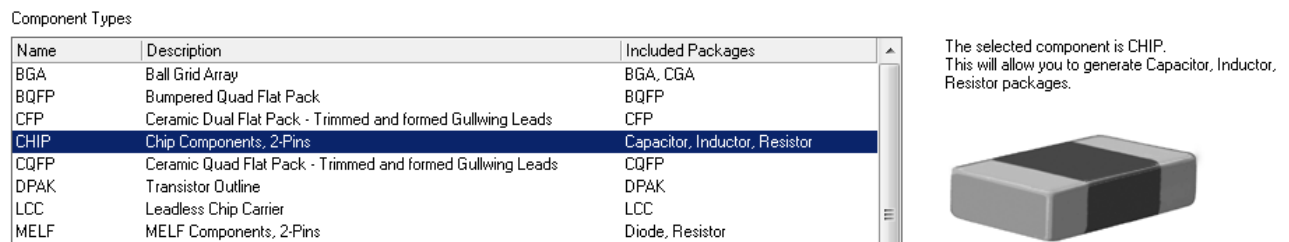
Fig. 6-66 The IPC footprint wizard in Altium.

- Specify the dimension following the wizard. The finished component is as shown in Fig. 6-67, and it is them added in the project library.
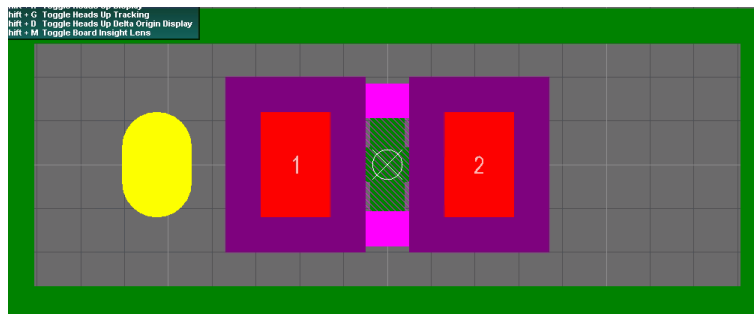
Fig. 6-67 The finished footprint in Altium.

- Add the generated footprint in the *Top Solder* layer, and the generated soldering mask is shown in Fig. 6-68.
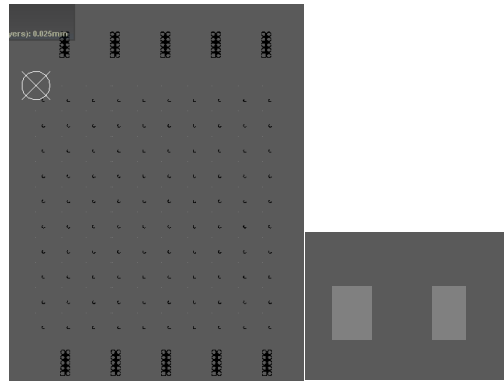
Fig. 6-68 The generated soldering mask in Altium.

6.4.3 Soldering Technique

Since the PIN diodes are so small ($0.6 \times 0.3 \ mm^2$) that it is quite inefficient to solder all of them manually, the programmable table reflow oven is used to do the soldering job. Fig. 6-69 is a picture of the reflow oven and the RRA with soldered PIN diodes is shown in Fig. 6-70.

Fig. 6-69 The programmable table reflow.
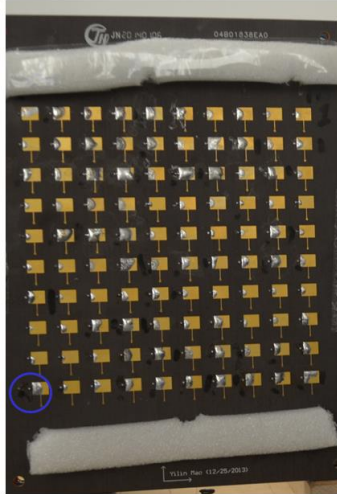
Fig. 6-70 The fabricated RRA with solder PIN diodes.

6.4.4 The Control GUI

A small software is developed to control the states of all the PINs, and the GUI is shown in Fig. 6-71. The loading procedure is very simple: import the configuration file and confirm the operation after it is made sure that the phase distribution is as expected.
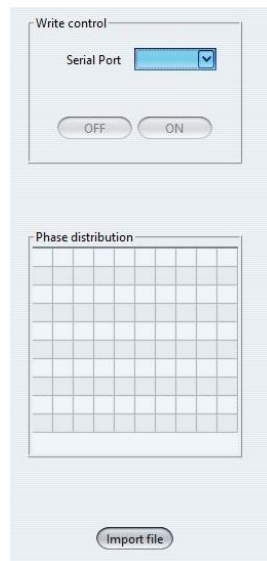
Fig. 6-71 The GUI of the control software.

6.5 Measurement Results and Analysis

6.5.1 Far-field Measurement

6.5.1.1 Measurement Setup

The measurement is conducted in a compact anechoic chamber using the far-filed method. As displayed in Fig. 6-72, the RRA is placed on top of a big pillar to receive the impinging wave which could be regarded as plane wave.

Fig. 6-72 The anechoic chamber.

The experiment of this 10×10 RRA is configured as displayed in Fig. 6-73 (a).

- Feed position: x=0 mm, y=-110 mm, z=143mm. When the feed position is selected, the oblique incident angles on each unit and the distance between feed and the reflectarary are consequently determined. Therefore, the choice of the feed location is somehow a tradeoff:
  - Oblique angle: large oblique angles leads to large phase errors, while small ones result in large blockage;

- Distance: a longer distance between the feed and the reflectarray leads to lower spillover efficiency, while a shorter one will place the reflectarray in the near-field range of the feed;

And the corresponding feed illumination on the reflectarray is displayed in Fig. 6-73 (b).

(a)   (b)
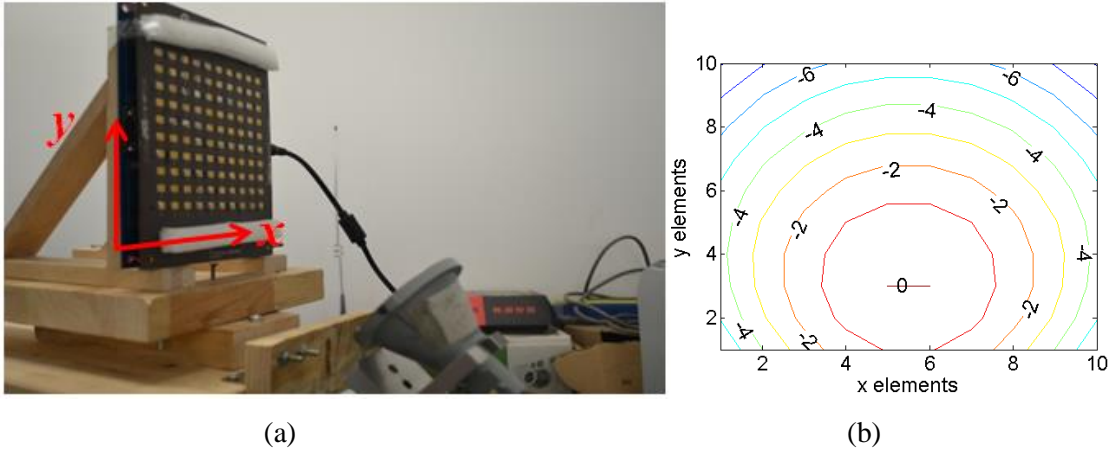
Fig. 6-73 (a) The setup configuration to measure the RRA (b) Feed illumination on the reflectarray (contour in dB).

- Polarization: linear polarization, in x direction

- Measured plane: only the radiation pattern in PP1 is measured in practical operation

- Measured frequency range: 12 GHz: 0.005 GHz:13 GHz

- Measured angular step: 1°

- Desired phase distribution:

As shown in Fig. 6-74, five different configurations are implemented in terms of the compensation phase, with the main beam targeting at 0°, 10°, 20°, 30°, and 40°. It is worthwhile mentioning that these practically implemented phases are calculated based on the optimization of $\Delta\varphi$.

|(a)|(b)|(c)|(d)|(e)|
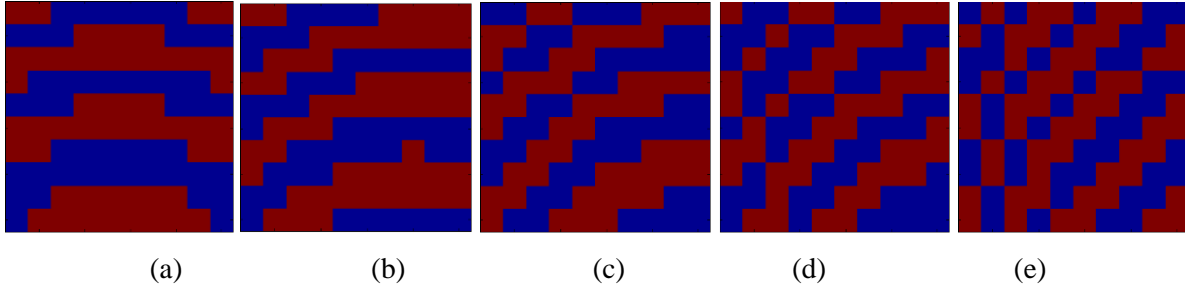
Fig. 6-74 The implemented element phases for the RRA when the beam is steered to (a) 0°, (b) 10°, (c) 20°, (d) 30°, and (e) 40°.

6.5.1.2 Measurement Results

All the measured radiation patterns for these five configurations are displayed in Fig. 6-75, and the comparison with the simulation results are demonstrated in Fig. 6-76, as well as tableted in Table 6-11.
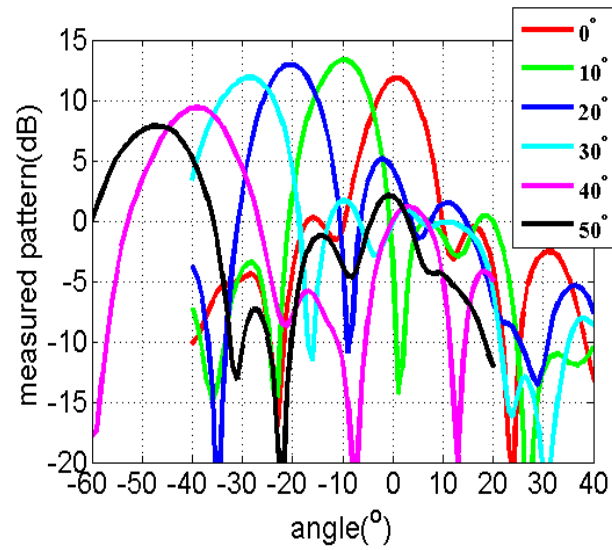
Fig. 6-75 Radiation patterns of the five configurations in PP1.
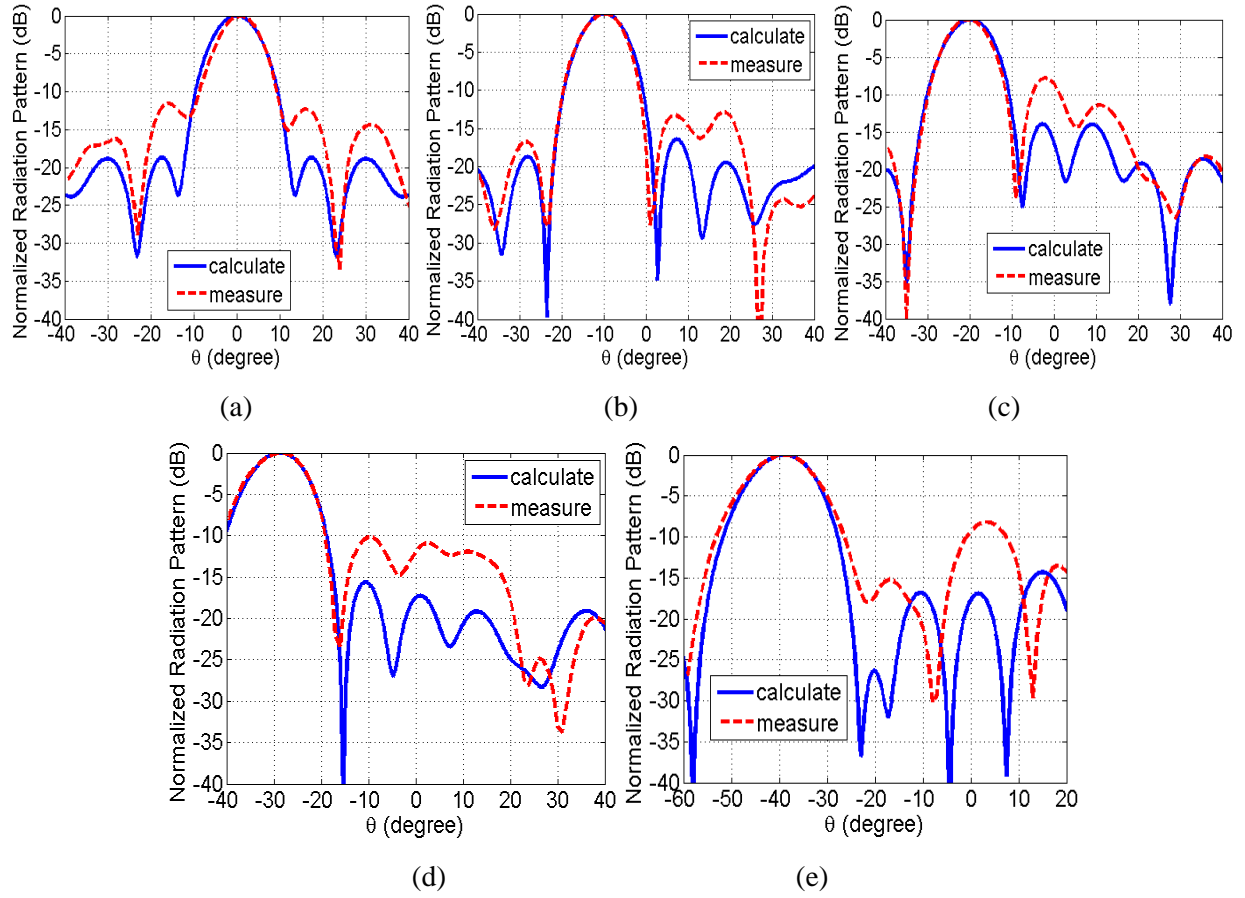
Fig. 6-76 Comparison between measured and simulated radiation patterns of the 10×10 reflectarrays at 12.5 GHz when the beam is steered to (a) 0°, (b) 10°, (c) 20°, (d) 30°, and (e) 40°.

Table 6-11 Summary of the simulation and measurement results

	Target	Δφ	Beam point		Gain (dB)		HPBW(°)		SLL(PP1,dB)	
			Com.	Mea.	Com.	Mea.	Com.	Mea.	Com.	Mea.
1	0°	95°	0°	1°	20.3	11.85	11	11	-18.7	-11.56
2	10°	5°	9.75°	10°	20.3	13.32	11	11	-16.4	-13.26
3	20°	75°	19.75°	20°	20.3	12.93	11.5	11	-14.0	-7.81
4	30°	135°	28.75°	29°	20.1	20.1	12.5	12	-15.6	-10.20
5	40°	135°	39°	39°	19.8	19.8	13	15	-14.3	-8.16

6.5.2 Analysis of Measurement Results

6.5.2.1 Overview of the Loss Factors

It is observed that the discrepancy between the simulation and measurement results is small for beam point direction and HPBW, but large for the SLL and gain. The possible reasons for the measured low SLL could be edge diffraction, element phase error and amplitude error, while for the low gain, it could be due to high SLL and large beamwidth in the other principle plane.

The analysis starts from the formula for the practical gain calculation, expressed as:

$$G = D \times \eta_{spill} \times \eta_{ill} \times \eta_{phase} \times \eta_{ele\_loss} \tag{6.2}$$

From the view of the formula, the possible calculation error for each factor is:

- η_{spill}: the spillover efficiency is calculated assuming that the reflectarray is in the far-field range while actually it is not this case;

- η_{ill}: this calculation is also based on the assumption that the reflectarray is in the far-field range while actually it is not this case;

- η_{phase}: the phase error could be introduced by both the inaccurate simulation of the PIN diode and the approximation of the oblique incidence;

- η_{ele_loss}: the element loss is not considered in the previous calculation;

From the view of the configurations, the two main contributors to the discrepancy between simulation and measurement results are:

- Near-field effect: usually it is required that all the following requirements are satisfied:

$$R > \frac{2D^2}{\lambda} \tag{6.3.a}$$

$$R \gg D \tag{6.3.b}$$

$$R \gg \lambda \qquad\qquad (6.3.c)$$

Where the 1st condition simply states that it should be maintained that the maximum phase error of an antenna equal to or less than $\pi/8$ radian; the 2nd condition is to ensure that the power radiated in a given direction from distinct parts of the antenna are approximately parallel; and the 3rd condition is to rule out the fields those die off with distance as $1/_{R^2}$. Apparently, the setup distance between the feed and the reflectarray does not meet the 1st requirement.

In such case, $cos^q\theta$ model might not be a good approximation for the horn pattern; the field strength does not attenuate in the way of $1/r$; and the RA elements could not be considered as being illuminated by plane waves anymore.

- Oblique incidence effect: for a simple patch, usually the approximation of normal incidence remains a good one when the incident angle is increased up to 30°, however, for this RRA unit which is much more complicated, the reflection magnitudes and phases illuminated by oblique incidence could differ a lot from the normal case.

In general, the effects of the possible reasons on various efficiencies are summarized as below:

Table 6-12 The effects of the possible reasons on various efficiencies

	Simulation model for PIN diodes (minor factor)	Near field (major factor)	Oblique incidence (major factor)
η_{spill}		Effect ($\lvert E_{inc} \rvert$)	
η_{ill}	Effect ($\lvert\Gamma\rvert$)	Effect($\angle E_{inc}$)	Effect ($\lvert\Gamma\rvert$)
η_{phase}	Effect ($\angle\Gamma$)		Effect ($\angle\Gamma$)
η_{ele_loss}	Effect ($\lvert\Gamma\rvert$)		Effect ($\lvert\Gamma\rvert$)

6.5.2.2 Effect of the Oblique Incidence Effect

Among the two major factors, it is difficult to evaluate the near field effect; however, the investigation of the oblique incidence effect could be somehow conducted in simulation software. The incident angle could be configured in the Master/Slave boundary condition in HFSS, as displayed in Fig. 6-77. And the effect of the oblique incidence will be analyzed following the method in [45].
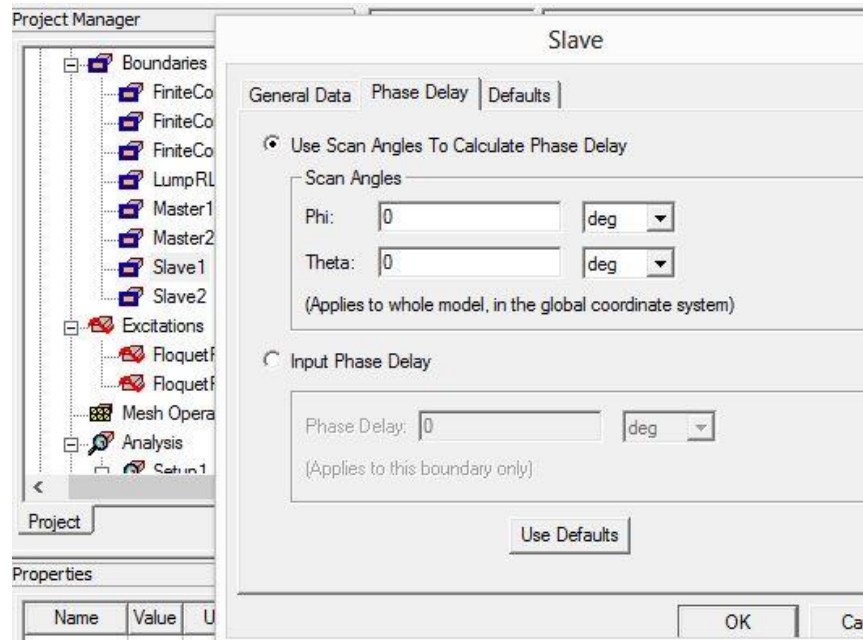
Fig. 6-77 Display of the master/slave boundary condition in HFSS.

As shown in Fig. 6-78, two cases ($\varphi = 0°$, $\theta = 0°$) and ($\varphi = 30°$, $\theta = 0°$) are studied in both TE and TM modes, and it can be seen that the φ essentially defines the incident plane, i.e. the E field direction. The same to the spherical coordinate, φ measures the azimuthal angle. Regarding the angle θ, its definition has been illustrated in Fig. 6-79, and the field plots for case ($\varphi = 0°$, $\theta = 30°$) in TE and TM modes are shown in Fig. 6-80.

172

(a)   (b)

(c)   (d)
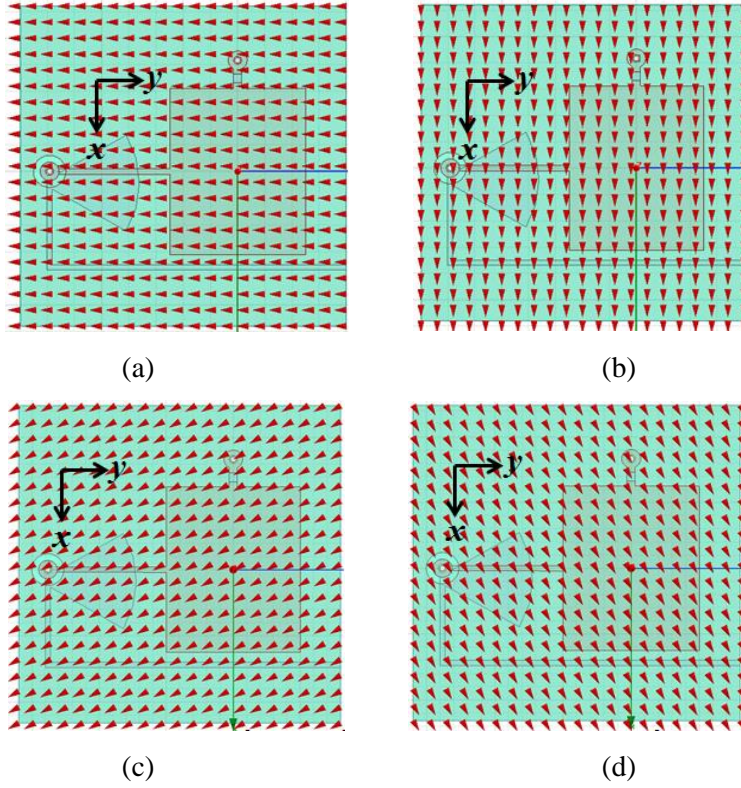
Fig. 6-78 Display of field port in (a) TE mode ($\varphi = 0°$, $\theta = 0°$), (b) TM mode ($\varphi = 0°$, $\theta = 0°$), (c) TE mode ($\varphi = 30°$, $\theta = 0°$), and (d) TM mode ($\varphi = 30°$, $\theta = 0°$).
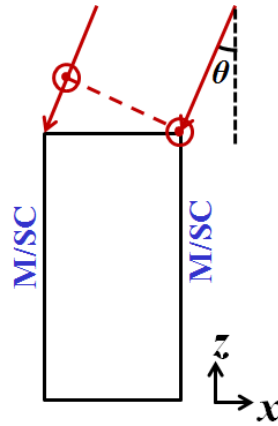
Fig. 6-79 Demonstration of the definition of theta in PCB in HFSS.

(a)   (b)
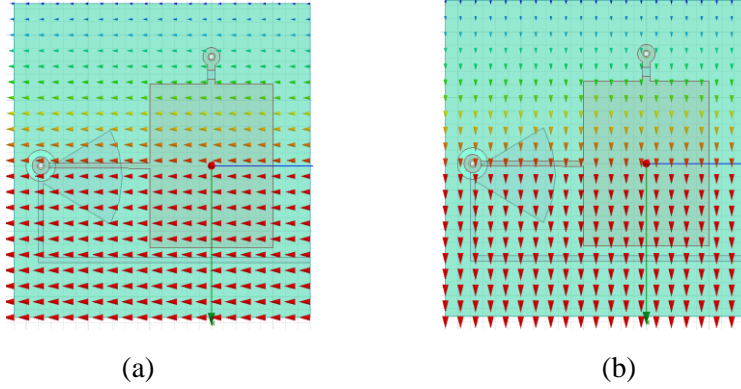
Fig. 6-80 Display of field port in (a) TE mode ($\varphi = 0°$, $\theta = 30°$), and (b) TM mode ($\varphi = 0°$, $\theta = 30°$).

The φ and θ of all the elements are calculated and displayed in Fig. 6-81, as well as summarized in Fig. 6-82 in the way of (φ, θ).

(a)   (b)
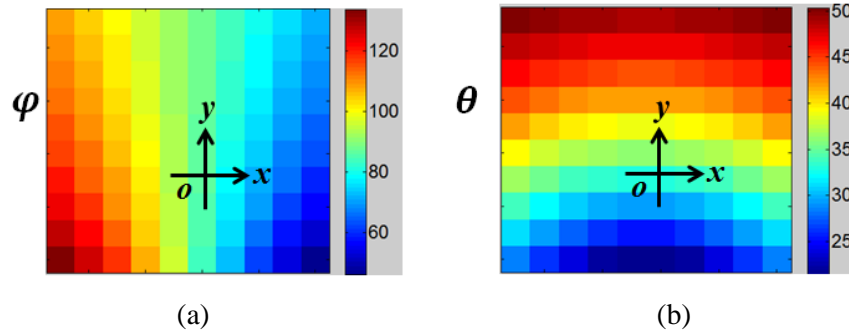
Fig. 6-81 Display of the incident fields on the elements in terms of (a) φ, and (b) θ.

x polarized

$(46°,29°)$	$(53°,26°)$	$(62°,24°)$	$(72°,22°)$	$(84°,21°)$	$(96°,21°)$	$(108°,22°)$	$(118°,24°)$	$(127°,26°)$	$(134°,29°)$
$(52°,31°)$	$(58°,29°)$	$(66°,27°)$	$(75°,26°)$	$(85°,26°)$	$(95°,26°)$	$(105°,26°)$	$(114°,27°)$	$(122°,29°)$	$(128°,31°)$
$(56°,34°)$	$(62°,32°)$	$(69°,31°)$	$(77°,30°)$	$(86°,29°)$	$(94°,29)$	$(103°,30°)$	$(111°,31°)$	$(118°,32°)$	$(124°,34°)$
$(60°,37°)$	$(65°,35°)$	$(72°,34°)$	$(79°,33°)$	$(86°,33°)$	$(94°,33°)$	$(101°,33°)$	$(108°,34°)$	$(115°,35°)$	$(120°,37°)$
$(63°,39°)$	$(68°,38°)$	$(74°,37°)$	$(80°,36°)$	$(87°,36°)$	$(93°,36°)$	$(100°,36°)$	$(106°,37°)$	$(112°,38°)$	$(117°,39°)$
$(65°,42°)$	$(70°,41°)$	$(75°,40°)$	$(81°,39°)$	$(87°,39°)$	$(93°,39°)$	$(99°,39°)$	$(105°,40°)$	$(110°,41°)$	$(115°,42°)$
$(67°,44°)$	$(72°,43°)$	$(77°,43°)$	$(82°,42°)$	$(87°,42°)$	$(93°,42°)$	$(98°,42°)$	$(103°,43°)$	$(108°,43°)$	$(113°,44°)$
$(69°,46)$	$(73°,46°)$	$(78°,45°)$	$(83°,45°)$	$(88°,44°)$	$(92°,45°)$	$(97°,45°)$	$(102°,45°)$	$(107°,46°)$	$(111°,46°)$
$(70°,48°)$	$(75°,48°)$	$(79°,47°)$	$(83°,47°)$	$(88°,47°)$	$(92°,47°)$	$(97°,47°)$	$(101°,47°)$	$(105°,48°)$	$(110°,48°)$
$(72°,50°)$	$(76°,50)$	$(80°,49°)$	$(84°,49°)$	$(88°,49°)$	$(92°,49°)$	$(96°,49°)$	$(100°,49°)$	$(104°,50°)$	$(108°,50°)$

Fig. 6-82 Display of the incident angle on all the elements in the means of (φ, θ).
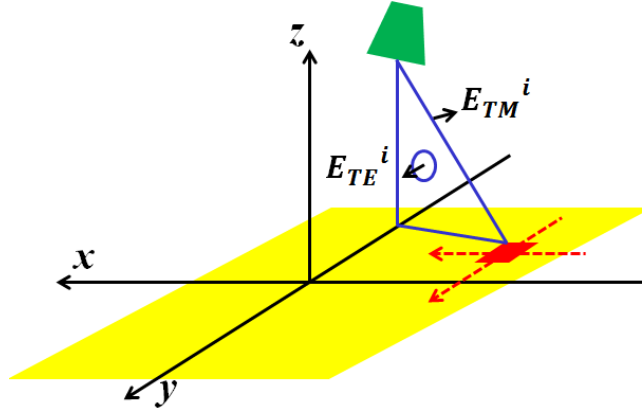
Fig. 6-83 Display the incident E-fields defination for TE/TM mode in HFSS.

The E-fields in TE/TM modes defined in HFSS are as showin in Fig. 6-83, i.e. the direction of the E-fields are dependent on the configuration of φ, while the magnitudes of the tangential compoents rely on the θ.

The oblique incidence effect on reflectarray elements in ON/OFF states and in TE/TM modes are investigated as using both HFSS and CST softwres as below:

- The Oblique incidence effect in OFF state in TE mode

The calculated results regarding the co-polarization and cross-polarization reflection coefficients are displayed in Fig. 6-84, and it is observed that the reflection phase generally varies more significantly along y axis. Besides, it looks like that φ has a big effect on the co-polarization reflection coefficients, and θ mainly affects the phase of the co-polarization reflection coefficients.
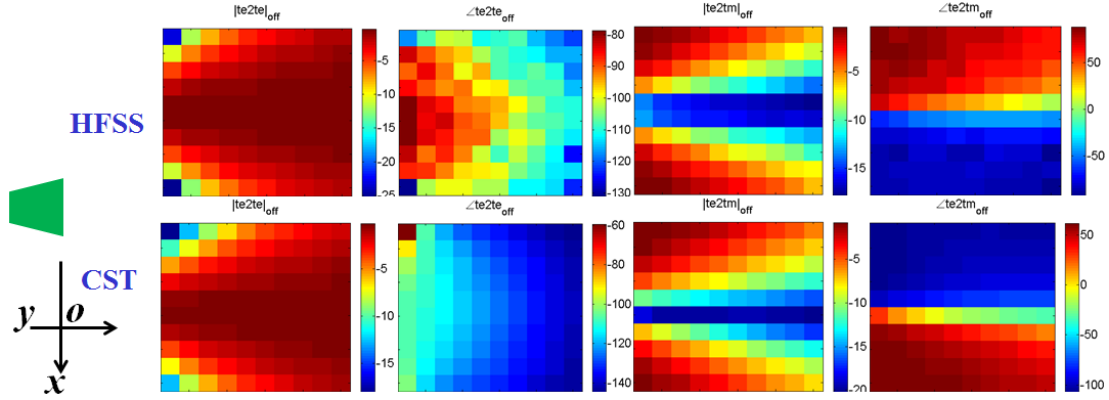
Fig. 6-84 Display of the calculated results regarding the co-polarization and cross-polarization reflection coefficients in OFF staste in TE mode.

- The oblique incidence effect in ON state in TE mode

The calculated results regarding the co-polarization and cross-polarization reflection coefficients are displayed in Fig. 6-85, and similar effects of φ and θ are observed.
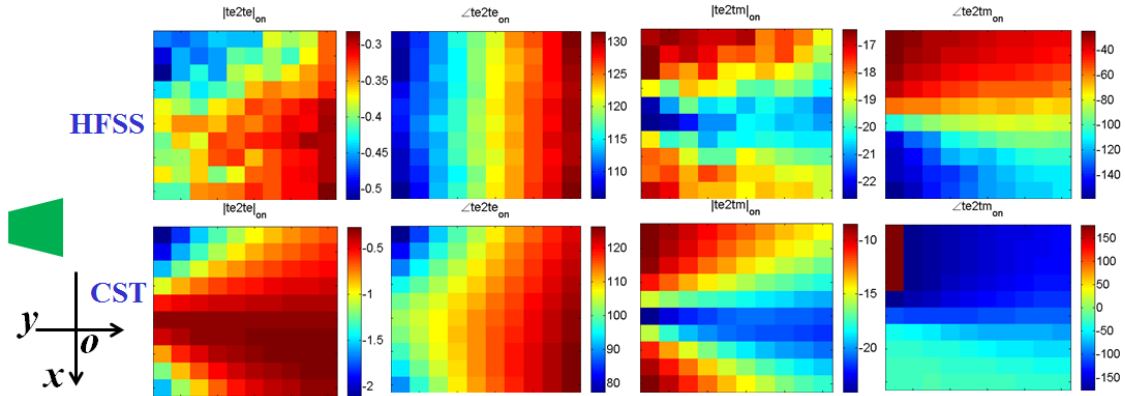
Fig. 6-85 Display of the calculated results regarding the co-polarization and cross-polarization reflection coefficients in ON staste in TE mode.

- The oblique incidence effect in OFF state in TM mode

The calculated results regarding the co-polarization and cross-polarization reflection coefficients are displayed in Fig. 6-86.
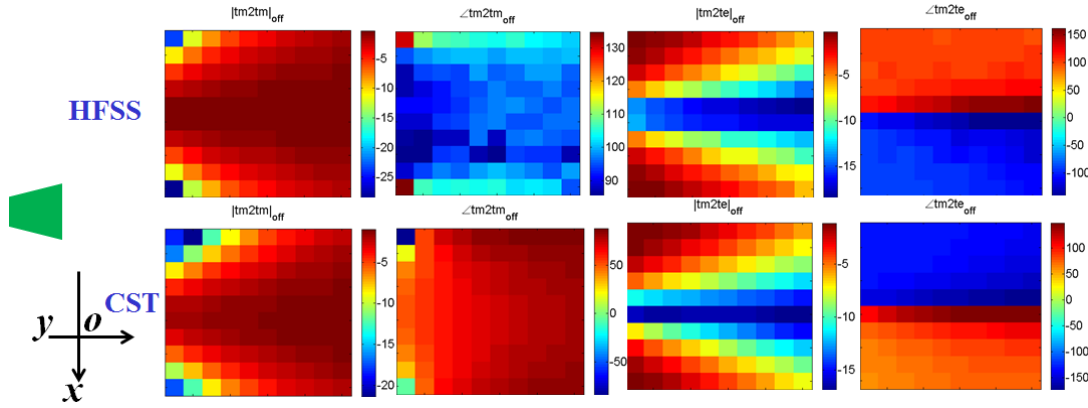
Fig. 6-86 Display of the calculated results regarding the co-polarization and cross-polarization reflection coefficients in OFF staste in TM mode.

- The oblique incidence effect in ON state in TM mode

The calculated results regarding the co-polarization and cross-polarization reflection coefficients are displayed in Fig. 6-87.
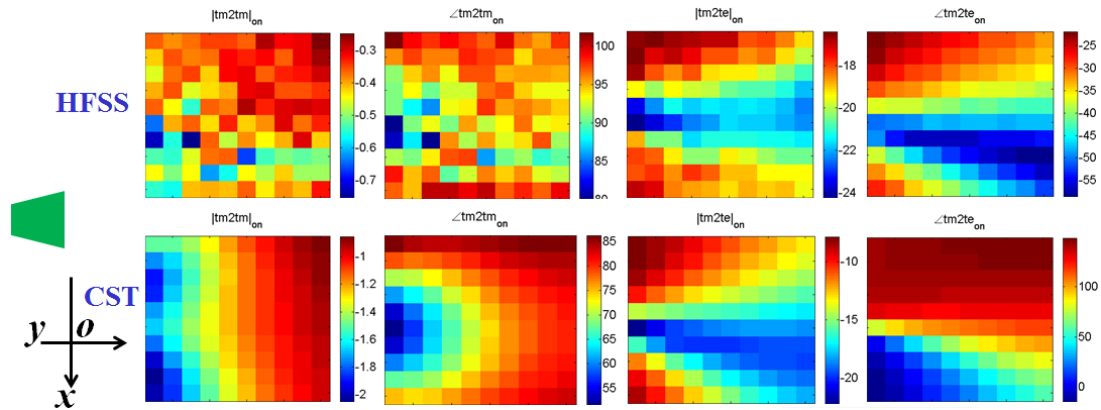
Fig. 6-87 Display of the calculated results regarding the co-polarization and cross-polarization reflection coefficients in ON staste in TM mode.

Starting from the incident fields, the x components of the reflected E-fields are calculated as below:

- As demonstrated in Fig. 6-88, the incident plane waves in TE and TM modes are calculated as expressed in (6.5), where E_x^i could be readily computed based on the configuration of the reflectarray;

$$E_{TM}^i = -E_x^i \times \sin\left(\varphi - \frac{\pi}{2}\right) \div \cos\theta \qquad (6.5.a)$$

$$E_{TE}^i = E_x^i \times \cos\left(\varphi - \frac{\pi}{2}\right) \qquad (6.5.b)$$
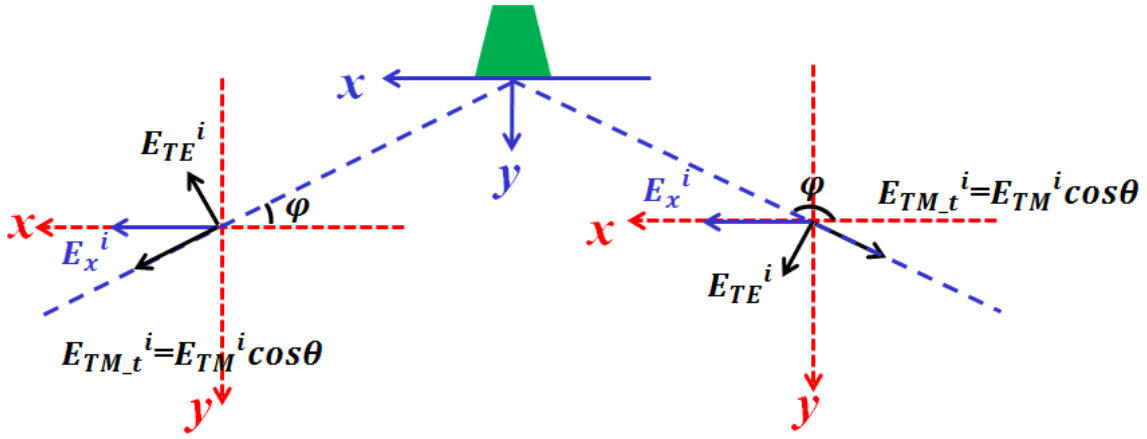
Fig. 6-88 Decompositon of x fields into ones in TE and TM modes.

- The reflected E-fields in TE and TM mode could be calculated as:

$$\begin{bmatrix} E_{TM}^r \\ E_{TE}^r \end{bmatrix} = \begin{bmatrix} r_{TM2TM} & r_{TE2TM} \\ r_{TM2TE} & r_{TE2TE} \end{bmatrix} \begin{bmatrix} E_{TM}^i \\ E_{TE}^i \end{bmatrix} \qquad (6.6)$$

Where the reflection coefficients for the co-polarization and cross-polarization could be computed based on the previous analysis

- Then, as demonstrated in Fig. 6-89, the reflection E-fields in the x direction could be composed with E_{TE} and the tangential component of E_{TM} and.

$$E_x^r = -E_{TM_t}^r \times \sin\left(\varphi - \frac{\pi}{2}\right) + E_{TE}^r \times \cos\left(\varphi - \frac{\pi}{2}\right) \qquad (6.7)$$

178
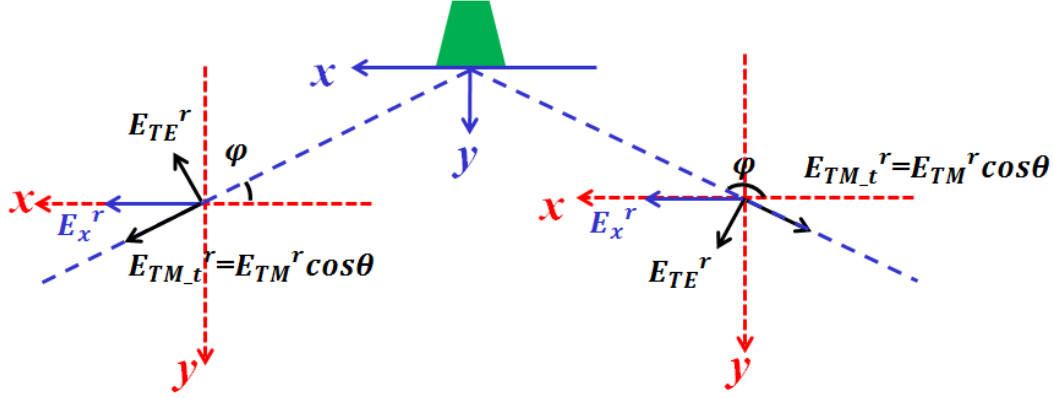
Fig. 6-89 Composition of x fields based on ones in TE and TM modes.

And the finally achieved compensated phase and the strengh of the reflection E-fields are diaplsyed in Fig. 6-90, which suggests that not only phase errors, but also severe element losses are introduced due to the oblique incidence.
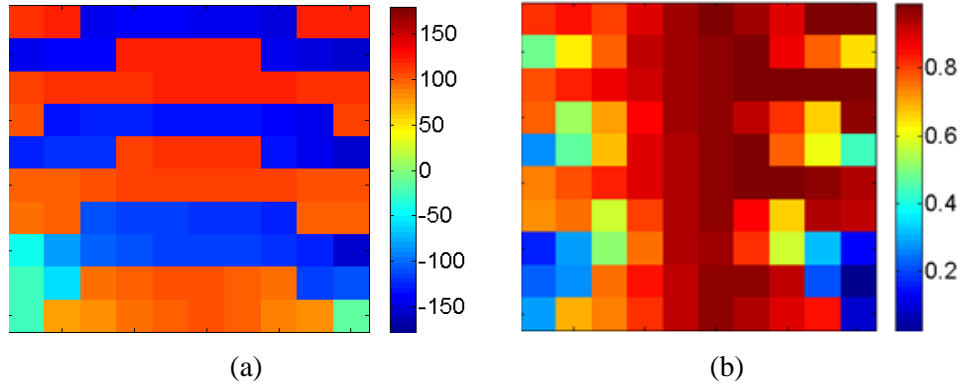
Fig. 6-90 (a) The compensated element phase and (b) the magnitude of the reflected E fields.

The results obtained by taking into account the effect of oblique incidence are compared with the one which uses the normal incidence approximation for all the cells. The measured and calculated radiation patterns in PP1 are displayed in Fig. 6-91(a), while the comparison between the computed patterns in PP2 is made in Fig. 6-91(b). It can be seen that ignorance of the inaccurate reflection coefficient calculations lead to a higher SLL in both planes.
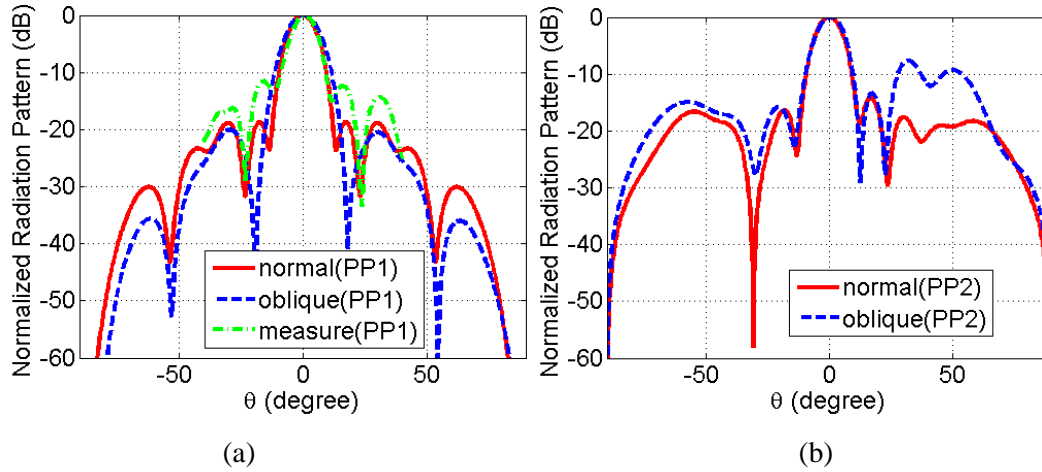
Fig. 6-91 (a) The measured and calculated radiation patterns in PP1, and the comparison of the radiation patterns in PP2.

6.5.3 Near-field Measurement

6.5.3.1 Measurement Setup

The experiment of this 10×10 RRA is configured as displayed in Fig. 6-92 (a). As it shows, the RRA is placed on the top of a table made of absorbing material and the feeding horn is supported by a tripod.

- The feed position is the same as the one in the 1st experiment: x=0 mm, y=-110 mm, z=143mm, and the corresponding feed illumination on the reflectarray is displayed in Fig. 6-92 (b).
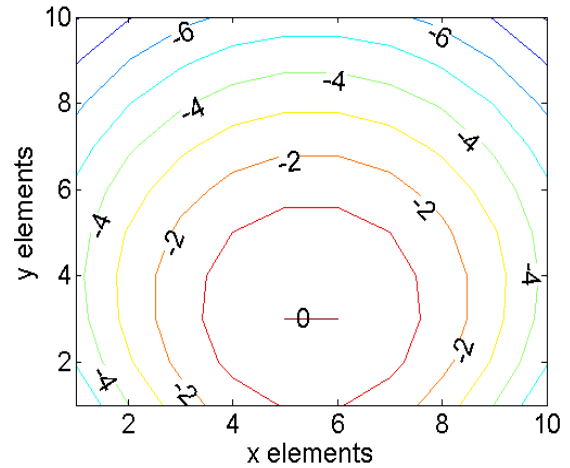
| (a) | (b) |

Fig. 6-92 (a) The setup configuration to measure the RRA (b) Feed illumination on the reflectarray (contour in dB).

- Polarization: linear polarization, in *x* direction

- Measured methods: near-field method

The measurement is conducted in an anechoic chamber using the NSI near-filed measurement system (Planar XY system), and the configuration in the NSI system is as below:

- X-Span: span range = 47.75725 inch, #pts = 106

- Y-Span: span range = 47.75725 inch, #pts = 106

- X-Sampling: delta = 0.45483 inch

- Y-Sampling: delta = 0.45483 inch

- AUT Width/Height: 4.7 inch, 4.7 inch

- H/V Max Far-field angles: 60.0 deg, 60.0 deg

- Probe-to-AUT spacing: 12.25 inch

- Probe model: OEWG WR62: 12.4~18.00 GHz

- Probe-1: Lin-0 (*Ex*), Probe-2: Lin-90 (*Ey*)

It is worthwhile to mention that if a larger area is expected to scan to ensure a proper measurement area truncation, it is better to: put the probe to the AUT as close as possible; and set the scan center as the zero position of the original geometrical system.

- Measured frequency range: 12.5 GHz

- Gain measurement method: comparison method[46]

It is worthwhile mentioning that the standard antenna should be accurately positioned and aligned as the AUT, which usually introduces some errors. And the gain for the standard antenna at 12.5 GHz is 14 dB.

- Designed measurement cases

Totally five cases are designed to validate the reconfigurability of the RRA, and the targeted pointing directions are summarized in Table 6-13.

Table 6-13 The targeted main beam directions of the designed cases for the near-field measurement

Case number	Targeted θ	Targeted φ
Case 1	0°	0°
Case 2	10°	0°
Case 3	20°	0°
Case 4	90°	20°
Case 5	90°	40°

6.5.3.2 Measurement Results and the Corresponding Analysis

The scanned amplitude distribution and phase distribution for each case is demonstrated in Fig. 6-93 and Fig. 6-94, respectively. It could be observed that the edge taper is close to -30 dB for almost all five cases. More importantly, the blockage of the horn and tripod can be seen clearly from the near-field results of the amplitude and phase.

(a)

(b)

(c)

(d)
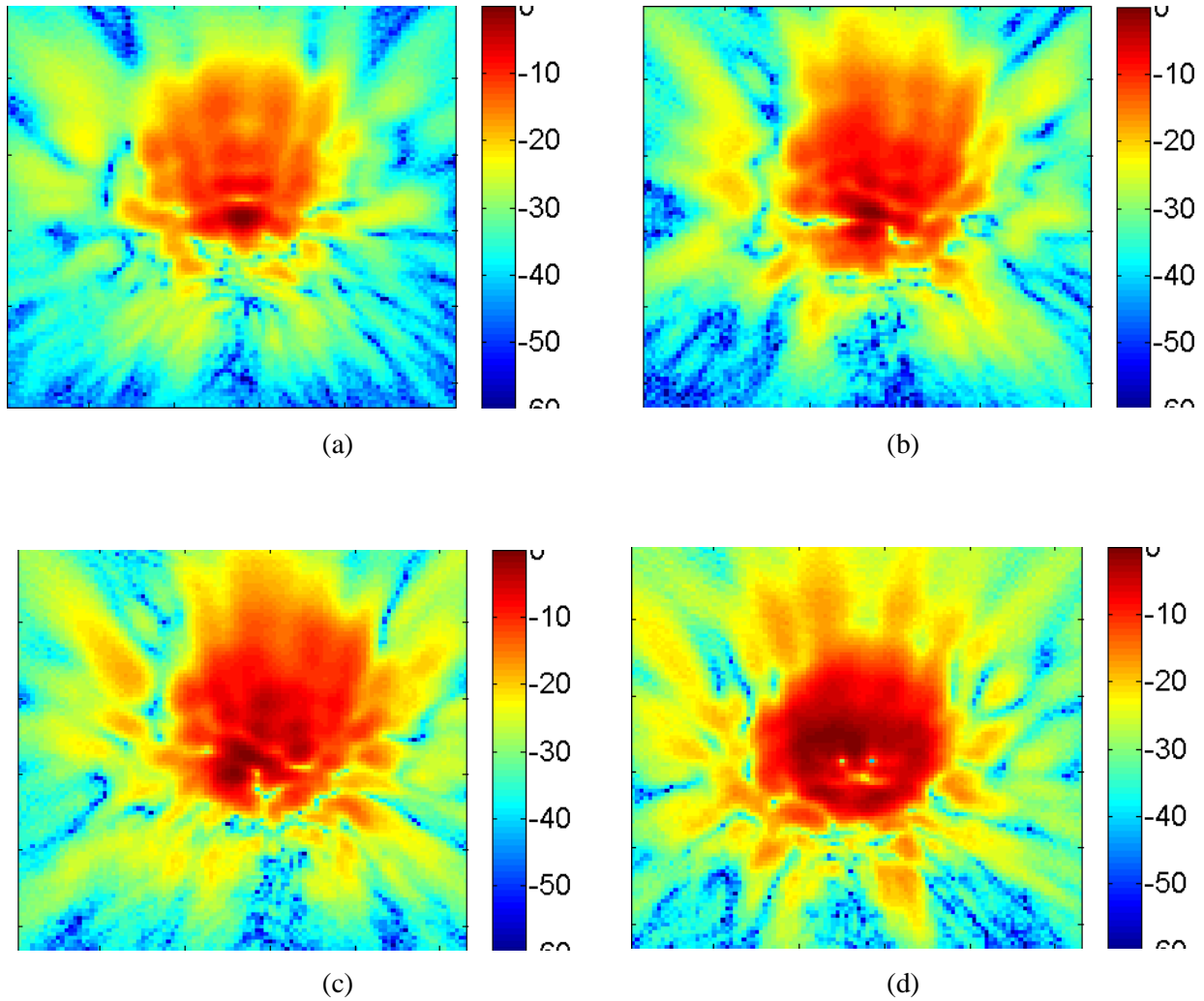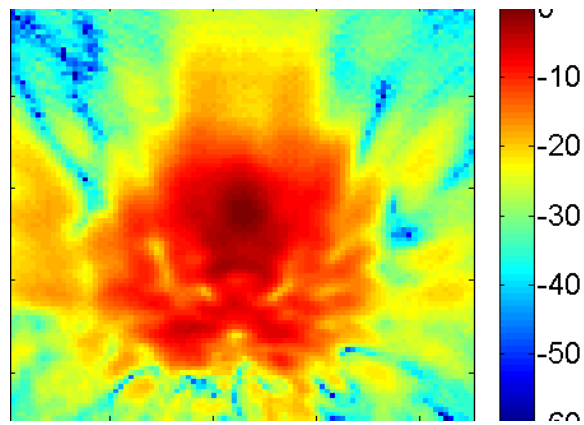
(e)

Fig. 6-93 The amplitude distribution in the near-field for Ex for (a) case 1 (b) case 2 (c) case 3 (d) case 4, and (e) case 5 .
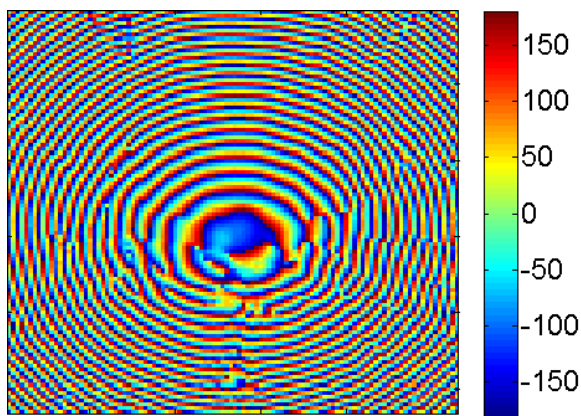
(a)
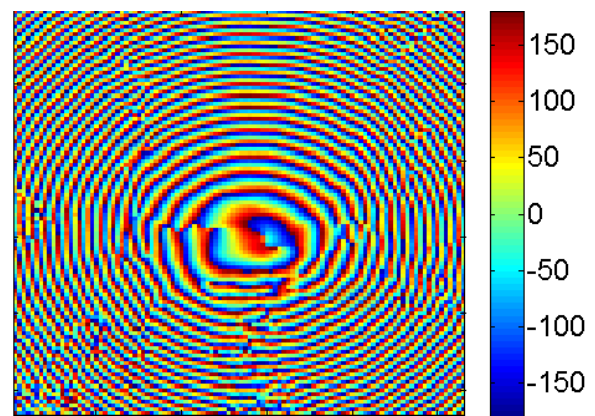
(b)
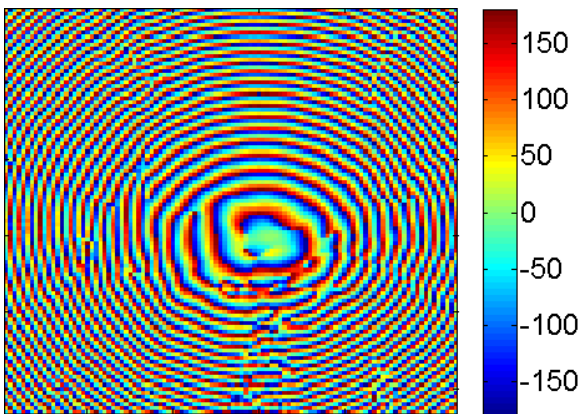
(c)
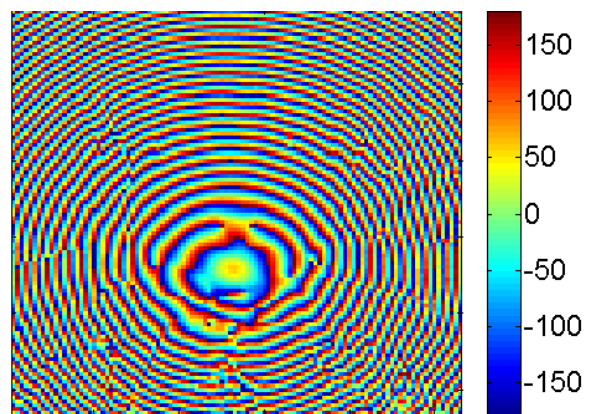
(d)
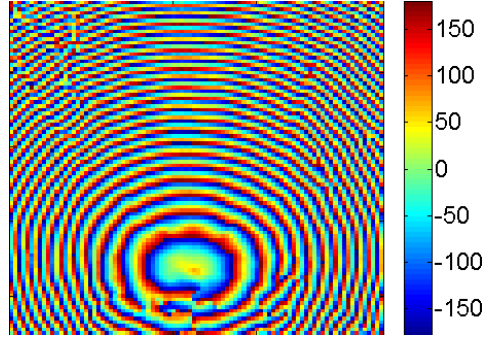
(e)

Fig. 6-94 The phase distribution in the near-field for Ex for (a) case 1 (b) case 2 (c) case 3 (d) case 4, and (e) case 5.

The measured and simulated radiation patterns in the *u-v* plane for these five cases are illustrated in Fig. 6-95, Fig. 6-96, Fig. 6-97, Fig. 6-98, and Fig. 6-99 for comparison, which validates the reconfigurability of the RRA. The measured main beam directions are (1.7°, -1.8°), (-2.0°, 10.0°), (-1.5°, 18.9°), (88.4°, 23.2°), and (87.0°, 39.9°), which are in good agreement with calculated ones. What is more interesting is that it can be seen from the radiation patterns for the 1st three cases that a higher level side-lobe appears in the specular direction of the feeding horn, which looks like the a mirror-like reflection behavior. More investigation is needed in the future work.

(a)   (b)
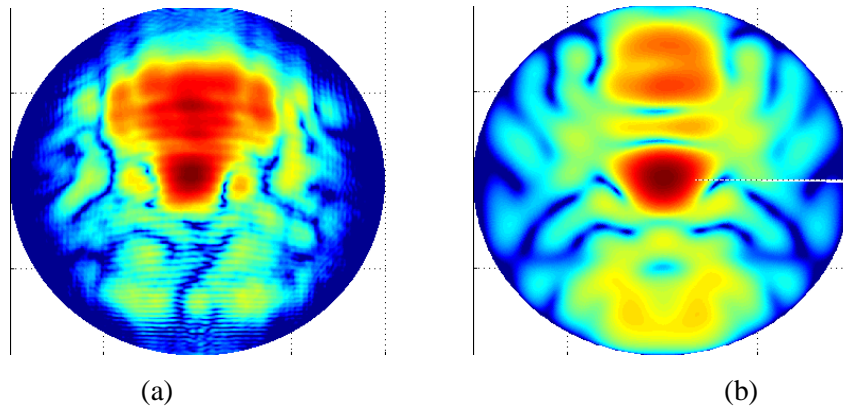
Fig. 6-95 (a) Measured and (b) simulated radiation patterns in the u-v plane for case 1.

(a)   (b)
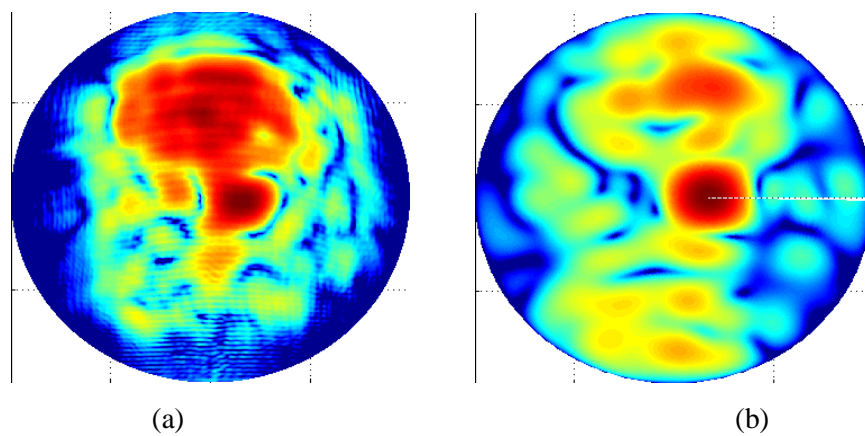
Fig. 6-96 (a) Measured and (b) simulated radiation patterns in the u-v plane for case 2.

(a)   (b)
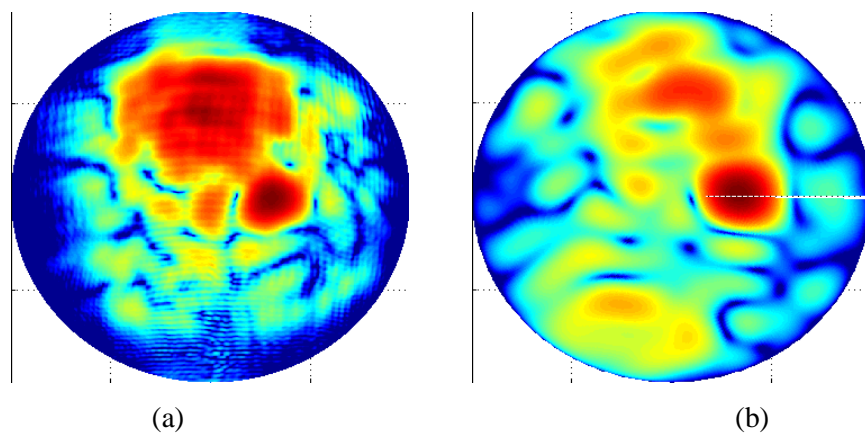
Fig. 6-97 (a) Measured and (b) simulated radiation patterns in the u-v plane for case 3.

(a)   (b)
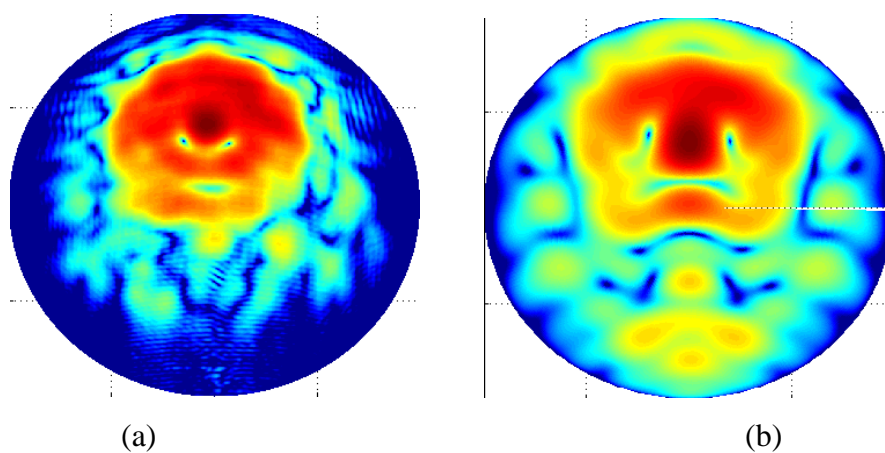
Fig. 6-98 (a) Measured and (b) simulated radiation patterns in the u-v plane for case 4.

| (a) | (b) |
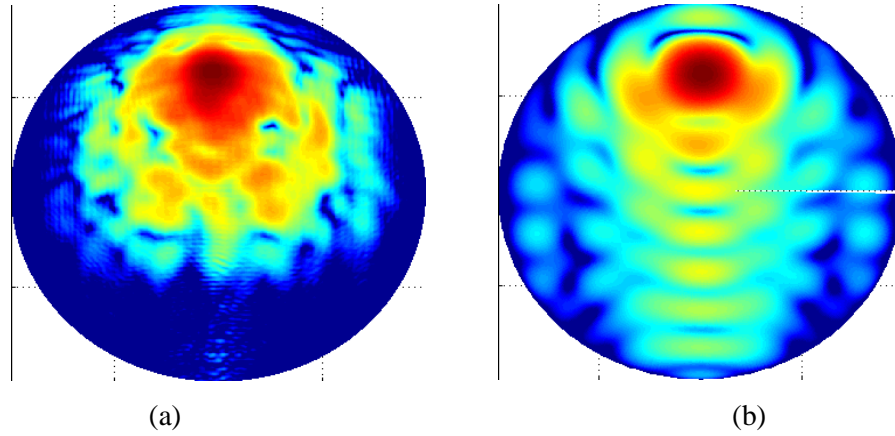
Fig. 6-99 (a) Measured and (b) simulated radiation patterns in the u-v plane for case 5.

Together with the near-field measurement results, all the efficiency-related ones are tabled in Table 6-14. It is observed:

- The directivity for the case (90°, 40°) is maximum, which might due to the least bloackage.

- The efficiency for the case (90°, 40°) reaches 14.1%, which is almost the same as the one in the published analog design with varactors.

- The spillover efficiency is very low for our experimental setup. However, as stated before, if the feeding horn is put even more closed to the reflectarray, the oblique angles become larger, thereby increasing the phase errors. More over, the near-field effect becomes more significant, the it will more difficult to predit the unit reflection coefficients.

- It is noticed that the differences between measured directivies and gains using near-field system are all around 3.6 dB, which somehow agrees well with the sum of the calcualted spillover and element losses.

- The maximum and minimum discrepancies between the calculated and measured directivies are 3.1 dB and 0.7 dB, respectively, however, for other cases, the dscrepancy is roughly 2 dB. The reasons for the discrepany could be the blockage and misalignment

187

in the measurement system, however, it is believed that the major contributor is still the phase error caused by the oblique incidence, which could not be accurately predicted using the simulation software.

- Since the gain of the feeding horn is 14 dB, it looks like that the measured gains using near-field method are more resonable. And the underestimated gain results using far-field method might due to the misalignment setup. Due to the limited time, the position of the RRA was not fine adjusted until the peak received signal is detected.

Table 6-14 Summaries of the simulation and measurement results

Target	D_{max} (dB)	η_{ill} (cal)	D (dB) Cal.	D (dB) Mea. (NF)	η_{spill} (cal)	$\eta_{element}$ (cal)	G (dB) Cal.	G (dB) Mea. (FF)	G (dB) Mea. (NF)	η_{tot} Mea. (NF)
(0°, 0°)	25.0	37.7% (-4.25 dB)	20.7	18.5	59.0% (-2.29 dB)	69.2% (-1.60 dB)	16.8	11.9	14.8	9.6%
(0°, 10°)	24.9	42.1% (-3.76 dB)	20.8	17.7	59.0% (-2.29 dB)	70.4% (-1.52 dB)	17.4	13.3	14.1	8.3%
(0°, 20°)	24.7	39.3% (-4.06 dB)	20.6	18.8	59.0% (-2.29 dB)	68.4% (-1.65 dB)	16.7	12.9	15.3	11.5%
(0°, 30°)	24.3	35.4% (-4.52dB)	19.8	--	59.0% (-2.29 dB)	67.6% (-1.7 dB)	15.8	11.9	--	--
(0°, 40°)	23.8	36.4% (-4.39 dB)	19.4	--	59.0% (-2.29 dB)	68.5% (-1.64 dB)	15.5	9.4	--	--
(90°, 20°)	24.7	25.5% (-5.96 dB)	18.7	18.0	59.0% (-2.29 dB)	75.0% (-1.25 dB)	15.2	--	14.4	9.3%
(90°, 40°)	23.8	58.2% (-2.35dB)	21.5	19.4	59.0% (-2.29 dB)	69.1% (-1.61 dB)	17.6	--	15.3	14.1%

Based on the measurement results, it could be concluded that if higher efficiency is desired, we need to design a unit structure less sensitive to oblique incidence and with even smaller element loss, which will also be part of the future work.

In order to investigate the element loss, tow more measurements are carried out, where all the PIN diodes are either on or off. Based on the results summarized in Table 6-15, it can be seen that although the calculation results predicts the element losses are 0.83 dB and 2.56 dB for the all-on and all-off cases, respectively, and differences between D and G are still roughly 3.6 dB for both cases, which requires more investigation in the future.

Table 6-15 Summaries of the results for all-on and all-off cases

Case	D (dB): Mea. (NF)	η_{spill}(cal)	$\eta_{element}$(cal)	G (dB): Mea. (NF)
All-on	17.9	59.0%(-2.29 dB)	83.4%(-0.83 dB)	14.3
All-off	16.5	59.0%(-2.29 dB)	55.4%(-2.56 dB)	13.0

CHAPTER VII

CONCLUSIONS

As a combination of traditional well-developed antennas, reflector antenna and microstrip antenna array, microstrip reflectarray antennas show significant promise as a new generation high-gain antenna with low-profile, low-mass and low-cost features. However, it still confronts with some new challenges in modeling, design, and practical application. In general, the research in this dissertation is focused on two different aspects, the bandwidth performance and the scanning performance.

7.1 Contribution of this Dissertation

The primary contributions of this dissertation are as follows. Regarding the bandwidth study:

- The bandwidth performance of different elements is firstly studied, because it is the most crucial contributor to the inherent narrow bandwidth of reflectarray. The effect of element shape is investigated based on the comparison among patch, cross dipole and square loop shapes, and the study results show that the element etched with patch shape. In addition the impact of the substrate thickness is also inspected, and it is shown that when a thicker substrate is utilized, the element bandwidth performance improves.

- The bandwidth performance is studied on the system level. The study is performed in two different aspects: the "hardware" and "software" perspectives. From the view of "hardware", effects of the aperture size and element characteristics are investigated, and it is shown that as the aperture size increases, the bandwidth decreases which is mainly due to the spatial phase delay and the improvement on the element bandwidth results in a reflectarray with larger bandwidth as expected. More importantly, from the view of "software", a novel phase synthesis method is proposed. With this method, the reflectarray bandwidth could be dramatically increased with elements with even narrow bandwidth at the cost of less than 1.5 dB gain loss. And this method could be very helpful especially when the element space becomes a constrained factor.

- Reflectarrays with different element shapes, substrate thicknesses, and phase synthesis methods are fabricated and measured, and all the theoretical conclusions were validated experimentally.

- Regarding the study of scanning performance, since the reflectarray is a hybrid of the reflector antenna and the microstrip antenna array, two different designs are made:

  o In the 1st design, the beam is steered by rotating the feeding array mechanically. The scanning mechanism is the same as the one for the cylindrical reflectarray; however, the phase distribution is optimized based on the analysis of the phase error introduced by the varied spatial phase delay, and the calculated results show that the scanning range is greatly improved.

  o In the 2nd design, the main beam direction is re-configured by changing the status of the PIN diodes integrated in the elements electrically. A 10×10 1-bit reconfigurable reflectarray is designed, implemented and measured, and during the procedure, some

light is shed on the selection of analog vs. digital designs, lower-bit vs. higher-bit designs, cross-polarization problems in element designs, and biasing-circuitry designs. Three different element structures are compared and it is found that if the element is not properly designed, significant cross-polarization could be introduced. And it is also found that for this 10×10 element design, the selection of the reference phase affects the reflectarray performance greatly in terms of both gain performance and side lobe level. This RRA is measured with both far-field and near-field methods, and the experimental results validate its 2-D dimensional reconfigurability. It is found that after the oblique incidence is taken into account in the cell simulation, the calculated and measured directivities agree with each other very well.

7.2 Future Work

The main focus of this dissertation was the improvement of the bandwidth and scanning performance of reflectarray antennas. However, a variety of possible topics remain on these two aspects:

- Regarding the bandwidth study, since much higher data rate is desired in the satellite communications, multi-band wide-band reflectarray becomes more attractive, which could support large high-speed data transmission for both up and down links. The phase optimization method proposed in chapter 4 should be very helpful in such case.

- Regarding the reflectarray with rotated feeding array, the calculation results have already shown the scanning performance could be greatly improved after the optimization of the phases. In the next, a prototype will be prepared and measured to validate the effectiveness of the phase optimization method.

- Regarding the reconfigurable reflectarray antenna, it looks like that the efficiency is a big problem for now. Based on the previous study, it is believed that if elements with better having cross-polarizations, being less sensitive to oblique angles and with even smaller loss could be designed, the efficiency will be further improved. Considering the application requirement in practice, elements with dual-linear and circular polarizations with good performance might be more desirable. Element design and DC supply design might be the challenges. Furthermore, since the PIN diodes are of very small size, reliable soldering techniques are required in the practical implementation.

BIBLIOGRAPH

[1]   J. Huang and J. A. Encinar, *Reflectarray Antennas*. John Wiley & Sons, 2007.

[2]   D. M. Pozar, "Bandwidth of reflectarrays," *Electron. Lett.*, vol. 39, no. 21, pp. 1490–1491, Oct. 2003.

[3]   E. Carrasco, J. A. Encinar, and M. Barba, "Bandwidth Improvement in Large Reflectarrays by Using True-Time Delay," *IEEE Trans. Antennas Propag.*, vol. 56, no. 8, pp. 2496–2503, Aug. 2008.

[4]   P. De Vita, A. Freni, G. L. Dassano, P. Pirinoli, and R. E. Zich, "Broadband element for high-gain single-layer printed reflectarray antenna," *Electron. Lett.*, vol. 43, no. 23, p. -, Nov. 2007.

[5]   O. Luukkonen, C. Simovski, G. Granet, G. Goussetis, D. Lioubtchenko, A. V. Raisanen, and S. A. Tretyakov, "Simple and Accurate Analytical Model of Planar Grids and High-Impedance Surfaces Comprising Metal Strips or Patches," *IEEE Trans. Antennas Propag.*, vol. 56, no. 6, pp. 1624–1632, Jun. 2008.

[6]   O. Luukkonen, P. Alitalo, C. R. Simovski, and S. A. Tretyakov, "Experimental verification of analytical model for high impedance surfaces," *Electron. Lett.*, vol. 45, no. 14, p. 720, 2009.

[7]   M. Bozzi, S. Germani, and L. Perregrini, "Performance comparison of different element shapes used in printed reflectarrays," *IEEE Antennas Wirel. Propag. Lett.*, vol. 2, no. 1, pp. 219–222, 2003.

[8]   P. Nayeri, A. Z. Elsherbeni, and F. Yang, "Radiation analysis approaches for reflectarray antennas," *IEEE Antennas Propag. Mag.*, vol. 55, no. 1, p. 127, 2013.

[9]   W. V. Cappellen, "Efficiency and sensitivity definitions for reflector antennas in radio-astronomy," presented at the SKADS MCCT Workshop, 2007, pp. 26–30.

[10]   "IEEE Standard Definitions of Terms for Antennas," *IEEE Std 145-1983*, pp. 1–31, Jun. 1983.

[11]   A. W. Rudge, *The Handbook of antenna design*. P. Peregrinus on behalf of the Institution of Electrical Engineers, 1986.

[12]   A. Yu, F. Yang, A. Z. Elsherbeni, J. Huang, and Y. Rahmat-Samii, "Aperture efficiency analysis of reflectarray antennas," *Microw. Opt. Technol. Lett.*, vol. 52, no. 2, pp. 364–372, Feb. 2010.

[13]   J. . Encinar, "Design of two-layer printed reflectarrays using patches of variable size," *IEEE Trans. Antennas Propag.*, vol. 49, no. 10, pp. 1403–1410, Oct. 2001.

[14]   J. A. Encinar and J. A. Zornoza, "Broadband design of three-layer printed reflectarrays," *IEEE Trans. Antennas Propag.*, vol. 51, no. 7, pp. 1662–1664, Jul. 2003.

[15]   M. R. Chaharmir and J. Shaker, "Broadband reflectarray with combination of cross and rectangle loop elements," *Electron. Lett.*, vol. 44, no. 11, pp. 658–659, May 2008.

[16]   M. E. Bialkowski and K. H. Sayidmarie, "Investigations Into Phase Characteristics of a Single-Layer Reflectarray Employing Patch or Ring Elements of Variable Size," *IEEE Trans. Antennas Propag.*, vol. 56, no. 11, pp. 3366–3372, Nov. 2008.

[17]   N. Misran, R. Cahill, and V. F. Fusco, "Design optimisation of ring elements for broadband reflectarray antennas," *Microw. Antennas Propag. IEE Proc.*, vol. 150, no. 6, pp. 440–444, Dec. 2003.

[18]   M. R. Chaharmir and J. Shaker, "Broadband reflectarray with combination of cross and rectangle loop elements," *Electron. Lett.*, vol. 44, no. 11, pp. 658–659, May 2008.
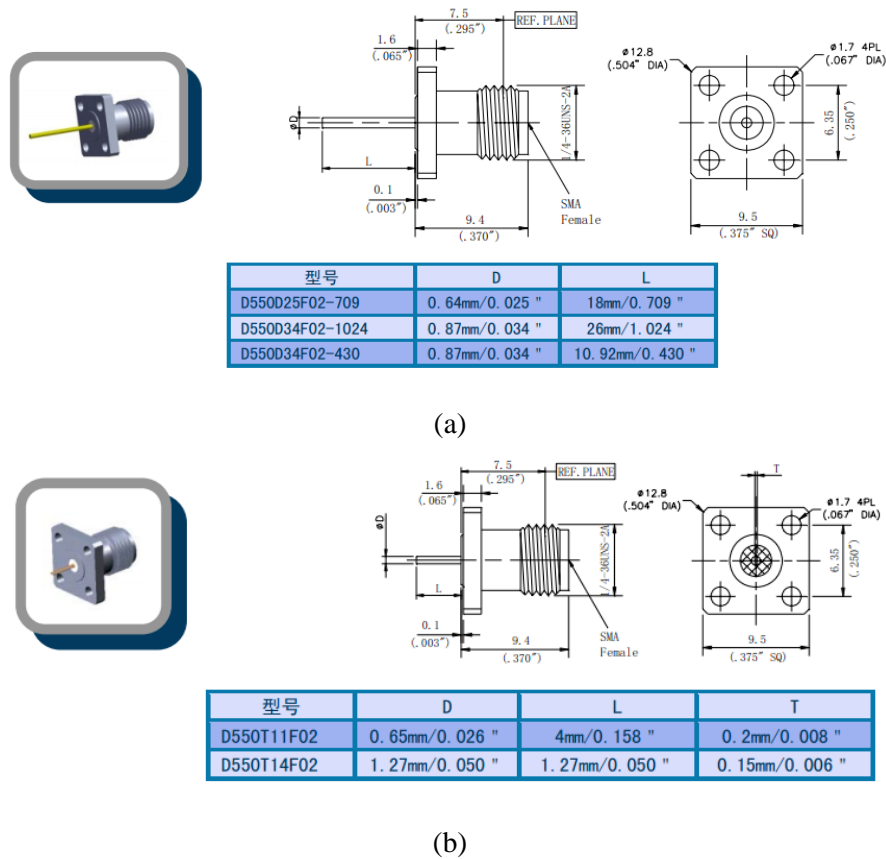
[19] M. R. Chaharmir, J. Shaker, and H. Legay, "Broadband Design of a Single Layer Large Reflectarray Using Multi Cross Loop Elements," *IEEE Trans. Antennas Propag.*, vol. 57, no. 10, pp. 3363–3366, Oct. 2009.

[20] J.-J. Zhao, S.-X. Gong, Y.-X. Xu, and L.-S. Ren, "A novel broadband reflectarray antenna using windmill elements," in *2010 9th International Symposium on Antennas Propagation and EM Theory (ISAPE)*, 2010, pp. 148–150.

[21] A. Capozzoli, C. Curcio, G. D'Elia, A. Liseno, and S. Sparice, "A Design Technique of Reflectarrays with Improved Frequency Performances," in *The Second European Conference on Antennas and Propagation, 2007. EuCAP 2007*, 2007, pp. 1–6.

[22] A. Capozzoli, C. Curcio, A. Liseno, and G. Toso, "Phase-only Synthesis of Flat Aperiodic Reflectarrays," *Prog. Electromagn. Res.*, vol. 133, pp. 53–89, 2013.

[23] P. Nayeri, F. Yang, and A. Elsherbeni, "Design of single-feed reflectarrays with asymmetric multi-beams," in *2012 IEEE Antennas and Propagation Society International Symposium (APSURSI)*, 2012, pp. 1–2.

[24] S. R. Rengarajan, "Scanning and Defocusing Characteristics of Microstrip Reflectarrays," *IEEE Antennas Wirel. Propag. Lett.*, vol. 9, pp. 163–166, 2010.

[25] P. Nayeri, F. Yang, and A. Z. Elsherbeni, "Bifocal Design and Aperture Phase Optimizations of Reflectarray Antennas for Wide-Angle Beam Scanning Performance," *IEEE Trans. Antennas Propag.*, vol. 61, no. 9, pp. 4588–4597, Sep. 2013.

[26] Y. Rahmat-Samii, J. Huang, B. Lopez, M. Lou, E. Im, S. L. Durden, and K. Bahadori, "Advanced Precipitation Radar Antenna: Array-Fed Offset Membrane Cylindrical Reflector Antenna," *IEEE Trans. Antennas Propag.*, vol. 53, no. 8, pp. 2503–2515, Aug. 2005.

[27] S.-H. Hsu, C. Han, J. Huang, and K. Chang, "An Offset Linear-Array-Fed Ku/Ka Dual-Band Reflectarray for Planet Cloud/Precipitation Radar," *IEEE Trans. Antennas Propag.*, vol. 55, no. 11, pp. 3114–3122, Nov. 2007.

[28] R. S. Elliott, "Antenna Theory and Design," Englewood Cliffs, NJ: Prentice-Hall, 1981.

[29] H. Kamoda, T. Iwasaki, J. Tsumochi, T. Kuki, and O. Hashimoto, "60-GHz Electronically Reconfigurable Large Reflectarray Using Single-Bit Phase Shifters," *IEEE Trans. Antennas Propag.*, vol. 59, no. 7, pp. 2524–2531, Jul. 2011.

[30] M. Riel and J. Laurin, "Design of an Electronically Beam Scanning Reflectarray Using Aperture-Coupled Elements," *IEEE Trans. Antennas Propag.*, vol. 55, no. 5, pp. 1260–1266, May 2007.

[31] J. Huang, "Analysis of a Microstrip Reflectarray Antenna for Microspacecraft Applications." Jet Propulsion Laboratory, TDA Progress Rep. 42-120, 1995.

[32] E. Carrasco, M. Barba, and J. A. Encinar, "X-Band Reflectarray Antenna With Switching-Beam Using PIN Diodes and Gathered Elements," *IEEE Trans. Antennas Propag.*, vol. 60, no. 12, pp. 5700–5708, Dec. 2012.

[33] O. Bayraktar, O. A. Civi, and T. Akin, "Beam Switching Reflectarray Monolithically Integrated With RF MEMS Switches," *IEEE Trans. Antennas Propag.*, vol. 60, no. 2, pp. 854–862, Feb. 2012.

[34] F. Venneri, S. Costanzo, and G. Di Massa, "Design and Validation of a Reconfigurable Single Varactor-Tuned Reflectarray," *IEEE Trans. Antennas Propag.*, vol. 61, no. 2, pp. 635–645, Feb. 2013.

[35] S. V. Hum, M. Okoniewski, and R. J. Davies, "Modeling and Design of Electronically Tunable Reflectarrays," *IEEE Trans. Antennas Propag.*, vol. 55, no. 8, pp. 2200–2210, Aug. 2007.

[36] R. Sorrentino, R. V. Gatti, and L. Marcaccioli, "Recent advances on millimetre wave reconfigurable reflectarrays," in *3rd European Conference on Antennas and Propagation, 2009. EuCAP 2009*, 2009, pp. 2527–2531.

[37] S. V. Hum and J. Perruisseau-Carrier, "Reconfigurable Reflectarrays and Array Lenses for Dynamic Antenna Beam Control: A Review," *IEEE Trans. Antennas Propag.*, vol. 62, no. 1, pp. 183–198, Jan. 2014.

[38] B. Wu, A. Sutinjo, M. E. Potter, and M. Okoniewski, "On the Selection of the Number of Bits to Control a Dynamic Digital MEMS Reflectarray," *IEEE Antennas Wirel. Propag. Lett.*, vol. 7, pp. 183–186, 2008.

[39] O. G. Vendik and M. Parnes, "A phase shifter with one tunable component for a reflectarray antenna," *IEEE Antennas Propag. Mag.*, vol. 50, no. 4, pp. 53–65, Aug. 2008.

[40] L. Boccia, F. Venneri, G. Amendola, and G. Di Massa, "Application of varactor diodes for reflectarray phase control," in *IEEE Antennas and Propagation Society International Symposium, 2002*, 2002, vol. 3, p. 132–.

[41] S. V. Hum, M. Okoniewski, and R. J. Davies, "Realizing an electronically tunable reflectarray using varactor diode-tuned elements," *IEEE Microw. Wirel. Compon. Lett.*, vol. 15, no. 6, pp. 422–424, Jun. 2005.

[42] H. Salti, E. Fourn, R. Gillard, and H. Legay, "Minimization of MEMS Breakdowns Effects on the Radiation of a MEMS Based Reconfigurable Reflectarray," *IEEE Trans. Antennas Propag.*, vol. 58, no. 7, pp. 2281–2287, Jul. 2010.

[43] H. Rajagopalan, Y. Rahmat-Samii, and W. A. Imbriale, "RF MEMS Actuated Reconfigurable Reflectarray Patch-Slot Element," *IEEE Trans. Antennas Propag.*, vol. 56, no. 12, pp. 3689–3699, Dec. 2008.

[44] F. Venneri, S. Costanzo, G. Di Massa, A. Borgia, P. Corsonello, and M. Salzano, "Design of a reconfigurable reflectarray based on a varactor tuned element," in *2012 6th European Conference on Antennas and Propagation (EUCAP)*, 2012, pp. 2628–2631.

[45] A. H. Abdelrahman, A. Z. Elsherbeni, and F. Yang, "Transmitarray Antenna Design Using Cross-Slot Elements With No Dielectric Substrate," *IEEE Antennas Wirel. Propag. Lett.*, vol. 13, pp. 177–180, 2014.

[46] A. C. Newell, R. D. Ward, and E. J. McFarlane, "Gain and power parameter measurements using planar near-field techniques," *IEEE Trans. Antennas Propag.*, vol. 36, no. 6, pp. 792–803, 1988.

APPENDIX I: AN EXPERIMENT OF A RECONFIGURABLE PATCH ANTENNA

AI.1 The Selection of Feeding Method

There are a variety of feeding methods for microstrip patch antennas. For the simplicity of design, probe-fed method is considered in 1st priority. Two categories of connectors, as displayed in Fig. AI-1, are investigated. For the purpose of matching, the diameter of the coaxial line is calculated using the online software displayed in Fig. AI-2, and the results are tableted in Table AI-1. However, the diameter of the outer probe, which is the same as that of the hole cut on the ground, looks so large that the ground could not behave well. Therefore, the usual MSL feeding line is selected.

型号	D	L
D550D25F02-709	0.64mm/0.025 "	18mm/0.709 "
D550D34F02-1024	0.87mm/0.034 "	26mm/1.024 "
D550D34F02-430	0.87mm/0.034 "	10.92mm/0.430 "

(a)

型号	D	L	T
D550T11F02	0.65mm/0.026 "	4mm/0.158 "	0.2mm/0.008 "
D550T14F02	1.27mm/0.050 "	1.27mm/0.050 "	0.15mm/0.006 "

(b)

Fig. AI-1 The dimension of the connectors of (a) 1st category, and (b) 2nd category.
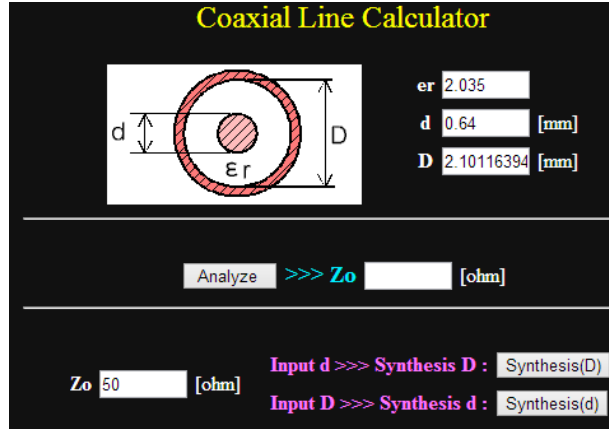
Fig. AI-2 The GUI online software to calculate the dimension for the coaxial line with specified material permittivity and inner diameter.

Table AI-1 Calculated diameters of the outer probe

Diameter of inner probe	Diameter of outer probe
0.64 mm	2.1 mm
0.65 mm	2.1 mm
0.87 mm	2.8 mm
1.27 mm	4.1 mm

AI.2 The Selection of Substrate Thickness

TLX-8 is selected for the substrate material, and its thickness is somehow dependent on the available connectors. Similarly, the schematic of the connector and the most important dimensions are displayed in Fig. AI-3. For the purpose of matching, the width of the 50Ω transmission line is calculated using the online software displayed in Fig. AI-4, and the results are summarized in Table AI-2. Considering the dimension of the patch is close to half of wavelength at 12.5 GHz, 0.25 mm is selected to be the substrate thickness.

Fig. AI-3 The dimension of the connecter.
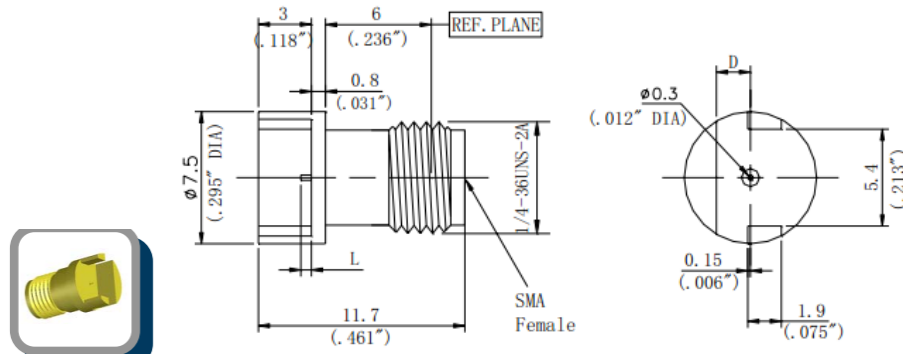
型号	D	L	适合板材厚度
D550B12E01-023	1.93mm/0.076 "	0.6mm/0.023 "	1.78mm/0.070 "
D550B12E02-023	0.76mm/0.030 "	0.6mm/0.023 "	0.61mm/0.024 "
D550B12E03-023	1.02mm/0.040 "	0.6mm/0.023 "	0.87mm/0.034 "
D550B12E01-048	1.93mm/0.076 "	1.22mm/0.048 "	1.78mm/0.070 "
D550B12E02-048	0.76mm/0.030 "	1.22mm/0.048 "	0.61mm/0.024 "
D550B12E03-048	1.02mm/0.040 "	1.22mm/0.048 "	0.87mm/0.034 "
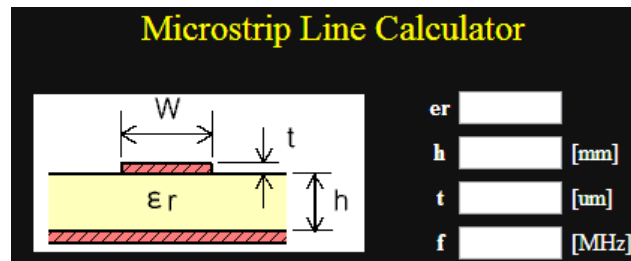
Fig. AI-4 Online software to calculate the width of transmission line with specified material permittivity, substrate thickness and frequency.

Table AI-2 The calculated width of 50Ω transmission line etched on substrate of different thicknesses

h(mm)	0.25	0.51	0.79	1.58
w(mm)	0.65	1.35	2.08	4.00

AI.3 The Design Procedure

The design procedure is described as below:

- 1st step: as shown in Fig. AI-5, a simple rectangular patch antenna is configured for simulation. A parametric study is made on *a*, which mainly decide the resonant frequency. The results of the parametric study are shown in Fig. AI-6, and *a* is selected to be 7.25 mm to set the resonance to be 12.5 GHz.
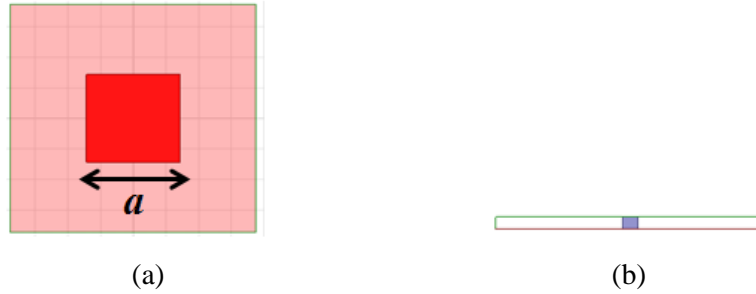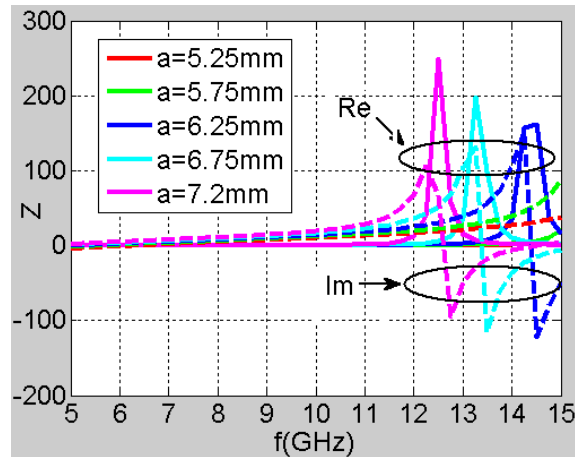

(a)   (b)

Fig. AI-5 (a) The top view and (b) side view of a simple patch.

Fig. AI-6 The real and imaginary parts of the input impedance for a simple rectangular patch.

- 2nd step: as shown in Fig. AI-7, an inset is cut at one edge to do the matching between the transmission line and the patch. In order to check the input impedance looking into the patch, the feeding transmission line will be added in the next step. Parametric study is done to *inset*, and the results demonstrated in Fig. AI-8 shows that when the value of

inset changes, the resonant frequency barely shifts but the real part of the input impedance does vary correspondingly. *Inset* is finally determined 2 mm.

(a)   (b)
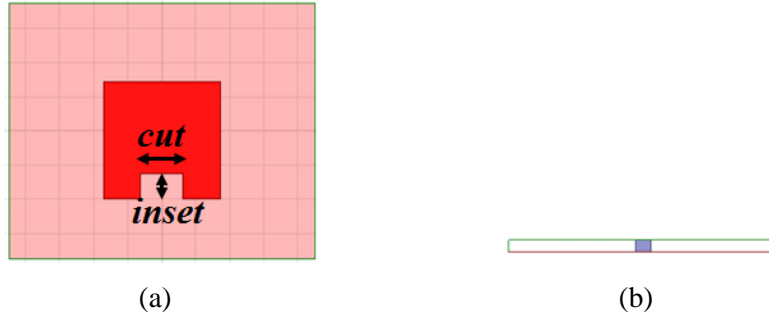
Fig. AI-7 (a) The top view and (b) side view of a simple patch with an inset.
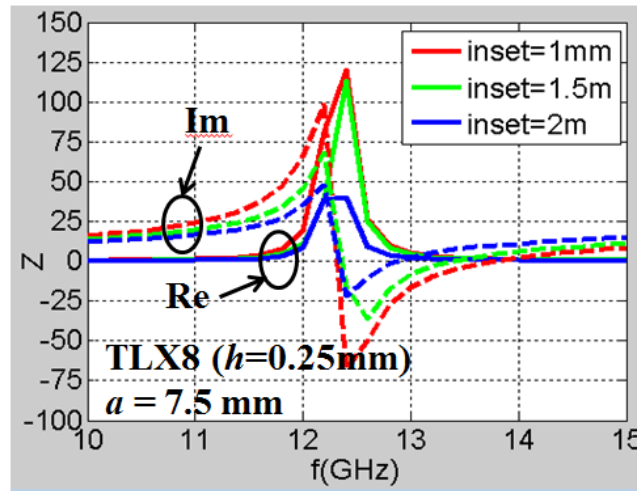
Fig. AI-8 The real and imaginary parts of the input impedance for a simple rectangular patch with an inset.

- 3rd step: a conventional inset-fed microstrip patch antenna is designed, and the geometry is drawn in Fig. AI-9, with all the parameters specified in Table AI-3. The simulated results of input impedance and S parameters are displayed in Fig. AI-10, which shows a very good resonance at the desired frequency 12.5 GHz.
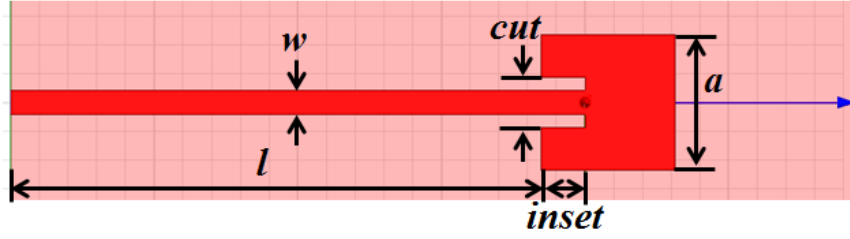
Fig. AI-9 The geometry of a conventional inset-fed patch antenna.

Table AI-3 Information of different tools

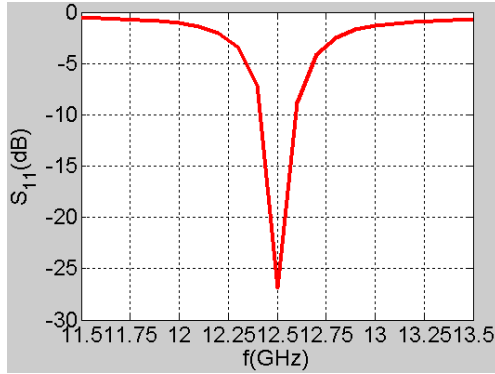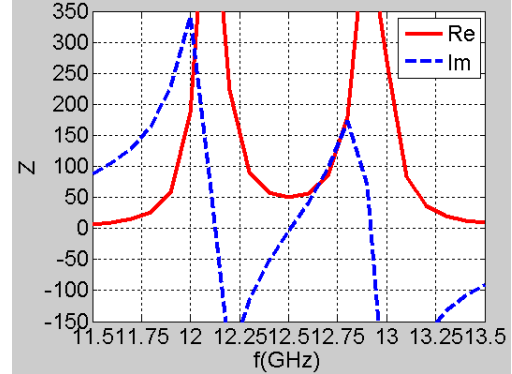| Material	h	w	a	inset	cut	l
TLX8	0.25mm	0.65 mm	7.46 mm	2.3 mm	1.95 mm	20 mm

(a)   (b)

Fig. AI-10 (a) The magnitude of S_{11} performance (b) The real and imaginary parts of the input impedance.

- 4th step: a via is added near to one of the edges. In practical implementation, there is a upper limit for the diameter of the via, which is dependent on the thickness of the substrate, and the diameter of the drilled hole is finally selected to be 0.2mm as shown in Fig. AI-11.

The S_{11} performance of the microstrip antenna integrated with pre-mentioned typical RLC model for the PIN diode is compared one with an ideal switch, where the entire slot

between the patch and the via is shorted for the ON state, and left as a gap for the OFF state. The

results are displayed in Fig. AI-12, which showed that the equivalent resistor/capacitor model for

the PIN diode has some small effect on the resonant frequencies for both ON and OFF states.
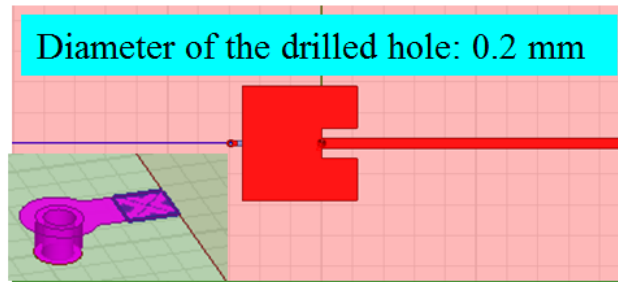
Fig. AI-11 A detailed illustration of a via drilled near the edge.
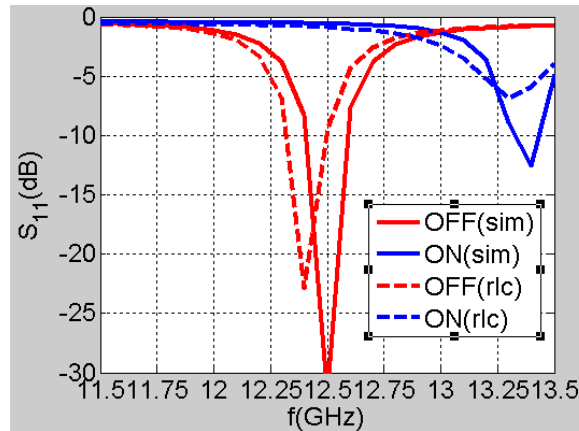
Fig. AI-12 The S_{11} performance of the microstrip patch antenna integrated with a practical PIN diode modeled with R or C, and an ideal switch.

However, it is noticed the resonant frequency for the ON state is lower than that for the

OFF state, which is out of expectation. We assume that this via acts like a shorting pin, therefore

the fundamental resonant frequency will be shifted down to even less than half of the original

one. In order to find out what was going on there, further study was performed in a much wider

frequency range from 1~18 GHz. A comparison is made between two configurations, one with

only one shorting pin in the middle of the edge and the other one with three shorting pins located with equi-distance between each other along the edge. Fig. AI-13 shows the S_{11} performance for these two configurations. As expected, the fundamental resonance for the one-pin case is much lower than half of the original resonant frequency, and the 2nd resonance is a little bit higher. For the three-pin one, the fundamental resonance is more close to half of the original resonant frequency, and the 2nd is even higher than that of the one-pin configuration.
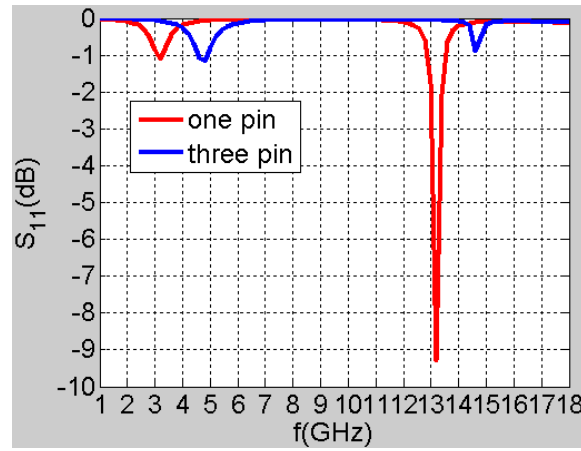
Fig. AI-13 The S_{11} performance of two patch antennas with one and three pins, respectively.

The corresponding E-field distributions for the fundamental mode are displayed in Fig. AI-14. The E-field distribution is more like the one for a quarter-wavelength shorted patch antenna. However, for the one-pin case, since there is only one pin located in the middle of the edge, it takes the current a longer path to travel from the opposite edge to the ground via the shorting pin. However, for the patch loaded with three shorting pins, it behaves more like one with a totally shorted edge.

(a)   (b)
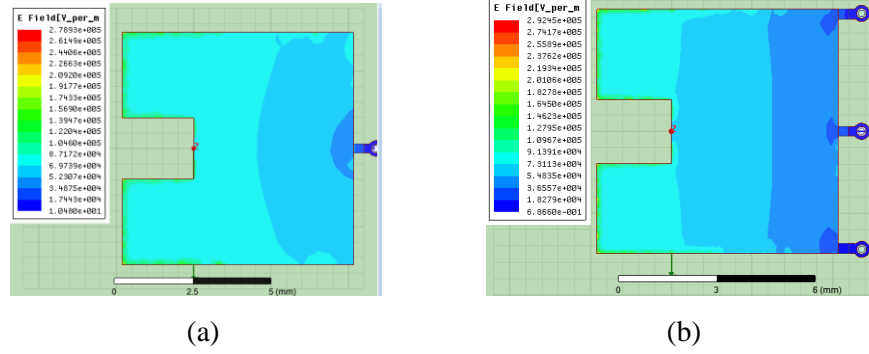
Fig. AI-14 The E-field distribution for the fundamental mode for patch loaded with (a) one and (b) three pins.

The corresponding E-field distributions for the higher mode are displayed in Fig. AI-15. They behave more like a half-wavelength patch antenna. Therefore, it could be concluded that the resonance for the ON state is actually the 2nd but not the 1st one for the shorted patch.

(a)   (b)
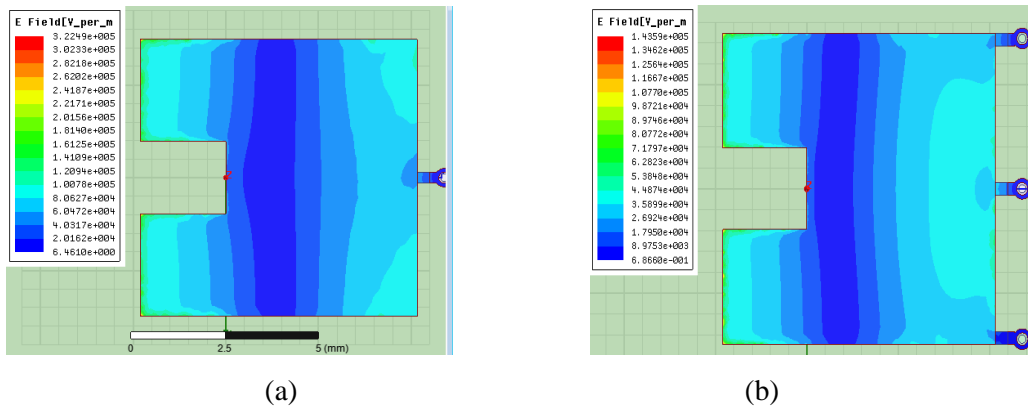
Fig. AI-15 The E-field distribution for the 2nd mode for patch loaded with (a) one and (b) three pins.

The equivalent circuit model is used to explain why the 2nd resonance of the shorted patch is a little bit higher than the original one. Fig. AI-16 (a) displays an equivalent circuit model for a simple patch, which is a parallel connection of a resistor and a capacitor, and the resonance frequency is calculated as:
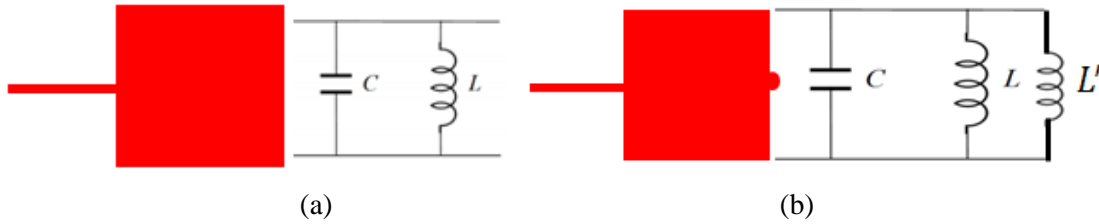
$$\omega_{01} = \sqrt{\frac{1}{LC}} \qquad\qquad (6.2)$$

However, when a shorting pin is added in the middle of edge, as shown in Fig. AI-16 (b), it is equivalent to add another inductor in parallel with the original circuit, and the resonance frequency becomes:

$$\omega_{01} = \sqrt{\frac{1}{(L \parallel L')C}} \qquad\qquad (6.3)$$

Which is a little bit higher than that of the simple patch.

(a)   (b)

Fig. AI-16 The equivalent circuit model for (a) a simple patch and (b) a simple patch loaded with a shorting pin.

Fig. AI-17 is the schematic of the reconfigurable patch antenna with DC biasing circuit. It is worthwhile mentioning that in addition to the RF choke structure consisted of a quarter-wavelength transmission line and radial stub, a capacitor needs to be inserted in the middle of the feeding transmission line to block the DC current. A 0.4 pf capacitor (ATC 600S OR4BT) is selected to serve the purpose of DC blocking based on the curves shown in Fig. AI-18. It is important that the working frequency should be below self-resonance frequency; otherwise it will behave like an inductor.
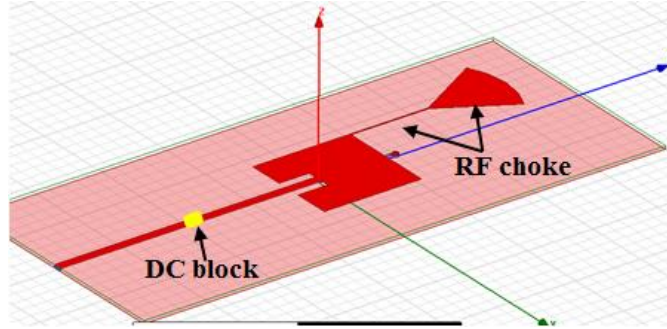
Fig. AI-17 The schematic of reconfigurable patch antenna with DC biasing circuit with both RF choke and DC block structures.
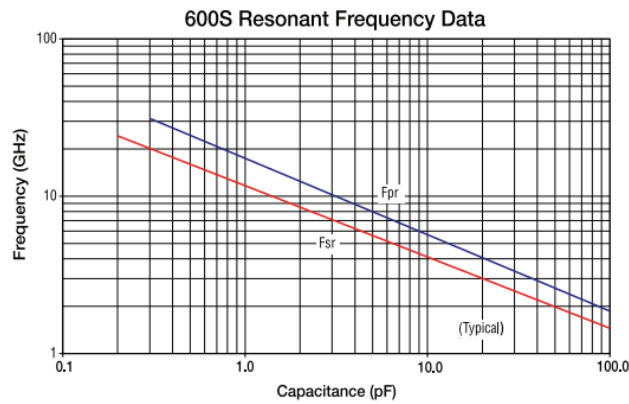
Fig. AI-18 The self-resonance frequencies of capacitors vs. capacitance.

AI.4 Fabrication and Measurement

A prototype was fabricated based on this configuration, and more fabrication details are shown in Fig. AI-19 and both the simulated and measured results are displayed in Fig. AI-20:


(a)   (b)   (c)
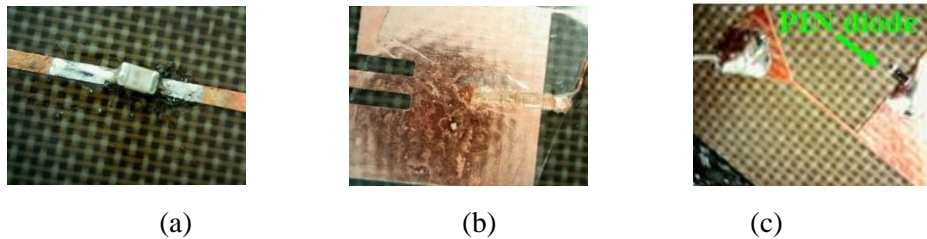
Fig. AI-19 (a) DC blocking capacitor (b) the patch (c) the RF choking and the PIN diode.

There are three kinds of results: 1st, the simulated results, referred as "sim"; 2nd, the corresponding measurement results of a prototype without a PIN diode, which is substituted by either a metal strip or an open circuit; 3rd, the corresponding measurement results of a prototype with a PIN diode, where the applied voltage is 1.01v for the OFF state while 1.31v for the ON state;

- For each case: the dash curve corresponds to the ON case, and the solid one corresponds to the OFF case;

- For the curves for ON state, there is some discrepancy between these three resonant frequencies;

- For the curves for OFF state, there is also some discrepancy between these three resonant frequencies;
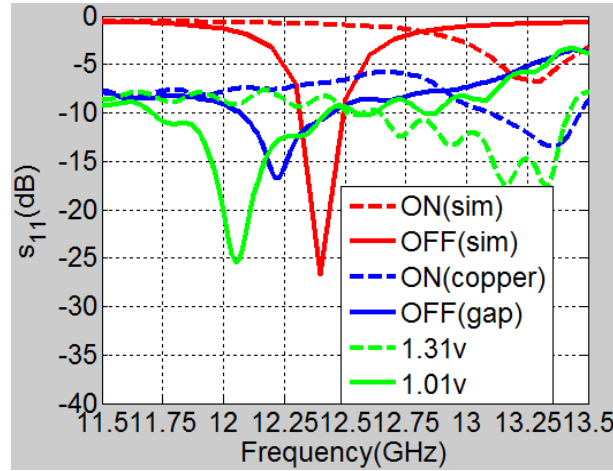
Fig. AI-20 The magnitude of S_{11} curves for the simulation model, the fabricated prototype without a PIN diode, which is substituted by either a metal strip or an open circuit, and the fabricated prototype with a PIN diode.
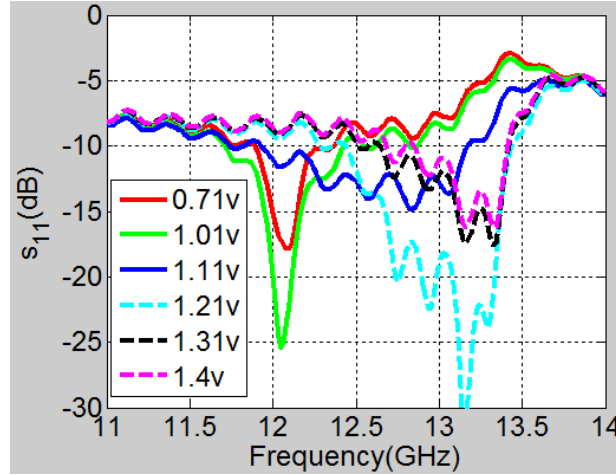
Fig. AI-21 The magnitude of S_{11} curves for the fabricated prototype with a PIN diode with different biasing voltages.

The applied voltage to the PIN diode is swept and all of the results are displayed in Fig.

AI-21. It is observed:

- When the voltage is below 1.01 v, it is safe to assume that the PIN diode is switched off;

- When the voltage is higher than 1.31 v, it is safe to assume that the PIN diode is switched on;

- When the applied voltage is between 1.01 v and 1.31 v, the PIN diode might neither work as a capacitor nor a resistor as simulated.

VITA

YILIN MAO

(662) 801-0884

yilin.juan@gmail.com

EDUCATION

Ph.D., Electrical Engineering, University of Mississippi, August 2014

B.A., Electrical Engineering, Beijing University of Aeronautics and Astronautics, July 2004

PUBLICATIONS and PRESENTATIONS

- H. Yang, Y. Mao, S. Xu, F. Yang and A. Z. Elsherbeni, "Analysis and Optimization of the Scanning Performance of 1-bit Reconfigurable Reflectarrays," *IEEE Antennas and Propagation Society International Symposium (AP-S)*, Memphis, Tennessee, 2014.

- F. Guo, Y. Mao, S. Xu, Fan Yang and A.. Z. Elsherbeni, "A Modified Parabolic-Cylindrical Reflectarray Antenna for Wide Beam Scanning Capability," *IEEE Antennas and Propagation Society International Symposium (AP-S)*, Memphis, Tennessee, 2014.

- Y. Mao, F. Yang and A. Z. Elsherbeni, "Closely Separated Dual-Band Reflectarray Design," *IEEE Antennas and Propagation Society International Symposium (AP-S)*, Orlando, Florida, 2013.

- Y. Mao, C. Wang, F. Yang, and A. Z. Elsherbeni, "A single-Layer Broad-band Reflectarray Design Using Dual-Frequency Phase Synthesis Method," *Asia Pacific Microwave Conference*, Taiwan, Dec. 2012.

- Y. Mao, Y. R. Padooru, K. Lee, A. Z. Elsherbeni, and Fan Yang, "Air Gap Tuning of Patch Antenna Resonance," *IEEE Antennas and Propagation Society International Symposium (AP-S)*, Spokane, Washington, 3-8 July, 2011.

- Y. Mao, J. Xue, F. Yang, and A. Z. Elsherbeni, "Development of an RFID system for indoor target localization," *URSI/USNC National Meeting*, Boulder, CO, Jan. 5 – 8, 2011.